Next-Generation Nanospectroscopy: Analytical and Numerical Models of New Developments in Electron Beam and Scanning Probe Experiments

Jacob A Busche

A dissertation
submitted in partial fulfillment of the
requirements for the degree of

Doctor of Philosophy

University of Washington

2021

Reading Committee:
David J. Masiello, Chair
David S. Ginger, Jr.
Bruce H. Robinson

Program Authorized to Offer Degree:
Chemistry

University of Washington

Abstract

Next-Generation Nanospectroscopy: Analytical and Numerical Models of New Developments in Electron Beam and Scanning Probe Experiments

Jacob A Busche

Chair of the Supervisory Committee:
Professor David J. Masiello
Chemistry

The research field of nanophotonics, which aims to understand the propagation of light at the nanoscale and design novel optically-active materials, has risen to prominence since the discovery of the surface plasmon in 1957. Early efforts to describe the intertwined motion of electrons, atomic nuclei, and electromagnetic waves inside small crystals have been built upon in recent decades, producing an increasingly precise picture of the spatial and spectral characteristics of polaritonic surface waves. The resulting range of proposed applications for materials and machines with nanoscopic components is enormously broad, stemming from ultrathin lenses to nanoscopic chemical reactors to biosensors.

Recent work toward the design and realization of new optical nanotechnologies has relied on the invention of near-field spectroscopic probes, or probes that bring free or bound charges near a sample to characterize its response to electrical stimulus. In contrast to optical microscopes, which rely on freely-propagating light to interact with a sample, near-field probes have much smaller fundamental resolution limits and are more capable of investigating the nanoscopic features and local fields of individual nanostructures.

In this dissertation, theoretical models are developed to improve the understanding of the coupling of two important surface phenomena, namely surface plasmons and surface phonons, with their environments in the context of electron beam and scanning-probe spec-

troscopies. These models are built with an eye toward the augmentation of existing experimental techniques and the invention of new ones. In particular, the influence of substrates on the plasmonic properties of mounted nanoparticles, the quantum-mechanical processes governing laser-stimulated electron-plasmon interactions, the extraction of intrinsic material properties from electron energy-loss spectroscopy, and the influence of the motion of hybridized plasmon-phonon polaritons on the radiation from nearby atomic force microscopy tips are discussed in detail. Finally, the models herein are combined with numerical simulations and compared with experimental data provided by collaborators to provide an intuitive and quantitative theoretical framework with which to interpret the observed signals.

TABLE OF CONTENTS

ACKNOWLEDGMENTS

This journey was made possible by my advisors at the graduate and undergraduate levels. Professor David Masiello, my advisor here at UW, introduced me to the universe of nanoscience and all of the unspoken rules it operates upon. He invited me into his group after a summer of undergraduate research through the NSF's 2014 National Nanotechnology Initiative (then referred to as an Infrastructure Network) REU program, and has done a wonderful job of showing me the ropes ever since. I will be forever grateful for the opportunities he has afforded me. I would also like to thank Professor Oksana Ostroverkhova of Oregon State University for giving me the opportunity to dip my toes into research at an early age (20!) and for having the patience to oversee my relatively slow start in the research world. She pushed me to apply to the REU program that eventually led me here, so in many ways she kickstarted this whole show. What an irreplicable gift.

I would also like to thank the many students and postdocs that I studied under and with throughout my time here at UW. Dr. Charles Cherqui was a second advisor to me, showing an uncommon degree of patience and providing a younger me all the support and guidance one could ask for. Drs. Niket Thakkar and Steven Quillin, as senior students in the group, helped me understand what a young scientist could and ought to be. Drs. Harrison Goldwyn and Kevin Smith, as my classmates, helped support me and commiserate as we suffered through Jackson problems and (barf) Smythe problems together. I'm so grateful to both of them for the years we got to spend together in the office, on a hiking trail, at a bar, or running around the lake. Elliot Beutler, who was the first scientist I ever attempted to mentor, was a great sport, travel companion, and friend and will soon enough get to call himself doctor. So too will Claire West, who has been a joy to work with over the past

half a decade. Last but not least, I'd like to thank Dr. Zhongwei Hu, Praise Anyanwu, Dr. Nicholas Montoni, Austin Nixon, Siamak Khorasani, Dr. Marc Bourgeois, Dr. Aniruddha Battacharya, and Nicole Panek for their insight, humor, and time.

My experience in graduate school would have been much less rich without the input of all of the group's experimental collaborators. Professors Jon Camden, Philip Rack, Daniel Gamelin, and Gerd Duscher, along with Dr. Juan Carlos Idrobo, provided an invaluable pool of talent to work with and learn from. Agust Olafsson and Joe Liberko, both of whom were very patient and thoughtful throughout our projects together, were wonderful to work with and learn from. Finally, I'd like to thank Dr. Jordan Hachtel, who took me in during my short time at Oak Ridge National Lab. Although we haven't published together yet, I hope to one day take full advantage of his prodigious talents.

My committee members have also all been gracious and generous with their support. Professor David Ginger, who always showed an abundance of enthusiasm for my research, was a fantastic pain during my examinations. Professor Arka Majumdar provided a wealth of insight into the engineering side of our field that I would never have been exposed to without him. And Professor Bruce Robinson, who can claim to be the only member of my committee to buy me a beer, was always the first to begin giving a hard time and the last to stop.

Last but not least, I'd like to thank my friends and family. Dr. Josh Mutch, (soon-to-be Dr.) Raphael Cervantes, Lillian Mutch, Sam Carlson and my brother Peter Busche were all wonderful roommates and friends to keep me company throughout my time in Seattle. Drs. Sam Barlow, Andrew Francis, Ben Figueroa, Amrita Basu, Emily Rabe, Meagan Gadzuk-Shea, Victor Lee, Trevor Johnston, as well as Jake Precht, Dr. Lucas Flagg, Camille Houferak, and many others of my cohort that I'm forgetting provided me with more friendship than I knew what to do with. Dr. Mitch Senger, D. Rene Zeto, and Mattson Thieme kept me going when times in undergrad got tough and I'm glad we stayed

in contact to stick together afterward. Tus Henry, Haley Bull, Marcus Weinman, Bianca Orozco, Megan Haverman, Aaron Seipel, Jacob Reimers, Dillon Snyder, Luke Chouinard, Spencer Nelson, Alex Main, Chadd Bergland, Darrin Bush, and Cory Gambill have been true friends for years and I'm deeply in debt to all of them. Finally, I'd like to thank my brother, Peter Busche for all his companionship, my (sort-of) sisters Melanie Gambill and Amy Garland for their lifelong friendship, and my parents, Susan and Al Busche, for being the parents a guy could ask for.

DEDICATION

To my parents, who made this long journey possible,
and to my brother, who made this long journey enjoyable

Chapter 1
INTRODUCTION

The vast majority of the technological advancements made by humanity over the past century have been spurred by the ability of scientists and engineers to observe and manipulate the structure of matter at the micron and nanometer length scales, beginning in the early 20^{th} century with discoveries in metallurgy [1, 2] and polymer chemistry [3] and later with cellular tissue culture [4] and the invention of the microchip [5, 6]. The microchip above the rest has led to a revolution in the global economy since its invention in 1959 [7] by automating computation tasks and vastly increasing the rate at which businesses, researchers, and, eventually, laymen could collect, transmit, process, and store data.

Microchips are capable of providing so much utility while consuming small amounts of power and volume because their components—transistors, wires, memory units—are constructed from pieces of silicon and metal only a few nanometers in any dimension. They are the most striking present-day example of a nanomaterial, i.e. a material whose useful properties emerge from carefully engineered nanoscopic features and cannot be found in naturally-occurring substances. Inspired by the successes of nanoscopic integrated circuits, scientists and engineers have proposed nanomaterials be used to provide performance benefits across an enormous range of applications, from chemical synthesis to biological sensing to body armor [8]. However, the efficient design and production of nanomaterials has been an outstanding challenge for the research community for over half a century, and most variants remain in development.

Given the extreme difficulties of observing and manipulating materials at the nanoscale, this is perhaps not so surprising. In fact, one can trace the long path to the invention and manufacture of nanomaterials actually to the beginning 20th century. Early work moved

slowly and focused on the basic features of electron motion within metals (Drude, 1900 [9]), which were poorly understood at the time, and the light scattered from metal colloids (Mie, 1908 [10]). Theoretical and experimental work a few decades later by Tonks & Langmuir [11] and Merrill & Webb [12], respectively, explored the ability of plasmas made of interacting charged particles to oscillate under excitation, and was followed by the efforts of Ledermann & Born [13] to understand the properties of electrons that exist in small crystals. The experimental works of Ruthemann [14] and Lang [15], which suggested that electrons within metals undergo low-energy oscillations when excited by passing electrons, led to the theoretical identification of the bulk plasmon by Pines & Bohm [16]. Alongside the works of Tamm [17], Landau [18], Pekar [19], and Fröhlich [20] on the motion of electrons and nuclei within nonmetal polar crystals and Frenkel [21], Wannier [22], and Mott [23] on the motion of electrons in semiconductors, the discovery of the bulk plasmon led to a burst of productivity in materials research.

The existence of the surface plasmon, a consequence of collective electron oscillations that occur near the surface of a metal, was proposed by Ritchie [24] in 1957. Powell & Swan [25] and and Stern & Ferrell [26] quickly confirmed this finding, demonstrating that nanoscopic features of a metal crystal have strong effects on its plasmon resonances and marking, arguably, the birth of the field of nanoscience as it exists today. Immediately following this discovery, the 1960s and 1970s witnessed the development of transistors with nanoscopic features [27, 28], the invention of the silicon-mounted integrated circuit, advancements in the understanding of the propagation and confinement of surface plasmons and polaritons along surfaces, and new strategies for focusing far-field light into propagating surface waves [29–33].

During this time, the study of nanoscopic semiconductors diverged from the study of metals and dielectric crystals due to the immediate industrial applications of integrated circuits and the invention of highly-precise semiconductor manufacturing techniques [34, 35]. In fact, these techniques, which allowed for the controllable deposition of single layers of semiconductor atoms on a substrate, represented the first surmounting of the longstanding

challenge to engineer materials with nanoscopic features. With this success in hand, the field of nanoelectronics separated from the other branches of nanoscience to pursue the minimization, optimization, and commercialization of integrated circuits.

The other branches, among them nanophotonics, nanomechanics, nanomaterials, and nanobiotechnology, aimed to develop technologies further afield which involved the confinement and manipulation of optical, kinetic, and chemical energy at the nanoscale. The field of nanophotonics, which will herein be the focus of this dissertation, was concerned primarily with the propagation of light within nanostructures and along surfaces. However, it faced a fundamental problem: because photons do not interact with matter as electrons do and much more readily "leak" from their nanoscopic confines, achieving optical confinement proved much more challenging than miniaturizing electrical components. Moreover, while some methods existed for the synthesis of individual nanoscopic particles [36], the ability of scientists to tailor them as needed or analyze them individually was lacking.

It was clear by the late 20^{th} century that new measurement techniques were required to answer many basic questions that governed the future utility of nanooptical technologies, including quantification of the magnitude of the interaction between individual nanoparticles and light, characterization of the strength and scale of the electric and magnetic fields set up near their surfaces, elucidation of their ability to form networks of interacting structures, and determination of the effects that particle size, shape, and surface roughness have on the motion of their excited electrons and nuclei. The only readily available measurement techniques involved optical microscopy, which has a fundamental resolution limit known as the diffraction limit that is roughly equal to half the wavelength of the light passing through the microscope. For problems involving visible light, the diffraction limit is around a few hundred nanometers, making optical microscopes of limited utility for observing characteristics of particles less than 100 nm in any dimension.

Proposals for the application of near-field probes, which use localized current sources rather than light waves to probe samples, arose in the late 1960s [32, 37]. Such probes are not restricted by the resolution limits of optical microscopes and were shown theoretically

to provide much more spatially precise measurements of nanoparticles. In the early 1980s, the theoretical predictions were proved correct, and two separate classes of experimental techniques were invented to fulfill the measurement needs of the field, giving rise to the modern era of nanophotonics.

The first, electron microscopy, uses a steady stream of accelerated electrons either to excite the electrons and nuclei within a nanostructure or to carry energy away from a sample. Early 20^{th}-century techniques were developed from the cathode-ray experiments of the late 1800s [38] and, as evidenced by the successes of Ruthemann, Lang, and Powell & Swan, were useful in the excitation and characterization of collective electron resonances known as plasmons. These results were improved upon dramatically by the pioneering work of Batson [39], Cowley [40], and Howie & Milne [41], conducted in the early 1980s, that demonstrated the ability of the electron beam to analyze the complete spatial and spectral profiles of the resonances of plasmons in individual nanoparticles. Measurements only expanded in resolving power from there: through the 1990s, 2000s, and 2010s, electron microscopes of different configurations were developed that could, via various techniques, probe the surfaces and individual nanoparticle excitations with spatial and spectral resolutions of 0.1–10 nm and $0.1\text{–}1 \times 10^{-4}$ eV, respectively, across a range of energies from the mid-infrared to energies well over 100 eV [42].

The second model of near-field probe that arose after the discoveries of the 1960s is the scanning probe, which uses a very sharp, optically polarized tip as either a current source or a focusing element. Developed from the early ideas of Synge [43] and O'Keefe [44] as a method for funneling light through a nanoscopic aperture, a working near-field optical microscope of this type with sub-diffraction resolution was first demonstrated in 1972 [45]. Following this advancement, the 1980s–2010s saw improvement of the spectral resolution of scanning-probe microscopy to below 20 nm [46–48] and its extension to infrared frequencies [49, 50], providing a nanomicroscopy technique with a wide operating frequency range, $\sim 1 \times 10^{-4}$ eV spectral resolution, a non-contact mode of operation capable of analyzing soft-matter and biological samples without damage and, most importantly, the ability to observe the

complete set of resonances of a nanoscopic target.

With the increased control over the nanoscale provided by these experimental tools, the study of nanophotonics has blossomed over the past two decades to provide numerous theoretical and experimental discoveries important for the understanding and design of novel technologies [42, 51]. Correspondingly, the number of proposed applications for optically-active nanostructures has ballooned: precision chemical and biological sensing [52, 53], photovoltaic conversion improvement [54–57], cancer treatments [58, 59], medical and biomolecular imaging [60, 61], and thermometry and temperature control[62, 63] stand to benefit from the ability of surface plasmons to focus light and heat at the nanoscale. Plasmon-mediated photocatalysis [64, 65] and polariton chemistry [66] may, one day, leverage the coupling bewteen electronic states in molecules and tailored optical cavities to enable new chemical synthesis methods. Signal processing [67], aviation sensing [68, 69], and artificial intelligence [70] may all be made more efficient, sensitive, and powerful by the rapid transport of light in integrated optical circuits.

1.1 Organization of this Dissertation

Although these technologies currently exist only in laboratories, prototypes, and clinical trials, the importance of optically-active nanomaterials may rival that of nanoelectronics in the technologies of tomorrow. To realize the potential of nanophotonics, a great deal of work in both experiment and theory remains to be done. This dissertation is inspired by this challenge, as well as the long and successful tradition of collaboration between experimental and theoretical work within the field that has brought it to its current state [42, 71–75]. It focuses on the interpretation of data from novel applications of existing electron energy-loss and scanning near-field optical microscopy techniques as well as the development of new experimental methods. Both analytical models and numerical simulations are presented, and both classical and quantum electrodynamics theories are used to describe the material resonances, particles, and fields relevant to each given problem. As the variety of the problems presented is wide, the solutions and discussions are presented as they appear in their original

published forms. In detail:

- Chapter 2 details the solution of the long-standing nanophotonics problem wherein the localized surface plasmon modes of a metal nanocube interact with a supporting substrate in a scanning transmission electron microscope to produce both resonance energy splitting and mode localization effects in electron energy-loss experiments. A simple model demonstrates why these effects appear in nanocubes and not in nanospheres and how the substrate can affect the cube's plasmon properties even when the substrate is thin and has a small refractive index. The material for this chapter is reproduced with permission from Ref. [76] (©American Chemical Society 2018).

- Chapter 3 details the development of a new stimulated electron energy-loss and energy-gain spectroscopy as demonstrated both by experiment and theory. In particular, it showcases the first stimulated electron energy-gain measurements made using a light sources operating in continuous-wave mode as well as the first theoretical decomposition of the complete set of first- and second-order quantum mechanical scattering processes that contribute to stimulated loss and gain signals. The material for this chapter is reproduced with permission from Ref. [77] (©American Chemical Society 2019).

- Chapter 4 details the development of a first-of-its-kind ellipsometry experiment that infers the dielectric function of a single nanoparticle from an electron energy-loss spectrum. Experimental energy-loss data are presented for 20 nm diameter indium tin oxide nanospheres excited by electron beams in aloof and penetrating trajectories, and a theoretical description is constructed from first principles that connects the loss signal to the material properties of the spheres. Implications of the development are discussed. The material for this chapter is reproduced with permission from Ref. [78] (©American Chemical Society 2020).

- Chapter 5 details the interpretation of scanning infrared nanospectroscopy experiments performed on long gold nanorods mounted on silicon dioxide and boron nitride sub-

strates. The plasmon modes of the nanorods are shown to hybridize with the surface phonon resonances of the substrates both in experimental data and by analytical modeling. The relationship between the unusual experimental signal and the anticrossing behavior of the target resonances is discussed. The material for this chapter is reproduced with permission from Ref. [79] (©American Physical Society 2021).

1.2 List of Publications

The author's peer-reviewed work in the Masiello group includes seven published or accepted papers and an eighth and ninth in preparation to be published with all haste. Works in which the author was a lead or co-lead theorist have his name shown in bold. Authors of equal contribution are indicated with a †. Publications in preparation are subject to minor changes in author and title.

1. Charles Cherqui, Yueying Wu†, Guoliang Li†, Steven C. Quillin†, Jacob A. Busche, Niket Thakkar, Claire A. West, Nicholas P. Montoni, Philip D. Rack, Jon P. Camden, and David J. Masiello. STEM/EELS imaging of magnetic hybridization in symmetric and symmetry-broken plasmon oligomer dimers and all-magnetic Fano interference.*Nano Lett.*, 16(10):6668–6676, 2016.

2. Connor G. Bischak, Rebecca B. Wai, Charles Cherqui, Jacob A. Busche, Steven C. Quillin, Craig L. Hetherington, Zhe Wang, Clarice D. Aiello, Darrell G. Schlom, Shaul Aloni, D. Frank Ogletree, David J. Masiello, and Naomi S. Ginsberg. Noninvasive cathodoluminescence-activated nanoimaging of dynamic processes in liquids. *ACS Nano*, 11(10):10583–10590, 2017.

3. Charles Cherqui†, Guoliang Li†, **Jacob A. Busche**†, Steven C. Quillin, Jon P. Camden, and David J. Masiello. Multipolar nanocube plasmon mode-mixing in finite substrates. *J. Phys. Chem. Lett.*, 9(3):504–512, 2018.

4. Harrison J. Goldwyn, Kevin C. Smith, Jacob A. Busche, and David J. Masiello. Mislocalization in plasmon-enhanced single-molecule fluorescence microscopy as a dynamical Young's interferometer. *ACS Photonics*, 5(8):3141–3151, 2018.

5. Chenze Liu†, Yueying Wu†, Zhongwei Hu†, **Jacob A. Busche**†, Elliot K. Beutler, Nicholas P. Montoni, Thomas M. Moore, Gregory A. Magel, Jon P. Camden, David J. Masiello, Gerd Duscher, and Philip D. Rack. Continuous wave resonant photon stimulated electron energy-gain and electron energy-loss spectroscopy of individual plasmonic nanoparticles. *ACS Photonics*, 6(10):2499–2508, 2019.

6. Agust Olafsson†, **Jacob A. Busche**†, Jose J. Araujo, Arpan Maiti, Juan Carlos Idrobo, Daniel R. Gamelin, David J. Masiello, and Jon P. Camden. Electron beam infrared nano-ellipsometry of individual indium tin oxide nanocrystals. *Nano Lett.*, 20(11):7987–7994, 2020.

7. Joseph J. Liberko, **Jacob A. Busche**, Robyn Seils, Hans A. Bechtel, Philip D. Rack, David J. Masiello, and Jon P. Camden. Probing nanoparticle substrate interactions with synchrotron infrared nanospectroscopy: Coupling gold nanorod Fabry-Pérot resonances with SiO_2 and h-BN phonons. *Phys. Rev. B*, Just Accepted, 2021.

8. R. Faryad Ali, **Jacob A. Busche**, Saied Kamal, David J. Masiello, and Byron D. Gates. Enhancement of optical second harmonic emission by nanoradiative plasmonic nanoparticles. *In Prep.*

9. Agust Olafsson, Siamak Khorasani, Jacob A. Busche, Jose J. Araujo, Juan Carlos Idrobo, Daniel R. Gamelin, David J. Masiello, Jon P. Camden. Infrared Plasmon Hybridization in Doped Semiconductor Nanocrystals Imaged in STEM-EELS. *In Prep.*

Chapter 2

MULTIPOLAR NANOCUBE PLASMON MODE-MIXING IN FINITE SUBSTRATES

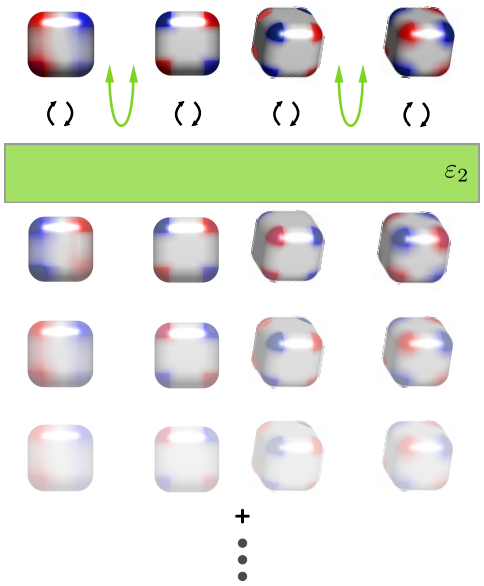

Facile control of the radiative and nonradiative properties of plasmonic nanostructures is of practical importance to a wide range of applications in the biological, chemical, optical, information, and energy sciences. For example, the ability to easily tune not only the plasmon spectrum but also the degree of coupling to light and/or heat, quality factor, and optical mode volume would aid the performance and function of nanophotonic devices and molecular sensors that rely upon plasmonic elements to confine and manipulate light at nanoscopic dimension. While many routes exist to tune these properties, identifying new approaches—especially when they are simple to apply experimentally—is an important task. Here, we demonstrate the significant and underappreciated effects that substrate thickness and dielectric composition can have upon plasmon hybridization as well as downstream properties that depend upon this hybridization. We find that even substrates as

thin as ∼10 nm can nontrivially mix free-space plasmon modes, imparting bright character to those that are dark (and vice versa) and, thereby, modifying the plasmonic density of states as well as the system's near- and far-field optical properties. A combination of electron energy-loss spectroscopy (EELS) experiment, numerical simulation, and analytical modeling is used to elucidate this behavior in the finite substrate-induced mixing of dipole, quadrupole, and octupole corner-localized plasmon resonances of individual silver nanocubes.

2.1 Introduction

Due to their ability to capture and convert light into intense, nanoscopic surface-bound electric fields, localized surface plasmons (LSPs) in noble metal nanostructures are currently the focus of a vigorous worldwide research effort [65, 80–86]. The high sensitivity of LSPs to subtle changes in their host environment make them excellent candidates for a wide range of biological [87–90], chemical [91–94], and optical sensing applications [95–97], and their giant absorption cross sections [98, 99] and extraordinarily small mode volumes [100–102] hold great promise in future photovoltaic and nanophotonic devices [62, 81, 103–107].

Past theoretical studies have addressed the interaction of plasmonic nanoparticles with both homogeneous dielectric environments [108–110] and semi-infinite substrates [111–116], but only few [114, 117] have explicitly accounted for the influence of the latter upon higher-order LSP modes. Effects of substrates of finite thickness are even more unexplored, as doing so is computationally demanding [118] and experimental data is lacking due to the weak coupling of higher-order LSP modes to the radiation field. Electron energy-loss spectroscopy (EELS), performed in a scanning transmission electron microscope (STEM), offers a route to overcome this challenge by using fast electrons as a probe of matter instead of light. Due to its high degree of spatial confinement and broad spectral range, STEM/EELS can access the complete plasmonic response (i.e., collective electronic excitations of both surface and bulk character), providing detailed spatial and spectral information on the influence of the substrate's dielectric properties and thickness upon the full plasmonic spectrum. This was clearly demonstrated in 2015 where Li et al. [116] used STEM/EELS to characterize the

complete surface and bulk plasmon responses of truncated silver nanospheres ranging from 20–1000 nm in diameter on semi-infinite substrates.

While having played an important role in the discovery and early understanding of the surface and bulk plasmon [24, 26], the last decade has witnessed a renaissance in the application of fast electron spectroscopy to plasmonic nanoparticles and their assemblies [42, 119, 120]. Unlike in optical spectroscopies where supporting substrates can be millimeters thick and well-approximated as semi-infinite, typical substrates in STEM-based electron spectroscopies must be thin enough to allow the electrons to pass through and reach the EEL detector. This requirement translates to substrates on the order of 1–100 nanometers, thicknesses comparable to the plasmonic specimens themselves. In this regime, substrate effects can be surprisingly nontrivial and distinctly different from semi-infinite substrates, uniform background environments, and vacuum, motivating the need for careful study.

Electrodynamics dictates that each plasmon mode (here referred to as a multipole) will interact and hybridize with its own image as well as with those of all other plasmon multipoles through the substrate. It is often assumed that only dielectric composition, i.e., refractive index, affects this image hybridization and that otherwise all substrates behave nearly identically, independent of thickness. It might also be expected that thin substrates, i.e., those that are of the same thickness as the plasmonic target specimens or thinner, would resemble vacuum and have little influence upon the LSP resonances, leaving each LSP mode essentially unhybridized. Surprisingly, however, neither presumption is true.

2.2 Discussion

Here we demonstrate the nontrivial impact that substrates of finite thickness (t) and varying refractive index (n) have upon LSP + image LSP mode mixing in individual silver nanocubes using monochromated and aberration-corrected STEM/EELS experiment combined with full-wave numerical electrodynamics simulations of the fast electron probe. Further analytical modeling serves as a basis to qualitatively and even semi-quantitatively expose the relevant hybridization physics. Most interesting is the "hall of mirrors" image effect pro-

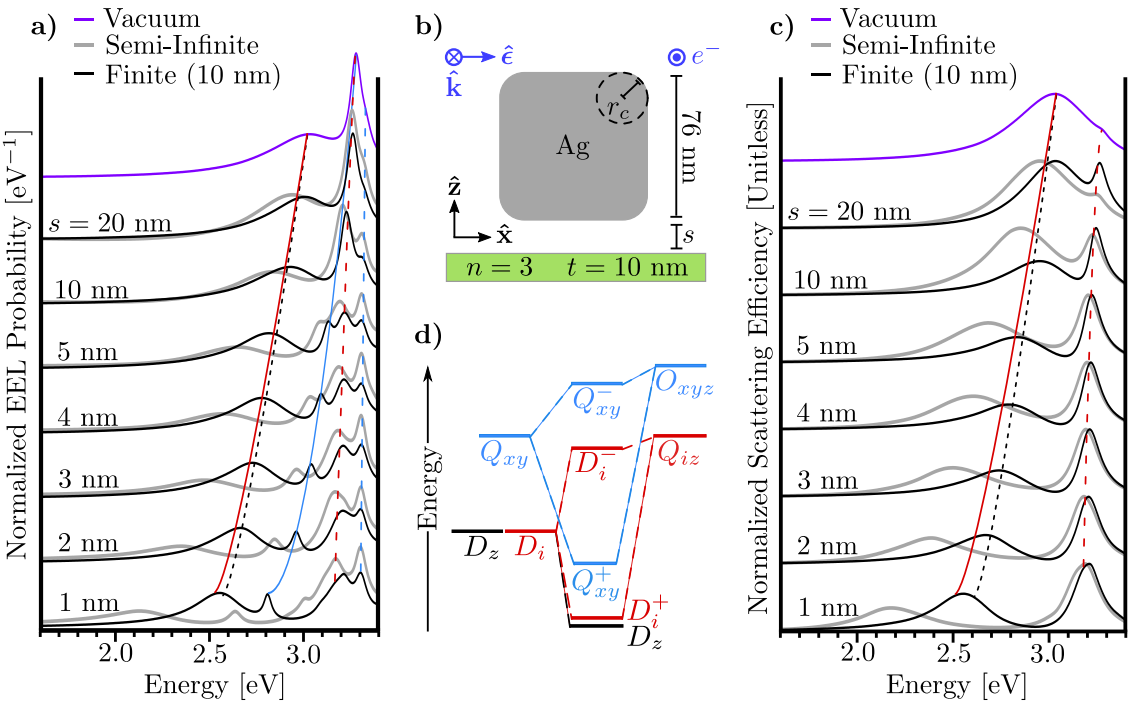

Figure 2.1: Computed evolution of nanocube LSP mode mixing versus separation distance in a substrate of refractive index $n = 3$ and thickness $t = 10$ nm. (a) Aloof EEL and (c) optical scattering spectra showing the progression of the nanocube's free-space dipolar (D_x, D_z), quadrupolar (Q_{xy}, Q_{xz}), and octupolar (O_{xyz}) modes interacting through either finite (black) or semi-infinite (gray) substrates. An illustration of the system is shown in panel (b), where s is the separation distance between the cube's base and the substrate surface and r is the radius of curvature of the naocube's corners. A schematic of the finite-substrate-induced hybridization is shown in panel (d). The y-oriented LSP modes D_y and Q_{yz} are not indicated explicitly since they are degenerate with those oriented in the x-direction. Of the five hybridized modes displayed, all are evident in the EEL spectrum while only those that are bright (red) are accessible via optical scattering. Note that significant LSP mode mixing occurs even on substrates as thin 10 nm in thickness.

duced uniquely by finite substrates [121], which, depending upon t and n, can mix LSPs in such a way that significant hybridization occurs even with substrate thicknesses well below 100 nm; see Fig. 2.1. In the following we will show that varying these parameters provides an opportunity to control the degree of LSP hybridization, even for higher-order modes beyond the usual dipole and quadrupole LSP resonances [114, 122–124]. Taken together, the presented work provides a new pathway to understand and exploit plasmon mode mixing to employ even intrinsically dark plasmons for nano-optical applications.

Nanocubes, in particular, have recently garnered significant attention [125, 126] due to the localization of their low-lying LSP modes to the cube's corners. Each so-called corner mode can either be dark or bright depending on mode's coupling efficiency to the radiation field. The high degree of curvature at the corners induces exceptionally strong electric near-fields there, leading to stronger LSP-environment coupling than in other nanoparticle shapes (e.g., spheres and rods). For this reason, nanocubes make an excellent platform for careful investigation of finite-substrate effects.

It is well known that the performance of nanocube-based sensors can be furthered enhanced via substrate interactions. For example, their free-space dipole LSP modes parallel to the substrate can mix with free-space quadrupole modes [114, 122–124] to produce hybridized surface charge oscillations that take on the same asymmetric character of the environment, i.e., with effective dipolar surface charge distributions localized toward (proximal) and away (distal) from the substrate. When excited by light, these hybridized modes can be made to interfere and produce Fano antiresonances in the scattering spectrum [114] which have been successfully implemented for use in asymmetric color routing [127, 128], ultrafast spontaneous emission [129], and a variety of solar light harvesting applications [117, 130, 131]. For example, Li et al. [117] used STEM/EELS to image the flow of energy between the proximal LSP modes of individual nanocubes and excitonic transitions in their supporting semiconductor substrates with nanoscopic precision, demonstrating that environmental transitions can be resonantly tuned to enhance plasmonic energy transfer [132, 133].

As demonstrated in Fig. 2.1 and shown schematically in Fig. 2.2a, the symmetry of the

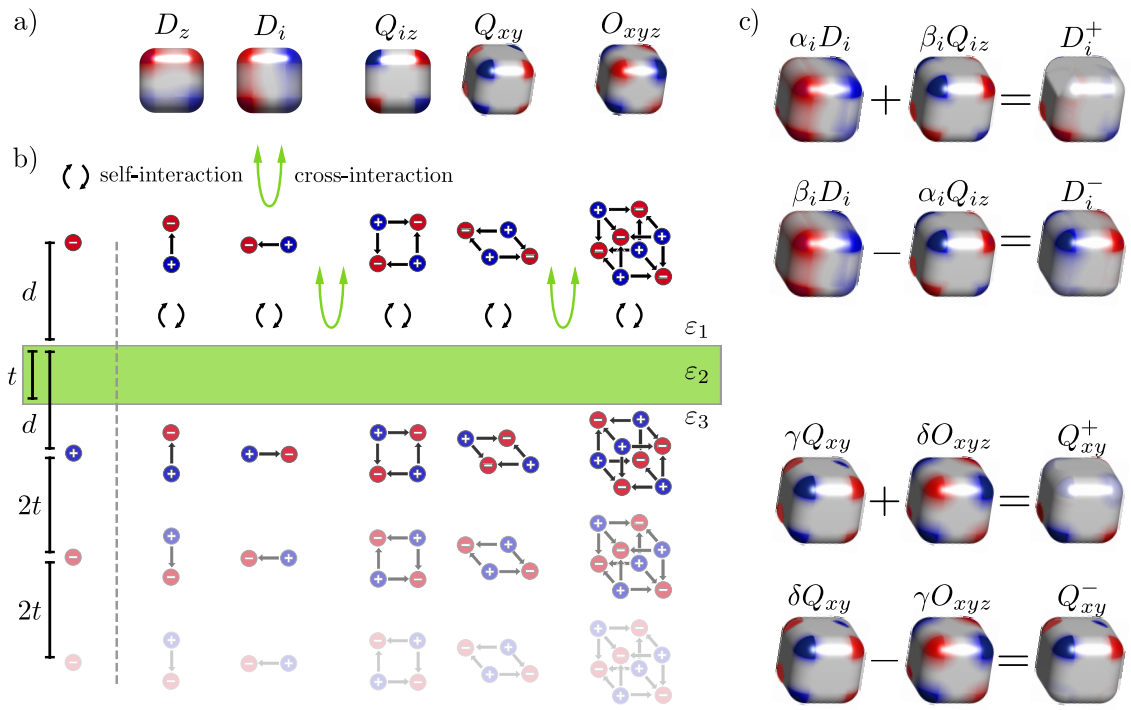

Figure 2.2: (a) Computed quasistatic surface charge distributions of the lowest-lying five non-degenerate free space LSP corner modes of the nanocube. Explicitly shown are the triply degenerate D_z and D_i, and Q_{iz} and Q_{xy} modes ($i \in \{x, y\}$), as well as the single corner octupole mode O_{xyz}. (b) Schematic of the image response of a finite substrate to these LSP modes, with the interaction between source and image organized into "self-interactions", represented by black arrows, and "cross-interactions", represented by green arrows. The relative phase between successive image multipoles is determined by the particular values of the dielectric constants ϵ_1, ϵ_2, and ϵ_3; the configuration shown here corresponds to $\epsilon_2 > \epsilon_1 = \epsilon_3$. (c) Computed mixing of the nanocube's free space LSP modes into substrate-dressed, hybridized LSP modes. The in-phase and out-of-phase modes D_i^+ and D_i^- are linear combinations of the bright D_i and the dark Q_{iz} modes. The former (latter) has a dipolar surface charge distribution localized to the corners proximal (distal) to the substrate. The in-phase and out-of-phase modes Q_{xy}^+ and Q_{xy}^- are linear combinations of the dark modes Q_{xy} and O_{xyz}. The former (latter) has a quadrupolar surface charge distribution localized to the corners proximal (distal) to the substrate.

nanocube dictates that the only distinct corner-localized free-space charge distributions are the triply degenerate dipole (D_x, D_y, D_z,) and quadrupole (Q_{xy}, Q_{xz}, Q_{yz}) modes as well as the single octupole mode, O_{xyz}. All other LSP modes involve some amount of surface charge localized at the edges and/or faces of the structure and are of higher energy and are ignored in the following. We approximate each nanocube corner mode as a pure cartesian multipole, associating the two via their respective surface charge distributions (Appendix A). Within a finite substrate, each LSP multipole induces an infinite collection of images of itself as illustrated in Fig. 2.2b. These images, in turn, act back on the LSP, allowing each LSP to couple to its own images (self-interactions) as well as to those of other LSPs (cross-interactions). The relative orientation between the free space modes and their images determines the selection rules: each mode interacts with its own image, but only the two pairwise cross-interactions between D_i and Q_{iz} and Q_{xy} and O_{xyz}, with $i \in \{x, y\}$, are allowed.

All self- and cross-interaction strengths are determined from the electrostatic image response

$$\Phi_{\text{ind}}(\mathbf{x}) = -\Delta_{21}\frac{q_0'}{\epsilon_1|\mathbf{x}-\mathbf{r}_0'|} + \sum_{m=1}^{\infty}\Delta_{21}\frac{q_j'}{\epsilon_1|\mathbf{x}-\mathbf{r}_j'|} \qquad (\text{for} z>0) \tag{2.1}$$

of a finite substrate of thickness t to a point charge q located a distance d from the top layer. Despite its complicated form, Eq. (2.1) has a simple interpretation which is illustrated in the first column of Fig. 2.2b. The first term is nothing more than the image potential of the semi-infinite substrate with image charge $q_0' = \Delta_{21}q$ located at $\mathbf{r}_0' = (0, 0, -d)$. The second term accounts for the finiteness of the substrate and is a sum over the potentials of image charges $q_j' = \Delta_{23}[1-\Delta_{21}^2](\Delta_{21}\Delta_{23})^{j-1}q$ located at $\mathbf{r}_j' = (0, 0, -d-2jt)$, with j a nonzero integer. The strength of all image charges is proportional to the surface jump condition $\Delta_{ab} = (\epsilon_a - \epsilon_b)/(\epsilon_a + \epsilon_b)$ with $a, b \in \{1, 2, 3\}$. As displayed in Fig. 2.2b, ϵ_1 is the dielectric constant in the upper half space, ϵ_2 is the dielectric constant of the finite substrate, and ϵ_3 is the dielectric constant in the lower half space, with $n_a = \sqrt{\epsilon_a}$. t can be larger or smaller than d, however we note that $\Phi_{\text{ind}} \to -q_0'/\epsilon_1|\mathbf{x}-\mathbf{r}_0|$ as $t \to \infty$ and $\Phi_{\text{ind}} \to 0$ as $t \to 0$.

Based on the image potential in Eq. (2.1), an LSP Hamiltonian [119] can be written with Φ_{ind} parametrizing the substrate-mediated multipolar LSP-LSP interaction energies (see Methods). Its diagonalization produces the amplitudes of the hybridized modes of the interacting nanocube-substrate system

$$\begin{aligned} D_i^+ &= \alpha_i D_i + \beta_i Q_{iz} \\ D_i^- &= \alpha_i Q_{iz} - \beta_i D_i \\ D_z &= D_z \\ Q_{xy}^+ &= \gamma Q_{xy} + \delta O_{xyz} \\ Q_{xy}^- &= \gamma O_{xyz} - \delta Q_{xy} \end{aligned} \tag{2.2}$$

as well as their natural frequencies

$$\begin{aligned} \Omega_i^+ &= \sqrt{\alpha_i^2(\omega_i^2 - f_i) + \beta_i^2(\omega_{iz}^2 - f_{iz}) - g_i\alpha_i\beta_i} \\ \Omega_i^- &= \sqrt{\alpha_i^2(\omega_{iz}^2 - f_{iz}) + \beta_i^2(\omega_i^2 - f_i) + g_i\alpha_i\beta_i} \\ \Omega_z &= \sqrt{\omega_z^2 - f_z} \\ \Omega_{xy}^+ &= \sqrt{\gamma^2(\omega_{xy}^2 - f_{xy}) + \delta^2(\omega_{xyz}^2 - f_{xyz}) - g_{xy}\gamma\delta} \\ \Omega_{xy}^- &= \sqrt{\gamma^2(\omega_{xyz}^2 - f_{xyz}) + \delta^2(\omega_{xy}^2 - f_{xy}) + g_{xy}\gamma\delta} \end{aligned} \tag{2.3}$$

with $i \in \{x, y\}$. Here, α_i, β_i, δ, and γ are expansion coefficients derived from Eq. (2.1) and indicate that the degree of mode mixing and corresponding amount of surface charge localization increases with increasing t or ϵ_2. Explicitly, these expansion coefficients are defined as $\alpha_i = \cos\theta_i$, $\beta_i = \sin\theta_i$, $\gamma = \cos\theta_{xy}$, and $\delta = \sin\theta_{xy}$, where $\theta_i = (1/2)\tan^{-1}(g_i/(\omega_{iz}^2 - \omega_i^2 + f_i - f_{iz}))$ and $\theta_{xy} = (1/2)\tan^{-1}(g_{xy}/(\omega_{xyz}^2 - \omega_{xy}^2 + f_{xyz} - f_{xy}))$ (Appendix A). Fig. 2.2c (upper panel) shows that the surface charge distributions resulting from interaction among D_i and Q_{iz} are effective substrate- and vacuum-localized hybridized LSP modes of dipolar character, labeled as D_i^+ and D_i^- for $i \in \{x, y\}$, while coupling among Q_{xy} and O_{xyz} (bottom panel, Fig. 2.2c) leads to effective substrate- and vacuum-localized quadrupole modes, labeled as Q_{xy}^+ and Q_{xy}^-. Interestingly, due to its symmetry, D_z does not efficiently interact with any

LSP multipole other than itself. Nonetheless, the spatial profile of its field is substrate-localized as the in-phase, collinear arrangement of the dipole and image dipoles within the self-hybridized mode induces a capacitive junction, biasing the field profile downward in the upper half plane; while counterintuitive, this means that the EEL profile of the D_z mode is vacuum localized as the probability to excite this in-phase arrangement of dipoles is largest immediately above the cube and falls to zero in the junction. The cross- and self-interaction coupling constants g and f are determined from the interaction energy of the $(\ell m)^{\text{th}}$ multipole with the induced potential of the $(\ell' m')^{\text{th}}$ image multipole. Further details of the model can be found in the Section 2.3 as well as in Appendix A.

Fig. 2.3a shows experimental STEM/EELS point spectra for individual 76±5 nm wide silver nanocubes with 13±1 nm corner radii, supported on SiN_x substrates with t = 10, 20, 30, and 100 nm. Fig. 2.3b shows analogous simulated STEM/EELS spectra for a 76 nm wide silver nanocube with 12.5 nm corner radii supported on an identical set of substrates. In both experiment and simulation, the entire system is first tilted and then excited using an aloof electron beam positioned at a distal corner (blue) and at a proximal corner (red) of the cube. At $t = 10$ nm ($n_{\text{SiN}_x} = 2.1$), mode mixing is weak but, surprisingly, not negligible. As t increases, so too does the strength of the interaction between nanocube and substrate, leading to a pronounced redshifting of the proximal D_i^+ modes. As dictated by Eqs. (2.1)–(2.3), their energy is lowered twice: once by self-interaction, and again by cross-interaction. Conversely, these two effects compete—with the self-interaction red-shifting and the cross-interaction blue-shifting the resonance position—to cause a relatively small energetic shift in the distal D_i^- modes relative to Q_{iz}. Indeed, simulations show a slight redshift, however, limitations in the resolution of the experiment (≈200 meV) and presence of the nearby Q_{xy}^- mode make its independent spectral identification challenging. Nevertheless, a small redshift in the superposition of D_i^- and Q_{xy}^- peaks (Fig. 2.3a) is experimentally observed in the $t = 10 - 30$ nm data.

Due to its symmetry, the remaining quadrupolar corner mode Q_{xy} does not interact with any of the three dipole modes nor any other quadrupole mode. Its substrate-induced

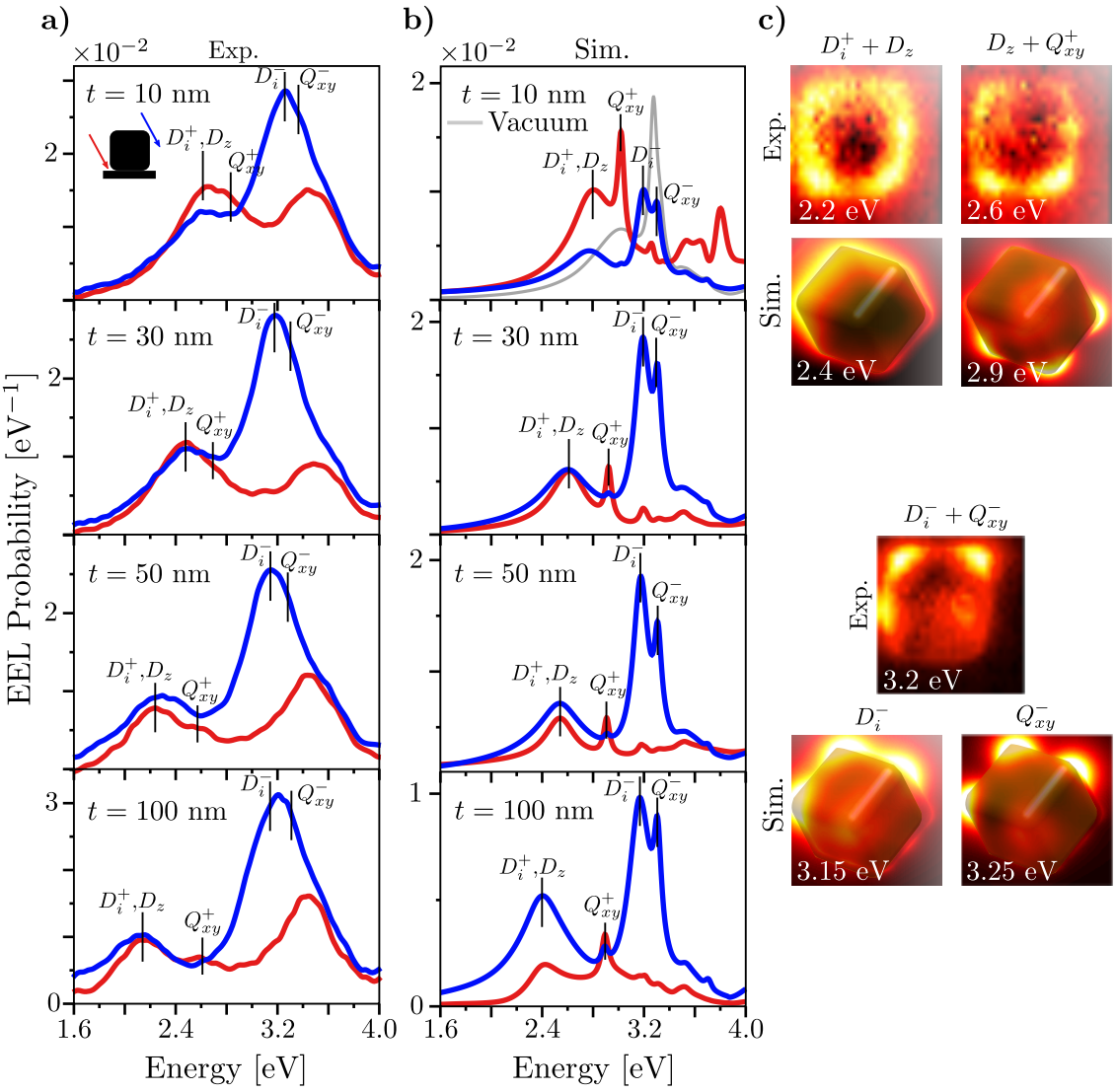

Figure 2.3: Experimental (a) and simulated (b) point spectra for tilted 76 nm nanocubes supported by $t = 10$, 30, 50, and 100 nm SiN_x substrates with $n_{SiN_x} = 2.1$. EEL spectra are acquired at two aloof beam positions: one at a distal corner of the cube (blue) and the other at a proximal corner (red). (c) Experimental and simulated EEL mode maps corresponding to the resonance energies in the EEL spectra for the $t = 100$ nm SiN_x substrate. The upper panels correspond to superpositions of the substrate-localized D_i^+ and Q_{xy}^+ modes, and the D_z mode. The lower panels show an experimental EEL mode map that is a superposition of D_i^- and Q_{xy}^-, alongside EEL maps of the same modes individually resolved via simulation.

localization, therefore, must be generated by interaction with the image of the octupole mode O_{xyz} in addition to its own. These couplings lead to a significantly redshifted Q_{xy}^{+} in comparison to Q_{xy}, and a slightly redshifted Q_{xy}^{-} in comparison to O_{xyz}; the reasons for these energy shifts are identical to those explained previously for the $D_i^{\pm}$ modes. Figs. 2.3a,b show the appearance of the Q_{xy}^{+} peak only in the proximal beam position (red). In the simulations (b), this occurs at $t = 30$ nm, while, in experiment (a) it occurs at $t = 50$ nm. Again the vacuum-localized Q_{xy}^{-} mode can clearly be seen in all simulated spectra for all substrate thicknesses considered, but limitations in energy resolution cause both the Q_{xy}^{-} and D_i^{-} to appear as a single $\sim$3.2 eV peak in the data. In both experiment and theory, Q_{xy}^{-} and D_i^{-} are identified as vacuum-localized since they are only significantly excited from the distal beam position. The (lack of) evolution of these modes with substrate thickness is representative of the more general behavior that higher-order LSP modes quickly saturate to a final energy due to the competing effects of self- and cross-interactions as well as the more rapid fall-off of the electric fields.

EEL probability maps for the nanocube on a $t = 100$ nm SiN_x substrate are shown in Fig. 2.3c for all five distinct hybridized modes. In the upper panel, we see that, because D_z does not hybridize with any other LSP mode, it retains its spectrally bright, free-space character, causing its broad resonance profile to overlap with both Q_{xy}^{+} and D_i^{+}. Thus, D_z appears as a background signal and only superpositions of D_z with D_i^{+} and Q_{xy}^{+} can be measured. Easier to resolve in both experiment and simulation and shown in the lower panel of Fig. 2.3c is the vacuum localization expected of the D_i^{-} and Q_{xy}^{-} modes. Again, as for the data presented in Fig. 2.3, limitations in experimental resolution means that D_i^{-} and Q_{xy}^{-} can only be measured simultaneously in experiment, but individually in simulations.

The experimental and simulated data presented in Fig. 2.4 demonstrate that, as predicted by Eqs. (2.1)–(2.3), mode hybridization can be controlled either by changing the substrate's thickness or dielectric composition. To explore the remainder of this parameter space, individual 76 ± 2 nm nanocubes are prepared on four different dielectric substrates and excited under the same conditions described above. Rather than vary substrate thick-

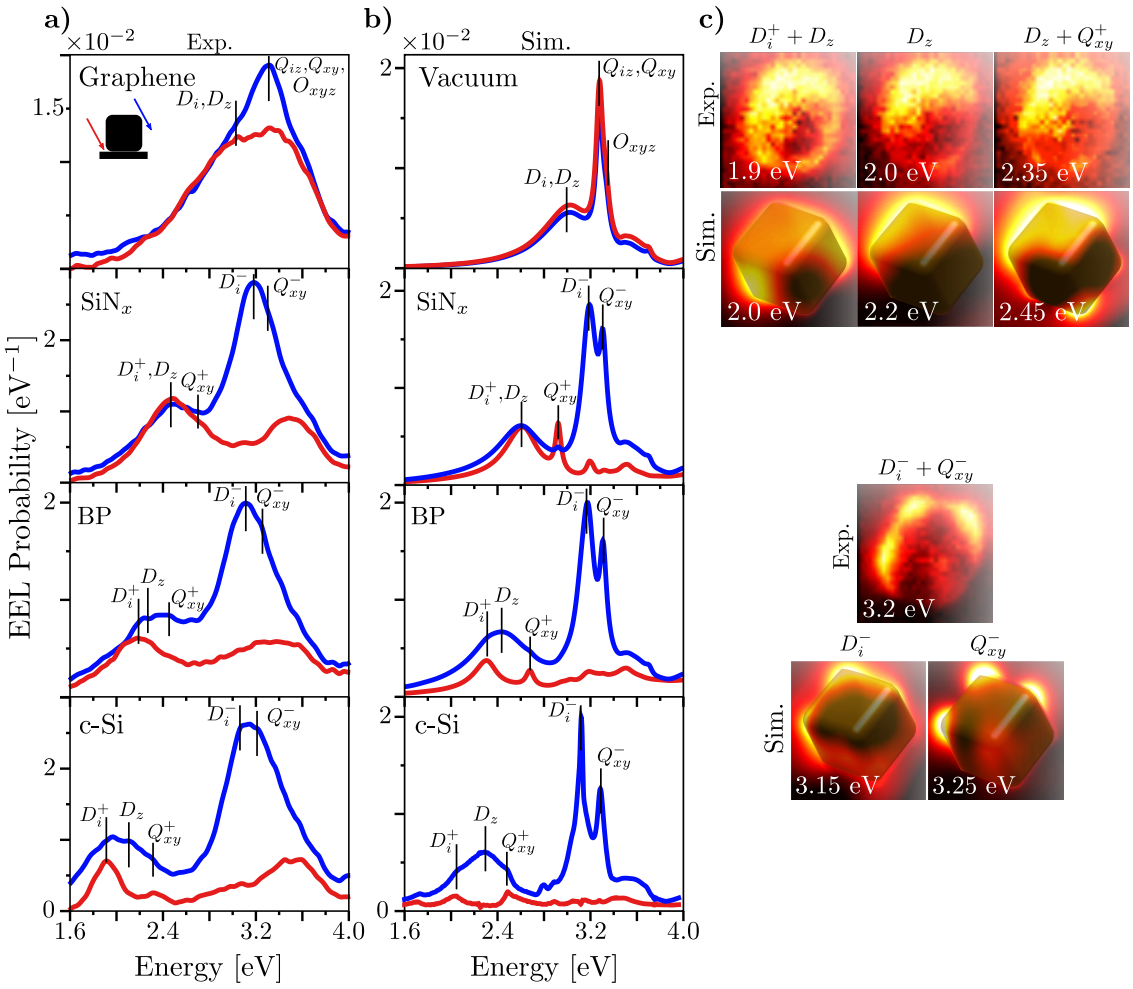

Figure 2.4: Experimental (a) and simulated (b) point spectra for tilted 76 nm nanocubes supported on single layer graphene (modeled as vacuum in simulation), $t = 30$ nm SiN_x, $t = 30$ nm BP, and $t = 35$ nm c-Si. The system is excited at two electron beam positions, one at a distal corner (blue) and the other at a proximal corner (red) of the nanocube. (c) Experimental and simulated EEL maps for the peaks found in the spectra of the $t = 35$ nm c-Si nanocube-substrate system. The upper panels correspond to a superposition of the substrate-localized D_i^+ and Q_{xy}^+ modes with the vacuum-localized D_z mode, as well as the isolated vacuum-localized D_z mode. The lower panels display an experimental EEL map corresponding to a superposition of D_i^- and Q_{xy}^-, alongside maps of the same modes individually resolved in simulation.

ness, EEL spectra are collected for both proximal and distal beam positions for individual nanocubes deposited on (i) single layer graphene (modeled as vacuum in simulation), (ii) $t = 30$ nm silicon nitride (SiN_x, $n_{SiN_x} = 2.1$), (iii) $t = 30$ nm boron phosphide (BP, $n_{BP} = 3$), and (iv) $t = 35$ nm crystalline silicon (c-Si, $n_{c-Si} = 3.7$). As expected, the spectra presented in Fig. 2.4 exhibit a spectral evolution similar to what was shown previously in Fig. 2.3 where substrate thickness was increased at constant composition.

In examining Eq. (2.1), it is evident that maximum coupling occurs when the first term dominates over the second. As described earlier, this is the limit of the semi-infinite substrate. However, independent of t, the same qualitative behavior can be attained by increasing the substrate's dielectric constant, as $q'_m \to 0$ ($m \geq 1$) when $\epsilon_2 \gg \epsilon_1$. 2.5. In this limit, the maximum amount of mode mixing is determined by the jump condition $\Delta_{21} = (\epsilon_2 - \epsilon_1)/(\epsilon_2 + \epsilon_1)$. Fig. 2.5 highlights the symmetry between the mode-mixing enhancements induced by an increase of t and an increase of ϵ_2. The strength of the electrostatic interactions between each LSP mode and the polarized substrate are comparably magnified as the substrate's polarizability is increased, either via an addition of dielectric material (t), or an increase to the permittivity of the existing substrate (ϵ_2). Surprisingly, substrates composed of high dielectric materials such as c-Si can more strongly mix LSP modes at $t = 35$ nm than a $t = 100$ nm SiN_x substrate can. This is most clearly evident in the experimental and simulated EEL mode maps of the c-Si nanocube-substrate system displayed in Fig. 2.4c. The high value of ϵ_2 produces a significant enough splitting that the vacuum-localized D_z mode can be isolated in between D_i^+ and Q_{xy}^+. As predicted by the model, the competing nature of self- and cross-interactions dictates that the lower-energy member of a hybridized pair can continue to redshift until $\Delta_{21} \sim 1$, eliminating the second term in Eq. (2.1) and maximizing the associated image response. This implies that D_i^+ and Q_{xy}^+ have the most potential for application, as they can conveniently be tuned across a wide range of frequencies simply by adjusting substrate thickness and/or refractive index.

In conclusion, we have combined STEM/EELS experiment with numerical simulation and analytical modeling to elucidate the behavior of plasmon mode mixing in substrates

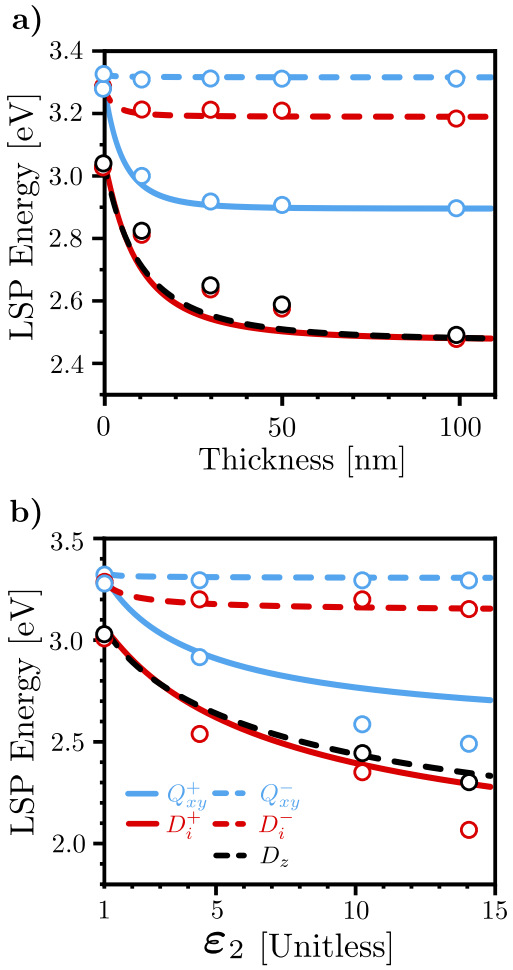

Figure 2.5: Spectral evolution of the nanocube's lowest-lying five nondegenerate corner-localized LSP modes versus (a) substrate thickness and (b) substrate dielectric constant. In both panels, the bullets correspond to the simulated resonance peak positions and the lines the energies predicted by the analytic model. Quantitative disagreements between the analytic model and the simulations arise because 1) the projection of spherical plasmon modes onto the basis of the cube with rounded corners is approximate and 2) because the model is quasistatic and the simulations are fully retarded. However, this qualitative approach highlights the symmetry between increasing dielectric constant and thickness. The t values in panel (a) and ϵ_2 values in panel (b) span the full range of substrate thicknesses and refractive indices considered in our reported experimental data. Panel (a) uses the SiN_x dielectric constant value $\epsilon_{SiN_x} = 4.41$, while panel (b) uses the same experimental substrate thicknesses from Fig. 2.4b for single-layer graphene ($t = 0$ nm, $\epsilon_g = 1$), SiN_x ($t = 30$ nm, $\epsilon_{SiN_x} = 4.41$), BP ($t = 30$ nm, $\epsilon_{BP} = 10$), and c-Si ($t = 35$ nm, $\epsilon_{c-Si} = 13.7$). In comparing both panels, it is evident that thinner substrates of higher index can mix LSP modes equally as efficiently as thicker substrates of lower index.

of finite thickness. Substrate-induced hybridization of the seven lowest-lying LSP modes of individual silver nanocubes are investigated, with both the spectral and spatial behavior of their hybridization imaged by the fast electron probe. Varying substrate thickness from 10–100 nm at constant refractive index as well as varying substrate refractive index from 1–4 at constant thickness reveals that substrates as thin as 10 nm can significantly mix free-space LSP modes, imparting bright character to initially dark LSPs and vice versa, thereby strongly modifying the radiative and nonradiative properties of the resulting hybridized modes. The surprising fact that substrate thickness matters and can be readily changed in the laboratory has far-reaching impact across a wide range of applications.

2.3 Methods

2.3.1 EELS Experiments.

EEL spectra were acquired in a monochromated Carl Zeiss Libra 200MC (S)TEM operated with an accelerating voltage of 200 kV. Each spectrum acquisition was executed with a collection semi-angle of 12 mrad, a convergence semi-angle of 9 mrad, and a dispersion of 29 meV per channel. Energy resolution, defined as the full width at half-maximum of the zero-loss peak, for each acquisition is 150 meV with the electron beam probing only the substrate. For each nanocube, EEL spectrum images responsible for producing LSP mode maps were collected by defining a pixelated region of interest around the particle, where 1 pixel is $\sim 4 \times 4$ nm^2.

Experimentally obtained EEL mode maps are analyzed using the Gatan Digital Micrograph software. Such maps are generated by removing the background using the reflected-tail model and normalized to the total spectral area. LSP mode maps were prepared by plotting spectral intensities from energy slices in which the peak maxima of the distal/proximal point spectra are located.

2.3.2 EELS Simulations.

Simulations were performed using both the electron-driven discrete dipole approximation (*e*-DDA) [134, 135] and the metal nanoparticle boundary element method (MNPBEM14) [136]. In these codes, a nanoparticle's volume or boundary surfaces are divided into a collection of discrete elements that are polarized by an external field as well by each other. Using a plane wave and an electron beam as a source, scattering and EEL spectra were calculated. The electron beam was given an initial energy of 200 keV and an impact parameter of 0.5 nm from the specified proximal or distal corner of the cube. As was done experimentally, EEL maps were calculated by filtering the EEL spectra acquired within a region of interest surrounding the target at a specific loss energy value.

2.3.3 Hamiltonian Formalism.

The total energy of the seven corner-localized modes of the nanocube discussed in the text above can be described by the Hamiltonian

$$\begin{aligned} H = &\sum_{i=x,y,z} \left(\frac{P_i^2}{2m_i} + \frac{1}{2} m_i \omega_i^2 D_i^2 \right) + \sum_{i=x,y} \left(\frac{P_{iz}^2}{2m_{iz}} + \frac{1}{2} m_{iz} \omega_{iz}^2 Q_{iz}^2 \right) \\ &+ \left(\frac{P_{xy}^2}{2m_{xy}} + \frac{1}{2} m_{xy} \omega_{xy}^2 Q_{xy}^2 \right) + \left(\frac{P_{xyz}^2}{2m_{xyz}} + \frac{1}{2} m_{xyz} \omega_{xyz}^2 O_{xyz}^2 \right) + H_{\text{int}}, \end{aligned} \tag{2.4}$$

where the first term in brackets accounts for the internal energy of the dipole modes, the second and third the quadrupole modes, and the fourth the octupole mode. The effective masses of each LSP mode, m_i, m_{iz}, m_{xy}, and m_{xyz} are proportional to the inverse of the modes polarizability [119], and are taken as fitting parameters along with the uncoupled mode energies ω_i, ω_{iz}, ω_{xy}, and ω_{xyz}.

The interaction Hamiltonian H_{int} describes the coupling between the LSP modes as mediated by the image response of the substrate. Explicitly, the interaction terms are given by

$$H_{\text{int}} = \sum_{\boldsymbol{\alpha}\boldsymbol{\alpha}'} \iint \rho_{\boldsymbol{\alpha}}(\mathbf{x}, t) G_{\text{ind}}(\mathbf{x}, \mathbf{x}'; t) \rho_{\boldsymbol{\alpha}'}(\mathbf{x}', t) \, \mathrm{d}^3\mathbf{x} \, \mathrm{d}^3\mathbf{x}', \tag{2.5}$$

with $\boldsymbol{\alpha}$ a composite index (x or yz or xyz, etc.) and $\rho_{\boldsymbol{\alpha}}(\mathbf{x},t)$ the charge density of the $\boldsymbol{\alpha}^{\text{th}}$ LSP multipole located at the origin. The Green function $G_{\text{ind}}(\mathbf{x},\mathbf{x}';t)$, which translates the force from one multipole to another, is proportional to Eq. (2.1) and given explicitly by

$$\begin{aligned} G_{\text{ind}}(\mathbf{x},\mathbf{x}';t) = &-\frac{\epsilon_2-\epsilon_b}{\epsilon_2+\epsilon_b}\frac{1}{|\mathbf{r}-\mathbf{r}'_0|} \\ &+\sum_{n=1}^{\infty}\frac{\epsilon_2-\epsilon_3}{\epsilon_2+\epsilon_3}\left[1-\left(\frac{\epsilon_2-\epsilon_b}{\epsilon_2+\epsilon_b}\right)^2\right]\left(\frac{\epsilon_2-\epsilon_b}{\epsilon_2+\epsilon_b}\frac{\epsilon_2-\epsilon_3}{\epsilon_2+\epsilon_3}\right)^{n-1}\frac{1}{|\mathbf{r}-\mathbf{r}'_n|}. \end{aligned} \tag{2.6}$$

The corner modes of the cube are each approximated as a single cartesian plasmon coordinate, leading directly to the definition of the uncoupled plasmon Hamiltonian $H - H_{\text{int}}$. The interactions between the corner modes are limited by symmetry and produce

$$\begin{aligned} H_{\text{int}} = &-\sum_{i=x,y,z}\frac{1}{2}m_i f_i D_i^2 - \sum_{j=x,y}\frac{1}{2}m_{jz}f_{jz}Q_{jz}^2 - \frac{1}{2}m_{xy}f_{xy}Q_{xy}^2 - \frac{1}{2}m_{xyz}f_{xyz}O_{xyz}^2 \\ &+\sum_{i=x,y} g_i\sqrt{m_i m_{iz}}D_i Q_{iz} + \sqrt{m_{xy}m_{xyz}}Q_{xy}O_{xyz} \end{aligned} \tag{2.7}$$

in which the self-coupling constants are defined as

$$\begin{aligned} f_i &= \frac{2\Delta_{21}}{m_i\epsilon_b(2a)^3} - \sum_{j=1}^{\infty}\frac{2\Delta_{23}[1-\Delta_{21}^2](\Delta_{21}\Delta_{23})^{j-1}}{m_i\epsilon_b(2a+2jt)^3}, \\ f_z &= \frac{4\Delta_{21}}{m_z\epsilon_b(2a)^3} - \sum_{j=1}^{\infty}\frac{4\Delta_{23}[1-\Delta_{21}^2](\Delta_{21}\Delta_{23})^{j-1}}{m_z\epsilon_b(2a+2jt)^3}, \\ f_{xy} &= \frac{16}{3}\frac{a^2\Delta_{21}}{m_{xy}\epsilon_b(2a)^5} - \sum_{j=1}^{\infty}\frac{16}{3}\frac{a^2\Delta_{23}[1-\Delta_{21}^2](\Delta_{21}\Delta_{23})^{j-1}}{m_{xy}\epsilon_b(2a+2jt)^5}, \\ f_{iz} &= \frac{144a^2\Delta_{21}}{3m_{iz}\epsilon_b(2a)^5} - \sum_{j=1}^{\infty}\frac{144a^2\Delta_{23}[1-\Delta_{21}^2](\Delta_{21}\Delta_{23})^{j-1}}{3m_{iz}\epsilon_b(2a+2jt)^5}, \\ f_{xyz} &= \frac{576a^4\Delta_{21}}{m_{xyz}\epsilon_b(2a)^7} - \sum_{j=1}^{\infty}\frac{576a^4\Delta_{23}[1-\Delta_{21}^2](\Delta_{21}\Delta_{23})^{j-1}}{m_{xyz}\epsilon_b(2a+2jt)^7} \end{aligned} \tag{2.8}$$

and the cross-coupling constants are

$$\begin{aligned} g_i &= \frac{4a\Delta_{21}}{\sqrt{m_i m_{iz}}\epsilon_b}\frac{1}{(2a)^4} - \sum_{j=1}^{\infty}\frac{4a\Delta_{23}[1-\Delta_{21}^2](\Delta_{21}\Delta_{23})^{j-1}}{\sqrt{m_i m_{iz}}\epsilon_b}\frac{1}{(2a+2jt)^4}, \\ g_{xy} &= \frac{24a^3\Delta_{21}}{\sqrt{m_{xy}m_{xyz}}\epsilon_b}\frac{1}{(2a)^6} - \sum_{j=1}^{\infty}\frac{24a^3\Delta_{23}[1-\Delta_{21}^2](\Delta_{21}\Delta_{23})^{j-1}}{\sqrt{m_{xy}m_{xyz}}\epsilon_b}\frac{1}{(2a+2jt)^6}. \end{aligned} \tag{2.9}$$

Diagonalization of H produces the renormalized modes and frequencies defined in the text. Further details of the model are provided in Appendix A.

Chapter 3

CONTINUOUS WAVE RESONANT PHOTON STIMULATED ELECTRON ENERGY-GAIN AND ELECTRON ENERGY-LOSS SPECTROSCOPY OF INDIVIDUAL PLASMONIC NANOPARTICLES

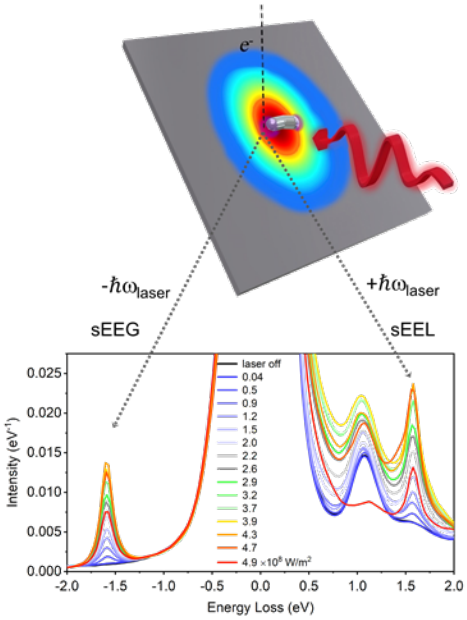

The unique optical properties of surface plasmon resonances in nanostructured materials have attracted considerable attention, broadly impacting both fundamental research and applied technologies ranging from sensing and optoelectronics to quantum computing. Electron energy-loss spectroscopy in the transmission electron microscope has revealed valuable information about the full plasmonic spectrum of these materials with nanoscale spatial resolution. Here we report a novel approach for experimentally accessing the photon-stimulated electron energy-gain and stimulated electron energy-loss responses of individual plasmonic nanoparticles via the simultaneous irradiation of a continuous wave laser and continuous current, monochromated electron probe. Stimu-

lated gain and loss probabilities are equivalent and increase linearly in the low irradiance range of $0.5 \times 10^8 - 4 \times 10^8$ W/m^2, above which excessive heating reduces the observed probabilities; importantly in our low irradiance regime, the photon energy must be tuned in resonance with the plasmon energy for the stimulated gain and loss peaks to emerge. Theoretical modeling based on Fermi's golden rule elucidates how the plasmon resonantly and coherently shuttles energy quanta between the electron probe and the radiation field and vice versa in stimulated electron energy-loss and gain events. This study opens a fundamentally new approach to explore the quantum physics of excited-state plasmon resonances that does not rely on high intensity laser pulses or any modification to the EELS detector.

3.1 Introduction

The ability of nanostructured metals to support plasmon resonances in response to light has implications on many scientific fields and applications such as optoelectronics [137–139], optical computing [140, 141], and readout strategies for quantum computing [142, 143]. Because plasmon excitations are sensitive to their environment, biological and chemical processes can be probed using environment-induced plasmon modulation [144, 145]. Plasmons can also transfer electromagnetic energy radiatively,10 non-radiatively [132], and/or via hot electron injection and thus can be used to catalyze reactions [83, 146, 147]. Due to these, and other, emerging uses, a deeper understanding of plasmon excited states is essential. Electron energy loss spectroscopy in the (scanning) transmission electron microscope ((S)TEM) has been used to gain insight into the physics of plasmonic structures at the nanoscale [42, 120, 148]. While theory has facilitated the distinction of bright and dark plasmon modes in more simple structures, distinguishing these modes in complex geometries remains a challenge as does imaging their photoexcited internal field structure.

Optical pump-probe strategies have long been critical tools to unravel complex materials phenomena. While the probe size typically limits spatial resolution, the temporal domain of pump-probe techniques is virtually un-paralleled with sub-femtosecond laser pulses. To push the spatial resolution, over the past two decades optical pumps and focused electron probes

have merged into ultrafast electron microscopies (UEMs) with modalities such as diffraction [149, 150] and photo-induced near field electron microscopy (see Refs. [151–155] for recent perspectives and reviews). For instance, 4D (x, y, z, t) UEM systems utilize photocathodes, which are exposed to short laser pulses to generate electron beamlets (and single electrons) that synchronously arrive at the sample relative to a pulsed laser. Though only a few UEM systems exist worldwide, a wealth of interesting excited state nearfield information has been revealed as described below.

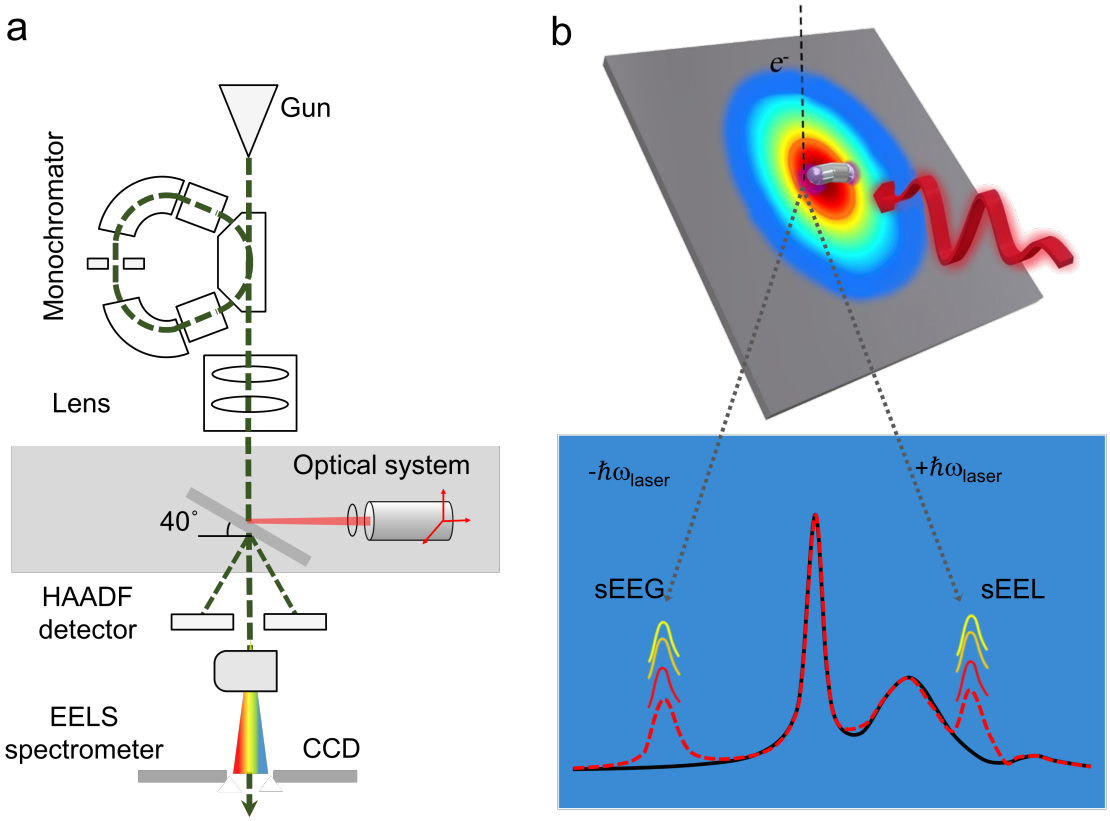

Figure 3.1: Overview of (S)TEM/EELS and laser system. (a), Schematic of the monochromated (S)TEM/EELS instrument with the optical delivery system mounted orthogonal to the electron beam. (b), Illustration of the coincident and cw focused laser light and 200 keV electron beam; the laser spot has a 3.7 mm radius Gaussian profile and interacts with the sample to produce signature sEEL and sEEG peaks whose intensities vary with laser irradiance.

Electron energy-gain due to electron/phonon coupling was first observed by Boerch et al. in 1966 [156] and more recently in high energy resolution (S)TEM-based electron energy-loss spectroscopy (EELS) [157, 158]. Photon-stimulated electron energy-gain (sEEG) spectroscopy was first suggested by Howie [159] and later García de Abajo et al. [160] developed a theoretical framework for sEEG and suggested optical power densities of $\sim 10^{10}$ W/m^2 would be necessary to observe continuous wave (cw) sEEG spectroscopy of gold nanostructures. The allure of sEEG spectroscopy is the possibility of accessing nearfield phenomena not limited by the width of the zero loss peak (ZLP) or detector energy resolution, but rather by the spectral resolution of the stimulating optical pump. More recently, Barwick et al. [161] introduced photo-induced nearfield electron microscopy (PINEM), which couples an intense laser pulse indirectly to a fast electron probe through the laser-induced evanescent nearfield of the target material, thereby generating stimulated electron energy-loss (sEEL) and sEEG signals at discrete multiples of the photon energy ($\pm n\hbar\omega$). They studied the electron energy-gain and stimulated energy-loss spectra of carbon nanotubes and compared them to silver nanorods [161]. The $\sim 10^{14}$ W/m^2, 200 fs pulses produced symmetric gain/loss spectra evidencing photon-plasmon-electron interactions involving up to 8 photon quanta. Later, energy-filtered PINEM maps were used to image the interference of Fabry-Perot type surface plasmon polariton waves [151] as well as to visualize the channel-like patterns formed in the near-fields of entangled silver nanoparticles [162]. Recently, spectrally resolved PINEM experiments of silver nanorods have confirmed that optical energy resolutions of ~ 20 meV can be obtained via a tunable light source [163]. Theoretical treatments of photoinduced sEEG have also been developed15 [164–166], and it was suggested that cw sEEG could be realized with irradiance values on the order of $\sim 10^8$ W/m^2 for silver nanoparticles, though some have hypothesized [153] that impractically high sample heating would result at these cw irradiances, thus rendering cw sEEG/sEEL unfeasible.

In an attempt to circumvent then need for a photocathode as done in standard PINEM experiments, recently, Das et al. [167] has reported a new method in which a high-power pulsed nanosecond laser (~ 2 eV photons, 5 ns pulse width, 10 kHz, duty cycle of 5×10^{-3}%

and peak irradiance on the order of 10^{14} W/m^2) is used to expose the sample. sEEL and sEEG peaks at ± 1 and $\pm 2\hbar\omega$ were realized with a modified detector that is synchronized with the laser pulse and only collects electrons that have interacted concurrent with the laser irradiation. Importantly, because they operated in a perturbative regime where no more than one gain event occurs per electron, they realized a resonant mode when the photon energy was tuned to the plasmon peak resonance energy. Furthermore, they overviewed a theory of dissipative quantum evolution and determined the number of photoexcited plasmons generated by the illumination to be on the order of 1.2 in their resonant regime.

As most PINEM experiments have demonstrated, at high enough photon irradiance virtually any photon-target interaction can stimulate loss/gain signals even when the optical transition (plasmonic or not) is weak. Here, through a combination of experiment and theory, we demonstrate a low irradiance cw regime (10^8 W/m^2) where strong photon-plasmon coupling is critical to observing the sEEL and sEEG signals; in this way, we expect bright plasmon modes to couple stronger than dark plasmon modes. This resonant mode provides the ability to spectrally and spatially map the steady- state near field of individual plasmonic nanostructures via cw photo-excitation and a continuous electron source in the (S)TEM.

3.2 Experimental Results

Motivated by these studies and the desire to investigate excited state phenomena in plasmonic nanomaterials, we leveraged a recently developed optical delivery system that can be attached to any (S)TEM for both photothermal heating [168] and excitation modalities and used it to image the plasmonic responses of individual silver nanoparticles in the weak-field cw limit. The particles are photothermally dewetted from a continuous 30 nm thick silver film (see Ref. [169] for detailed image) using our *in situ* laser delivery system. Fig. 3.1a is a schematic illustrating the system, developed by Waviks, Inc., attached to a monochromated (S)TEM. The system consists of a laser diode with an emission wavelength of 785 nm and a 1 nm (or 1.4 meV) full-width-half-maximum (FWHM) linewidth. The tunable laser optical power (up to 215 mW) is coupled to a 5 μm diameter single mode fiber optic and the end of the

fiber is placed at the focal distance of the lens sub-system which re-images the fiber optic end with unit magnification at an approximate working distance of 1 cm. As shown in Fig. 3.1a and b, the unpolarized 3.7 μm radius Gaussian laser spot (at $1/e^2$ irradiance measured at normal incidence and thus slightly elongated due to the tilt) is focused and aligned to the (S)TEM electron coincident point on a 40° tilted sample via a 3-axis nanomanipulator system (see Ref. [168] for system details). While all results presented here were operated in cw, the laser can be pulsed down to a several ns pulse width at up to 16 MHz frequency at a wavelength of 785 nm (1.58 eV). At maximum power and focus, a cw irradiance on the 40° tilted substrate can reach up to $\sim 2 \times 10^9$ W/m^2.

Fig. 3.2a shows the unprocessed low-loss sEEL/sEEG point spectra of a photothermally dewetted silver nanoparticle (see HAADF (S)TEM image in inset) as a function of laser power at the aloof beam position indicated by position A (see Ref. [169] for full spectra). Inspection of the EEL spectrum (without laser irradiation) reveals an energy resolution of about 0.136 eV as measured by the FWHM of the ZLP. During the experiment, there are slight changes in the ZLP attributed to microscope instabilities and a change in the high-energy side of the background consistent with electron beam induced carbon deposition from prolonged electron exposure. The surface plasmons are clearly visible and no noise reduction or other data enhancement was performed on the spectra. In the laser irradiated spectra, two additional peaks emerge, and are attributed to the sEEL and sEEG peaks at $\pm\hbar\omega_{\text{laser}}$, respectively, at $\pm$1.58 eV. For clarity we plot the data using standard EELS convention so the sEEG signature is at negative electron energy-loss.

For the zero irradiance spectra (laser off), there are two plasmon peaks in this low loss region of interest: one centered at $\sim$ 1.05 eV and another small peak centered near the laser wavelength 1.48 eV. Detailed peak fitting of the spectra was performed to analyze the full low-loss/gain spectra (see Ref. [169] for details). Notably, the average FWHM of the sEEL and sEEG peaks fits (0.136 ± 0.0089 eV) match well with the FWHM of the ZLP.

Fig. 3.2b is a plot of the integrated sEEG and sEEL probabilities as a function of laser irradiance for the spectra in Fig. 3.2a. Interestingly, the EEL spectrum in Fig. 3.2a at zero

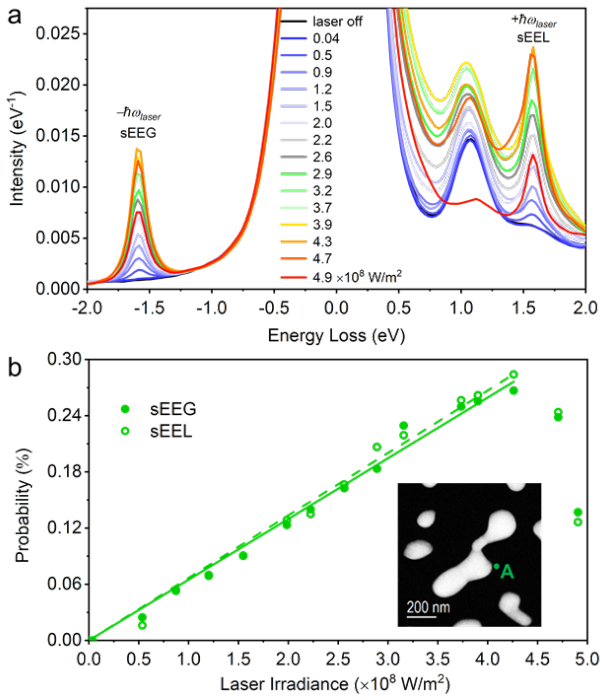

Figure 3.2: sEEL and sEEG of a silver irregular nanoparticle as a function of laser irradiance. (a), The unprocessed low-loss EEL/EEG point spectra of a photo-thermally dewetted silver nanoparticle as a function of laser irradiance ($\times 10^8$ W/m^2) at the aloof beam position indicated by the green bullet and label A. (b), The integrated sEEG and sEEL probabilities as a function of laser irradiance for the spectra in (a). The solid and dashed lines are linear fits to the sEEG and sEEL data, respectively.

laser irradiance has only a small plasmon peak near the 1.58 eV laser energy; however, the laser couples strongly to this apparent bright mode, which also interacts with the field of the swift ($<$ 500 attosecond interaction time) passing STEM electron as evidenced by the strong sEEL and sEEG peaks in the spectrum. Notably, the sEEL and sEEG peaks increase approximately linearly as a function of laser irradiance in the range of 8.8×10^7 W/m^2 to 4.3×10^8 W/m^2. Consistent with previous PINEM results [161, 162], and as discussed below in our modeling results, the sEEL and sEEG peak intensities have approximately the same integrated probability. Note that because of the relatively low cw laser irradiance values relative to PINEM, only single quantum exchanges of energy between the laser, target, and

electron beam are observed as no multi-photon sEEL and sEEG responses are detected. Additionally, and consistent with the lower irradiance, there is no detectable change in the ZLP intensity. Interestingly, both peak intensities decrease at irradiance values $> 4.3 \times 10^8$ W/m^2, which is attributed to photothermal heating of the silver nanostructure, which is known to damp plasmons and shift the resonance to lower energy. Anecdotally, when the laser is increased slightly to 5×10^8 W/m^2, the silver nanostructures studied evaporate completely (see [169] for images). Furthermore, the broad plasmon modes associated with the electron-beam induced carbon deposition also concurrently decrease in the $> 4.3 \times 10^8$ W/m^2 irradiance region.

Fig. 3.3a and b show the point spectra as a function of irradiance at the aloof positions of the rod-like structure shown in the inset of Fig. 3.3c (see Ref. [169] for full low-loss spectra); again no data processing was performed for the spectra. Fig. 3.3c is a plot of the integrated sEEL and sEEG probabilities as a function of irradiance taken at these two positions (ignoring the spontaneous EEL contribution convoluted on the loss side); note the sEEL and sEEG probabilities are again comparable for each position. The rod has approximate dimensions of $\sim$ 330 nm long, an average width of $\sim$ 120 nm and average height of $\sim$ 100 nm (assuming an equilibrium wetting angle for the trans-axial dimension of 135 degrees). At the aloof positions at the rod ends, the spectra consist of peaks associated with the longitudinal dipole (1.21 eV), longitudinal quadrupole (2.3 eV), and several higher-energy (> 3 eV) modes including the transverse dipole among higher-order modes. Note the intensity of the higher order mode peak at $\sim$ 3.5 eV varies in the unprocessed data, which has contributions from carbon deposition (and removal at higher irradiance) and likely slight electron beam mispositioning over the duration of the experiment. No multi-photon sEEL is contributing as evidenced by the energy gain region having no peaks at $-2\hbar\omega_{\text{laser}} = 3.16$ eV. Fig. 3.3d illustrates the 1.21 eV dipole mode EELS map at zero irradiance, which has the expected high probability distribution at the rod ends (see Ref. [169] for complementary 2.3 eV quadrupole mode map). Figs. 3.3e and f are the associated sEEG and sEEL probability maps, respectively, when exposed to an irradiance of $\sim 2 \times 10^8$ W/m^2. The sEEG probability

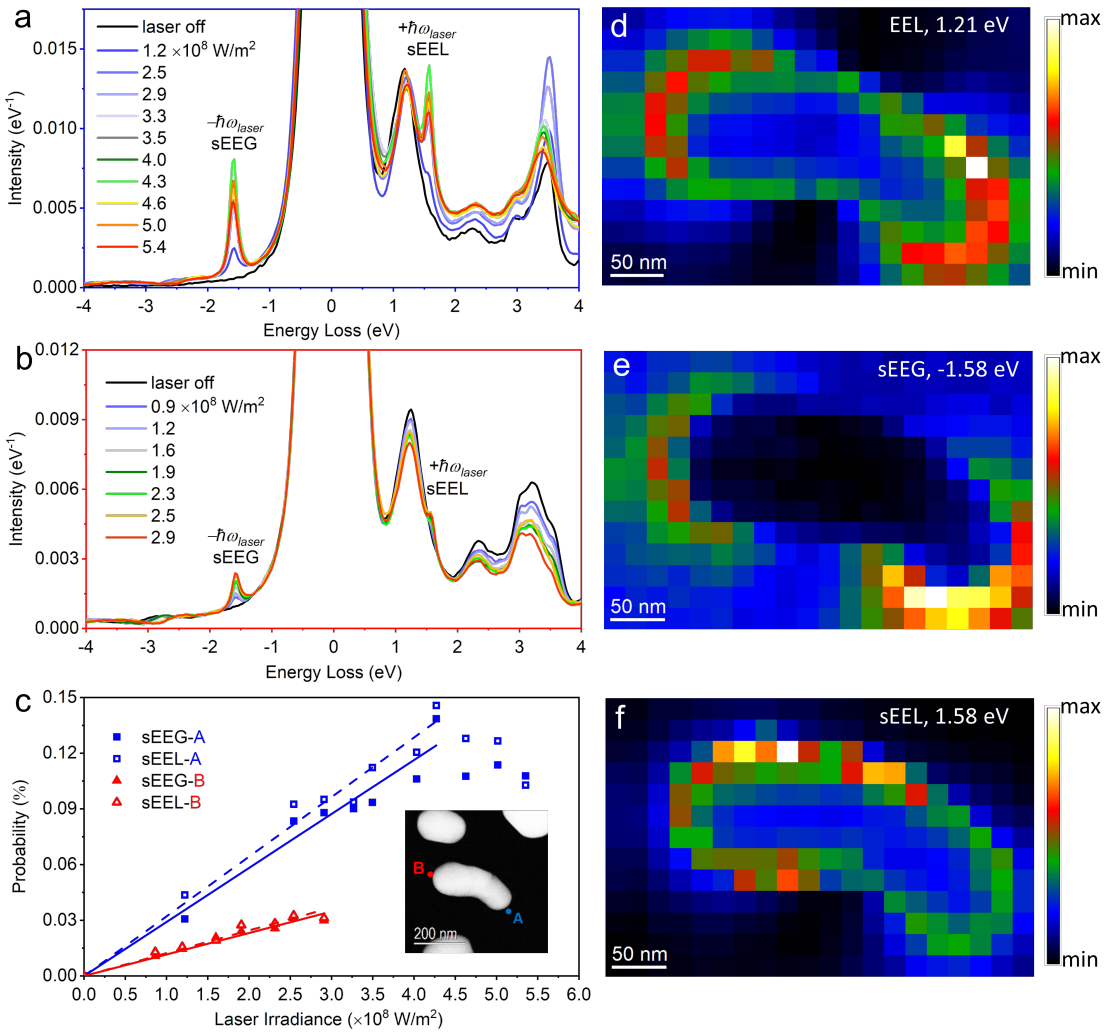

Figure 3.3: sEEL and sEEG of a silver rod-like nanoparticle as a function of laser irradiance. Unprocessed low-loss EEL spectra of silver rod-like structures at (a), position A and (b), position B as a function of laser irradiance ($\times 10^8$ W/m^2) at the aloof beam position. The positions A and B are indicated in the inset of (c). (c), Integrated sEEG and sEEL probabilities as a function of laser irradiance. The solid (sEEG) and dashed (sEEL) lines are linear fits for the data obtained at position A and B, respectively. The solid and dashed lines are linear fits to the sEEG and sEEL data, respectively. EEL maps of (d), the 1.21 eV dipole peak at zero irradiance; (e), -1.58 eV sEEG map and (f), the $+1.58$ eV sEEL map, both at 2×10^8 W/m^2 irradiance.

map is consistent with the longitudinal dipole map, which suggests good coupling to this bright mode despite the laser energy being detuned $\sim$ 0.37 eV to higher energy from the dipole plasmon resonance. As the spectra illustrate in Fig. 3.3a and b and the longitudinal dipole map suggests in fig. 3.3d, the EEL probability is slightly higher on the right side of the rod and thus concomitantly the sEEG and sEEL probabilities are slightly higher on the right hand side of the rod. For position A, where relatively higher laser powers were explored, the sEEL and sEEG probabilities decrease when the irradiance exceeded $\sim 4 \times 10^8$ W/m^2 and the silver nanostructure evaporated when the irradiance exceeded 5.4×10^8 W/m^2 (see image in Ref. [169]).

According to Ref. [167], at low laser intensities where the stimulated sEELS and sEEGS intensities are on the order of the spontaneous EELS intensity, the mean number of stimulated plasmons (M) can be deduced by taking a ratio of the spontaneous plus stimulated loss intensity to the stimulated gain intensity, where this ratio is equal to $(M+1)/M$. Based on the deconvolved spectra that includes only the longitudinal dipole peak (at 1.2 eV) and the stimulated gain (at -1.58 eV) and loss (at 1.58 eV) peaks, the experimental peak integrated intensities were determined from Fig. 3.3a spectra collected at 1.2, 2.5 and 4×10^8 W/m^2 irradiance. The experimental ratios were determined to be 24.1, 10.5, and 8.7, respectively; thus the mean number of photoexcited plasmons at these irradiances were estimated to be 0.04, 0.10, and 0.13, respectively.

3.3 Theoretical Model

Due to the weak interaction of light with matter and the low cw laser intensity and (S)TEM electron current used herein, the spectral signatures of sEEL and sEEG can be well understood using time-dependent perturbation theory up to second order in electron-plasmon and photon-plasmon interactions. Each of these interactions either reduce or increase the (S)TEM electron momentum from $\hbar k_i$ to $\hbar k_f = \hbar k_i - \hbar q$, with $\hbar q$ a small ($|\hbar q| \ll \hbar k_i$) transfer momentum that is positive in energy-loss events and negative in energy-gain events.

In both cases, the cw laser and nanoparticle plasmons are assumed to have reached a

steady state prior to the electron-plasmon interaction. Additionally, we choose the the initial population $M_\lambda(\omega) = M_\lambda^{\max}\gamma_{\text{laser}}^2/([\omega-\omega_{\text{laser}}]^2+\gamma_{\text{laser}}^2)$ of each plasmon state λ to be frequency-dependent to model the excitation of a continuous plasmon density of states by a laser of linewidth γ_{laser} and peak frequency ω_{laser}. Letting the laser polarization and longitudinal dipole plasmon be oriented along the x-axis, the longitudinal plasmon occupation number is $M_x(\omega) \geq 0$ such that the initial state of the three dipole plasmons is $|M_x(\omega), 0_y, 0_z\rangle$, with the occupation numbers of the undriven transverse (y,z) plasmons taken to be zero. The initial state of the laser-populated photon field is given by the collective photon state $|\{N\}\rangle = |\ldots, N_\alpha, N'_\alpha, N''_\alpha, \ldots\rangle$, with α the collective index of each photon mode and N_α the occupation number of the α^{th} photon mode. Additionally, the initial state of the (S)TEM electron, whose motion along directions perpendicular to its propagation axis can be safely neglected for sufficiently small q, is well-approximated as a box-quantized, one-dimensional free particle with a wavefunction $\langle \mathbf{r}|k_i\rangle = \phi_R(\mathbf{R})\exp(\mathrm{i}k_i z)/\sqrt{L}$. Here, R is the cylindrical radial vector and $|\phi_R(\mathbf{R})|^2 \approx \delta(\mathbf{R}-\mathbf{R}_0)$, with $\mathbf{R}_0$ the impact parameter of the electron [166]. To be consistent with the definition of the photon field, the electron wavefunction is described in second quantization (see Appendix B) as $|k_i\rangle = |\ldots, 0, 1_{k_i}, 0, \ldots\rangle$, with all modes having an occupation number of zero except the k_i^{th} state of momentum $\hbar k_i$ which has an occupation number of one.

Collectively, the initial state of the system is then $|i\rangle = |k_i, \{N\}, \{M_x(\omega), 0_y, 0_z\}\rangle$, and the allowed final states are determined by the electron-plasmon and photon-plasmon coupling, $\hat{H}_{el-pl} = -\hat{\mathbf{d}}\cdot\hat{\mathbf{E}}_{el} = \sum_{kk'\lambda}(g_{k'k\lambda}\hat{c}_{k'}^\dagger\hat{c}_k\hat{b}_\lambda^\dagger + g_{k'k\lambda}^*\hat{c}_k^\dagger\hat{c}_{k'}\hat{b}_\lambda)$ and $\hat{H}_{ph-pl} = -\hat{\mathbf{d}}\cdot\hat{\mathbf{E}}_{ph} = \sum_{\alpha\lambda} g_{\alpha\lambda}(\hat{b}_\lambda^\dagger\hat{a}_\alpha - \hat{b}_\lambda\hat{a}_\alpha^\dagger)$, with $\lambda = x, y, z$ labeling the three nanoparticle dipole plasmons and $\hat{\mathbf{E}}_{el}$ and $\hat{\mathbf{E}}_{ph}$ the time-dependent electric field operators of the electron and photon fields. Here, $\hat{\mathbf{d}} = \sum_\lambda d_\lambda(\hat{b}_\lambda + \hat{b}_\lambda^\dagger)\mathbf{e}_\lambda$ is the transition dipole operator of the dipole plasmon modes of the rod with $\hat{b}_\lambda$ the annihilation operator of the dipole plasmon oriented in the λ-direction, denoted by the unit vector $\mathbf{e}_\lambda$. Analogously, $\hat{a}_\alpha$ and $\hat{c}_k$ are the annihilation operators of the α^{th} photon mode and k^{th} electron mode, respectively. The coupling strengths $g_{k'k\lambda} = -(2ed_\lambda|k'-k|/\gamma^2 L)\,\kappa_\lambda(|k'-k|R_0/\gamma)$ and $g_{\alpha\lambda} = -\mathrm{i}\sqrt{2\pi\hbar\omega_\alpha/V}\,d_\lambda(\mathbf{e}_\lambda\cdot\boldsymbol{\epsilon}_\alpha)$, in which $\kappa_{x,y}(|k'-k|R_0/\gamma) =$

$-\gamma K_1(|k'-k|R_0/\gamma)\mathbf{R}_0\cdot\mathbf{e}_{x,y}/R_0$ and $\kappa_z(|k'-k|R_0/\gamma) = -\mathrm{i}K_0(|k'-k|R_0/\gamma)(k'-k)/|k'-k|$, depend upon the radiation mode frequencies ω_α, polarizations ϵ_α, and quantization volume V, as well as the Lorentz contraction factor γ and quantization length L (see Appendix B).

Inspection of the different allowed time orderings of $\hat{H}_{el-pl}$ and $\hat{H}_{ph-pl}$ within the calculation of a second-order transition rate from $|i\rangle = |k_i, \{N\}, \{M_x(\omega), 0_y, 0_z\}\rangle$, to $|f\rangle = |k_f, \{N'\}, \{M'_x(\omega), M'_y, M'_z\}\rangle$, reveals that only four second-order scattering processes contribute: the plasmon may gain (simultaneous plasmon excitation [SPE]) or lose (simultaneous plasmon deexcitation [SPD]) two quanta of energy during the interaction, or it may simply mediate energy transfer from the photon field to the electron probe (stimulated electron energy-gain [sEEG]) or vice versa (stimulated electron-induced emission of radiation [sEIRE]).

Of the four processes, only SPE and sEIRE can contribute to the total loss signal. As SPE is the stimulated analog of the more commonly known EEL process, one might expect its contribution to the loss signal to be of prime importance. The transition rate for SPE is given by

$$\begin{aligned} w^{(2)}_{\mathrm{SPE}} = \frac{2\pi}{\hbar}\Bigg| \sum_m \frac{1}{E_i - E_m} \langle k_f, \{\ldots, N_\alpha - 1, \ldots\}, \{M_x(\omega)+2, 0_y, 0_z\}|\hat{H}_{el-pl}|m\rangle \\ \times \langle m|\hat{H}_{ph-pl}|k_i, \{N\}, \{M_x(\omega), 0_x, 0_y\}\rangle \\ + \sum_{m'} \frac{1}{E_i - E_{m'}} \langle k_f, \{\ldots, N_\alpha - 1, \ldots\}, \{M_x(\omega)+2, 0_y, 0_z\}|\hat{H}_{ph-pl}|m'\rangle \\ \times \langle m'|\hat{H}_{el-pl}|k_i, \{N\}, \{M_x(\omega), 0_x, 0_y\}\rangle \Bigg|^2 \delta(E_f - E_i) \end{aligned} \tag{3.1}$$

wherein the first term describes the properly time-ordered single-electron and single-photon interaction with the initial plasmon state $|\{M_x(\omega), 0_y, 0_z\}\rangle$, leaving the (S)TEM electron decelerated ($q > 0$) by interaction with the excited surface plasmon. The second represents the improper time-ordering of the two interactions, in which the electron scattering precedes the absorption of a photon. While not intuitive, the fact that both time orderings contribute to this scattering process (as opposed to the strictly causal interactions) has been discussed

extensively in the literature [170–172]. Remarkably, the addition of the two oppositely time-ordered terms in Eq. (3.1) (see Appendix B) results in a transition rate of zero. As a result, the second-order contribution to the total loss signal is completely determined by the rate of the sEIRE process as demonstrated below (see also Appendix B), with SPE providing no contribution.

Analyzing the two possible gain processes, SPD and sEEG, one can show that the transition rate of SPD,

$$\begin{aligned} w^{(2)}_{\mathrm{SPD}} = \frac{2\pi}{\hbar} \Bigg| \sum_m \frac{1}{E_i - E_m} \langle k_f, \{\ldots, N_\alpha + 1, \ldots\}, \{M_x(\omega) - 2, 0_y, 0_z\} | \hat{H}_{el-pl} | m \rangle \\ \times \langle m | \hat{H}_{ph-pl} | k_i, \{N\}, \{M_x(\omega), 0_x, 0_y\} \rangle \\ + \sum_{m'} \frac{1}{E_i - E_{m'}} \langle k_f, \{\ldots, N_\alpha + 1, \ldots\}, \{M_x(\omega) - 2, 0_y, 0_z\} | \hat{H}_{ph-pl} | m' \rangle \\ \times \langle m' | \hat{H}_{el-pl} | k_i, \{N\}, \{M_x(\omega), 0_x, 0_y\} \rangle \Bigg|^2 \delta(E_f - E_i) \end{aligned} \tag{3.2}$$

is also zero by similar reasoning (see Appendix B). Therefore, the second-order contributions to the total loss and gain signals are entirely described by the transition rates $w^{(2)}_{\mathrm{sEIRE}}$ and $w^{(2)}_{\mathrm{sEEG}}$, respectively, which describe the likelihood that the (S)TEM electron and a photon will interact simultaneously with the plasmon causing a deceleration and acceleration of the electron, respectively. These transition rates can be calculated as

$$\begin{aligned} w^{(2)}_{\mathrm{sEIRE}} = \frac{2\pi}{\hbar} \Bigg| \sum_m \frac{1}{E_i - E_m} \langle k_f, \{\ldots, N_\alpha + 1, \ldots\}, \{M_x(\omega), 0_y, 0_z\} | \hat{H}_{el-pl} | m \rangle \\ \times \langle m | \hat{H}_{ph-pl} | k_i, \{N\}, \{M_x(\omega), 0_x, 0_y\} \rangle \\ + \sum_{m'} \frac{1}{E_i - E_{m'}} \langle k_f, \{\ldots, N_\alpha + 1, \ldots\}, \{M_x(\omega), 0_y, 0_z\} | \hat{H}_{ph-pl} | m' \rangle \\ \times \langle m' | \hat{H}_{el-pl} | k_i, \{N\}, \{M_x(\omega), 0_x, 0_y\} \rangle \Bigg|^2 \delta(E_f - E_i) \end{aligned} \tag{3.3}$$

and

$$
\begin{aligned}
w^{(2)}_{\mathrm{SPD}} = \frac{2\pi}{\hbar} \Bigg| \sum_{m} \frac{1}{E_i - E_m} \langle k_f, \{\ldots, N_\alpha - 1, \ldots\}, \{M_x(\omega) - 2, 0_y, 0_z\} | \hat{H}_{el-pl} | m \rangle \\
\times \langle m | \hat{H}_{ph-pl} | k_i, \{N\}, \{M_x(\omega), 0_x, 0_y\} \rangle \\
+ \sum_{m'} \frac{1}{E_i - E_{m'}} \langle k_f, \{\ldots, N_\alpha - 1, \ldots\}, \{M_x(\omega) - 2, 0_y, 0_z\} | \hat{H}_{ph-pl} | m' \rangle \\
\times \langle m' | \hat{H}_{el-pl} | k_i, \{N\}, \{M_x(\omega), 0_x, 0_y\} \rangle \Bigg|^2 \delta(E_f - E_i)
\end{aligned}
\tag{3.4}
$$

with $k_f < k_i$ in $w^{(2)}_{\mathrm{sEIRE}}$ and $k_f > k_i$ in $w^{(2)}_{\mathrm{sEEG}}$. It is straightforward to show that the second-order sEEG transition rate recovers the same result given in Ref. [166] with $M_x(\omega) \to 0$, as the second (improper) term of Eq. (3.4) becomes zero. However, even at finite $M_x(\omega)$, both $w^{(2)}_{\mathrm{sEEG}}$ and $w^{(2)}_{\mathrm{sEIRE}}$ turn out to be independent of the initial plasmon occupation number (see Appendix B) and $w^{(2)}_{\mathrm{sEEG}}$ agrees with previous work for any $M_x(\omega)$. It is also important to note that even though sEIRE photons are not detected in our experiment, Eq. (3.3) nonetheless shows that the loss signatures of the sEIRE process are encoded in the final electron energy spectrum.

In addition to the second-order contributions to the total loss rate, the fast electron probe can also lose or gain energy by interacting with the laser-excited plasmon mode without the simultaneous creation or destruction of a photon. The rates of these phenomena are calculated at first order. In the case of energy loss, the electron can further lose energy to modes beyond those that are pumped by the laser such that the total first-order energy loss rate of all three plasmons is $w_{\mathrm{EEL}} + w^{(1)}_{\mathrm{sEEL}} = \sum_\lambda (2\pi/\hbar) | \langle k_f, \{N\}, \{\ldots, M_\lambda(\omega) + 1, \ldots\} | \hat{H}_{el-pl} | k_i, \{N\}, \{M_x(\omega), 0_y, 0_z\} \rangle |^2 \delta(E_f - E_i)$, with w_{EEL} the well-known spontaneous EEL rate and $w^{(1)}_{\mathrm{sEEL}}$ the first-order stimulated EEL rate (SI-vi). Therefore, $w^{(1)}_{\mathrm{sEEL}}$ and w_{EEL} must be added to $w^{(}_{\mathrm{sEIRE}}2)$ to reconstruct the total loss spectrum measured in our experiment.

Similarly, the total first-order contribution to the gain rate is $w^{(1)}_{\mathrm{sEEG}} = (2\pi/\hbar) | \langle k_f, \{N\}, \{M_x(\omega)\} - 1, 0_y, 0_z | \hat{H}_{el-pl} | k_i, \{N\}, \{M_x(\omega), 0_y, 0_z\} \rangle |^2 \delta(E_f - E_i)$ which, in

contrast to the first-order loss rate, contains no spontaneous contributions. It is thus clear that the total gain signal, $w^{(1)}_{\mathrm{sEEG}} + w^{(2)}_{\mathrm{sEEG}}$, is entirely caused by the sEEG process, allowing the label "total gain" to be dropped. Similarly dropping the label "total loss" in favor of sEEL now that all loss processes are accounted for, the sEEL and sEEG functions can be expressed in the following intuitive forms (see Appendix B),

$$\Gamma_{\mathrm{sEEL}}(\omega) \approx \Gamma_{\mathrm{EEL}}(\omega) + \left[M_x(\omega) + \frac{\pi}{2\hbar\omega_x}\sigma_x(\omega_x)\mathcal{I}(\omega) \right] \Gamma_{\mathrm{EELx}}(\omega) \tag{3.5}$$

and

$$\Gamma_{\mathrm{sEEG}}(\omega) = \left[M_x(-\omega) + \frac{\pi}{2\hbar\omega_x}\sigma_x(\omega_x)\mathcal{I}(-\omega) \right] \Gamma^{(-)}_{\mathrm{EELx}}(\omega) \tag{3.6}$$

which are simply related to the sum of the individual rates35 over the full spectrum of possible final states of the electron probe and photon field and are expressed in units of percent per unit loss/gain energy. Specifically, $\Gamma_{\mathrm{EELx}}(\omega)$ is a measure of EEL to only the longitudinal dipole plasmon with natural frequency $\Omega_x = \omega_x - \mathrm{i}\gamma_x(\omega)$ while $\Gamma_{\mathrm{EEL}}(\omega)$ is simply the sum of the EEL contributions from all three dipolar plasmons modes. $\mathcal{I}(\omega)$ is the spectral intensity, measured in units of intensity per unit frequency of the cw laser source and $\sigma_x(\omega)$ is the extinction cross section of the longitudinal dipole plasmon. In Eq. (3.6), the superscript $(-)$ indicates that the EELx function of Eq. (3.5) has been reflected across $\omega = 0$ such that the sEEG signal appears at negative frequencies. Explicitly, $\Gamma_{\mathrm{EELx}}(\omega) = (4e^2\omega^2/\pi\hbar^2v^4\gamma^4)(\gamma^2[\mathbf{R}_0 \cdot \mathbf{e}_x]^2/R_0^2)K_1^2(|\omega R/v\gamma|)\mathrm{Im}\{\alpha_x(\omega)\}$, with $\alpha_x(\omega) = d_x^2/(\hbar\Omega_x - \hbar\omega)$; the expression for $\Gamma^{(-)}_{\mathrm{EELx}}(\omega)$ can then be acquired by letting $\omega \to -\omega$.

3.4 Discussion

For sufficiently narrow laser linewidths, Eqs. (3.5) and (3.6) can be simplified by letting $\mathcal{I}(\omega)\Gamma_{\mathrm{EELx}}(\omega) \to I_{\mathrm{laser}}(1/\pi)\gamma_{\mathrm{laser}}/([\omega - \omega_{\mathrm{laser}}]^2 + \gamma^2_{\mathrm{laser}})\Gamma_{\mathrm{EELz}}(\omega_{\mathrm{laser}})$ and $\mathcal{I}(-\omega)\Gamma^{(-)}_{\mathrm{EELx}}(\omega) \to I_{\mathrm{laser}}(1/\pi)\gamma_{\mathrm{laser}}/([-\omega - \omega_{\mathrm{laser}}]^2 + \gamma^2_{\mathrm{laser}})\Gamma^{(-)}_{\mathrm{EELz}}(-\omega_{\mathrm{laser}})$, respectively, with I_{laser} the peak laser

irradiance, giving (see Appendix B)

$$\begin{aligned}\Gamma_{\mathrm{sEEL}}(\omega) \approx{}& \Gamma_{\mathrm{EEL}}(\omega) + M_x(\omega)\Gamma_{\mathrm{EELx}}(\omega) \\ &+ \left[\frac{\sigma_x(\omega_x)I_{\mathrm{laser}}}{2\hbar\omega_x}\frac{N+1}{N}\frac{\gamma_{\mathrm{laser}}}{(\omega-\omega_{\mathrm{laser}})^2+\gamma_{\mathrm{laser}}^2}\right]\Gamma_{\mathrm{EELx}}(\omega_{\mathrm{laser}})\end{aligned} \tag{3.7}$$

and

$$\Gamma_{\mathrm{sEEL}}(\omega) \approx M_x(-\omega)\Gamma^{(-)}_{\mathrm{EELx}}(\omega) + \left[\frac{\sigma_x(\omega_x)I_{\mathrm{laser}}}{2\hbar\omega_x}\frac{\gamma_{\mathrm{laser}}}{(-\omega-\omega_{\mathrm{laser}})^2+\gamma_{\mathrm{laser}}^2}\right]\Gamma^{(-)}_{\mathrm{EELx}}(-\omega_{\mathrm{laser}}). \tag{3.8}$$

Here N is the occupation number of the single cw laser mode modeled in the narrow-width limit. Note that for large N, the sEEL and sEEG functions become equivalent, up to the magnitude of the EEL signal, at each $\pm\omega$. Note also that sEEL reduces to EEL while sEEG vanishes in the limit where the laser irradiance (and therefore $M_x(\omega)$) is reduced to zero. These expressions, while approximate, make explicit the dependence of sEEL and sEEG upon optical extinction and EELS and provide a simple route to computing sEEL and sEEG spectra using continuum optical and electron scattering codes like the DDA [173, 174], MNPBEM [136], and e-DDA [134, 135].

Fig. 3.4 shows the theoretical sEEL, sEEG, and EEL spectra calculated for a $321 \times 120 \times 120$ nm^3 silver nanorod lying on a SiO_2 substrate in vacuum. Here, the electron beam and laser field co-propagate down an axis that is oriented normal to the long axis of the nanorod (see inset). The spectra are convolved pointwise with a normalized Lorentzian distribution of variance determined by the width of the ZLP (150 meV). Subtraction of the EEL spectrum from the sEEL spectrum would show that the stimulated gain and loss functions are nearly equivalent in amplitude as noted previously [166] with the difference arising only from the ratio $(N+1)/N$ that appears in $w^{(2)}_{\mathrm{sEIRE}}$. In the limit of large laser occupation numbers ($N+1 \approx N$), integration of the experimental sEEL and sEEG spectra of Fig 3.3a as well as the theory given in Eqs. (3.5) and (3.6) between 0 and ± 2 eV allows for the inference of $M_x^{\max}$. For peak laser intensities of 1.2, 2.5, and 4.0×10^8 W/m^2, the inferred maximum plasmon occupation numbers are 0.04, 0.10, and 0.13, respectively. Comparison of Figs. 3.4 and 3.3a highlights the remarkable quantitative agreement between the sEEG and sEEL

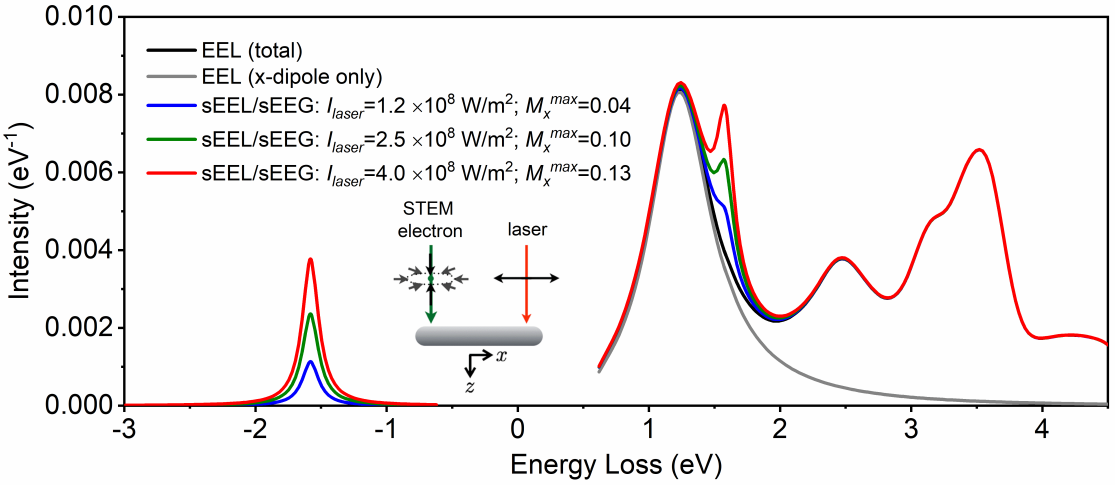

Figure 3.4: Computed total loss and gain spectra of a silver nanorod interacting with the pair of co-propagating cw laser and STEM-electron beams illustrated in the inset. The simulated EEL spectrum is also shown for reference and is the limiting behavior of the sEEL signal when the laser field is removed. The sEEL and sEEG profiles are symmetrically distributed at $\omega\hbar\omega_{\text{laser}} = \pm 1.58$ eV and, after subtracting the EEL spectral profile, are otherwise of equal amplitude up to a factor of $(N+1)/N$. The sEEL and sEEG spectra were calculated with an electron beam impact parameter of 107 nm and a plasmon effective mass of 1.6×10^{-34} g. Additionally, the theoretical curves were calculated with a maximum plasmon occupation number of $M_x^{\max}$ of 0.04, 0.10, and 0.13, which are extracted from the measured I_{laser} =1.2, 2.5, and $4.0{\times}10^8$ W/m^2 spectra in Fig. 3.3a together with Eqs. (7)-(8). Finally, all curves were convolved with a normalized Lorentzian distribution with a FWHM of 150 meV to model the finite energy resolution of the instrument.

peaks of experiment and theory. This supports the idea that the low intensity cw laser used in our experiment only weakly populates the nanoparticle plasmon mode, yet, we are still able to measure gain signal.

The experimental demonstration and theoretical underpinnings of low irradiance laser sEEL and sEEG illustrated here are an exciting first step in co-continuous electron and photon photoinduced nearfield electron microscopy using a monochromated STEM and high-resolution EELS. To extend the optical power range, higher thermal conductivity and smaller membranes could be used to enhance heat dissipation at high irradiance. Furthermore, multi-spectral cw photoexcited sEEL and sEEG would be possible by coupling other laser diode

wavelengths to the single mode fiber, a project that is now underway. For instance, while EELS conveniently has access to the entire plasmonic spectrum, the combination of EELS and multi-spectral low-irradiance photoexcited sEEL and sEEG could distinguish between optically bright and dark modes as well as the excited state internal field structure of the former. Thus we envision that the nearfield optical phenomena previously only visible with highly specialized UEMs will be accessible with a standard (S)TEM system equipped with the cw optical delivery source [168].

3.5 Conclusion

In summary, we have demonstrated stimulated electron energy-loss and stimulated electron energy-gain spectroscopy with a continuous wave laser source and monochromated electron source in a (S)TEM. These signatures emerge at an irradiance value of $\sim 5 \times 10^7$ W/m^2 and increase approximately linearly to $\sim 5 \times 10^8$ W/m^2. Above this irradiance range, photothermal heating causes the sEEG and sEEL probability to decrease. sEEL and sEEG mapping of a rod-like silver nanostructure confirms that 1.58 eV photons couple to the bright longitudinal dipole plasmon mode. Analytical modeling of the simultaneous (S)TEM electron- and cw laser photon-plasmon interactions based on time-dependent perturbation theory demonstrates the connection between the total loss and gain spectra and the more intuitive optical extinction, laser intensity, and normal EEL spectrum. By exploiting this connection, model simulations of the sEEL and sEEG of an individual silver nanorod elucidate the fundamental processing underlying our experimental observations. The ability to visualize the field structure of excited state plasmons opens up new directions for optically-stimulated fast electron spectroscopy of electronically excited nanomaterials, such as, e.g., the direct testing of optoelectronic circuits. One can also imagine that coupled with a gas cell, plasmon-based sensors and catalytic reactions can be synchronously imaged and correlated to those modes that are bright. Importantly, the photon delivery instrument used in this study can be attached to practically any microscope and equipped with various light sources, thus providing a more universal approach to visualizing atomic scale nearfield phenomena that are critical to many

photonic applications.

3.6 Methods

3.6.1 Sample Preparation

An $\sim$ 25 nm silver film was RF magnetron sputter deposited directly onto 20 nm SiO_2 membranes (TEMwindows.com, a division of SiMPore Inc., Rochester, New York.). The silver film was sputtered at: 20 W RF power, 25 standard cubic cm per minute Ar flow, and 5 mTorr chamber pressure.

3.6.2 Experimental Apparatus

A new photon delivery system was mounted on the monochromated Carl Zeiss LIBRA 200MC (S)TEM, as shown schematically in Fig. 3.1a. The optical delivery setup and laser information were elaborated in our previous work [168]. Peak powers up to $>$ 200 mW can be delivered to the sample from a 785 nm wavelength laser diode system coupled through a 5 μm single-mode fiber. The laser is gated by a software-controlled pulse generator that can vary the laser pulse width from a few ns to cw at repetition rates up to 16 MHz.

3.6.3 EELS Experiments

The TEM was operated at 200 kV in (S)TEM mode with a camera length of 945 mm. The collection semi-angle (β) was 45 mrad, and the convergence semi-angle (α) was 10 mrad. The low loss spectra were collected with a monochromator slit of 0.5 μm, and a dispersion of 30 meV per channel was chosen for the spectrometer acquisition. The average energy resolution (defined as the full width at half maximum of the zero-loss peak) was measured to be 136 meV for a summed spectrum; the energy spread for all single and summed spectra collected was between 120 and 150 meV. For each low-loss point spectrum, 10 frames with a dwell time of 0.1 s each were summed up to yield high count values and signal-to-noise ratios. The average energy resolution (defined as the full width at half maximum of the zero-loss

peak) was measured to be 136 meV. For the EELS map acquisition, a region of interest with 20×13 pixel spectra (1 pixel $\sim$ 19.5 nm $\times$19.5 nm) is defined over the entire silver nanoparticle. The pixel dwell time for each pixel in the EEL maps is 0.3 s. The maps of the sEEG (-1.58 eV), sEEL (1.58 eV), 1.21 eV dipole mode, and the 2.3 eV quadrupole mode are generated using the Gatan Digital Micrograph software by plotting spectra intensity in designated energy slices within the 3D spectrum image data cube (x, y, energy-loss).

Chapter 4

ELECTRON BEAM INFRARED NANO-ELLIPSOMETRY OF INDIVIDUAL INDIUM TIN OXIDE NANOCRYSTALS

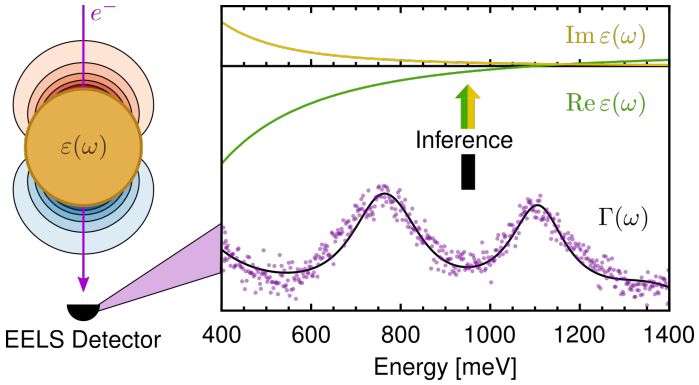

Leveraging recent advances in electron energy monochromation and aberration correction we record the spatially-resolved infrared plasmon spectrum of individual tin-doped indium oxide nanocrystals using electron energy-loss spectroscopy (EELS). Both surface and bulk plasmon responses are measured as a function of tin doping concentration from $1-10$ atomic percent. These results are compared to theoretical models, which elucidate the spectral detuning of the same surface plasmon resonance feature when measured from aloof and penetrating probe geometries. We additionally demonstrate a unique approach to retrieving the fundamental dielectric parameters of individual semiconductor nanocrystals via EELS. This method, devoid from ensemble averaging, illustrates the potential for electron-beam ellipsometry measurements on materials that cannot be prepared in bulk form or as thin films.

4.1 Introduction

Carrier doped semiconductor nanocrystals (NCs) are an emerging class of materials with tunable near-to-mid infrared (IR) optical responses that vary with dopant concentration [175–181]. Similar to noble metals, doped semiconductors have sufficient free carrier densities ($10^{18} - 10^{20}$ cm^{-3}) to produce localized surface plasmon (LSP) and bulk plasmon resonances [182–188]. In addition to greatly expanded IR tunability, doped NCs are also attractive because they offer IR plasmonic responses at truly nanoscale dimensions, something that typically cannot be achieved in noble metal nanostructures [189–193]. Beyond these qualities, altering geometric properties such as size, shape, and aggregation provides another route to exert control over their spectrum [194–196]. Due to this versatility, NC materials are being harnessed for applications such as surface-enhanced infrared absorption [197, 198], molecular sensing [52, 199, 200], medical therapeutics and imaging [201, 202], photovoltaics [203, 204], and photocatalysis [205–207] among many others.

Heterogeneity between NCs leads to spectral broadening of plasmon resonances in ensemble measurements [80], making the study of individual NCs essential for the development and application of IR plasmons [192, 208]. Studying the IR responses of individual NCs, however, is limited by instrumentation challenges. At these wavelengths, the diffraction limit is much larger than the NCs themselves ($\gtrsim 1$ μm versus < 50 nm, respectively), making dark field scattering [209, 210] and interferometric methods [211, 212] ineffective. Alternatively, near-field scanning optical microscopy (NSOM) [213, 214] is hampered by the lack of bright IR light sources and high quantum efficiency detectors. Nevertheless, when coupled to a synchrotron radiation source, NSOM variants like synchrotron infrared nanospectroscopy (SINS) have been used to measure the IR plasmons in individual NCs [215–217] and have found their resonance energies and line widths to differ from ensemble values. The limited spectral range ($\sim 100 - 600$ meV) of SINS [215], however, has precluded the characterization of NC responses over a wide range of plasmon energies.

Recent advances in aberration correction and monochromation of scanning transmission

electron microscopes (STEMs) have driven the energy resolution of electron energy-loss spectroscopy (EELS) as low as ~ 5 meV (40 cm^{-1}), enabling the study of IR materials responses for the first time [218–220]. Despite these developments, there have been no studies of the dependence of NC plasmons on dopant concentration at the single-particle level. Additionally, no methods exist to retrieve the underlying dielectric parameters of individual NCs that give rise to IR plasmons. Herein, we use high-resolution monochromated STEM-EELS to characterize the broadband spectral evolution of the surface and bulk plasmons of individual tin-doped indium oxide (ITO) NCs by controlling the relative number of free carriers per NC through Sn^{4+} dopant concentration. Our results are combined with theoretical modeling to extract the underlying material parameters that give rise to this spectral tunability, thereby informing the rational design of future NC-based plasmonic materials with desired IR responses.

4.2 Experimental Results

Fig. 4.1a shows a representative TEM image of 7.5% ITO NCs cast from bulk, displaying NC geometry ranging from cuboid to spherical. To minimize interparticle and particle-environment interactions in the STEM-EELS measurements, dilute NC solutions are cast onto 5 nm thick amorphous SiN grids. The NCs are then stripped of their native oleate ligands by submerging the sample in an acetonitrile solution of $(Et_3O)BF_4$ [221]. Due to the sensitive nature of the LSP to particle geometry, we are careful to inspect the high-angle annular darkfield (HAADF) image (Fig. 4.1b inset) prior to measuring for obvious faceting and cornering. While cubic nanoparticles have multipolar LSPs encoded in their spectral response [76, 222, 223], the effect is less pronounced in spherical-cuboid particles and may broaden the dipolar plasmon response depending on the degree of edge and corner formation (see Appendix C).

All EEL spectra are collected on an aberration corrected and monochromated STEM operating at 60 kV with 20 mrad and 20 mrad convergence and collection angles, and an approximately 18 meV zero-loss peak at full width at half maximum (FWHM). Two impact

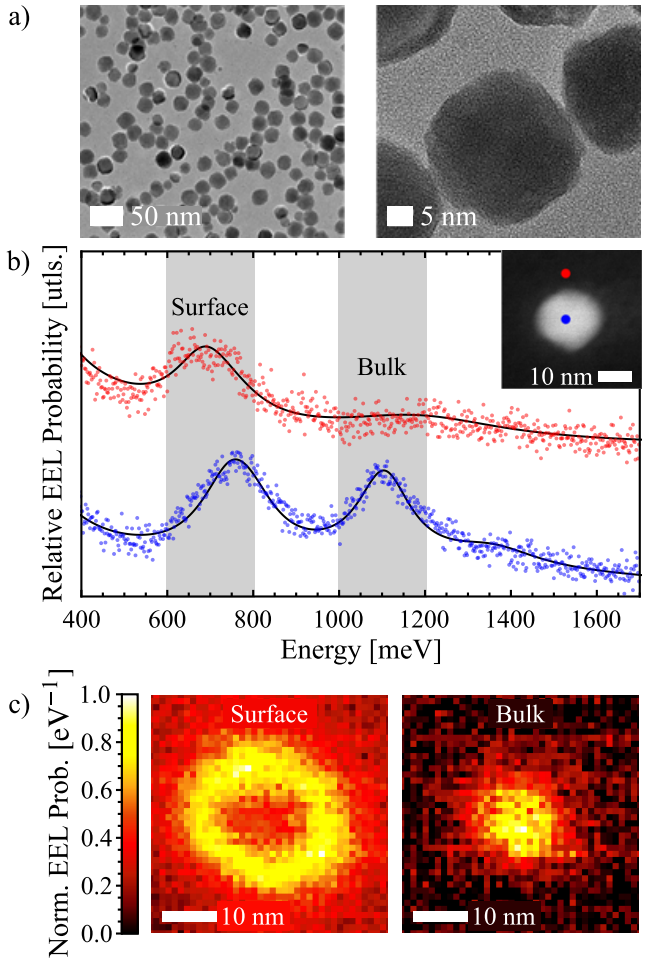

Figure 4.1: Representative ITO NC images and EEL spectra. a) TEM images of a 10% Sn^{4+} doped ITO NC sample displayed at two different magnifications, showing heterogeneity in NC shape and size. b) Characteristic aloof (red, $b - a = 5$ nm) and penetrating (blue, $b = 0$ nm) EEL spectra of an individual 7.5% Sn^{4+} doped ITO NC, along with best numerical fits. The inset shows a HAADF image of the NC along with the two probe positions. Interestingly, the surface plasmon resonance energies are observed to differ between aloof and penetrating spectra. c) Spectrum images of the same NC acquired at the surface and bulk plasmon peak energies.

parameters are recorded (Fig. 4.1b) for each NC. First, an aloof position (red) is recorded 5 nm away from the NC surface, with the resulting point spectrum showing the LSP resonance. This resonance is symmetric and does not appear to be multipolar, which suggests deviations

from spherical geometry are minimally impacting the LSP signature. Second, a penetrating trajectory (blue) passing through the center of the particle is recorded with the resulting point spectrum exposing two resonance features, one due to the LSP responses and the other to the bulk plasmon as modified by the finite NC boundaries. The spectrum images in Fig. 4.1c confirm this identification, and the uniform distribution of the surface plasmon supplies additional evidence for our spherical approximation of NCs.

Fig. 4.2a shows substrate subtracted aloof (upper) and penetrating (lower) EEL spectra recorded for individual ITO NCs ranging from $0-10\%$ Sn^{4+}. In general, the peak energies of the LSP and bulk plasmons exhibit a gradual blue-shift as the Sn^{4+} concentration increases, which is consistent with ensemble measurements of ITO colloids [224, 225]. This result also agrees with studies that measure the electrical properties of ITO thin films, which show that increased doping increases the electron density and lowers the resistivity [226, 227]. This behavior is directly correlated to the changing crystal structure of the In_2O_3 by the substitution of an In^{3+} ion with an Sn^{4+} ion in the In_2O_3 lattice, providing an available free carrier [226]. As shown in Fig. 4.2b, the plasmon energy shows a nonlinear dependence on the dopant concentration, leveling off around 10%. Once again, this result is consistent with previous analysis, which suggests that at higher concentrations of Sn^{4+}, crystal defects and trap state formation begin to affect the particle's electrical properties [226, 228]. Additionally, changes to the atomic structure of the NCs, especially at the surface, may be responsible for the variation in individual particle resonance energies and line widths measured (Appendix C) [229, 230].

4.3 Theoretical Model

Examination of the data further reveals a surprising difference between LSP energies depending upon the location of the electron probe. Although the spectrum images in Fig. 4.1c identify the lower energy resonance peak as the LSP, they do little to explain the $\sim$ 100 meV energy shift observed in the point spectra recorded for aloof and penetrating beam trajectories of the same LSP resonance feature. The origin of this shift can be understood

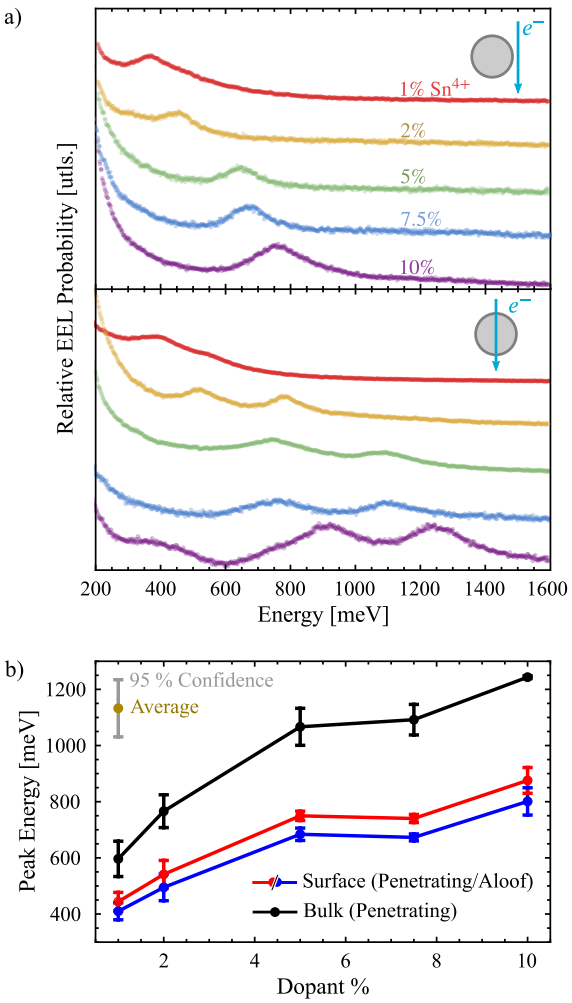

Figure 4.2: EEL spectra of individual ITO NCs as a function of Sn^{4+} dopant concentration. a) Both surface and bulk plasmon resonance energies increase as the Sn^{4+} dopant concentration increases from $1-10$ atomic percent for both aloof (upper) and penetrating (lower) beam trajectories. b) Average surface and bulk plasmon resonance energies and 95% confidence intervals for all measured point spectra at all dopant concentrations. Note that the surface plasmon resonance profile differs between aloof and penetrating spectra of the same particle due to the differing multipolar contributions driven by the electron probe at each position.

theoretically by considering the inelastic electron scattering from a spherical particle containing the bulk free-electron gas dielectric function $\varepsilon(\omega) = \varepsilon_\infty - \omega_p^2/(\omega^2 + i\omega\gamma)$. Here, ω_p is the semiconductor's plasma frequency, γ is its electron-ion scattering rate, and ε_∞ is its high

frequency dielectric constant. Retardation effects and the response of the substrate (∼5 nm thick SiN) to the fields of the electron are neglected as the small NC sizes (< 25 nm) and low carrier densities studied justify working in the quasistatic approximation with negligible substrate-induced plasmon mode mixing [76].

Under these assumptions, the Laplace equation can be solved exactly and used to determine the EEL probability function for both aloof and penetrating beam trajectories (Appendix C) [231, 232]. Fundamental to the solution is the Green's function G, which encodes the complete set of bulk and geometry-induced surface responses of the target system. When probed by a fast electron with charge density $\rho(\mathbf{x},t) = -e\delta(\mathbf{R} - b\hat{\mathbf{R}})\delta(z - vt)$, the potential at the arbitrary point $(\mathbf{x},t)$ is the superposition of independent Coulombic and induced plasmonic components defined by

$$\Phi(\mathbf{x},t) = \int_{-\infty}^{t} dt' \int d^3x' G(\mathbf{x},t;\mathbf{x}',t')\rho(\mathbf{x}',t'), \tag{4.1}$$

where $G = G_0 + G_{\text{ind}}$ similarly factors into the sum of a direct Coulombic response $G_0 = 1/|\mathbf{x} - \mathbf{x}'|$ to the STEM electron and the induced responses

$$\begin{aligned} G_{\text{ind}}^{r'<a}(\mathbf{x},\mathbf{x}';\omega) &= \left[\frac{g_\infty(\omega)}{|\mathbf{x}-\mathbf{x}'|} + \frac{1}{a}\sum_{\ell m}\left[g_\ell^{<}(\omega) - g_B(\omega)\right] f_{\ell m}^{<}(\mathbf{x}) f_{\ell m}^{<*}(\mathbf{x}')\right]\Theta(a-r) \\ &\quad + \frac{1}{a}\sum_{\ell m} g_\ell^{><}(\omega) f_{\ell m}^{>}(\mathbf{x}) f_{\ell m}^{<*}(\mathbf{x}')\Theta(r-a), \\ G_{\text{ind}}^{r'>a}(\mathbf{x},\mathbf{x}';\omega) &= -\frac{1}{a}\sum_{\ell m} g_\ell^{>}(\omega) f_{\ell m}^{>}(\mathbf{x}) f_{\ell m}^{>*}(\mathbf{x}')\Theta(r-a) \\ &\quad + \frac{1}{a}\sum_{\ell m} g_\ell^{><}(\omega) f_{\ell m}^{<}(\mathbf{x}) f_{\ell m}^{>*}(\mathbf{x}')\Theta(a-r) \end{aligned} \tag{4.2}$$

set up by the target, taken to be a sphere of radius a. The latter are expressed in their spectral representation in terms of the surface and bulk response functions $g_\ell^{>}(\omega) = \ell[\varepsilon(\omega) - 1]/(\ell\varepsilon(\omega) + \ell + 1)$, $g_\ell^{<}(\omega) = (2\ell+1)/(\ell\varepsilon(\omega)+\ell+1)$, $g_\ell^{><}(\omega) = g_\ell^{<}(\omega) - 1$, and $g_B(\omega) = 1/\varepsilon(\omega)$, $g_\infty(\omega) = g_B(\omega) - 1$, each dependent upon $\varepsilon(\omega)$. Together, they set the time dynamics of the ITO plasmon responses including their natural frequencies, line widths, and effective masses.

For example, it is from the poles of the surface response functions $g_\ell^>, g_\ell^<$, and $g_\ell^{><}$, which depend on the multipole order ℓ, that the natural frequencies $\omega_\ell = \omega_p\sqrt{\ell/(\ell\varepsilon_\infty + \ell + 1)}$ of the LSPs are defined, while the bulk plasmon frequency [16, 24] $\omega_B = \omega_p/\sqrt{\varepsilon_\infty}$ is defined by the pole of the bulk response functions g_B and g_∞. The spatial variation of $G_{\rm ind}$ is determined by the (ℓ, m)-dependent LSP mode functions $f_{\ell m}^{<,>}(\mathbf{x}) = \sqrt{4\pi/(2\ell+1)}Y_{\ell m}(\hat{\mathbf{x}})\{(r/a)^\ell, (a/r)^{\ell+1}\}$ with $\mathbf{x} = (\mathbf{R}, z)$ and $r = |\mathbf{x}| = \sqrt{|\mathbf{R}|^2 + z^2}$ (see Appendix C).

As the localized electron probe travels near or through the NC, it interacts with its plasmon modes, losing a small fraction $\hbar\omega$ of its initial kinetic energy $mv^2/2$ with probability $\Gamma(\omega) = \Gamma^{\rm surf}(\omega) + \Gamma^{\rm geo}(\omega) + \Gamma^\infty(\omega)$ per unit energy loss. Each contribution arises from the work done by the electron's induced potential upon itself via

$$\Gamma(\omega) = -\frac{1}{\pi\hbar^2}\int d^3x d^3x' \,\mathrm{Im}\Big\{\rho^*(\mathbf{x},\omega)G_{\rm ind}(\mathbf{x},\mathbf{x}';\omega)\rho(\mathbf{x}',\omega)\Big\}, \tag{4.3}$$

where both $\mathbf{x}$ and $\mathbf{x}'$ extend over all space and include configurations where $r, r' > a$, $r, r' < a$, and $r < a, r' > a$ and vice versa. The first term

$$\begin{aligned}\Gamma^{\rm surf}(\omega) = -\frac{1}{a\pi\hbar^2}\sum_{\ell m} &|A_{\ell m}^>(\omega)|^2 \,\mathrm{Im}\, g_\ell^>(\omega) + |A_{\ell m}^<(\omega)|^2 \,\mathrm{Im}\, g_\ell^<(\omega) \\ &+ 2\mathrm{Re}\left\{A_{\ell m}^>(\omega)A_{\ell m}^<(\omega)\right\}\mathrm{Im}\, g_\ell^{><}(\omega)\end{aligned} \tag{4.4}$$

describes the energy losses due to excitation of LSPs. The functions $A_{\ell m}^{<,>}(\omega) = \int_{V_{<,>}} \rho^*(\mathbf{x},\omega) f_{\ell m}^{<,>}(\mathbf{x}) d^3x$ are projection integrals of the electron's charge density against the LSP mode functions along the electron's trajectory through the volumes within ($V_<$) and outside ($V_>$) of the NC. These trajectory integrals dictate the change in magnitude of the response of each LSP mode as the impact parameter b is varied relative to the sphere radius a.

The latter two terms of $\Gamma(\omega)$ are the geometry-induced and infinite-medium contributions to the bulk plasmon response, given by

$$\begin{aligned}\Gamma^{\rm geo}(\omega) &= \frac{1}{a\pi\hbar^2}\sum_{\ell m}|A_{\ell m}^<(\omega)|^2 \,\mathrm{Im}\, g_B(\omega) \\ \Gamma^\infty(\omega) &= -\frac{2e^2\mathrm{Re}\{\sqrt{a^2-b^2}\}}{\hbar^2 v^2}\ln\left(1 + \frac{k_c^2 v^2}{\omega^2}\right)\mathrm{Im}\, g_\infty(\omega).\end{aligned} \tag{4.5}$$

These contributions have opposite signs: the geometric bulk plasmon terms (Γ^{geo}) serve to reduce the overall bulk plasmon EEL probability and are responsible for the well-known *begrenzungseffekt* (see Fig. 4.3a) [24, 42, 231], while the infinite medium term (Γ^{∞}) is directly proportional to the path length of the electron's trajectory within the ITO NC, $2\sqrt{a^2-b^2}$, and is dependent on the quantity k_c. This is a cutoff wavenumber that imposes a smoothing of the lateral components of the bulk plasmon's polarization response as the electron passes through the sphere and is defined by the half-aperture collection angle of the STEM spectrometer [42]. Without this cutoff, $\Gamma^{\infty} \to \infty$ as $k_c \to \infty$ (Appendix C).

4.4 Discussion

The contributions of each of these terms to the total EEL signal are highlighted in Fig. 4.3a. First, the bulk plasmon contributions are zero when the beam passes outside the particle, as $A^{<}_{\ell m}(\omega) = 0 = \text{Re}\{\sqrt{a^2-b^2}\}$ for $b > a$. In this case, the total signal is almost entirely determined by the dipolar ($\ell = 1$) LSP mode. As the beam approaches the surface, contributions from the higher-order ℓ modes increase until the probe penetrates the sphere. For penetrating trajectories, the signal contains significant contributions from both the surface and bulk plasmon responses. The bottom panel of Fig. 4.3a demonstrates the relative magnitudes of each multipole contribution to both Γ^{surf} and Γ^{geo}, as well as the magnitude of Γ^{∞}. It is important to note that the relative contribution from each multipole ℓ changes as the probe is brought inside the particle. For $b/a = 0$, the odd-parity modes contribute negligibly while the even-parity modes $2 \leq \ell \lesssim 10$ dominate the signal, shifting the apparent LSP peak position to a higher energy relative to the LSP resonance in the aloof spectrum. This effect explains the detuning between the aloof and penetrating LSP peak positions of the surface modes observed in Fig. 4.2b.

Because they contain responses at both surface and bulk plasmon energies, the penetrating trajectory EEL data allow for the extraction of unique values for the dielectric parameters ω_p and ε_∞ from the surface and bulk plasmon peak positions via nonlinear least-squares fitting to $\Gamma(\omega)$ in Eqs. (1) and (2). The peak line widths are determined completely by γ

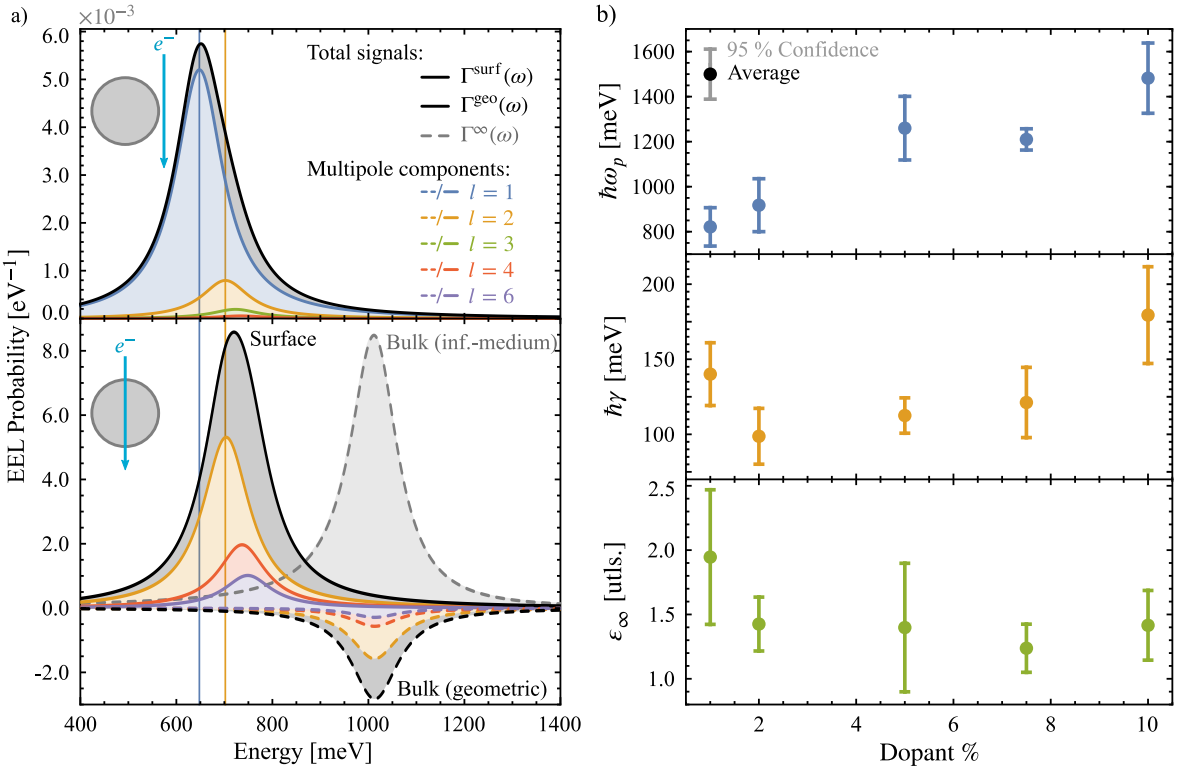

Figure 4.3: Theoretical analysis of the inelastic electron scattering function $\Gamma(\omega)$ for both aloof and penetrating trajectories. a) The relative contributions of $\Gamma^{\text{surf}}(\omega)$, $\Gamma^{\text{geo}}(\omega)$, and $\Gamma^{\infty}(\omega)$, along with their multipolar decompositions, to $\Gamma(\omega)$ at aloof (upper, $b - a = 5$ nm) and penetrating (lower, $b = 0$ nm) beam positions show the origin of the observed shift between aloof and penetrating spectra of the same LSP resonance feature. b) Extracted Drude dielectric parameters from numerical fits of $\Gamma(\omega)$ to the full set of individual NC data. The variance-weighted average values of the plasma frequency ω_p (blue), electron-ion scattering rate γ (yellow), and high-frequency dielectric constant ε_∞ (green) at each dopant concentration are shown with points, with the parameter variances estimated from each fit. 95% confidence intervals are shown with error bars.

in the quasistatic limit so that the bulk electron-ion scattering rate can also be uniquely determined from the same fitting routine. Our extraction of these peak paramters, however, is obstructed by numerous interfering radiative processes in the low-loss EELS region (< 5 eV) that are considered background when studying LSPs [120, 233]. Various model based, peak fitting, experimental "blank", and other combined methods have been utilized

for background removal, however, the suitability of a method is specific to the system being probed [220, 234, 235]. Prior to fitting, we perform a background subtraction using the signal obtained from a non-plasmonic In_2O_3 NC positioned on an identical 5 nm thick SiN substrate [236–238]. Heuristic fitting of the penetrating EEL spectrum of a similarly sized In_2O_3 NC (Appendix C) acts as reference which we use to fit the inelastic scattering due to the collective excitation of free carriers in ITO at each Sn^{4+} doping concentration. The final model is a combination of Lorentzian and exponential features that can accurately resolve the plasmons (see Appendix C for model details).

Once the plasmon signals are properly isolated from the background, two theoretical scale parameters, N and k_c, are tuned to normalize the total signal and align the relative heights of the theoretical surface and bulk peaks to their experimental values (Appendix C). Importantly, The extraction of ω_p, γ, and ε_∞ from the data relies only on knowledge of the peak positions and line widths so that no parameter is affected by the values of N and k_c chosen. Because acquiring absolute EEL probabilities from experiments is difficult, even in modern STEMs, the independence of the Drude parameters from the scale parameters makes determining the dielectric properties of individual NCs dramatically more feasible. Extension of this approach to materials that are better characterized by a Drude-Lorentz dielectric model is straightforward but requires additional aloof and penetrating point spectrum measurements to uniquely resolve the additional fit parameters.

In this manner, the Drude parameter values are inferred from 28 separate penetrating trajectory EEL spectra of ITO NCs ranging from $16 - 24$ nm in diameter and with Sn^{4+} dopant concentrations ranging from $1 - 10$ atomic percent. An additional 22 separate aloof-beam measurements (which do not contain bulk plasmon signals) are used to provide further estimates of γ, for which the existence of two observable peaks is not necessary. Results of the parameter extraction are shown in Fig. 4.3b. They show that the plasma frequency increases with the addition of free carriers in a nonlinear fashion that approaches a maximum around 10% Sn^{4+} composition. The lowest inferred value of $\hbar\omega_p$ is 705 meV at 1% Sn^{4+}, while the highest is 1575 meV at 10% Sn^{4+}, corresponding to a range of carrier densities of

$1.12 \times 10^{20} - 5.58 \times 10^{20}$ cm^{-3}, consistent with Refs. [228, 239–241] when assuming a free carrier effective mass of $m^* = 0.31m$ [240, 242–244].

Fit values of $\hbar\gamma$, the FWHM of the bulk plasmon peak as well as each multipole component of the LSP peak, are slightly higher at low and high Sn^{4+} concentrations than at intermediate levels of doping, with a dip at 2% Sn^{4+} where the fit average is 99 meV, which corresponds to $1.30 - 2.10$ times the Drude damping rate of gold extracted with modern methods [245, 246]. These results are also in good agreement with established thin film measurements of ITO [239–241]. Beyond these comparisons, this approach further opens up the potential of STEM-EELS to investigate the dependence of other factors such as grain boundaries [247–249], surface depletion layers [229, 230, 250], and environmental effects upon γ at the single particle level [177, 195, 197, 251].

Finally, the extracted values of ε_∞ are tightly grouped around 1.37 ± 0.025 for all dopant concentrations except for 1%, which shows an abrupt increase to 1.950. These results disagree with earlier measurements on thin films [239–241] that suggest ε_∞ to be near 4. We do not speculate on the physical origin of these ε_∞ differences between thin films, NC ensembles, and individual NCs, but point out that hybridization between the LSPs of different NCs or with environmental resonances is suppressed at values of ε_∞ greater than ~ 1 [51] (Appendix C). We also note that particles are unlikely to hybridize with the substrate in our system due to limited coupling to such thin substrates ($\sim$ 5 nm) [76] and the minimization of corners and sharp features, which suppresses the particles interaction with the environment. Thus, extraction of ε_∞ values near unity suggests that ITO NC plasmons should be capable of hybridizing into collective IR resonances that are additionally tunable by LSP coupling strength and detuning.

4.5 Conclusion

In summary, we use high-resolution monochromated STEM-EELS to characterize the evolution of the IR plasmon spectrum in individual ITO NCs with changing dopant concentration for the first time. We show that increasing the free carrier density via increased Sn^{4+} concen-

tration is an effective method for tuning plasmon responses over a wide range of IR energies and that individual NC heterogeneity can easily account for broad LSP responses measured by ensemble averages. Furthermore, we use a numerical fitting procedure to extract the frequency-dependent ITO Drude dielectric function at each Sn^{4+} concentration from $1 - 10$ atomic percent. By modeling the surface and bulk plasmon responses, this approach demonstrates the ability of STEM-EELS to determine dielectric material parameters in a single measurement and with less difficulty than standard thin film ellipsometry methods, paving the way for the facile retrieval of dielectric information from other doped semiconductor NCs at the single particle level. This work further demonstrates a route to extract key materials properties normally obtained from ellipsometry measurements but on materials that cannot be prepared in bulk form or as thin films.

Chapter 5

PROBING NANOPARTICLE SUBSTRATE INTERACTIONS WITH SYNCHROTRON INFRARED NANOSPECTROSCOPY: COUPLING GOLD NANOROD FABRY-PÉROT RESONANCES WITH SIO_2 AND HBN PHONONS

Spectroscopic interrogation of materials in the mid-infrared with nanometer spatial resolution is inherently difficult due to the long wavelengths involved, reduced detector efficiencies, and limited availability of spectrally bright, coherent light sources. Technological advances are driving techniques that overcome these challenges, enabling material characterization in this relatively unexplored spectral regime. Synchrotron infrared nanospectroscopy (SINS) is an imaging technique that provides local sample information of nanoscale target specimens in an experimental energy window between 330 and 5000 cm^{-1}. Using SINS, we analyzed a series of individual gold nanorods patterned on a SiO_2 substrate and on a flake of hexagonal boron nitride. The SINS spectra reveal interactions between the nanorod photonic Fabry-Pérot resonances and the surface phonon polaritons of each substrate which are characterized as avoided crossings. A coupled oscillator model of the hybrid system provides a deeper understanding of the coupling and provides a theoretical framework for future exploration.

5.1 Introduction

Advances in the design of nanoengineered materials endowed with tailorable mid-infrared (IR) responses have been accelerated by decades of prior research in plasmonics, photonics, and phononics. By leveraging knowledge gained from these communities, new strategies for creating tunable light-matter states that operate across the IR have emerged based on hybridizing electronic, optical, and vibrational degrees of freedom [252–254]. In such materials, their composite responses find origin in their bulk dielectric properties together with particle

morphology and cluster geometry [255–260]. Characterizing these properties with simultaneously high spatial and spectral resolution is difficult but essential for the rational design of advanced materials with novel functionalities [120, 261–264]. Today, a number of studies have made progress in this direction through a variety of near-field imaging and spectroscopy techniques [76, 265–272], yet considerable work still lies ahead to better understand material design principles and characterization methods in the IR spectral regime.

In this work, we investigate the resonant coupling between the mid-IR Fabry-Pérot (F-P) modes of high-aspect ratio noble-metal nanorods [193, 273–277] with the surface-phonon polaritons (SPhPs) [278, 279] of their supporting substrates. Due to their light like nature, we will refer to these surface plasmon polaritons as Fabry-Pérot (F-P) modes [193]. Previous work by Huck *et al.* [280] measured far-field extinction spectra from gold nanorods on SiO_2 substrates of various thicknesses and discovered an avoided crossing when the resonance positions of the nanorod series were plotted versus inverse nanorod length; however, these measurements did not probe the coupling in the near-field. More recently, Tizei *et al.* [281] explored strong coupling between SPhPs and the first F-P mode in long metal nanowires using electron energy-loss spectroscopy (EELS) performed in a scanning transmission electron microscope. In this study, silver nanorods were placed on thin hexagonal boron nitride (hBN) flakes with their ends suspended off the substrate. Probing the vacuum end of the nanorod minimized substrate losses and allowed the nanorod length to be systematically milled, via the electron beam, to tune the F-P response and produce an avoided crossing in the EEL spectrum. In general, the presence or absence of an avoided crossing depends on the specifics of the nanoparticle-substrate system and an avoided crossing is not expected when dealing with lossy modes or weak coupling [282]. The facile tunability of the nanorod F-P resonances employed here makes it an ideal system to study particle-substrate coupling.

Scattering-type scanning near-field optical microscopy (s-SNOM) utilizes light that is coupled into an atomic force microscope (AFM) to create a region of concentrated surface charges induced at its tip. The scattered field of these charges subsequently interacts with a target material, simultaneously gathering information about the spatial and spectral profiles

of the target's optical modes [213, 283–287]. Since the scattered field contains both radiative and nonradiative components, the selection rules for s-SNOM are relaxed compared to far-field plane-wave illumination, as the actual collected signal in s-SNOM is the radiation from the coupled tip-sample region. Direct measurement of a nanoparticle's dielectric response using such techniques provides: (1) a window into resonant energy transfer between nanostructured materials with their supporting substrates, (2) a method for analyzing irregularities of thin-film structures, and (3) an avenue for exploring quantum-size and surface-scattering effects [288–291]. Additionally, because the tip's characteristic length scale is on the order of tens of nanometers, near-field effects allow s-SNOM to overcome Abbe's diffraction limit [292].

By design, s-SNOM relies on a spectrally bright, collimated, and coherent light source because the tip focusing and scattering processes are inefficient. While this limitation has largely been overcome in the optical and ultraviolet spectral regions by advancements in laser technology, highly tunable IR sources remain limited [284]. Recently, Bechtel and co-workers [215] implemented an s-SNOM variant using the broadband and high-intensity IR radiation available from the synchrotron at the Advanced Light Source (ALS) at Lawrence Berkeley National Laboratory called synchrotron infrared nanospectroscopy (SINS); see Fig. 5.1. The rich IR spectral contents of the ALS allow the response of a sample to be simultaneously collected at all IR frequencies to which available photon detectors are sensitive. Current detector models provide a $\sim$ 0.5 meV spectral resolution that is considerably better than the $\sim$ 5 meV resolution of STEM EELS such that, taken together with the 25 nm spatial resolution provided by the AFM tip, SINS is a uniquely powerful technique with which to probe nanostructures, especially those with narrow resonances, in the mid-IR region [216, 293–301].

We begin by presenting SINS data to explore the transfer of energy between the low-energy multipolar F-P modes of individual gold nanowires and the IR SPhPs in a polar crystal substrate. nanorod lengths are systematically fabricated and measured to evolve these F-P modes through the highest energy SPhP substrate mode of SiO_2. Next, the substrate

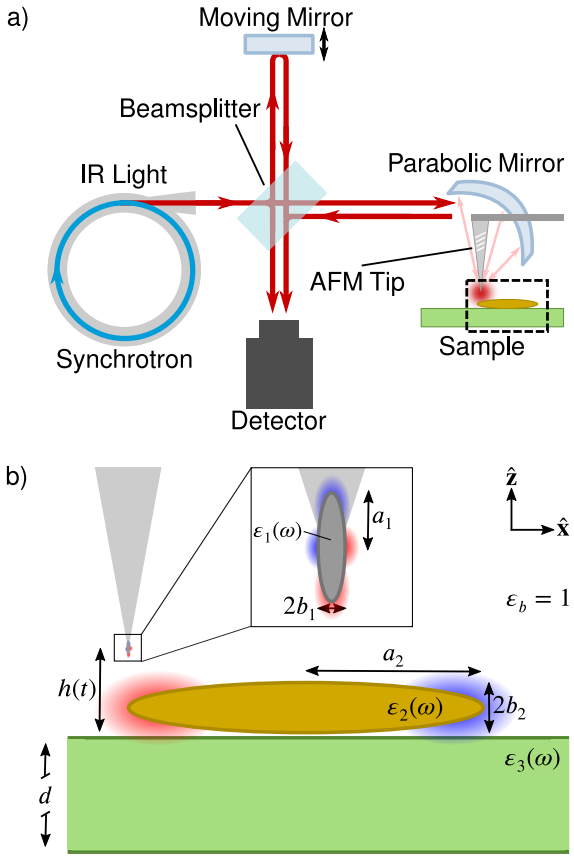

Figure 5.1: (a) Schematic of the experimental SINS setup. The dashed box encloses the tip-sample interaction region. (b) Geometry of the idealized sample system and the model parameters used to build an analytical oscillator model of the tip-sample interaction (see text for details).

is exchanged for a van der Waals material to explore how the nanowire F-P modes interact with a different inherent set of IR SPhPs. To gain physical insight, we model the system analytically, deriving the SINS signal from the tip's effective polarizability and interpreting the spectral features contained therein with a simple oscillator model.

5.2 Experimental Results

The second harmonic SINS response of two nanorods (1.13 μm and 2.18 μm) on SiO_2 are shown in Fig. 5.2 as a function of scan distance along the centerline of each nanorod. SINS of

the bare SiO_2 substrate (Fig. D.1 of the Appendix D, (Appendix D)) reveals a SPhP at 1219 cm^{-1} in the phase spectrum, and at 1126 cm^{-1} in the magnitude spectrum. Interestingly, this substrate feature is able to be detected through the 30 nm thick gold nanorod as seen in the SINS phase and magnitude spectra of the 1.13 μm nanorod along its full length. Lobes are observed at both nanorod ends around 2500 cm^{-1} in the SINS phase spectra and around 2200 cm^{-1} in the magnitude spectra (Fig. 5.2ab) . The spatial distribution and energy range of this feature, together with previous studies [120, 190, 193], indicates that this is the first, $m = 1$, F-P mode. As the nanorod's first F-P mode and substrate's SPhP are separated by $\sim$1200 cm^{-1}, little mixing is expected.

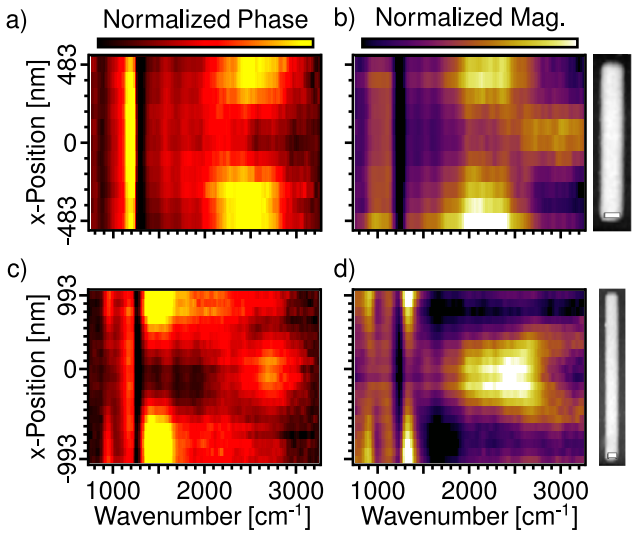

Figure 5.2: SINS linescans showing the normalized phase (a and c) and normalized magnitude (b and d) for 1.13 (a and b) and 2.18 (c and d) μm long nanorods on an SiO_2 substrate as a function of distance from the nanorod center. AFM images of the nanorods scanned are included on the right, with each horizontal scale bar representing 100 nm. The unmixed $m = 1$ F-P mode is observed in the shorter nanorod whereas the longer nanorod shows the mixing of the $m = 1$ F-P mode with the substrate phonon and the emergence of the unmixed $m = 2$ F-P mode. To better highlight these behaviors, SINS intensity information is displayed over a given range ($0.1 - 0.7$ rad and $0.4 - 1.0$ V) so that data outside of it saturates the image.

Increasing the nanorod length shifts the $m = 1$ F-P feature toward the lower energy SiO_2

SPhP [193], promoting interactions between the nanorod and substrate. SINS phase and magnitude linescan spectra of a 2.18 μm nanorod are shown in Figs. 5.2c and 5.2d, where the $m = 1$ F-P mode energy approaches the SPhP and a splitting is observed on either side of the SiO_2 phonon, with peaks at 950 cm^{-1} and 1450 cm^{-1} in both SINS phase and magnitude. Lengthening the nanorod also introduces a new feature in both spectra (around 2700 cm^{-1} in the phase spectra), which we attribute primarily to the second, $m = 2$, F-P mode based upon strong localization at the center of the nanorod. To further explore the peak splitting attributed to the first two F-P modes and SPhP mixing, we performed additional SINS characterization on more than two dozen nanorods of varying length on both SiO_2 and hBN substrates.

A series of Au nanowires ($L = 0.7 - 10.0$ μm, details in Table D.1 of Appendix D) were lithographically patterned onto two different substrates: (1) 100 nm thick amorphous SiO_2 on a Si wafer and (2) 330 nm thick flake of exfoliated hBN on a Si wafer. Measurements were performed at the tip and center of each nanorod in the series to track the $m = 1$ and $m = 2$ F-P modes, respectively. The second harmonic SINS magnitude components are reported in Fig. 5.3 (phase is reported in Fig. D.3 of Appendix D), where the top of each waterfall plot begins with the shortest nanorod and ends at the bottom with the longest nanorod. For the SINS magnitude measurements obtained at the tip of the shortest nanorods (top traces of Fig. 5.3) the SPhP feature is clearly isolated at 1126 and 1389 cm^{-1} for SiO_2 and hBN, respectively, with only the beginning of the red shoulder from the $m = 1$ F-P mode appearing in the high energy region. We confirm this as a SPhP feature by performing SINS on each substrate, in the absence of nanorods, to isolate and identify the substrate phonons (see Figs. D.1 and D.2 of Appendix D). SINS performed at the center of the shortest nanorods (top red traces in Fig. 5.3) also exhibit an isolated SPhP feature.

Increasing the nanorod length allows the F-P modes [193] to mix with the SPhP, causing a secondary peak to emerge at 987 cm^{-1} in SiO_2 and at 1296 cm^{-1} in hBN. Interestingly, these secondary peaks emerge asymptotically, shifting to lower energies. While the secondary peaks on the SiO_2 substrate quickly diverge out of the observation window, the secondary

peaks on hBN appear to converge towards 849 cm^{-1}. Concurrently, the F-P peak redshifts and asymptotes on the high energy side of the SPhP. This peak splitting around the isolated SPhP energy is indicative of an avoided crossing and further insight is provided by plotting the peak positions of both modes versus inverse nanorod length for each substrate (Fig. 5.4).

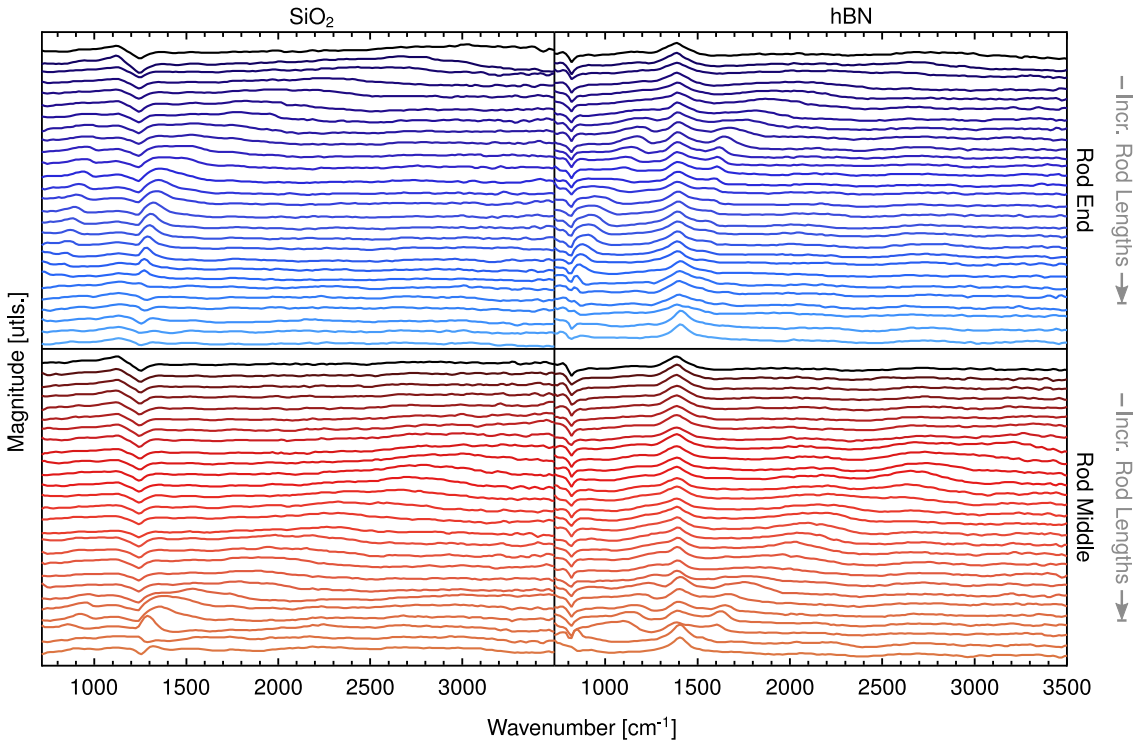

Figure 5.3: SINS magnitude spectra from a series of nanorods ($L = 0.7 - 10.0$ μm) obtained at the end (blue tones) or middle (red tones) of the nanorod on SiO_2 (first column) and hBN (second column) substrates. The spectrum obtained from the shortest nanorod is plotted at the top in each panel with longer nanorod spectra vertically offset until the longest nanorod in each series is plotted at the bottom.

Fig. 5.4, displays the avoided crossings between the substrate SPhPs and the nanorod $m = 1$ (blue) and $m = 2$ (red) F-P modes as measured in SINS magnitude (the associated avoided crossing in phase is presented in Appendix D as Fig. D.3). In the SiO_2 avoided

crossing, the asymptotic energies are 1248 cm^{-1} for the upper branch and 987 cm^{-1} for the lower branch. For the substrate thickness probed here, the upper branch of the avoided crossing is expected to align with the substrate's longitudinal optical phonon (LO) energy while the lower branch should align with the transverse optical phonon (TO) [280]. Our results are in good agreement with the previously reported LO and TO energies in amorphous SiO_2 (1248 cm^{-1} and 1064 cm^{-1}, respectively) [278], and are further consistent with the previously described far-field extinction measurements of a similar system [280].

Analyzing the nanorod evolution on hBN yields asymptotic energies of 1527 cm^{-1} for the upper branch and 1296 cm^{-1} for the lower branch of the avoided crossing. The branch energies observed here are in good agreement with previous measurements of the LO and TO in hBN [302]. In a similar experiment, Ag nanorods on thinner flakes of hBN were investigated using EELS to reveal an avoided crossing [281], although the mixing of the $m = 2$ F-P mode with the SPhP was not fully observed. Nevertheless, the avoided crossing in Fig. 5.3 clearly indicates the mixing of the $m = 1$ and $m = 2$ F-P modes of Au nanorods with SPhPs in hBN. In addition, the upper branch of a second avoided crossing in hBN is evidenced by a concavity change around 1050 cm^{-1} in the lower $m = 1$ branch and energies asymptotically approaching 849 cm^{-1} for the lowest values of inverse nanorod length. The latter energy aligns well with the next highest LO present in hBN which has a recorded value of 828 cm^{-1} [302]. The forbidden region in the avoided crossings is the spectral range between the upper and lower branches and has a maximum value determined by the energy separation of a substrate's LO and TO values. Known as the Reststrahlen band, this spectral region is most often where $\mathrm{Re}(\varepsilon)$ is negative [303]. In our experiments, we find branch separation energies of 261 cm^{-1} and 231 cm^{-1} for the SiO_2 and hBN substrates, respectively. These results are in good agreement with the expected Reststrahlen bands calculated from their previously reported LO and TO values [278, 302]. Interestingly, these values correspond to roughly half of the minimum separation energies between the upper and lower peak position of both F-P nanorod resonances on each substrate; see Table D.2 of Appendix D.

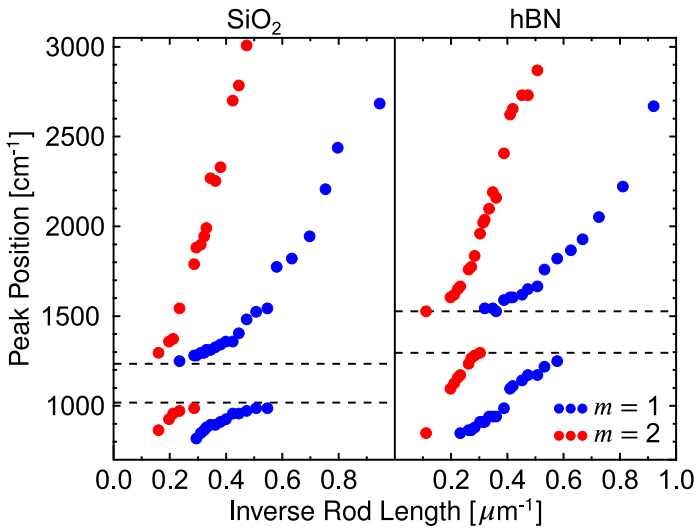

Figure 5.4: Avoided crossing diagram derived from the SINS magnitude measurements for the complete nanorod series on both SiO_2 and hBN substrates. The $m = 1$ (blue) and $m = 2$ (red) F-P modes are plotted versus inverse nanorod length. Dotted black lines are the asymptotic energies.

5.3 Theoretical Model

To augment the interpretation of the SINS signal, we present a reduced-order analytical model of the interactions between a F-P mode of the Au nanorod and a SPhP of the substrate. The model provides a simple and intuitive picture of the electromagnetic interactions within the sample and how each contributes to the observed spectra. As quantitative calculations involving the resonant surface modes of large particles are mathematically complicated and computationally expensive, we substitute these phenomena with simpler resonances that qualitatively reproduce the behavior of the system.

The $m = 1$ F-P mode of the target nanorod is modeled as the nonradiative long-axis dipolar mode of a prolate spheroid with long-axis radius a_2 and short-axis radius b_2; see Fig. 5.1. The long axis is taken to lie along the x-axis and the short axes lie in the yz-plane. The spectral properties of the dipolar mode are recovered from its polarizability, $\alpha_2(\omega)$, which

encodes the contributions of both the nanorod's dielectric function $\varepsilon_2(\omega)$ and geometry and allows the dipolar mode to be approximated as a point dipole located at the spheroid's center (Appendix D) [304]. The dipole is defined as $\mathbf{p}_2(\omega) = \alpha_2(\omega)\boldsymbol{\mathcal{E}}_{2x}(\mathbf{0},\omega)$, wherein $\mathbf{p}_2(\omega)$ is the nanorod's long-axis dipole moment and $\boldsymbol{\mathcal{E}}_{2x}(\mathbf{r},\omega)$ is the x-component of the total electric field $\boldsymbol{\mathcal{E}}_2(\mathbf{r},\omega)$ that impinges on the nanorod.

The coupling between the nanorod and its surroundings is provided through this total field. It can be expanded as $\boldsymbol{\mathcal{E}}_2(\mathbf{r},\omega) = \mathbf{E}_0(\omega) + \mathbf{E}_1(\mathbf{r},\omega) + \mathbf{E}_3(\mathbf{r},\omega)$, where $\mathbf{E}_0(\omega)$ is the electric field provided by the synchrotron light source, assumed here to be spatially uniform within the tip-sample region and linearly polarized with components along both the x- and z-axes. Further, $\mathbf{E}_1(\mathbf{r},\omega)$ is the field scattered from the AFM tip and $\mathbf{E}_3(\mathbf{r},\omega)$ is the field scattered from the substrate. The last field can be modeled as the image response of the substrate to the excitation provided by the synchrotron, tip, and target, and is proportional to the surface response function $\beta(\omega) = [\varepsilon_3(\omega) - 1]/[\varepsilon_3(\omega) + 1]$, with $\varepsilon_3(\omega)$ representing the substrate's dielectric function.

The tip's scattered field is modeled as originating from a superposition of two dipoles, one oriented parallel to the surface of the substrate and the other normal, that lie at the centroid of the tip, $\mathbf{r}_1$. The tip is taken to be a z-oriented prolate spheroid of long-axis radius a_1, short-axis radius b_1, and dielectric $\varepsilon_1(\omega)$ with a centroid raised a height $h > a_1$ above the substrate (see Fig. 5.1), such that the substrate-normal dipole is oriented along the tip's long axis, and the substrate-parallel dipole along the short axis. Similar to the treatment of the target nanorod, the tip's long (l) and short (s) axis dipole modes are given the polarizabilities of their spheroidal counterparts, $\mathbf{p}_1^{l,s}(\omega) = \alpha_1^{l,s}(\omega)\boldsymbol{\mathcal{E}}_{1z,1x}(\mathbf{r}_1,\omega)$ (see Eq. (A16) of Appendix D), with $\boldsymbol{\mathcal{E}}_{1i}(\mathbf{r},\omega)$ the i^{th} component of the total electric field $\boldsymbol{\mathcal{E}}_1(\mathbf{r},\omega) = \mathbf{E}_0(\omega) + \mathbf{E}_2(\mathbf{r},\omega) + \mathbf{E}_3(\mathbf{r},\omega)$ acting on the tip. A more detailed discussion of these approximations is given further on.

The complete spectral response of the tip is especially useful, as it encodes the observable SINS spectrum. The most convenient way to describe this response is through the effective polarizabilities $\hat{\alpha}_1^{l,s}(\omega)$. These polarizabilities encapsulate the influence of all external sources

on $\mathbf{p}_1^{l,s}(\omega)$, including sources which are in turn influenced by $\mathbf{p}_1^{l,s}(\omega)$ through coupling forces [305]. In this way, only a single force of the many that dictate the tip's polarization needs to be tracked, and the details of the rest of the system's motion follow from $\hat{\alpha}_1^{l,s}(\omega)$. In general, the only source of the tip's polarization that is experimentally characterizable is the synchrotron light, so it is singled out in the implicit definition $\mathbf{p}_1^{l,s}(\omega) = \hat{\alpha}_1^{l,s}(\omega)\mathbf{E}_{0z,0x}(\omega)$, wherein $\mathbf{E}_{0i}(\omega)$ is the i^{th}-component of the synchrotron field. Thus, with knowledge of the explicit forms of the effective polarizabilities and the synchrotron field, the magnitude and phase of the tip's dipole moment and associated scattered fields can be recovered and converted, through oscillation of the tip and lock-in detection, into the SINS observable (see Eq. (5.3)).

The derivations of $\hat{\alpha}_1^{l,s}(\omega)$ are lengthy (see Appendix D) but result in

$$\begin{aligned}\hat{\alpha}_1^{l}(\omega) &= \alpha_1^{l}(\omega)\frac{1+\beta(\omega)}{1-\alpha_1^{l}(\omega)\beta(\omega)/4h^3},\\ \hat{\alpha}_1^{s}(\omega) &= \alpha_1^{s}(\omega)\frac{1+2\hat{\alpha}_2(\omega)/\left(a_2^2+[h-b_2]^2\right)^{\frac{3}{2}}}{1-\alpha_1^{s}(\omega)\beta(\omega)/8h^3+4\alpha_1^{s}(\omega)\hat{\alpha}_2(\omega)/\left(a_2^2+[h-b_2]^2\right)^{3}}.\end{aligned} \tag{5.1}$$

For both tip dipoles, the effective polarizability is the product of its free-space polarizability $\alpha_1^{l,s}(\omega)$ and a frequency-dependent dressing factor. In the limit both $\hat{\alpha}_2(\omega)$ and $\beta(\omega)$ go to zero, either factor goes to one and the effective polarizabilities return to their free-space values. Further,

$$\hat{\alpha}_2(\omega) = \alpha_2(\omega)\frac{1}{1-\alpha_2(\omega)\beta(\omega)/8b_2^3} \tag{5.2}$$

is the nanorod dipole's effective polarizability. Note that Eq. (5.2) does not depend on either polarizability $\alpha_1^{l,s}(\omega)$ of the tip, such that the nanorod's spectral response is assumed to be altered only by the substrate. This approximation is valid here because the tip's long-axis dipole cannot couple to the target nanorod's dipolar mode at all by symmetry and the tip's short-axis dipole (which can couple) is both far-detuned from the nanorod's response and many orders of magnitude weaker. More specifically, the detuning between the maxima of $\operatorname{Im}\alpha_1^{s}(\omega)$ and $\operatorname{Im}\alpha_2(\omega)$ is roughly $70\gamma_2$, with γ_2 the nanorod mode's FWHM, and the ratio of the maxima is $\sim 10^{-5}$.

The substrate's modification of the nanorod's response is contained in the second term in the denominator of $\hat{\alpha}_2(\omega)$, which indicates coupling between the dipole and resonances in the substrate. In the case where $\alpha_2(\omega)$ and $\beta(\omega)$ each have a sufficiently strong single resonance, this term leads to mode splitting, as can be checked by comparison to the spectrum of two coupled oscillators (Appendix D).

Each of the terms in the dressing factors of $\hat{\alpha}_1^{l,s}(\omega)$ are similarly responsible for encoding coupling effects into the tip's response. The numerator of either factor builds in additional driving forces on the tip that arise as the synchrotron directly excites the substrate (in $\hat{\alpha}_1^l$) or target (in $\hat{\alpha}_1^s$) and causes surface charges in either to push back on the tip. Meanwhile the denominators encode coupling effects: the terms that go like $\alpha_1^{l,s}(\omega)\beta(\omega)/h^3$ describe tip-substrate coupling and the term in $\hat{\alpha}_1^s$'s denominator proportional to $\alpha_1^s(\omega)\hat{\alpha}_2(\omega)$ builds tip-target coupling into the tip's response. From these terms, one can conclude that only the short-axis dipole of the tip can couple to $\mathbf{p}_2(\omega)$. The long-axis dipole can only couple to the substrate, such that the observables of $\mathbf{p}_1^l(\omega)$ serve only to obscure the features of $\hat{\alpha}_1^s(\omega)$.

Translation of the effective polarizabilities of the tip to a SINS signal is performed by allowing the tip-substrate separation to become time dependent, such that $h \to h(t) = h_0 + \Delta h \cos(\Omega_0 t)$, where h_0 is the time-average separation, Δh is the modulation depth, and $\Omega_0 \sim 100$ kHz is the tip's oscillation frequency. The resulting time-dependent polarziabilities $\hat{\alpha}_1^{l,s}(\omega)$ can be expanded into a Fourier series with complex coefficients

$$A_n^{l,s}(\omega) = \frac{\Omega_0}{2\pi} \int_{-\frac{\pi}{\Omega_0}}^{\frac{\pi}{\Omega_0}} \hat{\alpha}_1^{l,s}(\omega, t) \mathrm{e}^{ni\Omega_0 t} dt \tag{5.3}$$

which are known to reproduce both the magnitude and phase of the SINS signal up to a scaling factor [213]. The synchrotron's light is assumed to be polarized at 45 degrees to the x-axis, such that both the long- and short-axis dipole modes of the tip are driven equally. The second-order Fourier coefficient of the total field flux at the location of the detector is

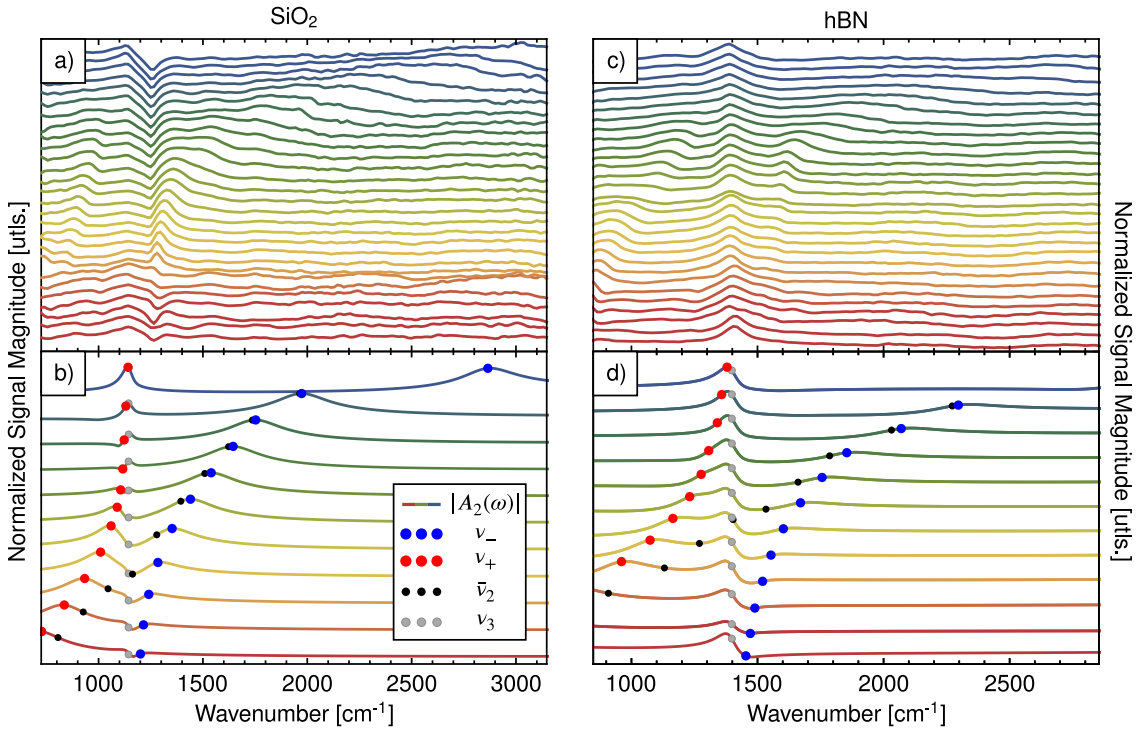

Figure 5.5: Comparison of experimentally collected (a, c) and theoretically constructed (b, d) SINS magnitude spectra $|A_2(\omega)|$ of the $m = 1$ nanorod F-P mode. The experimental spectra were obtained from a series of target gold nanorods of lengths varying from $L = 0.7-10.0$ μm, while the theoretical spectra were generated using a target spheroid of long axis radius $a_2 = 9$ μm, short-axis radius $b_2 = 550$ nm, plasma wavenumber $\omega_{p2}/2\pi c = 1633$ cm^{-1}, scattering wavenumber $\gamma_2/2\pi c = 256.5$ cm^{-1}, and variable Lorentz wavenumber $\omega_2/2\pi c = 805.5-2977$ cm^{-1}. The nanorods were mounted on SiO_2 (a) and hBN (c) substrates, and these substrates were modeled theoretically (b, d) with plasma wavenumbers $\omega_{p3}/2\pi c = 362.9$ and 1169 cm^{-1}, damping wavenumbers $\gamma_3/2\pi c = 64.12$ and 92.75 cm^{-1}, Lorentz wavenumbers $\omega_3/2\pi c = 1147$ and 1398 cm^{-1}, and intraband dielectrc constants $\varepsilon_{\infty 3} = 1.2$ and 2.68, respectively [236, 306, 307]. Additionally, the spectral locations of the uncoupled nanorod dipole ($\bar{\nu}_2$), uncoupled substrate SPhP (ν_3), and hybridized modes ($\nu_\pm$) are superimposed on the spectra to demonstrate the effects of the nanorod-substrate coupling on the observable signal.

then proportional to the average of the coefficients of the fields from each tip dipole, and can be modeled up to a constant scale factor by $A_2(\omega) = [A_2^l(\omega) + A_2^s(\omega)]/2$.

5.4 Discussion

Fig. 5.5 shows the absolute magnitude $|A_2(\omega)|$. The tip is made of PtSi, which in the range of energies considered in Fig. 5.5 is well-modeled by a Drude-model dielectric $\varepsilon_1(\omega) = 1 - \omega_{p1}^2/(\omega^2 + i\omega\gamma_1)$ with plasma wavenumber $\omega_{p1}/2\pi c = 2.98 \times 10^4$ cm^{-1} and damping wavenumber $\gamma_1/2\pi c = 645$ cm^{-1} [308]. The metallic motion of the tip's electrons as well as its micron-scale length and conical geometry likely impart on it an optical response dominated by a continuous spectrum of propagating surface plasmon modes. While the existence and properties of these modes have not yet been experimentally explored in PtSi tips, they have recently been investigated in similarly conductive gold tips [309–311]. We take from these earlier studies two conclusions, namely that the electric response of the tip does not contain resonances in the mid-IR when driven by sources near its apex and that the field profiles of its low-energy response are dipolar at each driving frequency ω just below its apex.

Building on previous successes modeling AFM tips using point dipoles and/or spheroidal particles, we model the tip's apex as a pair of point-dipoles $\mathbf{p}_1^{l,s}$ with spheroidal polarizabilities that reproduce the apex's featureless low-energy spectral response and field profile [213, 285, 312]. Both properties are achieved naturally. The spheroid model assumes the tip's response is dominated by a pair of localized surface plasmon dipoles, both of which resonate at energies far higher than the resonance frequencies of the target nanorod dipoles and substrate SPhPs due to the reliatively large value of ω_{p1}. Thus, the low-energy tails of the resonances provide the tip a flat spectral response below 4000 cm^{-1} (see Fig. D.6) that minimally modifies the responses of the nanorod and substrate. The dipolar field profile of the tip immediately emerges from the dipole model.

The target nanorod is given a Lorentz-model dielectric function $\varepsilon_2(\omega) = 1 + \omega_{p2}^2/(\omega_2^2 - \omega^2 - i\omega\gamma_2)$, which provides $\mathbf{p}_2$ a singly-peaked resonant spectrum. Although the experiment uses a Au nanorod that is better modeled with a Drude dielectric function, we choose a Lorentz-model to easily tune the nanorod's resonance frequency $\Omega_2 = \sqrt{\omega_2^2 + \omega_{p2}^2 A_{10}(X_2)/[A_{10}(X_2) - B_{10}(X_2)]}$ and mimic the hitherto ignored red-shift brought

on by radiation damping (Appendix D). Further, adjustments to the oscillator strength ω_{p2}^2 and damping rate γ_2 allow us to account for the related resonance suppression and linewidth modifications that appear in a fully-retarded treatment [193]. Each of the parameters of $\varepsilon_2(\omega)$ was fit to the experimental data and corroborated with gold nanorod data collected from Refs. [190, 193].

The substrate's dielectric is simplified, in both Fig. 5.5 b and d, to a Lorentz dielectric with a single phonon mode at the LO phonon frequency ω_3 with oscillator strength ω_{p3}^2, damping rate γ_3, and static contribution $\varepsilon_{\infty 3}$ such that $\varepsilon_3(\omega) = \varepsilon_{\infty 3} + \omega_{p3}^2/(\omega_3^2 - \omega^2 - i\omega\gamma_3)$. This simplification allows for a clear depiction of mixing between the dipole's resonance at Ω_2 and the substrate's lone SPhP at $\Omega_3 = \sqrt{\omega_3^2 + \omega_{p3}^2/(\varepsilon_{\infty 3} + 1)}$ at the expense of neglecting the width of the Reststrahlen band of either substrate, within which many SPhPs exist and clear identification of individual hybrid modes is very difficult [278, 302, 303].

The only significant error brought on by this approximation appears near the extremes of the nanorod series, where one pair of hybrid mode energies asymptotes to the edges of the Restrahlen band in the experiment (Fig. 5.4) and to Ω_3 in the theoretical reproduction. Because the Reststrahlen band of either substrate is narrower than the linewidth of the nanorod's dipolar mode and largely obscured by a strong peak in each collected spectrum, the vast majority of the observable features in the experimental signal lie outside this region and are well-modeled by the single-phonon approximation.

In particular, with an hBN substrate (Fig. 5.5c,d) the single-phonon approximation reproduces the spectral shifts and avoided crossing of the two peaks observed clearly in the experimental data on either side of the SPhP energy. It also reveals that the observed peaks reach a minimum separation at $|\Omega_2^2 - \Omega_3^2| = 0$, as expected from hybridization theory, and that the dipole's linewidth is reduced due to its mixing with the narrower SPhP.

5.4.1 Oscillator Model of the Nanorod and Substrate Resonances

In the case of the SiO_2 substrate this behavior is not so clear. The ever-present feature at the SPhP energy, caused by coupling between $\mathbf{p}_1^l(\omega)$ and the SPhP, is altered at many

values of Ω_2. This is contrary to the behavior of hBN and produces asymmetries in the line shapes of the hybridized modes. While the effective polarizability model reproduces this behavior and reveals its cause to be the relatively weak phonon oscillator strength of SiO_2, it alone cannot help us to extract the resonance positions of the two hybrid modes from the atypical spectrum with significantly greater certainty than the approximations used to generate Fig. 5.4 already provide. Instead, the hybridized modes can be extracted with the aid of an oscillator model of the system because it provides analytical expressions for the hybrid resonance frequencies $\Omega_\pm$ via standard mode-mixing techniques. We begin with the definition of a coordinate $x(\omega) = \mathbf{p}_2(\omega) \cdot \hat{\mathbf{x}}/e$, which represents the complex magnitude of $\mathbf{p}_2(\omega)$ and is

$$x(\omega) = \frac{F(\omega)}{m_2} \frac{1}{\Omega_2^2 - \omega^2 - i\omega\gamma_2}. \tag{5.4}$$

Here, $F(\omega) = e\mathcal{E}_{2x}(\mathbf{0}, \omega)$ is the external force acting on the oscillator (assumed to be located at the origin, $\mathbf{r} = \mathbf{0}$) and $m_2 = 3e^2(A_{10} - B_{10})/c_2^3\omega_{p2}^2$ is the oscillator's mass.

While the connection between $\mathbf{p}_2(\omega)$ and $x(\omega)$ is straightforward, the connection between the substrate's SPhP and an oscillator coordinate is not. Leaving the details for Appendix D, the substrate's scattered field at the origin can be defined as

$$\mathbf{E}_3(\mathbf{0}, \omega) = -\frac{e}{\sqrt{8L^3 b_2^3}} ([Q_{01}(\omega) + Y_{01}(\omega)]\, \hat{\mathbf{x}} + [Q_{00}(\omega) + Y_{00}(\omega)]\, \hat{\mathbf{z}}). \tag{5.5}$$

Here, the coordinates $Q_{pm}(\omega)$ represent independent SPhPs with azimuthal node structure $m = \{0, 1, \ldots\}$ and reflection parity about the x-axis (p even or odd). Their resonant behavior is similar to that of $x(\omega)$, with

$$Q_{pm}(\omega) = \frac{\mathcal{F}_{pm}(\omega)}{M_m} \frac{1}{\Omega_3^2 - \omega^2 - i\omega\gamma_3}, \tag{5.6}$$

wherein $M_m = (2 - \delta_{m0})e^2(\varepsilon_{\infty 3} + 1)^2/\omega_{p3}^2 d^3$ are the mode masses. Due to the substrate's infinite extent, a characteristic length factor, d, is used, akin to the quantization lengths often used in quantum optical theories. As is true in box quantization, the observables of the system are independent of d, and it serves only to provide sensible units and an overall scale to the oscillator picture.

From the forms of Eqs. (5.5) and (5.6), it is clear why both dipoles of the tip can couple to an SPhP resonance at Ω_3 in the substrate without indirectly coupling to each other. Because the SPhP responses $1/(\Omega_3^2 - \omega^2 - i\omega\gamma_3)$ are the same for all (p, m) and the tip-substrate couplings are $-\mathbf{p}_1^l(\omega) \cdot \mathbf{E}_{3z}(\mathbf{0}, \omega) \propto x(\omega)Q_{00}(\omega)$ and $-\mathbf{p}_1^s(\omega) \cdot \mathbf{E}_{3x}(\mathbf{0}, \omega) \propto x(\omega)Q_{01}(\omega)$, the dipoles interact with independent SPhP modes $Q_{pm}(\omega)$ of different symmetry but identical spectral behavior.

The coordinates $Y_{pm}(\omega)$ describe the excitation of independent substrate modes that respond instantaneously to stimuli and do not oscillate. From their definition $Y_{pm}(\omega) = L^3\beta_\infty\mathcal{F}_{pm}(\omega)/(2-\delta_{m0})e^2$, one can see that as $\varepsilon_{\infty 3} \to 1$ the factor $\beta_\infty = (\varepsilon_{\infty 3}-1)/(\varepsilon_{\infty 3}+1) \to 0$. Thus, the static coordinates do not contribute to the scattered field unless $\varepsilon_{\infty 3} > 1$.

The functional forms of the forces $\mathcal{F}_{pm}(\omega)$ on the SPhPs are complicated. Derivations of the forces are left for Appendix D, where their dependence upon the charge distribution of the nanorod and the nanorod coordinate are made explicit. Further, since the force $F(\omega)$ acting on the nanorod dipole contains a term $e\mathbf{E}_3(\mathbf{0}, \omega) \cdot \hat{\mathbf{x}}$, we note that $F(\omega) \propto Q_{01}(\omega)$. In this way, the forces on either oscillator mediate their coupling, and the forces' explicit forms lead to the coupled equations of motion

$$\begin{aligned} x(\omega)\left(\bar{\Omega}_2^2 - \omega^2 - i\omega\gamma_2\right) - \frac{g}{m_2}Q_{01}(\omega) &= \frac{F_0(\omega)}{m_2}, \\ Q_{01}(\omega)\left(\Omega_3^2 - \omega^2 - i\omega\gamma_3\right) - \frac{g}{m_3}x(\omega) &= 0. \end{aligned} \tag{5.7}$$

Here, $m_3 = M_1$ is the mass of the lone SPhP mode $Q_{01}(\omega)$ that can couple to the target nanorod's resonance and $F_0(\omega) = eE_{0x}(\omega)$ is the force applied on the nanorod by the synchrotron light. The lowered frequency $\bar{\Omega}_2 = \sqrt{\Omega_2^2 - \beta_\infty e^2/8b_2^3m_2}$ encapsulates the contribution of $Y_{01}(\omega)$ on the nanorod's spectrum: the substrate's static response induces a redshift on the nanorod's dipole that is small for $\varepsilon_{\infty 3} \sim 1$ and large as $\varepsilon_{\infty 3} \gg 1$. The static coordinates are thus not explicitly represented in Eq. (5.7).

It is convenient to decouple the equations of motion using standard techniques that produce normal modes $x_\pm$ and normal mode frequencies $\Omega_\pm^2 = \bar{\Omega}_2^2 S_\pm^2(\theta) + \Omega_3^2 S_\mp^2(\theta) \pm g\sin(2\theta)/\sqrt{m_2m_3}$, where $S_+(\theta) = \cos\theta$, $S_-(\theta) = \sin\theta$, and $\theta = (1/2)\tan^{-1}(2g/\sqrt{m_2m_3}[\bar{\Omega}_2^2 -$

$\Omega_3^2]$) is the mixing angle that determines the degree of hybridization between $x(\omega)$ and $Q_{01}(\omega)$. Here $g = -e^2/\sqrt{8d^3b_2^3}$ is a constant coupling strength that, along with the masses m_2 and m_3, sets the scale of mixing in the system, while the variable detuning $\bar{\Omega}_2^2 - \Omega_3^2$ between the modes' natural frequencies allows the system to transition through the point of maximal mixing where θ flips from $\pi/4$ to $-\pi/4$.

To visualize this transition, normal mode frequencies are superimposed on the spectra of Fig. 5.5 as the wavenumbers $\nu_\pm = \Omega_\pm/2\pi c$ with $d = 1$ cm and $|g| = 2.0 \times 10^{-13}$ g/s^2. They demonstrate that the observable peaks of $|A_2(\omega)|$ are indeed located near the normal modes of the system even when the peaks have strange lineshapes. Additionally, in cases where one peak is difficult to discern, the hybridization model shows that one of the normal mode wavenumbers $\nu_\pm$ has approached $\nu_3 = \Omega_3/hc$ such that the resonant lineshape of the associated mode $x_\pm(\omega)$ has become buried by the parasitic signal from the substrate mode $Q_{00}(\omega)$ that couples directly with the tip.

5.4.2 Coupling Characteristics of Substrate-Nanorod System

Finally, we note that strong coupling has been achieved in the experimental systems with both SiO_2 and hBN substrates. This can be observed directly from the marked separation between the coupled resonances of the hBN substrate and can be inferred from an analysis of the difference of the squared hybrid frequencies at maximal mixing, $\Omega_+^2(\pi/4) - \Omega_-^2(\pi/4) = 2g/\sqrt{m_2 m_3}$. With the uncoupled SPhP masses $m_3 = 1.194 \times 10^{-46}$ g and 3.219×10^{-47} g in the SiO_2 and hBN substrates, respectively, and the nanorod's dipole mode mass $m_2 = 2.686 \times 10^{-36}$ g, the characteristic splitting constant $\sqrt{2|g|/\sqrt{m_2 m_3}}/2\pi c$ is equal to 793 cm^{-1} (SiO_2) and 1100 cm^{-1} (hBN), at least a factor of three larger than the linewidths $\gamma_3/2\pi c = 64.1$ cm^{-1} (SiO_2), 92.6 cm^{-1} (hBN), and $\gamma_2/2\pi c = 256$ cm^{-1} of the system.

Using a more traditional metric, one can see from the theoretical model that the hybridized resonances of both the SiO_2 and hBN systems are always split by at least the average of the uncoupled mode linewidths, such that $R(\theta) = 2|\Omega_+(\theta) - \Omega_-(\theta)|/(\gamma_2 + \gamma_3) > 1$ is satisfied for all mixing angles [313–315]. At maximal mixing ($\theta = \pi/4$), R is minimized and

equal to 1.71 and 2.51, respectively. Additionally, with $\bar{\Omega}_2 = \Omega_3 = \Omega_0$ at maximal mixing, the splitting can be simplified via a power series to $\Omega_+(\pi/4) - \Omega_-(\pi/4) \approx g/\Omega_0\sqrt{m_2 m_3} = \sigma$, with σ the form of the coupling strength that appears in quantum-optical treatments of interacting cavities [316–318]. This simplification produces strong coupling ratios $R(\pi/4) \approx 2|\sigma|/(\gamma_2 + \gamma_3) = 1.71$ (SiO_2) and 2.48 (hBN), as well as values of 0.24 (SiO_2) and 0.31 (hBN) for the ultrastrong coupling condition $|\sigma|/\Omega_0$.

Experimental approximations of the strong and ultrastrong coupling conditions can also be recovered directly from the SINS data. However, as both substrates possess more than one SPhP that couples to the F-P mode of the rod and none of the SPhP linewidths can be directly extracted from the signal, the coupling ratio R must be replaced by a similar ratio R' that contains only measureable quantities and accounts for the width of the Reststrahlen band. The most convenient form of the new ratio is $R'(\theta) = 2[|\Omega'_+(\theta) - \Omega'_-(\theta)| - \Delta]/[\gamma'_+(\theta) + \gamma'_-(\theta)]$, where $\Omega'_\pm$ are the measured hybrid frequencies, $\gamma'_\pm$ are the measured linewidths of the hybrid modes, and Δ is the Reststrahlen band width as reported in Fig. 5.4. At maximal mixing, $R'(\pi/4) = 1.35$ (SiO_2) and 2.10 (hBN), in good agreement with the theory. Finally, approximating the shared natural frequency of the SPhP and F-P mode at maximal mixing, Ω'_0, to lie at the center of the Reststrahlen band, the ultrastrong coupling condition $|\sigma'|/\Omega'_0 \approx (\gamma_+ + \gamma_-)R'(\pi/4)/2\Omega'_0$ takes a value of 0.17 for either substrate material.

5.5 Conclusion

In conclusion, we report the observation of strong coupling between the $m = 1$ and 2 F-P modes of $L = 0.7 - 10.0$ μm long gold nanorods and the SPhP modes of a polar crystal (SiO_2) and a Van der Waals (hBN) substrate using SINS. The hybridization of the nanorod resonances with the substrate is made clear by the experiment, which leverages the unique IR sensitivity and spatial selectivity of SINS to characterize the anticrossing behavior of the hybrid F-P-SPhP mode pairs as the F-P modes are tuned in and out of resonance with the SPhPs. The coupling of the $m = 1$ mode is confirmed by a reduced-order model that describes in detail the individual interactions of the nanorod, substrate, and AFM tip

to produce both a reconstruction of the SINS observable and a mechanical analogy that interprets the spectral features therein. Importantly, the theoretical model accounts for the interference of the substrate in the SINS signal and allows for the clear interpretation of SINS spectra that lack the clearly defined resonances observed in more familiar optical and electron-beam spectroscopies. This combined experimental and theoretical investigation of interacting IR resonances in a tunable nanoscopic system provides a blueprint for the design and fabrication of more tailored IR nanophotonic systems for use in future molecular sensing, cavity-controlled chemistry, and optical circuit applications.

5.6 Materials and Methods

5.6.1 Apparatus

The SINS setup consists of a synchrotron light source, KBr beamsplitter, rapid-scan FTIR system, atomic force microscope (AFM), and a mercury cadmium telluride (MCT) detector. The beamsplitter forms an asymmetric Michelson type interferometer with the rapid-scan FTIR as one arm and the AFM tip/sample as the other [215]. Light from the synchrotron, $3-13$ μm wavelengths ($3333-769$ cm^{-1}), is focused onto the sample and platinum silicide AFM tip with a gold, 0.4 NA, parabolic mirror. Over multiple visits to the ALS we find that replicate samples yield quantitatively similar results indicating good reproducibility in the sample preparation and AFM tip conditions (see SM Fig S5). The MCT detector records the recombined signal which is demodulated by a lock-in amplifier at the second harmonic. These interferograms are Fourier Transformed, turning them into broadband spectral responses. The entirety of these experiments were collected with a spectral resolution of 32 cm^{-1}. A single point spectrum, which is actually an average of 256 individual scans, takes 90 seconds to acquire at this resolution. Since the setup is operating in the near to mid IR, the entire system is purged with N_2 to minimize atmospheric H_2O and CO_2 signatures.

5.6.2 Sample Fabrication

The Au nanorod lengths are designed to be $0.5 - 4.0$ (0.1 μm increments) and $1 - 10$ (1 μm increments) μm with a constant height of 30 nm, a width of 100 nm, and a 50 nm radius of curvature at their ends. We expect these to exhibit both $m = 1$ and $m = 2$ F-P mode resonances in the SINS energy range of $700 - 5000$ cm^{-1} [193]. Au nanorods were patterned using electron beam lithography on: 1) a 100 nm thermal SiO_2 film on a double side polished silicon wafer and 2) a a 330 nm thick exfoliated flake of hexagonal boron nitride (hBN) on a double side polished silicon wafer. Additionally, a 10 μm $\times$ 10 μm $\times$ 30 nm Au structure was patterned, which provides a reference for the phase and magnitude information and serves to optimize the SINS MCT detector signal. The substrate is cut to approximately 10 mm x 10 mm and mounted on a customized AFM sample holder with super glue.

BIBLIOGRAPHY

[1] Henri Moissan and Georges Charpy. On boron steel. *C. R. Acad. Sci.*, 120:130–132, 1895.

[2] Adolph W. Machlet. Treatment of steel, iron, &c. United States Patent US1065379A, 1913.

[3] H. Staudinger. Über Polymerisation. *Ber. Dtsch. Chem. Ges.*, 53(6):1073–1085, 1920.

[4] P. R. White. Cultivation of animal tissues in vitro in nutrients of precisely known constitution. *Growth*, 10(3):231–289, 1946.

[5] Jack S. Kilby. Miniaturized electronic circuits. United States Patent US3138743A, 1964.

[6] Robert N. Noyce. Semiconductor device-and-lead structure, 1961.

[7] Ernest Braun and Stuart MacDonald. *Revolution in Miniature: The History and Impact of Semiconductor Electronics*. Cambridge University Press, 2 edition, 1982.

[8] National Nanotechnology Initiative. Nanotechnology timeline, 2021. https://www.nano.gov/timeline.

[9] Paul Drude. Zur elektronentheorie der metalle. *Ann. Phys.*, 306(3):566–613, 1900.

[10] Gustav Mie. Beiträge zur optik trüber medien, speziell kolloidaler metallösungen. *Ann. Phys.*, 330(3):377–445, 1908.

[11] Lewi Tonks and Irving Langmuir. A general theory of the plasma of an arc. *Phys. Rev.*, 34(6):876–922, 1929.

[12] Harrison J. Merrill and Harold W. Webb. Electron scattering and plasma oscillations. *Phys. Rev.*, 55(12):1191–1198, 1939.

[13] Walter Ledermann and Max Born. Asymptotic formulae relating to the physical theory of crystals. *Proc. R. Soc. Lond. A.*, 182(991):362–377, 1944.

[14] Gerhard Ruthemann. Diskrete energieverluste mittelschneller elektronen beim durchgang durch dünne folien. *Ann. Phys.*, 437(3-4):113–134, 1948.

[15] W. Lang. Loss of velocity of moderately fast electrons in passing through thin metal foils. *Optik*, 3:233, 1948.

[16] David Pines and David Bohm. A collective description of electron interactions: Ii. collective vs individual particle aspects of the interactions. *Phys. Rev.*, 85(2):338–353, 1952.

[17] Igor Tamm. On the possible bound states of electrons on a crystal surface. *Phys. Z. Sowjetunion*, 1:733–735, 1932.

[18] Lev D. Landau. Uber die bewegung der elektronen in kristallgitter. *Phys. Z. Sowjetunion*, 3:644–645, 1933.

[19] Solomon Pekar. Local quantum states of electrons in an ideal ion crystal. *J. Exp. Theor. Phys.*, 16(4):341–348, 1946.

[20] Herbert Fröhlich. Interaction of electrons with lattice vibrations. *Proc. R. Soc. Lond. A.*, 215(1122):291–298, 1952.

[21] J. Frenkel. On the transformation of light into heat in solids. I. *Phys. Rev.*, 37(1):17–44o, 1931.

[22] Gregory H. Wannier. The structure of electronic excitation levels in insulating crystals. *Phys. Rev.*, 52(3):191–197, 1937.

[23] N. F. Mott. Note on the contact between a metal and an insulator or semi-conductor. *Math. Proc. Cambridge Philos. Soc.*, 34(4):568–572, 1938.

[24] R. H. Ritchie. Plasma losses by fast electrons in thin films. *Phys. Rev.*, 106(5):874–881, 1957.

[25] C. J. Powell and J. B. Swan. Origin of the characteristic electron energy losses in magnesium. *Phys. Rev.*, 116(1):81–83, 1959.

[26] E. A. Stern and R. A. Ferrell. Surface plasma oscillations of a degenerate electron gas. *Phys. Rev.*, 120(1):130–136, 1960.

[27] D. V. Geppert. The metal-base transistor. *IRE Trans. Electron Devices*, 9(6):507–507, 1962.

[28] M. M. Atalla and D. Kahng. A new "hot electron" triode structure with semiconductor-metal emitter. *IRE Trans. Electron Devices*, 9(6):507–508, 1962.

[29] Ronald Fuchs and K. L. Kliewer. Optical modes of vibration in an ionic crystal sphere*. *J. Opt. Soc. Am.*, 58(3):319, 1968.

[30] R. Fuchs. Theory of the optical properties of ionic crystal cubes. *Phys. Rev. B*, 11(4):1732–1740, 1975.

[31] R. H. Ritchie, E. T. Arakawa, J. J. Cowan, and R. N. Hamm. Surface-plasmon resonance effect in grating diffraction. *Phys. Rev. Lett.*, 21(22):1530–1533, 1968.

[32] Julian Crowell and R. H. Ritchie. Radiative decay of coulomb-stimulated plasmons in spheres. *Phys. Rev.*, 172(2):436–440, 1968.

[33] Hiroshi Watanabe. Experimental evidence for the collective nature of the characteristic energy loss of electrons in solids–studies on the dispersion relation of plasma frequency. *J. Phys. Soc. Jpn.*, 11(2):112–119, 1956.

[34] John E. Davey and Titus Pankey. Epitaxial GaAs films deposited by vacuum evaporation. *J. Appl. Phys.*, 39(4):1941–1948, 1968.

[35] A. Y. Cho and J. R. Arthur. Molecular beam epitaxy. *Prog. Solid. State Ch.*, 10(3):157–191, 1975.

[36] C. G. Granqvist, R. A. Buhrman, J. Wyns, and A. J. Sievers. Far-infrared absorption in ultrafine Al particles. *Phys. Rev. Lett.*, 37(10):625–629, 1976.

[37] Fuminori Fujimoto and Ken-ichiro Komaki. Plasma oscillations excited by a fast electron in a metallic particle. *J. Phys. Soc. Jpn.*, 25(6):1679–1687, 1968.

[38] Rointan F. Bunshah. *The history of electron-beam technology.* University of California Lawrence Radiation Laboratory, Livermore, California, 1961.

[39] P. E. Batson. Damping of bulk plasmons in small aluminum spheres. *Solid State Commun.*, 34(6):477–480, 1980.

[40] J. M. Cowley. Energy losses of fast electrons at crystal surfaces. *Phys. Rev. B*, 25(2):1401–1404, 1982.

[41] A. Howie and R. H. Milne. Electron energy loss spectra and reflection images from surfaces. *J. Microsc.*, 136(2):279–285, 1984.

[42] F. J. García de Abajo. Optical excitations in electron microscopy. *Rev. Mod. Phys.*, 82(1):209–275, 2010.

[43] E. H. Synge. XXXVIII. A suggested method for extending microscopic resolution into the ultra-microscopic region. *Philos. Mag.*, 6(35):356–362, 1928.

[44] John Aloysius O'Keefe. Resolving power of visible light. *J. Opt. Soc. Am.*, 46(5):359, 1956.

[45] Th. Kokkinakis and K. Alexopoulos. Observation of radiative decay of surface plasmons in small silver particles. *Phys. Rev. Lett.*, 28(25):1632–1634, 1972.

[46] D. W. Pohl, W. Denk, and M. Lanz. Optical stethoscopy: Image recording with resolution $\lambda/20$. *Appl. Phys. Lett.*, 44(7):651–653, 1984.

[47] F. Zenhausern, M. P. O'Boyle, and H. K. Wickramasinghe. Apertureless near-field optical microscope. *Appl. Phys. Lett.*, 65(13):1623–1625, 1994.

[48] G. Binnig, C. F. Quate, and Ch. Gerber. Atomic force microscope. *Phys. Rev. Lett.*, 56(9):930–933, 1986.

[49] Markus Brehm, Albert Schliesser, and Fritz Keilmann. Spectroscopic near-field microscopy using frequency combs in the mid-infrared. *Opt. Express*, 14(23):11222–11233, 2006.

[50] Florian Huth, Alexander Govyadinov, Sergiu Amarie, Wiwat Nuansing, Fritz Keilmann, and Rainer Hillenbrand. Nano-FTIR absorption spectroscopy of molecular fingerprints at 20 nm spatial resolution. *Nano Lett.*, 12(8):3973–3978, 2012.

[51] Charles Cherqui, Niket Thakkar, Guoliang Li, Jon P. Camden, and David J. Masiello. Characterizing localized surface plasmons using electron energy-loss spectroscopy. *Ann. Rev. Phys. Chem.*, 67(1):331–357, 2016.

[52] Leonetta Baldassarre, Emilie Sakat, Jacopo Frigerio, Antonio Samarelli, Kevin Gallacher, Eugenio Calandrini, Giovanni Isella, Douglas J. Paul, Michele Ortolani, and Paolo Biagioni. Midinfrared plasmon-enhanced spectroscopy with germanium antennas on silicon substrates. *Nano Lett.*, 15(11):7225–7231, 2015.

[53] Daniel Rodrigo, Odeta Limaj, Davide Janner, Dordaneh Etezadi, F. Javier García de Abajo, Valerio Pruneri, and Hatice Altug. Mid-infrared plasmonic biosensing with graphene. *Science*, 349(6244):165–168, 2015.

[54] Jifa Qi, Xiangnan Dang, Paula T. Hammond, and Angela M. Belcher. Highly efficient plasmon-enhanced dye-sensitized solar cells through metal@oxide core–shell nanostructure. *ACS Nano*, 5(9):7108–7116, 2011.

[55] Michael D. Brown, Teeraporn Suteewong, R. Sai Santosh Kumar, Valerio D'Innocenzo, Annamaria Petrozza, Michael M. Lee, Ulrich Wiesner, and Henry J. Snaith. Plasmonic dye-sensitized solar cells using core-shell metal-insulator nanoparticles. *Nano Lett.*, 11(2):438–445, 2011.

[56] P. Mandal and S. Sharma. Progress in plasmonic solar cell efficiency improvement: A status review. *Renew. Sustain. Energy Rev.*, 65:537–552, 2016.

[57] Philipp Reineck, Delia Brick, Paul Mulvaney, and Udo Bach. Plasmonic hot electron solar cells: The effect of nanoparticle size on quantum efficiency. *J. Phys. Chem. Lett.*, 7(20):4137–4141, 2016.

[58] Xuan Yi, Kai Yang, Chao Liang, Xiaoyan Zhong, Ping Ning, Guosheng Song, Dongliang Wang, Cuicui Ge, Chunying Chen, Zhifang Chai, and Zhuang Liu. Imaging-guided combined photothermal and radiotherapy to treat subcutaneous and metastatic tumors using iodine-131-doped copper sulfide nanoparticles. *Adv.Funct. Mater.*, 25(29):4689–4699, 2015.

[59] Xiaohua Huang, Prashant K. Jain, Ivan H. El-Sayed, and Mostafa A. El-Sayed. Plasmonic photothermal therapy (PPTT) using gold nanoparticles. *Lasers Med. Sci.*, 23(3):217, 2007.

[60] Emily A. Smith and Robert M. Corn. Surface plasmon resonance imaging as a tool to monitor biomolecular interactions in an array based format. *Appl. Spectrosc.*, 57(11):320A–332A, 2003.

[61] Xiao-Li Zhou, Yunze Yang, Shaopeng Wang, and Xian-Wei Liu. Surface plasmon resonance microscopy: From single-molecule sensing to single-cell imaging. *Angew. Chem. Int. Ed.*, 59(5):1776–1785, 2020.

[62] Kevin D. Heylman, Niket Thakkar, Erik H. Horak, Steven C. Quillin, Charles Cherqui, Kassandra A. Knapper, David J. Masiello, and Randall H. Goldsmith. Optical microresonators as single-particle absorption spectrometers. *Nature Photon.*, 10(12):788–795, 2016.

[63] Ujjal Bhattacharjee, Claire A. West, Seyyed Ali Hosseini Jebeli, Harrison J. Goldwyn, Xiang-Tian Kong, Zhongwei Hu, Elliot K. Beutler, Wei-Shun Chang, Katherine A. Willets, Stephan Link, and David J. Masiello. Active far-field control of the thermal near-field *via* plasmon hybridization. *ACS Nano*, 13(8):9655–9663, 2019.

[64] Linan Zhou, Dayne F. Swearer, Chao Zhang, Hossein Robatjazi, Hangqi Zhao, Luke Henderson, Liangliang Dong, Phillip Christopher, Emily A. Carter, Peter Nordlander, and Naomi J. Halas. Quantifying hot carrier and thermal contributions in plasmonic photocatalysis. *Science*, 362(6410):69–72, 2018.

[65] Xuming Zhang, Yu Lim Chen, Ru-Shi Liu, and Din Ping Tsai. Plasmonic photocatalysis. *Rep. Prog. Phys.*, 76(4):046401, 2013.

[66] Raphael F. Ribeiro, Luis A. Martínez-Martínez, Matthew Du, Jorge Campos-Gonzalez-Angulo, and Joel Yuen-Zhou. Polariton chemistry: controlling molecular dynamics with optical cavities. *Chem. Sci.*, 9(30):6325–6339, 2018.

[67] Cosimo Lacava, Mohamed A. Ettabib, and Periklis Petropoulos. Nonlinear silicon photonic signal processing devices for future optical networks. *Appl. Sci.*, 7(1):103, 2017.

[68] Raffaella Di Sante. Fibre optic sensors for structural health monitoring of aircraft composite structures: Recent advances and applications. *Sensors*, 15(8):18666–18713, 2015.

[69] Hank Hogan. Defense and aerospace, 2017.

[70] Apostolos Argyris, Julián Bueno, and Ingo Fischer. Photonic machine learning implementation for signal recovery in optical communications. *Sci. Rep.*, 8(1):8487, 2018.

[71] T. L. Ferrell, R. J. Warmack, V. E. Anderson, and P. M. Echenique. Analytical calculation of stopping power for isolated small spheres. *Phys. Rev. B*, 35(14):7365–7371, 1987.

[72] A. L. Cavalieri, N. Müller, Th. Uphues, V. S. Yakovlev, A. Baltuška, B. Horvath, B. Schmidt, L. Blümel, R. Holzwarth, S. Hendel, M. Drescher, U. Kleineberg, P. M. Echenique, R. Kienberger, F. Krausz, and U. Heinzmann. Attosecond spectroscopy in condensed matter. *Nature*, 449(7165):1029–1032, 2007.

[73] Rongchao Jin, Y. Charles Cao, Encai Hao, Gabriella S. Métraux, George C. Schatz, and Chad A. Mirkin. Controlling anisotropic nanoparticle growth through plasmon excitation. *Nature*, 425(6957):487–490, 2003.

[74] K. Lance Kelly, Eduardo Coronado, Lin Lin Zhao, and George C. Schatz. The optical properties of metal nanoparticles: The influence of size, shape, and dielectric environment. *J. Phys. Chem. B*, 107(3):668–677, 2003.

[75] Martin Aeschlimann, Michael Bauer, Daniela Bayer, Tobias Brixner, F. Javier García de Abajo, Walter Pfeiffer, Martin Rohmer, Christian Spindler, and Felix Steeb. Adaptive subwavelength control of nano-optical fields. *Nature*, 446(7133):301–304, 2007.

[76] Charles Cherqui†, Guoliang Li†, Jacob A. Busche†, Steven C. Quillin, Jon P. Camden, and David J. Masiello. Multipolar nanocube plasmon mode-mixing in finite substrates. *J. Phys. Chem. Lett.*, 9(3):504–512, 2018.

[77] Chenze Liu†, Yueying Wu†, Zhongwei Hu†, Jacob A. Busche†, Elliot K. Beutler, Nicholas P. Montoni, Thomas M. Moore, Gregory A. Magel, Jon P. Camden, David J. Masiello, Gerd Duscher, and Philip D. Rack. Continuous wave resonant photon stimulated electron energy-gain and electron energy-loss spectroscopy of individual plasmonic nanoparticles. *ACS Photonics*, 6(10):2499–2508, 2019.

[78] Agust Olafsson†, Jacob A. Busche†, Jose J. Araujo, Arpan Maiti, Juan Carlos Idrobo, Daniel R. Gamelin, David J. Masiello, and Jon P. Camden. Electron beam infrared nano-ellipsometry of individual indium tin oxide nanocrystals. *Nano Lett.*, 20(11):7987–7994, 2020.

[79] Joseph J. Liberko, Jacob A. Busche, Robyn Seils, Hans A. Bechtel, Philip D. Rack, David J. Masiello, and Jon P. Camden. Probing nanoparticle substrate interactions with synchrotron infrared nanospectroscopy: Coupling gold nanorod Fabry-Pérot resonances with SiO_2 and h-BN phonons. *Phys. Rev. B*, Just Accepted, 2021.

[80] Katherine A. Willets and Richard P. Van Duyne. Localized surface plasmon resonance spectroscopy and sensing. *Ann. Rev. Phys. Chem.*, 58:267–297, 2007.

[81] Harry A. Atwater and Albert Polman. Plasmonics for improved photovoltaic devices. *Nat. Mater.*, 9(3):205–213, 2010.

[82] Sarah Unser, Ian Bruzas, Jie He, and Laura Sagle. Localized surface plasmon resonance biosensing: Current challenges and approaches. *Sensors*, 15(7):15684–15716, 2015.

[83] Mark L. Brongersma, Naomi J. Halas, and Peter Nordlander. Plasmon-induced hot carrier science and technology. *Nat. Nanotechnol.*, 10(1):25–34, 2015.

[84] Jian Wang, Hong Zhi Zhang, Rong Sheng Li, and Cheng Zhi Huang. Localized surface plasmon resonance of gold nanorods and assemblies in the view of biomedical analysis. *TrAC-Trend Anal. Chem.*, 80:429–443, 2016.

[85] Guillaume Baffou and Romain Quidant. Thermo-plasmonics: Using metallic nanostructures as nano-sources of heat. *Laser Photonics Rev.*, 7(2):171–187, 2013.

[86] Boris Luk'yanchuk, Nikolay I. Zheludev, Stefan A. Maier, Naomi J. Halas, Peter Nordlander, Harald Giessen, and Chong Tow Chong. The Fano resonance in plasmonic nanostructures and metamaterials. *Nat. Mater.*, 9(9):707–715, 2010.

[87] Liang Tang, Justin Casas, and Meenakshi Venkataramasubramani. Magnetic nanoparticle mediated enhancement of localized surface plasmon resonance for ultrasensitive bioanalytical assay in human blood plasma. *Anal. Chem.*, 85(3):1431–1439, 2013.

[88] Mani Prabha Singh and Geoffrey F. Strouse. Involvement of the LSPR spectral overlap for energy transfer between a dye and Au nanoparticle. *J. Am. Chem. Soc.*, 132(27):9383–9391, 2010.

[89] Jing Zhao, Xiaoyu Zhang, Chanda Ranjit Yonzon, Amanda J. Haes, and Richard P. Van Duyne. Localized surface plasmon resonance biosensors. *Nanomedicine*, 1(2):219–228, 2006.

[90] Jie Cao, Tong Sun, and Kenneth T. V. Grattan. Gold nanorod-based localized surface plasmon resonance biosensors: A review. *Sensor Actuat. B-Chem.*, 195:332–351, 2014.

[91] Hao Huang, Lei Zhang, Zhiheng Lv, Ran Long, Chao Zhang, Yue Lin, Kecheng Wei, Chengming Wang, Lu Chen, Zhi-Yuan Li, Qun Zhang, Yi Luo, and Yujie Xiong. Unraveling surface plasmon decay in core–shell nanostructures toward broadband light-driven catalytic organic synthesis. *J. Am. Chem. Soc.*, 138(21):6822–6828, 2016.

[92] Jiangtian Li, Scott K. Cushing, Peng Zheng, Fanke Meng, Deryn Chu, and Nianqiang Wu. Plasmon-induced photonic and energy-transfer enhancement of solar water splitting by a hematite nanorod array. *Nat. Commun.*, 4:2651, 2013.

[93] Kun Li, Nathaniel J. Hogan, Matthew J. Kale, Naomi J. Halas, Peter Nordlander, and Phillip Christopher. Balancing near-field enhancement, absorption, and scattering for effective antenna-reactor plasmonic photocatalysis. *Nano Lett.*, 17(6):3710–3717, 2017.

[94] Dayne F. Swearer, Hangqi Zhao, Linan Zhou, Chao Zhang, Hossein Robatjazi, John Mark P. Martirez, Caroline M. Krauter, Sadegh Yazdi, Michael J. McClain, Emilie Ringe, Emily A. Carter, Peter Nordlander, and Naomi J. Halas. Heterometallic antenna- reactor complexes for photocatalysis. *P. Natl. Acad. Sci. USA*, 113(32):8916–8920, 2016.

[95] Wei-Shun Chang, Ji Won Ha, Liane S. Slaughter, and Stephan Link. Plasmonic nanorod absorbers as orientation sensors. *P. Natl. Acad. Sci. USA*, 107(7):2781–2786, 2010.

[96] J. Britt Lassiter, Heidar Sobhani, Jonathan A. Fan, Janardan Kundu, Federico Capasso, Peter Nordlander, and Naomi J. Halas. Fano resonances in plasmonic nanoclusters: Geometrical and chemical tunability. *Nano Lett.*, 10(8):3184–3189, 2010.

[97] Benjamin Gallinet and Olivier J. F. Martin. Refractive index sensing with subradiant modes: A framework to reduce losses in plasmonic nanostructures. *ACS Nano*, 7(8):6978–6987, 2013.

[98] Uwe Kreibig and Michael Vollmer. *Optical Poperties of Metal Clusters*, volume 25 of *Springer Series in Materials Science*. Springer-Verlag: New York, 1995.

[99] David D. Evanoff and George Chumanov. Size-controlled synthesis of nanoparticles. 2. measurement of extinction, scattering, and absorption cross sections. *J. Phys. Chem. B*, 108(37):13957–13962, 2004.

[100] Stefan A. Maier. Effective mode volume of nanoscale plasmon cavities. *Opt. Quant. Electron.*, 38(1-3):257–267, 2006.

[101] Christophe Sauvan, Jean-Paul Hugonin, I. S. Maksymov, and Philippe Lalanne. Theory of the spontaneous optical emission of nanosize photonic and plasmon resonators. *Phys. Rev. Lett.*, 110(23):237401, 2013.

[102] D. E. Chang, Anders Søndberg Sørensen, P. R. Hemmer, and M. D. Lukin. Quantum optics with surface plasmons. *Phys. Rev. Lett.*, 97(5):053002, 2006.

[103] K. R. Catchpole and A. Polman. Design principles for particle plasmon enhanced solar cells. *Appl. Phys. Lett.*, 93(19):191113, 2008.

[104] Anders Hagfeldt, Gerrit Boschloo, Licheng Sun, Lars Kloo, and Henrik Pettersson. Dye-sensitized solar cells. *Chem. Rev.*, 110(11):6595–6663, 2010.

[105] Di M. Wu, Aitzol García-Etxarri, Alberto Salleo, and Jennifer A. Dionne. Plasmon-enhanced upconversion. *J. Phys. Chem. Lett.*, 5(22):4020–4031, 2014.

[106] Niket Thakkar, Morgan T. Rea, Kevin C. Smith, Kevin D. Heylman, Steven C. Quillin, Kassandra A. Knapper, Erik H. Horak, David J. Masiello, and Randall H. Goldsmith. Sculpting Fano resonances to control photonic–plasmonic hybridization. *Nano Lett.*, 17(11):6927–6934, 2017.

[107] Charles Cherqui, Yueying Wu, Guoliang Li, Steven C. Quillin, Jacob A. Busche, Niket Thakkar, Claire A. West, Nicholas P. Montoni, Philip D. Rack, Jon P. Camden, and David J. Masiello. STEM/EELS imaging of magnetic hybridization in symmetric and symmetry-broken plasmon oligomer dimers and all-magnetic fano interference. *Nano Lett.*, 16(10):6668–6676, 2016.

[108] John B. Pendry, A. J. Holden, W. J. Stewart, and I. Youngs. Extremely low frequency plasmons in metallic mesostructures. *Phys. Rev. Lett.*, 76(25):4773, 1996.

[109] F. Javier García de Abajo. Nonlocal effects in the plasmons of strongly interacting nanoparticles, dimers, and waveguides. *J. Phys. Chem. B*, 112(46):17983–17987, 2008.

[110] Johann Toudert, Lionel Simonot, Sophie Camelio, and David Babonneau. Advanced optical effective medium modeling for a single layer of polydisperse ellipsoidal nanoparticles embedded in a homogeneous dielectric medium: Surface plasmon resonances. *Phys. Rev. B*, 86(4):045415, 2012.

[111] Pierre Berini. Plasmon-polariton modes guided by a metal film of finite width bounded by different dielectrics. *Opt. Express*, 7(10):329–335, 2000.

[112] P. Spinelli, M. Hebbink, R. De Waele, L. Black, F. Lenzmann, and A. Polman. Optical impedance matching using coupled plasmonic nanoparticle arrays. *Nano Lett.*, 11(4):1760–1765, 2011.

[113] P. Royer, J. P. Goudonnet, R. J. Warmack, and T. L. Ferrell. Substrate effects on surface-plasmon spectra in metal-island films. *Phys. Rev. B*, 35(8):3753, 1987.

[114] Shunping Zhang, Kui Bao, Naomi J. Halas, Hongxing Xu, and Peter Nordlander. Substrate-induced Fano resonances of a plasmonic nanocube: A route to increased-sensitivity localized surface plasmon resonance sensors revealed. *Nano Lett.*, 11(4):1657–1663, 2011.

[115] Yueying Wu, Guoliang Li, Charles Cherqui, Nicholas W. Bigelow, Niket Thakkar, David J. Masiello, Jon P. Camden, and Philip D. Rack. Electron energy loss spectroscopy study of the full plasmonic spectrum of self-assembled Au–Ag alloy nanoparticles: Unraveling size, composition, and substrate effects. *ACS Photonics*, 3(1):130–138, 2016.

[116] Guoliang Li, Charles Cherqui, Yueying Wu, Nicholas W. Bigelow, Philip D. Simmons, Philip D. Rack, David J. Masiello, and Jon P. Camden. Examining substrate-induced plasmon mode splitting and localization in truncated silver nanospheres with electron energy loss spectroscopy. *J. Phys. Chem. Lett.*, 6(13):2569–2576, 2015.

[117] Guoliang Li, Charles Cherqui, Nicholas W. Bigelow, Gerd Duscher, Patrick J. Straney, Jill E. Millstone, David J. Masiello, and Jon P. Camden. Spatially mapping energy transfer from single plasmonic particles to semiconductor substrates via STEM/EELS. *Nano Lett.*, 15(5):3465–3471, 2015.

[118] F. J. Beck, A. Polman, and K. R. Catchpole. Tunable light trapping for solar cells using localized surface plasmons. *J. of Appl. Phys.*, 105(11):114310, 2009.

[119] Charles Cherqui, Niket Thakkar, Gouliang Li, Jon P. Camden, and David J. Masiello. Characterizing localized surface plasmons using energy-loss spectroscopy. *Annu. Rev. of Phys. Chem.*, 67:331–357, 2016.

[120] Yueying Wu, Guoliang Li, and Jon P. Camden. Probing nanoparticle plasmons with electron energy loss spectroscopy. *Chem. Rev.*, 118(6):2994–3031, 2017.

[121] Kevin Cahill. Models of membrane electrostatics. *Phys. Rev. E*, 85(5):051921, 2012.

[122] L. J. Sherry, S. H. Chang, G. C. Schatz, R. P. Van Duyne, B. J. Wiley, and Y. N. Xia. Localized surface plasmon resonance spectroscopy of single silver nanocubes. *Nano Lett.*, 5(10):2034–2038, 2005.

[123] Olivia Nicoletti, Francisco de La Peña, Rowan K. Leary, Daniel J. Holland, Caterina Ducati, and Paul A. Midgley. Three-dimensional imaging of localized surface plasmon resonances of metal nanoparticles. *Nature*, 502(7469):80–84, 2013.

[124] Stefano Mazzucco, Nicolas Geuquet, Jian Ye, Odile Stéphan, Willem Van Roy, Pol Van Dorpe, Luc Henrard, and Mathieu Kociak. Ultralocal modification of surface plasmons properties in silver nanocubes. *Nano Lett.*, 12(3):1288–1294, 2012.

[125] Gleb M. Akselrod, Christos Argyropoulos, Thang B. Hoang, Cristian Ciracì, Chao Fang, Jiani Huang, David R. Smith, and Maiken H. Mikkelsen. Probing the mechanisms of large Purcell enhancement in plasmonic nanoantennas. *Nat. Photonics*, 8(11):835–840, 2014.

[126] Tyler J. Dill, Matthew J. Rozin, Stephen Palani, and Andrea R. Tao. Colloidal nanoantennas for hyperspectral chemical mapping. *ACS Nano*, 10(8):7523–7531, 2016.

[127] Koichiro Saito and Tetsu Tatsuma. Asymmetric three-way plasmonic color routers. *Adv. Opt. Mater.*, 3(7):883–887, 2015.

[128] Koichiro Saito and Tetsu Tatsuma. A transparent projection screen based on plasmonic Ag nanocubes. *Nanoscale*, 7(48):20365–20368, 2015.

[129] Thang B. Hoang, Gleb M. Akselrod, Christos Argyropoulos, Jiani Huang, David R. Smith, and Maiken H. Mikkelsen. Ultrafast spontaneous emission source using plasmonic nanoantennas. *Nat. Commun.*, 6, 2015.

[130] Tokuhisa Kawawaki, Haibin Wang, Takaya Kubo, Koichiro Saito, Jotaro Nakazaki, Hiroshi Segawa, and Tetsu Tatsuma. Efficiency enhancement of PbS quantum dot/ZnO nanowire bulk-heterojunction solar cells by plasmonic silver nanocubes. *ACS Nano*, 9(4):4165–4172, 2015.

[131] Se-Woong Baek, Garam Park, Jonghyeon Noh, Changsoon Cho, Chun-Ho Lee, Min-Kyo Seo, Hyunjoon Song, and Jung-Yong Lee. Au@Ag core-shell nanocubes for efficient plasmonic light scattering effect in low bandgap organic solar cells. *ACS Nano*, 8(4):3302–3312, 2014.

[132] Jiangtian Li, Scott K. Cushing, Fanke Meng, Tess R. Senty, Alan D. Bristow, and Nianqiang Wu. Plasmon-induced resonance energy transfer for solar energy conversion. *Nat. Photonics*, 9(9):601–607, 2015.

[133] Anneli Hoggard, Lin-Yung Wang, Lulu Ma, Ying Fang, Ge You, Jana Olson, Zheng Liu, Wei-Shun Chang, Pulickel M. Ajayan, and Stephan Link. Using the plasmon linewidth to calculate the time and efficiency of electron transfer between gold nanorods and graphene. *ACS Nano*, 7(12):11209–11217, 2013.

[134] Nicholas W. Bigelow, Alex Vaschillo, Vighter Iberi, Jon P. Camden, and David J. Masiello. Characterization of the electron- and photon-driven plasmonic excitations of metal nanorods. *ACS Nano*, 6(8):7497–7504, 2012.

[135] Nicholas W. Bigelow, Alex Vaschillo, Jon P. Camden, and David J. Masiello. Signatures of Fano interferences in the electron energy loss spectroscopy and cathodoluminescence of symmetry-broken nanorod dimers. *ACS Nano*, 7(5):4511–4519, 2013.

[136] Ulrich Hohenester and Andreas Trügler. MNPBEM–a Matlab toolbox for the simulation of plasmonic nanoparticles. *Comput. Phys. Commun.*, 183(2):370–381, 2012.

[137] Pavel Cheben, Robert Halir, Jens H. Schmid, Harry A. Atwater, and David R. Smith. Subwavelength integrated photonics. *Nature*, 560(7720):565–572, 2018.

[138] M. Salerno, J. R. Krenn, B. Lamprecht, G. Schider, H. Ditlbacher, N. Félidj, A. Leitner, and F. R. Aussenegg. Plasmon polaritons in metal nanostructures: The optoelectronic route to nanotechnology. *Opto-Electron. Rev.*, 10(3):217–224, 2002.

[139] Zhiqiang Liang, Jun Sun, Yueyue Jiang, Lin Jiang, and Xiaodong Chen. Plasmonic enhanced optoelectronic devices. *Plasmonics*, 9(4):859–866, 2014.

[140] Timothy J. Davis, Daniel E. Gómez, and Ann Roberts. Plasmonic circuits for manipulating optical information. *Nanophotonics*, 6(3):543–559, 2017.

[141] Hong Wei, Zhuoxian Wang, Xiaorui Tian, Mikael Käll, and Hongxing Xu. Cascaded logic gates in nanophotonic plasmon networks. *Nat. Commun.*, 2(1):387, 2011.

[142] Sergey I. Bozhevolnyi and N. Asger Mortensen. Plasmonics for emerging quantum technologies. *Nanophotonics*, 6(5):1185–1188, 2017.

[143] Mads Lykke Andersen, Søren Stobbe, Anders Søndberg Sørensen, and Peter Lodahl. Strongly modified plasmon–matter interaction with mesoscopic quantum emitters. *Nat. Phys.*, 7(3):215–218, 2011.

[144] Jiří Homola, Sinclair S. Yee, and Günter Gauglitz. Surface plasmon resonance sensors: Review. *Sens. Actuators B Chem.*, 54(1-2):3–15, 1999.

[145] Paresh Chandra Ray. Size and shape dependent second order nonlinear optical properties of nanomaterials and their application in biological and chemical sensing. *Chem. Rev.*, 110(9):5332–5365, 2010.

[146] César Clavero. Plasmon-induced hot-electron generation at nanoparticle/metal-oxide interfaces for photovoltaic and photocatalytic devices. *Nat. Photonics*, 8(2):95–103, 2014.

[147] Ravishankar Sundararaman, Prineha Narang, Adam S. Jermyn, William A. Goddard III, and Harry A. Atwater. Theoretical predictions for hot-carrier generation from surface plasmon decay. *Nat. Commun.*, 5(1):5788, 2014.

[148] Mathieu Kociak, Odile Stéphan, Alexandre Gloter, Luiz F. Zagonel, Luiz H.G. Tizei, Marcel Tencé, Katia March, Jean Denis Blazit, Zackaria Mahfoud, Arthur Losquin, Sophie Meuret, and Christian Colliex. Seeing and measuring in colours: Electron microscopy and spectroscopies applied to nano-optics. *C. R. Phys.*, 15(2-3):158–175, 2014.

[149] Marcus C. Newton, Aaron Parsons, Ulrich Wagner, and Christoph Rau. Coherent X-ray diffraction imaging of photo-induced structural changes in BiFeO $_3$ nanocrystals. *New J. Phys.*, 18(9):093003, 2016.

[150] X. Shen, R.K. Li, U. Lundström, T.J. Lane, A.H. Reid, S.P. Weathersby, and X.J. Wang. Femtosecond mega-electron-volt electron microdiffraction. *Ultramicroscopy*, 184:172–176, 2018.

[151] Brett Barwick and Ahmed H. Zewail. Photonics and plasmonics in 4D ultrafast electron microscopy. *ACS Photonics*, 2(10):1391–1402, 2015.

[152] Dmitry Shorokhov and Ahmed H. Zewail. Perspective: 4D ultrafast electron microscopy—evolutions and revolutions. *J. Chem. Phys.*, 144(8):080901, 2016.

[153] A. Howie. New instrumentation and cutting edge research. *Ultramicroscopy*, 180:52–58, 2017.

[154] Arthur Losquin and Tom T. A. Lummen. Electron microscopy methods for space-, energy-, and time-resolved plasmonics. *Front. Phys.*, 12(1):127301, 2016.

[155] Ahmed H. Zewail. Four-dimensional electron microscopy. *Science*, 328(5975):187–193, 2010.

[156] H. Boersch, J. Geiger, and W. Stickel. Interaction of 25-keV electrons with lattice vibrations in LiF. Experimental evidence for surface modes of lattice vibration. *Phys. Rev. Lett.*, 17(7):379–381, 1966.

[157] M. J. Lagos and P. E. Batson. Electron energy-gain processes in nanostructures induced by fast electrons. page 2, St. Louis, MO, 2017.

[158] Juan Carlos Idrobo, Andrew R. Lupini, Tianli Feng, Raymond R. Unocic, Franklin S. Walden, Daniel S. Gardiner, Tracy C. Lovejoy, Niklas Dellby, Sokrates T. Pantelides, and Ondrej L. Krivanek. Temperature measurement by a nanoscale electron probe using energy gain and loss spectroscopy. *Phys. Rev. Lett.*, 120(9):095901, 2018.

[159] Archie Howie. Electrons and photons: Exploiting the connection. volume 161, pages 311–314, 1999.

[160] F. J. García de Abajo and M. Kociak. Electron energy-gain spectroscopy. *New J. Phys.*, 10(7):073035, 2008.

[161] Brett Barwick, David J. Flannigan, and Ahmed H. Zewail. Photon-induced near-field electron microscopy. *Nature*, 462(7275):902–906, 2009.

[162] Aycan Yurtsever, J. Spencer Baskin, and Ahmed H. Zewail. Entangled nanoparticles: Discovery by visualization in 4D electron microscopy. *Nano Lett.*, 12(9):5027–5032, 2012.

[163] Enrico Pomarico, Ivan Madan, Gabriele Berruto, Giovanni Maria Vanacore, Kangpeng Wang, Ido Kaminer, F. Javier García de Abajo, and Fabrizio Carbone. meV resolution in laser-assisted energy-filtered transmission electron microscopy. *ACS Photonics*, 5(3):759–764, 2018.

[164] F. Javier García de Abajo, Ana Asenjo-Garcia, and Mathieu Kociak. Multiphoton absorption and emission by interaction of swift electrons with evanescent light fields. *Nano Lett.*, 10(5):1859–1863, 2010.

[165] Sang Tae Park, Milo Lin, and Ahmed H. Zewail. Photon-induced near-field electron microscopy (PINEM): theoretical and experimental. *New J. Phys.*, 12(12):123028, 2010.

[166] A. Asenjo-Garcia and F. J. García de Abajo. Plasmon electron energy-gain spectroscopy. *New J. Phys.*, 15(10):103021, 2013.

[167] P. Das, J.D. Blazit, M. Tencé, L.F. Zagonel, Y. Auad, Y.H. Lee, X.Y. Ling, A. Losquin, C. Colliex, O. Stéphan, F.J. García de Abajo, and M. Kociak. Stimulated electron energy loss and gain in an electron microscope without a pulsed electron gun. *Ultramicroscopy*, 203:44–51, 2019.

[168] Yueying Wu, Chenze Liu, Thomas M. Moore, Gergory A. Magel, David A. Garfinkel, Jon P. Camden, Michael G. Stanford, Gerd Duscher, and Philip D. Rack. Exploring photothermal pathways via in situ laser heating in the transmission electron microscope: Recrystallization, grain growth, phase separation, and dewetting in $Ag_{0.5}$ $Ni_0.5$ thin films. *Microsc. Microanal.*, 24(6):647–656, 2018.

[169] Chenze Liu, Yueying Wu, Zhongwei Hu, Jacob A. Busche, Elliot K. Beutler, Nicholas P. Montoni, Thomas M. Moore, Gregory A. Magel, Jon P. Camden, David J. Masiello, Gerd Duscher, and Philip D. Rack. Supporting information—Continuous wave resonant photon stimulated electron energy-gain and electron energy-loss spectroscopy of individual plasmonic nanoparticles. *ACS Photonics*, 6(10):2499–2508, 2019.

[170] Shaul Mukamel. Causal versus noncausal description of nonlinear wave mixing: Resolving the damping-sign controversy. *Phys. Rev. A*, 76(2):021803, 2007.

[171] Iwo Bialynicki-Birula and Tomasz Sowiński. Quantum electrodynamics of qubits. *Phys. Rev. A*, 76(6):062106, 2007.

[172] David J. Masiello and George C. Schatz. Many-body theory of surface-enhanced Raman scattering. *Phys. Rev. A*, 78(4):042505, 2008.

[173] Edward M. Purcell and Carlton R. Pennypacker. Scattering and absorption of light by nonspherical dielectric grains. *Astrophys. J.*, 186:705, 1973.

[174] Bruce T. Draine and Piotr J. Flatau. Discrete-dipole approximation for scattering calculations. *J. Opt. Soc. Am. A*, 11(4):1491, 1994.

[175] Gururaj V. Naik, Vladimir M Shalaev, and Alexandra Boltasseva. Alternative plasmonic materials: Beyond gold and silver. *Adv. Mater.*, 25(24):3264–3294, 2013.

[176] Ankit Agrawal, Shin Hum Cho, Omid Zandi, Sandeep Ghosh, Robert W. Johns, and Delia J. Milliron. Localized surface plasmon resonance in semiconductor nanocrystals. *Chem. Rev.*, 118(6):3121–3207, 2018.

[177] Ankit Agrawal, Robert W. Johns, and Delia J. Milliron. Control of localized surface plasmon resonances in metal oxide nanocrystals. *Annu. Rev. of Mater. Res.*, 47:1–31, 2017.

[178] Tracy M. Mattox, Xingchen Ye, Karthish Manthiram, P. James Schuck, A. Paul Alivisatos, and Jeffrey J. Urban. Chemical control of plasmons in metal chalcogenide and metal oxide nanostructures. *Adv. Mater.*, 27(38):5830–5837, 2015.

[179] Alberto Comin and Liberato Manna. New materials for tunable plasmonic colloidal nanocrystals. *Chem. Soc. Rev.*, 43(11):3957–3975, 2014.

[180] Zeke Liu, Yaxu Zhong, Ibrahim Shafei, Ryan Borman, Soojin Jeong, Jun Chen, Yaroslav Losovyj, Xinfeng Gao, Na Li, Yaping Du, Erik Sarnello, Tai Li, Dong Su, Wanli Ma, and Xingchen Ye. Tuning infrared plasmon resonances in doped metal-oxide nanocrystals through cation-exchange reactions. *Nature Commun.*, 10(1):1–11, 2019.

[181] Adam D. Dunkelberger, Chase T. Ellis, Daniel C. Ratchford, Alexander J. Giles, Mijin Kim, Chul Soo Kim, Bryan T. Spann, Igor Vurgaftman, Joseph G. Tischler, James P. Long, , Orest J. Glembocki, Jeffrey C. Owrutsky, and Joshua D. Caldwell. Active tuning of surface phonon polariton resonances via carrier photoinjection. *Nat. Photonics*, 12(1):50–56, 2018.

[182] Joseph M Luther, Prashant K. Jain, Trevor Ewers, and A. Paul Alivisatos. Localized surface plasmon resonances arising from free carriers in doped quantum dots. *Nat. Mater.*, 10(5):361–366, 2011.

[183] Jesper Jung and Thomas G. Pedersen. Analysis of plasmonic properties of heavily doped semiconductors using full band structure calculations. *J. Appl. Phys.*, 113(11):114904, 2013.

[184] Yixin Zhao, Hongcheng Pan, Yongbing Lou, Xiaofeng Qiu, JunJie Zhu, and Clemens Burda. Plasmonic $Cu_{2-x}S$ nanocrystals: optical and structural properties of copper-deficient copper (I) sulfides. *J. Am. Chem. Soc.*, 131(12):4253–4261, 2009.

[185] Shannon C. Riha, Derek C. Johnson, and Amy L. Prieto. Cu_2Se nanoparticles with tunable electronic properties due to a controlled solid-state phase transition driven by copper oxidation and cationic conduction. *J. Am. Chem. Soc.*, 133(5):1383–1390, 2011.

[186] Raffaella Buonsanti, Anna Llordes, Shaul Aloni, Brett A. Helms, and Delia J. Milliron. Tunable infrared absorption and visible transparency of colloidal aluminum-doped zinc oxide nanocrystals. *Nano Lett.*, 11(11):4706–4710, 2011.

[187] James C. Ginn, Robert L. Jarecki Jr, Eric A. Shaner, and Paul S. Davids. Infrared plasmons on heavily-doped silicon. *J. Appl. Phys.*, 110(4):043110, 2011.

[188] Alina M Schimpf, Niket Thakkar, Carolyn E. Gunthardt, David J. Masiello, and Daniel R. Gamelin. Charge-tunable quantum plasmons in colloidal semiconductor nanocrystals. *ACS Nano*, 8(1):1065–1072, 2014.

[189] Kevin C. Smith, Agust Olafsson, Xuan Hu, Steven C. Quillin, Juan Carlos Idrobo, Robyn Collette, Philip D. Rack, Jon P. Camden, and David J. Masiello. Direct observation of infrared plasmonic Fano antiresonances by a nanoscale electron probe. *Phys. Rev. Lett.*, 123(17):177401, 2019.

[190] Kyle Aleshire, Ilia M. Pavlovetc, Robyn Collette, Xiang-Tian Kong, Philip D. Rack, Shubin Zhang, David J. Masiello, Jon P. Camden, Gregory V. Hartland, and Masaru Kuno. Far-field midinfrared superresolution imaging and spectroscopy of single high aspect ratio gold nanowires. *Proc. Natl. Acad. Sci. U.S.A.*, 117(5):2288–2293, 2020.

[191] Andrew C. Jones, Robert L. Olmon, Sara E. Skrabalak, Benjamin J. Wiley, Younan N. Xia, and Markus B. Raschke. Mid-IR plasmonics: Near-field imaging of coherent plasmon modes of silver nanowires. *Nano Lett.*, 9(7):2553–2558, 2009.

[192] Ross Stanley. Plasmonics in the mid-infrared. *Nat. Photonics*, 6(7):409–411, 2012.

[193] Yueying Wu, Zhongwei Hu, Xiang-Tian Kong, Juan Carlos Idrobo, Austin G. Nixon, Philip D. Rack, David J. Masiello, and Jon P. Camden. Infrared plasmonics: STEM-EELS characterization of Fabry-Pérot resonance damping in gold nanowires. *Phys. Rev. B*, 101:085409, 4 2020.

[194] Craig F. Bohren and Donald R. Huffman. *Absorption and Scattering of Light by Small Particles*. John Wiley & Sons, 2008.

[195] Su-Wen Hsu, Whitney Bryks, and Andrea R. Tao. Effects of carrier density and shape on the localized surface plasmon resonances of $Cu_{2-x}S$ nanodisks. *Chem. of Mater.*, 24(19):3765–3771, 2012.

[196] Jongwook Kim, Ankit Agrawal, Franziska Krieg, Amy Bergerud, and Delia J. Milliron. The interplay of shape and crystalline anisotropies in plasmonic semiconductor nanocrystals. *Nano Lett.*, 16(6):3879–3884, 2016.

[197] Martina Abb, Yudong Wang, Nikitas Papasimakis, C. H. De Groot, and Otto L. Muskens. Surface-enhanced infrared spectroscopy using metal oxide plasmonic antenna arrays. *Nano Lett.*, 14(1):346–352, 2014.

[198] Xiaoxia Yang, Zhipei Sun, Tony Low, Hai Hu, Xiangdong Guo, F. Javier García de Abajo, Phaedon Avouris, and Qing Dai. Nanomaterial-based plasmon-enhanced infrared spectroscopy. *Adv. Mater.*, 30(20):1704896, 2018.

[199] Shreya Goel, Feng Chen, and Weibo Cai. Synthesis and biomedical applications of copper sulfide nanoparticles: from sensors to theranostics. *Small*, 10(4):631–645, 2014.

[200] Moran Guo, Wing-Cheung Law, Xin Liu, Hongxin Cai, Liwei Liu, Mark T. Swihart, Xihe Zhang, and Paras N. Prasad. Plasmonic semiconductor nanocrystals as chemical sensors: Pb^{2+} quantitation via aggregation-induced plasmon resonance shift. *Plasmonics*, 9(4):893–898, 2014.

[201] Colin M Hessel, Varun P. Pattani, Michael Rasch, Matthew G. Panthani, Bonil Koo, James W. Tunnell, and Brian A. Korgel. Copper selenide nanocrystals for photothermal therapy. *Nano Lett.*, 11(6):2560–2566, 2011.

[202] Min Zhou, Mei Tian, and Chun Li. Copper-based nanomaterials for cancer imaging and therapy. *Bioconjugate Chem.*, 27(5):1188–1199, 2016.

[203] Yue Wu, Cyrus Wadia, Wanli Ma, Bryce Sadtler, and A. Paul Alivisatos. Synthesis and photovoltaic application of copper (I) sulfide nanocrystals. *Nano Lett.*, 8(8):2551–2555, 2008.

[204] Lige Liu, Bin Zhou, Luogen Deng, Wenping Fu, Jiatao Zhang, Min Wu, Wenhua Zhang, Bingsuo Zou, and Haizheng Zhong. Thermal annealing effects of plasmonic $Cu_1.8S$ nanocrystal films and their photovoltaic properties. *J. Phys. Chem. C*, 118(46):26964–26972, 2014.

[205] Li An, Liang Huang, Hongyan Liu, Pinxian Xi, Fengjuan Chen, and Yaping Du. High-quality copper sulfide nanocrystals with diverse shapes and their catalysis for electrochemical reduction of h2o2. *Part. Part. Syst. Charact.*, 32(5):536–541, 2015.

[206] Guanwei Cui, Wen Wang, Mingyue Ma, Junfeng Xie, Xifeng Shi, Ning Deng, Jianping Xin, and Bo Tang. Ir-driven photocatalytic water splitting with WO_2–Na_x WO_3 hybrid conductor material. *Nano Lett.*, 15(11):7199–7203, 2015.

[207] Ke-Yi Jiang, Xiao-Cheng Dai, Yan Yu, Qiao-Ling Mo, and Fang-Xing Xiao. Boosting charge-transfer efficiency by simultaneously tuning double effects of metal nanocrystal in Z-scheme photocatalytic redox system. *J. Phys. Chem. C*, 122(23):12291–12306, 2018.

[208] Thierry Taliercio and Paolo Biagioni. Semiconductor infrared plasmonics. *Nanophotonics*, 8(6):949–990, 2019.

[209] Min Hu, Carolina Novo, Alison Funston, Haining Wang, Hristina Staleva, Shengli Zou, Paul Mulvaney, Younan Xia, and Gregory V. Hartland. Dark-field microscopy studies of single metal nanoparticles: Understanding the factors that influence the linewidth of the localized surface plasmon resonance. *J. Mater. Chem.*, 18(17):1949–1960, 2008.

[210] Wei Cao, Tao Huang, Xiao-Hong Nancy Xu, and Hani E. Elsayed-Ali. Localized surface plasmon resonance of single silver nanoparticles studied by dark-field optical microscopy and spectroscopy. *J. Appl. Phys.*, 109(3):034310, 2011.

[211] Kalkbrenner Lindfors, T. Kalkbrenner, P. Stoller, and Vahid Sandoghdar. Detection and spectroscopy of gold nanoparticles using supercontinuum white light confocal microscopy. *Phys. Rev. Lett.*, 93(3):037401, 2004.

[212] Anatoly V. Zayats, Igor I. Smolyaninov, and Alexei A. Maradudin. Nano-optics of surface plasmon polaritons. *Phys. Rep.*, 408(3-4):131–314, 2005.

[213] Fritz Keilmann and Rainer Hillenbrand. Near-field microscopy by elastic light scattering from a tip. *Philos. Trans. R. Soc. A*, 362(1817):787–805, 2004.

[214] Markus B. Raschke, Leopoldo Molina, Thomas Elsaesser, Dong Ha Kim, Wolfgang Knoll, and Karsten Hinrichs. Apertureless near-field vibrational imaging of block-copolymer nanostructures with ultrahigh spatial resolution. *ChemPhysChem*, 6(10):2197–2203, 2005.

[215] Hans A. Bechtel, Eric A. Muller, Robert L. Olmon, Michael C. Martin, and Markus B. Raschke. Ultrabroadband infrared nanospectroscopic imaging. *Proc. Natl. Acad. Sci. U.S.A.*, 111(20):7191–7196, 2014.

[216] Omar Khatib, Hans A. Bechtel, Michael C. Martin, Markus B. Raschke, and G. Lawrence Carr. Far infrared synchrotron near-field nanoimaging and nanospectroscopy. *ACS Photonics*, 5(7):2773–2779, 2018.

[217] Robert W. Johns, Hans A. Bechtel, Evan L. Runnerstrom, Ankit Agrawal, Sebastien D. Lounis, and Delia J. Milliron. Direct observation of narrow mid-infrared plasmon linewidths of single metal oxide nanocrystals. *Nat. Commun.*, 7(1):1–6, 2016.

[218] Ondrej L. Krivanek, Tracy C. Lovejoy, Niklas Dellby, Toshihiro Aoki, R. W. Carpenter, Peter Rez, Emmanuel Soignard, Jiangtao Zhu, Philip E. Batson, Maureen J. Lagos, Ray F. Egerton, and Peter A. Crozier. Vibrational spectroscopy in the electron microscope. *Nature*, 514(7521):209–212, Oct 2014.

[219] T. C. Lovejoy, G. C. Corbin, N. Dellby, M. V. Hoffman, and O. L. Krivanek. Advances in ultra-high energy resolution STEM-EELS. *Microsc. and Microanal.*, 24(S1):446–447, 2018.

[220] Jordan A. Hachtel, Andrew R. Lupini, and Juan Carlos Idrobo. Exploring the capabilities of monochromated electron energy loss spectroscopy in the infrared regime. *Sci. Rep.*, 8(1):1–10, 2018.

[221] Evelyn L. Rosen, Raffaella Buonsanti, Anna Llordes, April M. Sawvel, Delia J. Milliron, and Brett A. Helms. Exceptionally mild reactive stripping of native ligands from nanocrystal surfaces by using meerwein's salt. *Angew. Chem. Int. Ed.*, 51(3):684–689, 2012.

[222] Vighter Iberi, Nicholas W. Bigelow, Nasrin Mirsaleh-Kohan, Sarah Griffin, Philip D. Simmons Jr, Beth S. Guiton, David J. Masiello, and Jon P. Camden. Resonance-rayleigh scattering and electron energy-loss spectroscopy of silver nanocubes. *J. Phys. Chem. C*, 118(19):10254–10262, 2014.

[223] Maureen J. Lagos, Andreas Trügler, Ulrich Hohenester, and Philip E. Batson. Mapping vibrational surface and bulk modes in a single nanocube. *Nature*, 543(7646):529–532, 2017.

[224] Masayuki Kanehara, Hayato Koike, Taizo Yoshinaga, and Toshiharu Teranishi. Indium tin oxide nanoparticles with compositionally tunable surface plasmon resonance frequencies in the near-ir region. *J. Am. Chem. Soc.*, 131(49):17736–17737, 2009.

[225] Brandon M. Crockett, Adam W. Jansons, Kristopher M. Koskela, Darren W. Johnson, and James E. Hutchison. Radial dopant placement for tuning plasmonic properties in metal oxide nanocrystals. *ACS Nano*, 11(8):7719–7728, 2017.

[226] Haekwon Kim, a C. M. Gilmore, A. Pique, J. S. Horwitz, H. Mattoussi, H. Murata, Z. H. Kafafi, and D. B. Chrisey. Electrical, optical, and structural properties of indium–tin–oxide thin films for organic light-emitting devices. *J. Appl. Phys.*, 86(11):6451–6461, 1999.

[227] Liu Wei and Cheng Shuying. Photoelectric properties of ITO thin films deposited by DC magnetron sputtering. *J. Semicond.*, 32(1):013002, 2011.

[228] Sebastien D. Lounis, Evan L. Runnerstrom, Amy Bergerud, Dennis Nordlund, and Delia J. Milliron. Influence of dopant distribution on the plasmonic properties of indium tin oxide nanocrystals. *J. Am. Chem. Soc.*, 136(19):7110–7116, 2014.

[229] Omid Zandi, Ankit Agrawal, Alex B. Shearer, Lauren C. Reimnitz, Clayton J. Dahlman, Corey M Staller, and Delia J. Milliron. Impacts of surface depletion on the plasmonic properties of doped semiconductor nanocrystals. *Nat. Mater.*, 17(8):710–717, 2018.

[230] Bharat Tandon, Ankit Agrawal, Sungyeon Heo, and Delia J. Milliron. Competition between depletion effects and coupling in the plasmon modulation of doped metal oxide nanocrystals. *Nano Lett.*, 19(3):2012–2019, 2019.

[231] D. B. Tran Thoai and Elmar Zeitler. Inelastic scattering of fast electrons by small metal particles. *Phys. Status Solidi A*, 107(791):791–797, 1988.

[232] P. M. Echenique, J. Bausells, and A. Rivacoba. Energy-loss probability in electron microscopy. *Phys. Rev. B*, 35:1521–1524, Feb 1987.

[233] Ray F. Egerton. *Electron energy-loss spectroscopy in the electron microscope*. Springer Science & Business Media, 2011.

[234] BW. Reed and M. Sarikaya. Background subtraction for low-loss transmission electron energy-loss spectroscopy. *Ultramicroscopy*, 93(1):25–37, 2002.

[235] Ray F. Egerton. Electron energy-loss spectroscopy in the TEM. *Rep. Prog. Phys.*, 72(1):016502, 2008.

[236] Jan Kischkat, Sven Peters, Bernd Gruska, Mykhaylo Semtsiv, Mikaela Chashnikova, Matthias Klinkmüller, Oliana Fedosenko, Stephan Machulik, Anna Aleksandrova, Gergorii Monastyrskyi, Yuri Flores, and W. Ted Masselink. Mid-infrared optical properties of thin films of aluminum oxide, titanium oxide, silicon dioxide, aluminum nitride, and silicon nitride. *Appl. Opt.*, 51(28):6789–6798, 2012.

[237] Shuai Cai, Bin Liu, Hongbin Chen, Pan Jianguo, and Peng Chen. Homogeneous $(Lu_{1-x}In_x)_2O_3(x = 0 - 1)$ solid solutions: Controlled synthesis, structure features and optical properties. *Powder Technol.*, 317:224–229, 2017.

[238] Qianlang Liu, Steven C. Quillin, David J. Masiello, and Peter A. Crozier. Nanoscale probing of resonant photonic modes in dielectric nanoparticles with focused electron beams. *Phys. Rev. B*, 99:165102, 2019.

[239] Ivar Hamberg and Claes G. Granqvist. Evaporated Sn-doped In_2O_3 films: Basic optical properties and applications to energy-efficient windows. *J. Appl. Phys.*, 60(11):123–159, 1986.

[240] Christianus Hermanus Leopold Weijtens and Peter A. C. van Loon. Influence of annealing on the optical properties of indium tin oxide. *Thin Solid Films*, 196:1–10, 1991.

[241] Tobias Gerfin and Michael Grätzel. Optical properties of tin-doped indium oxide determined by spectroscopic ellipsometry. *J. Appl. Phys.*, 79(3):1722–1729, 1995.

[242] H. Köstlin, R. Jost, and W. Lems. Optical and electrical properties of doped In_2O_3 films. *Phys. Status Solidi A*, 29(1):87–93, 1975.

[243] Yutaka Ohhata, Fujitoshi Shinoki, and Sadafumi Yoshida. Optical properties of r.f. reactive sputtered tin-doped In_2O_3 films. *Thin Solid Films*, 59(2):255–261, 1979.

[244] Joachim Szczyrbowski, K. Schmalzbauer, and Horst Hoffman. Optical properties of In_2O_3–SnO_2 films in the transparent and plasma reflection region. *Thin Solid Films*, 137(2):169–183, 1986.

[245] Alexandre Vial, Anne-Sophie Grimault, Demetrio Macías, Dominique Barchiesi, and Marc Lamy de la Chapelle. Improved analytical fit of gold dispersion: Application to the modeling of extinction spectra with a finite-difference time-domain method. *Phys. Rev. B*, 71:085416, 2005.

[246] Robert L. Olmon, Brian Slovick, Timothy W. Johnson, David Shelton, Sang-Hyun Oh, Glenn D. Boreman, and Markus B. Raschke. Optical dielectric function of gold. *Phys. Rev. B*, 86:235147, 2012.

[247] Byung Hyo Kim, Corey M Staller, Shin Hum Cho, Sungyeon Heo, Carrie E. Garrison, Jongwook Kim, and Delia J. Milliron. High mobility in nanocrystal-based transparent conducting oxide thin films. *ACS Nano*, 12(4):3200–3208, 2018.

[248] Jérôme Steinhauser, Sylvie Fay, N. Oliveira, Evelyne Vallat-Sauvain, and Christophe Ballif. Transition between grain boundary and intragrain scattering transport mechanisms in boron-doped zinc oxide thin films. *Appl. Phys. Lett.*, 90(14):142107, 2007.

[249] C. Guillén and J. Herrero. Structural and plasmonic characteristics of sputtered SnO_2: Sb and ZnO:Al thin films as a function of their thickness. *J. Mater. Sci.*, 51(15):7276–7285, 2016.

[250] Stephen L. Gibbs, Corey M. Staller, and Delia J. Milliron. Surface depletion layers in plasmonic metal oxide nanocrystals. *Acc. Chem. Res.*, 52(9):2516–2524, 2019.

[251] Keke Ma, Ning Zhou, Meng Yuan, Dongsheng Li, and Deren Yang. Tunable surface plasmon resonance frequencies of monodisperse indium tin oxide nanoparticles by controlling composition, size, and morphology. *Nanoscale Res. Lett.*, 9(1):547, 2014.

[252] David Hagenmüller, Johannes Schachenmayer, Cyriaque Genet, Thomas W. Ebbesen, and Guido Pupillo. Enhancement of the electron–phonon scattering induced by intrinsic surface plasmon–phonon polaritons. *ACS Photonics*, 6(4):1073–1081, 2019.

[253] P. Pons-Valencia, F. J. Alfaro-Mozaz, M. M. Wiecha, V. Biolek, I. Dolado, S. Vélez, P. Li, P. Alonso-González, F. Casanova, L. E. Hueso, L. Martín-Moreno, R. Hillenbrand, and A. Y. Nikitin. Launching of hyperbolic phonon-polaritons in h-BN slabs by resonant metal plasmonic antennas. *Nat. Commun.*, 10(1):3242, 2019.

[254] Marta Autore, Lars Mester, Monika Goikoetxea, and R. Hillenbrand. Substrate matters: Surface-polariton enhanced infrared nanospectroscopy of molecular vibrations. *Nano Lett.*, 19(11):8066–8073, 2019.

[255] Yujun Zhong, Shyamala Devi Malagari, Travis Hamilton, and Daniel M. Wasserman. Review of mid-infrared plasmonic materials. *J. Nanophotonics*, 9(1):1–21, 21, 2015.

[256] D. N. Basov, M. M. Fogler, and F. J. García de Abajo. Polaritons in van der Waals materials. *Science*, 354(6309), 2016.

[257] Shijing Tan, Adam Argondizzo, Jindong Ren, Liming Liu, Jin Zhao, and Hrvoje Petek. Plasmonic coupling at a metal/semiconductor interface. *Nat. Photonics*, 11(12):806–812, 2017.

[258] Hugo Lourenço-Martins and Mathieu Kociak. Vibrational surface electron-energy-loss spectroscopy probes confined surface-phonon modes. *Phys. Rev. X*, 7:041059, 2017.

[259] Lukas Wehmeier, Denny Lang, Yongmin Liu, Xiang Zhang, Stephan Winnerl, Lukas M. Eng, and Susanne C. Kehr. Polarization-dependent near-field phonon nanoscopy of oxides: $SrTiO_3$, $LiNbO_3$, and $PbZr_{0.2}Ti_{0.8}O_3$. *Phys. Rev. B*, 100(3):035444, 2019.

[260] Ruishi Qi, Renfei Wang, Yuehui Li, Yuanwei Sun, Shulin Chen, Bo Han, Ning Li, Qing Zhang, Xinfeng Liu, Dapeng Yu, and Peng Gao. Probing far-infrared surface phonon polaritons in semiconductor nanostructures at nanoscale. *Nano Lett.*, 19(8):5070–5076, 2019.

[261] Michele Tamagnone, Antonio Ambrosio, Kundan Chaudhary, Luis A. Jauregui, Philip Kim, William L. Wilson, and Federico Capasso. Ultra-confined mid-infrared resonant phonon polaritons in van der waals nanostructures. *Sci. Adv.*, 4(6), 2018.

[262] Jinghuan Yang, Quan Sun, Kosei Ueno, Xu Shi, Tomoya Oshikiri, Hiroaki Misawa, and Qihuang Gong. Manipulation of the dephasing time by strong coupling between localized and propagating surface plasmon modes. *Nat. Commun.*, 9(1):4858, 2018.

[263] Y. Wu, J. Ordonez-Miranda, S. Gluchko, R. Anufriev, D. De Sousa Meneses, L. Del Campo, S. Volz, and M. Nomura. Enhanced thermal conduction by surface phonon-polaritons. *Sci. Adv.*, 6(40), 2020.

[264] Alexander M. Dubrovkin, Bo Qiang, Teddy Salim, Donguk Nam, Nikolay I. Zheludev, and Qi Jie Wang. Resonant nanostructures for highly confined and ultra-sensitive surface phonon-polaritons. *Nat. Commun.*, 11(1):1863, 2020.

[265] Hailong Hu, Huigao Duan, Joel K. W. Yang, and Ze Xiang Shen. Plasmon-modulated photoluminescence of individual gold nanostructures. *ACS Nano*, 6(11):10147–10155, 2012.

[266] Chase T. Ellis, Joseph G. Tischler, Orest J. Glembocki, Francisco J. Bezares, Alexander J. Giles, Richard Kasica, Loretta Shirey, Jeffrey C. Owrutsky, Dmitry N. Chigrin, and Joshua D. Caldwell. Aspect-ratio driven evolution of high-order resonant modes and near-field distributionsin localized surface phonon polariton nanostructures. *Sci. Rep.*, 6(1):32959, 2016.

[267] Fabio Medeghini, Aurélien Crut, Marco Gandolfi, Francesco Rossella, Paolo Maioli, Fabrice Vallée, Francesco Banfi, and Natalia Del Fatti. Controlling the quality factor of a single acoustic nanoresonator by tuning its morphology. *Nano Lett.*, 18(8):5159–5166, 2018.

[268] Mathias Geisler, Ximin Cui, Jianfang Wang, Tomas Rindzevicius, Lene Gammelgaard, Bjarke S. Jessen, P. A. D. Gonçalves, Francesco Todisco, Peter Bøggild, Anja Boisen, Martijn Wubs, N. Asger Mortensen, Sanshui Xiao, and Nicolas Stenger. Single-crystalline gold nanodisks on WS_2 mono- and multilayers for strong coupling at room temperature. *ACS Photonics*, 6(4):994–1001, 2019.

[269] Andrew B. Yankovich, Battulga Munkhbat, Denis G. Baranov, Jorge Cuadra, Erik Olsén, Hugo Lourenço-Martins, Luiz H. G. Tizei, Mathieu Kociak, Eva Olsson, and Timur Shegai. Visualizing spatial variations of plasmon–exciton polaritons at the nanoscale using electron microscopy. *Nano Lett.*, 19(11):8171–8181, 2019.

[270] Andrea Mancini, Christopher R. Gubbin, Rodrigo Berté, Francesco Martini, Alberto Politi, Emiliano Cortés, Yi Li, Simone De Liberato, and Stefan A. Maier. Near-field spectroscopy of cylindrical phonon-polariton antennas. *ACS Nano*, 14(7):8508–8517, 2020.

[271] Christopher R. Gubbin, Stefan A. Maier, and Simone De Liberato. Theoretical investigation of phonon polaritons in SiC micropillar resonators. *Phys. Rev. B*, 95(3):035313, 2017.

[272] Sebastián Castilla, Ioannis Vangelidis, Varun-Varma Pusapati, Jordan Goldstein, Marta Autore, Tetiana Slipchenko, Khannan Rajendran, Seyoon Kim, Kenji Watanabe, Takashi Taniguchi, Luis Martín-Moreno, Dirk Englund, Klaas-Jan Tielrooij, Rainer Hillenbrand, Elefterios Lidorikis, and Frank H. L. Koppens. Plasmonic antenna coupling to hyperbolic phonon-polaritons for sensitive and fast mid-infrared photodetection with graphene. *Nat. Commun.*, 11(1):4872, 2020.

[273] Garnett W. Bryant, F. Javier García de Abajo, and Javier Aizpurua. Mapping the plasmon resonances of metallic nanoantennas. *Nano Lett.*, 8(2):631–636, 2008.

[274] F. Neubrech, D. Weber, R. Lovrincic, A. Pucci, M. Lopes, T. Toury, and M. Lamy de La Chapelle. Resonances of individual lithographic gold nanowires in the infrared. *Appl. Phys. Lett.*, 93(16):163105, 2008.

[275] Tommaso Dattoma, Marco Grande, Roberto Marani, Giuseppe Morea, Valeria Marrocco, and Antonella D'Orazio. Resonance wavelength dependence and mode formation in gold nanorod optical antennas with finite thickness. *Prog. Electromagn. Res. B*, 30:337–353, 2011.

[276] P. Zijlstra and M. Orrit. Single metal nanoparticles: optical detection, spectroscopy and applications. *Rep. Prog. Phys.*, 74(10):106401, 2011.

[277] Aurélien Crut, Paolo Maioli, Natalia Del Fatti, and Fabrice Vallée. Optical absorption and scattering spectroscopies of single nano-objects. *Chem. Soc. Rev.*, 43(11):3921–3956, 2014.

[278] Marta Klanjšek Gunde. Vibrational modes in amorphous silicon dioxide. *Physica B Condens. Matter*, 292:286–295, 2000.

[279] Joshua D. Caldwell, Andrey V. Kretinin, Yiguo Chen, Vincenzo Giannini, Michael M. Fogler, Yan Francescato, Chase T. Ellis, Joseph G. Tischler, Colin R. Woods, Alexander J. Giles, Minghui Hong, Kenji Watanabe, Takashi Taniguchi, Stefan A. Maier, and Kostya S. Novoselov. Sub-diffractional volume-confined polaritons in the natural hyperbolic material hexagonal boron nitride. *Nat. Commun.*, 5(1):5221, 2014.

[280] Christian Huck, Jochen Vogt, Tomáš Neuman, Tadaaki Nagao, Rainer Hillenbrand, Javier Aizpurua, Annemarie Pucci, and Frank Neubrech. Strong coupling between phonon-polaritons and plasmonic nanorods. *Opt. Express*, 24(22):25528–25539, 2016.

[281] Luiz H. G. Tizei, Vahagn Mkhitaryan, Hugo Lourenço-Martins, Leonardo Scarabelli, Kenji Watanabe, Takashi Taniguchi, Marcel Tencé, Jean-Denis Blazit, Xiaoyan Li, Alexandre Gloter, Alberto Zobelli, Franz-Philipp Schmidt, Luis M. Liz-Marzán, F. Javier García de Abajo, Odile Stéphan, and Mathieu Kociak. Tailored nanoscale plasmon-enhanced vibrational electron spectroscopy. *Nano Lett.*, 20(5):2973–2979, 2020.

[282] Nikolai Christian Passler, Christopher R. Gubbin, Thomas Graeme Folland, Ilya Razdolski, D. Scott Katzer, David F. Storm, Martin Wolf, Simone De Liberato, Joshua D. Caldwell, and Alexander Paarmann. Strong coupling of epsilon-near-zero phonon polaritons in polar dielectric heterostructures. *Nano Lett.*, 18(7):4285–4292, 2018.

[283] A. Bouhelier, M. Beversluis, and L. Novotny. Plasmon coupled tip-enhanced near-field optical microscopy. In *Quantum Electronics and Laser Science Conference*. Optical Society of America, 2002.

[284] A. L. Lereu, A. Passian, and P. Dumas. Near field optical microscopy: a brief review. *Int. J. Nanosci.*, 9(3-7):488, 2012.

[285] Aitzol García-Etxarri, Isabel Romero, F. Javier García de Abajo, Rainer Hillenbrand, and Javier Aizpurua. Influence of the tip in near-field imaging of nanoparticle plasmonic modes: Weak and strong coupling regimes. *Phys. Rev. B*, 79(12):125439, 2009.

[286] J. M. Atkin, S. Berweger, A. C. Jones, and M. B. Raschke. Nano-optical imaging and spectroscopy of order, phases, and domains in complex solids. *Adv. Phys.*, 61(6):745–842, 2012.

[287] B. Knoll and F. Keilmann. Near-field probing of vibrational absorption for chemical microscopy. *Nature*, 399(6732):134–137, 1999.

[288] R. Carmina Monreal, Tomasz J. Antosiewicz, and S. Peter Apell. Diffuse surface scattering in the plasmonic resonances of ultralow electron density nanospheres. *J. Phys. Chem. Lett.*, 6(10):1847–1853, 2015.

[289] R. Carmina Monreal, S. Peter Apell, and Tomasz J. Antosiewicz. Surface scattering contribution to the plasmon width in embedded Ag nanospheres. *Opt. Express*, 22(21):24994–25004, 2014.

[290] R. Carmina Monreal, Tomasz J. Antosiewicz, and S. Peter Apell. Competition between surface screening and size quantization for surface plasmons in nanoparticles. *New J. of Phys.*, 15(8):083044, 2013.

[291] Niket Thakkar, Nicholas P. Montoni, Charles Cherqui, and David J. Masiello. Plasmonic Landau damping in active environments. *Phys. Rev. B*, 97(12):121403(R), 2018.

[292] Junho Kim and Ki-Bong Song. Recent progress of nano-technology with NSOM. *Micron*, 38(4):409–426, 2007.

[293] Hans A. Bechtel, Samuel C. Johnson, Omar Khatib, Eric A. Muller, and Markus B. Raschke. Synchrotron infrared nano-spectroscopy and -imaging. *Surf. Sci. Rep.*, 75(3):100493, 2020.

[294] Eric A. Muller, Benjamin Pollard, Hans A. Bechtel, Ronen Adato, Dordaneh Etezadi, Hatice Altug, and Markus B. Raschke. Nanoimaging and control of molecular vibrations through electromagnetically induced scattering reaching the strong coupling regime. *ACS Photonics*, 5(9):3594–3600, 2018.

[295] Ingrid D. Barcelos, Hans A. Bechtel, Christiano J. S. de Matos, Dario A. Bahamon, Bernd Kaestner, Francisco C. B. Maia, and Raul O. Freitas. Probing polaritons in 2D materials with synchrotron infrared nanospectroscopy. *Adv. Opt. Mater.*, 8:1901091, 2020.

[296] Francisco C. B. Maia, Brian T. O'Callahan, Alisson R. Cadore, Ingrid D. Barcelos, Leonardo C. Campos, Kenji Watanabe, Takashi Taniguchi, Christoph Deneke, Alexey Belyanin, Markus B. Raschke, and Raul O. Freitas. Anisotropic flow control and gate modulation of hybrid phonon-polaritons. *Nano Lett.*, 19(2):708–715, 2019.

[297] Ingrid D. Barcelos, Alisson R. Cadore, Ananias B. Alencar, Francisco C. B. Maia, Edrian Mania, Rafael F. Oliveira, Carlos C. B. Bufon, Ângelo Malachias, Raul O. Freitas, Roberto L. Moreira, and Hélio Chacham. Infrared fingerprints of natural 2D talc and plasmon–phonon coupling in graphene–talc heterostructures. *ACS Photonics*, 5(5):1912–1918, 2018.

[298] D.A. Schmidt, I. Kopf, and E. Bründermann. A matter of scale: from far-field microscopy to near-field nanoscopy. *Laser Photonics Rev.*, 6(3):296–332, 2012.

[299] Jiahua Duan, Yafeng Li, Yixi Zhou, Yuan Cheng, and Jianing Chen. Near-field optics on flatland: From noble metals to van der Waals materials. *Adv. Phys.: X*, 4(1):1593051, 2019.

[300] Xinzhong Chen, Debo Hu, Ryan Mescall, Guanjun You, D. N. Basov, Qing Dai, and Mengkun Liu. Modern scattering-type scanning near-field optical microscopy for advanced material research. *Adv. Mater.*, 31(24):1804774, 2019.

[301] Ilia M. Pavlovetc, Kyle Aleshire, Gregory V. Hartland, and Masaru K. Kuno. Approaches to mid-infrared, super-resolution imaging and spectroscopy. *Phys. Chem. Chem. Phys.*, 22:4313–4325, 2020.

[302] R. Geick, C. H. Perry, and G. Rupprecht. Normal modes in hexagonal boron nitride. *Phys. Rev.*, 146(2):543–547, 1966.

[303] Joshua D. Caldwell, Lucas Lindsay, Vincenzo Giannini, Igor Vurgaftman, Thomas L. Reinecke, Stefan A. Maier, and Orest J. Glembocki. Low-loss, infrared and terahertz nanophotonics using surface phonon polaritons. *Nanophotonics*, 4(1):44–68, 2015.

[304] Georg Jansen. Transformation properties of spheroidal multipole moments and potentials. *J. Phys. A*, 33(7):1375–1394, 2000.

[305] R. Hillenbrand, T. Taubner, and F. Keilmann. Phonon-enhanced light-matter interaction at the nanometre scale. *Nature*, 418:159–162, 2002.

[306] Rei Kitamura, Laurent Pilon, and Miroslaw Jonasz. Optical constants of silica glass from extreme ultraviolet to far infrared at near room temperature. *Appl. Opt.*, 46(33):8118, 2007.

[307] D. M. Hoffman, G. L. Doll, and P. C. Eklund. Optical properties of pyrolytic boron nitride in the energy range 0.05—10 eV. *Phys. Rev. B*, 30(10):6051–6056, 1984.

[308] J. W. Cleary, R. E. Peale, D. J. Shelton, G. D. Boreman, C. W. Smith, M. Ishigami, R. Soref, A. Drehman, and W. R. Buchwald. IR permittivities for silicides and doped silicon. *J. Opt. Soc. Am. B*, 27(4):730, 2010.

[309] Surong Guo, Nahid Talebi, Wilfried Sigle, Ralf Vogelgesang, Gunther Richter, Martin Esmann, Simon F. Becker, Christoph Lienau, and Peter A. van Aken. Reflection and phase matching in plasmonic gold tapers. *Nano Lett.*, 16(10):6137–6144, 2016.

[310] Benjamin Schröder, Thorsten Weber, Sergey V. Yalunin, Thomas Kiel, Christian Matyssek, Murat Sivis, Sascha Schäfer, Felix von Cube, Stephan Irsen, Kurt Busch, Claus Ropers, and Stefan Linden. Real-space imaging of nanotip plasmons using electron energy loss spectroscopy. *Phys. Rev. B*, 92(8):085411, 2015.

[311] Sergey V. Yalunin, Benjamin Schröder, and Claus Ropers. Theory of electron energy loss near plasmonic wires, nanorods, and cones. *Phys. Rev. B*, 93(11):115408, 2016.

[312] A. Cvitkovic, N. Ocelic, and R. Hillenbrand. Analytical model for quantitative prediction of material contrasts in scattering-type near-field optical microscopy. *Opt. Express*, 15(14):8550, 2007.

[313] G. Khitrova, H. M. Gibbs, S. W. Koch, and A. Scherer. Vacuum Rabi splitting in semiconductors. *Nat. Phys.*, 2:81–90, 2006.

[314] Lukas Novotny. Strong coupling, energy splitting, and level crossings: A classical perspective. *Am. J. Phys.*, 78(11):1199–1202, 2010.

[315] D. S. Dovzhenko, S. V. Ryabchuk, Yu. P. Rakovich, and I. R. Nabiev. Light–matter interaction in the strong coupling regime: configurations, conditions, and applications. *Nanoscale*, 10:3589–3605, 2018.

[316] Kevin C. Smith, Yueyang Chen, Arka Majumdar, and David J. Masiello. Active tuning of hybridized modes in a heterogeneous photonic molecule. *Phys. Rev. Appl.*, 13(4):044041, 2020.

[317] Daehan Yoo, Fernando de León-Pérez, Matthew Pelton, In-Ho Lee, Daniel A. Mohr, Markus B. Raschke, Joshua D. Caldwell, Luis Martín-Moreno, and Sang-Hyun Oh. Ultrastrong plasmon–phonon coupling via epsilon-near-zero nanocavities. *Nature Photonics*, 15(2):125–130, 2021.

[318] Anton Frisk Kockum, Adam Miranowicz, Simone De Liberato, Salvatore Savasta, and Franco Nori. Ultrastrong coupling between light and matter. *Nat. Rev. Phys.*, 1(1):19–40, 2019.

[319] Kimball Milton and Julian Schwinger. *Electromagnetic Radiation: Variational Methods, Waveguides and Accelerators: Including Seminal Papers of Julian Schwinger*. Particle Acceleration and Detection. Springer-Verlag, Berlin Heidelberg, 2006.

[320] Claude Cohen-Tannoudji, Jacques Dupont-Roc, and Gilbert Grynberg. *Photons and Atoms: Introduction to Quantum Electrodynamics*. Wiley-Interscience Publication. J. Wiley, 1997.

[321] Steven C. Quillin, Charles Cherqui, Nicholas P. Montoni, Guoliang Li, Jon P. Camden, and David J. Masiello. Imaging plasmon hybridization in metal nanoparticle aggregates with electron energy-loss spectroscopy. *The Journal of Physical Chemistry C*, 120(37):20852–20859, 2016.

[322] Claude Cohen-Tannoudji, Jacques Dupont-Roc, and Gilbert Grynberg. *Atom-Photon Interactions: Basic Processes and Applications*. Wiley-Interscience Publication. J. Wiley, 1992.

[323] R. Loudon. *The Quantum Theory of Light*. Oxford University Press, 2000.

[324] F. J. García de Abajo. Momentum transfer to small particles by passing electron beams. *Phys. Rev. B*, 70:115422, 2004.

[325] L. Ródriguez-Suné, M. Scalora, A. S. Johnson, C. Cojocaru, N. Akozbek, Z. J. Coppens, D. Perez-Salinas, S. Wall, and J. Trull. Study of second and third harmonic generation from an indium tin oxide monolayer: Influence of nonlocal effects and hot electrons. *APL Photonics*, 5:010801, 2020.

[326] P. Apell and D. R. Penn. Optical properties of small metal spheres: Surface effects. *Phys. Rev. Lett.*, 50(17):1316–1319, 1983.

[327] I. S. Gradshteyn and I. M. Ryzhik. *Table of Integrals, Series, and Products*. Elsevier/Academic Press, Amsterdam, seventh edition, 2007.

Appendix A

SUPPLEMENTARY INFORMATION — MULTIPOLAR NANOCUBE PLASMON MODE-MIXING IN FINITE SUBSTRATES

The derivation of the interaction strengths between the multipole plasmon modes of a metal nanocube is greatly simplified by the approximation of each mode as an oscillating point multipole. The interaction energies in the simplified picture flow directly from the multipole expansion of a charge distribution, allowing us to use standard methods to approximate the physics of an otherwise analytically intractable problem. We can begin with the Taylor series expansion of a scalar function f of 3-dimensional vector argument $\mathbf{x}$ about a point $\mathbf{a}$:

$$f(\mathbf{x}) = f(\mathbf{a}) + \sum_{i=1}^{3}(x_i - a_i)\left.\frac{\partial f(\mathbf{x})}{\partial x_i}\right|_{\mathbf{x}\to\mathbf{a}} + \frac{1}{2!}\sum_{j,k=1}^{3}(x_j - a_j)(x_k - a_k)\left.\frac{\partial^2 f(\mathbf{x})}{\partial x_j \partial x_k}\right|_{\mathbf{x}\to\mathbf{a}} + \dots . \quad \text{(A.1)}$$

This Taylor series is key to the expansion of the Coulomb potential

$$\Phi(\mathbf{r}, t) = \int \frac{\rho(\mathbf{r}', t)}{|\mathbf{r} - \mathbf{r}'|}\, \mathrm{d}^3\mathbf{r}' \quad \text{(A.2)}$$

around a chosen point in space (usually $\mathbf{a} = 0$) as a series of simpler functions.

To perform the expansion, we'll need a few identities. First, with $\mathbf{r} = \sum_i r_i \hat{\mathbf{e}}_i$, one finds

$$\begin{aligned}\frac{1}{|\mathbf{r} - \mathbf{r}'|} &= \frac{1}{[(\mathbf{r} - \mathbf{r}')\cdot(\mathbf{r} - \mathbf{r}')]^{\frac{1}{2}}} \\ &= \left(\sum_i r_i^2 + \sum_j r_j'^2 - 2\sum_k r_k r_k'\right)^{-\frac{1}{2}}\end{aligned} \quad \text{(A.3)}$$

and

$$\begin{aligned}\frac{\partial}{\partial r'_i}\frac{1}{|\mathbf{r}-\mathbf{r}'|} &= -\frac{1}{2}\left(\sum_\alpha r_\alpha^2 + \sum_\beta r_\beta'^2 - 2\sum_\gamma r_\gamma r'_\gamma\right)^{-\frac{3}{2}}\left(\sum_\beta 2r'_\beta\frac{\partial r'_\beta}{\partial r'_i} - 2\sum_\gamma r_\gamma\frac{\partial r'_\gamma}{\partial r'_i}\right)\\ &= \frac{r_i - r'_i}{|\mathbf{r}-\mathbf{r}'|^3}\end{aligned} \tag{A.4}$$

wherein we have used the independence of the elements of $\mathbf{r}'$ to say $\frac{\partial r'_i}{\partial r'_j} = \delta_{ij}$. The second and third derivatives of Eq. (A.1) follow similarly:

$$\begin{aligned}\frac{\partial^2}{\partial r'_i \partial r'_j}\frac{1}{|\mathbf{r}-\mathbf{r}'|} &= \frac{\partial}{\partial r'_i}\left((r_j - r'_j)\left[\sum_\alpha r_\alpha^2 + \sum_\beta r_\beta'^2 - 2\sum_\gamma r_\gamma r'_\gamma\right]^{-\frac{3}{2}}\right)\\ &= 3(r_i - r'_i)(r_j - r'_j)\left(\sum_\alpha r_\alpha^2 + \sum_\beta r_\beta'^2 - 2\sum_\gamma r_\gamma r'_\gamma\right)^{-\frac{5}{2}}\\ &\quad - \delta_{ij}\left(\sum_\alpha r_\alpha^2 + \sum_\beta r_\beta'^2 - 2\sum_\gamma r_\gamma r'_\gamma\right)^{-\frac{3}{2}}\\ &= \frac{3(r_i - r'_i)(r_j - r'_j) - \delta_{ij}|\mathbf{r}-\mathbf{r}'|^2}{|\mathbf{r}-\mathbf{r}'|^5}\end{aligned} \tag{A.5}$$

and

$$\begin{aligned}\frac{\partial^3}{\partial r'_i \partial r'_j \partial r'_k}\frac{1}{|\mathbf{r}-\mathbf{r}'|} &= \frac{\partial}{\partial r'_i}\left(3(r_i - r'_i)(r_j - r'_j)\left[\sum_\alpha r_\alpha^2 + \sum_\beta r_\beta'^2 - 2\sum_\gamma r_\gamma r'_\gamma\right]^{-\frac{5}{2}}\right.\\ &\quad \left. -\delta_{ij}\left[\sum_\alpha r_\alpha^2 + \sum_\beta r_\beta'^2 - 2\sum_\gamma r_\gamma r'_\gamma\right]^{-\frac{3}{2}}\right)\\ &= 15(r_i - r'_i)(r_j - r'_j)(r_k - r'_k)\left(\sum_\alpha r_\alpha^2 + \sum_\beta r_\beta'^2 - 2\sum_\gamma r_\gamma r'_\gamma\right)^{-\frac{7}{2}}\\ &\quad + 3[(r_j - r'_j)(-\delta_{ik}) + (r_k - r'_k)(-\delta_{ij})]\left(\sum_\alpha r_\alpha^2 + \sum_\beta r_\beta'^2 - 2\sum_\gamma r_\gamma r'_\gamma\right)^{-\frac{5}{2}}\\ &\quad - 3\delta_{jk}(r_i - r'_i)\left(\sum_\alpha r_\alpha^2 + \sum_\beta r_\beta'^2 - 2\sum_\gamma r_\gamma r'_\gamma\right)^{-\frac{5}{2}}\end{aligned}$$

$$= \frac{15(r_i - r'_i)(r_j - r'_j)(r_k - r'_k) - 3[(r_i - r'_i)\delta_{jk} + (r_j - r'_j)\delta_{ik} + (r_k - r'_k)\delta_{ij}]|\mathbf{r} - \mathbf{r}'|^2}{|\mathbf{r} - \mathbf{r}'|^7} \tag{A.6}$$

with higher-order derivatives becoming increasingly cumbersome to write explicitly. Eqs. (A.4)–(A.6) can be used to rewrite the Taylor series of Eq. (A.1) as

$$\begin{aligned}\frac{1}{|\mathbf{r} - \mathbf{r}'|} = \frac{1}{|\mathbf{r} - \mathbf{a}|} + \sum_i (r'_i - a_i)\frac{r_i - a_i}{|\mathbf{r} - \mathbf{a}|^3} + \frac{1}{2!}\sum_{ij}(r'_i - a_i)(r'_j - a_j) \\ \times \frac{3(r_i - a_i)(r_j - a_j) - \delta_{ij}|\mathbf{r} - \mathbf{a}|^2}{|\mathbf{r} - \mathbf{a}|^5} \\ + \frac{1}{3!}\sum_{ijk}\left[\prod_{\alpha=i,j,k}(r'_\alpha - a_\alpha)\right]\frac{15\prod_{\alpha=i,j,k}(r_\alpha - a_\alpha) - 3|\mathbf{r} - \mathbf{a}|^2\sum_{\alpha,\beta,\gamma=i,j,k}(r_\alpha - a_\alpha)\delta_{\beta\gamma}\sigma_{\alpha\beta\gamma}}{|\mathbf{r} - \mathbf{a}|^7} \\ + \ldots\end{aligned} \tag{A.7}$$

where σ_{ijk} is a symmetric tensor for which $\sigma_{iik} = \sigma_{iji} = \sigma_{ijj} = 0$ (a σ with repeated indices is zero) and otherwise $\sigma_{ijk} = \sigma_{jik} = \sigma_{kji} = 1$. A symmetry can be exploited in the second term on the right hand side to exchange the roles of the primed and unprimed coordinates. Specifically, since

$$\begin{aligned}\sum_{ij}\delta_{ij}(r'_i - a_i)(r'_j - a_j)|\mathbf{r} - \mathbf{a}| &= \sum_i (r'_i - a_i)(r'_j - a_j)|\mathbf{r} - \mathbf{a}| \\ &= |\mathbf{r}' - \mathbf{a}|^2|\mathbf{r} - \mathbf{a}|^2\end{aligned} \tag{A.8}$$

is invariant under an exchange of coordinates and $\sum_{ij}(r'_i - a_i)(r'_j - a_j)(r_i - a_i)(r_j - a_j)$ is clearly symmetric in $\mathbf{r}$ and $\mathbf{r}'$, the second term can be rewritten with $\mathbf{r} \leftrightarrow \mathbf{r}'$. The third term is symmetric by similar reasoning:

$$\begin{aligned}\sum_{ijk}(r'_i - a_i)(r'_j - a_j)(r'_k - a_k)[(r_i - a_i)\delta_{jk} + (r_j - a_j)\delta_{ik} + (r_k - a_k)\delta_{ij}]|\mathbf{r} - \mathbf{a}|^2 \\ = |\mathbf{r} - \mathbf{a}|^2|\mathbf{r}' - \mathbf{a}|^2(\mathbf{r} - \mathbf{a}) \cdot (\mathbf{r}' - \mathbf{a}).\end{aligned} \tag{A.9}$$

Therefore, exchanging the primed and unprimed coordinates in the second and third terms

of Eq. (A.7) provides

$$\frac{1}{|\mathbf{r}-\mathbf{r}'|} = \frac{1}{|\mathbf{r}-\mathbf{a}|} + \sum_i (r_i - a_i)\frac{r'_i - a_i}{|\mathbf{r}-\mathbf{r}'|^3} + \frac{1}{2!}\sum_{ij}(r_i - a_i)(r_j - a_j) \times \frac{3(r'_i - a_i)(r'_j - a_j) - \delta_{ij}|\mathbf{r}' - \mathbf{a}|^2}{|\mathbf{r}-\mathbf{a}|^5} + \frac{1}{3!}\sum_{ijk}\left[\prod_{\alpha=i,j,k}(r_\alpha - a_\alpha)\right]\frac{15\prod_{\alpha=i,j,k}(r'_\alpha - a_\alpha) - 3|\mathbf{r}'-\mathbf{a}|^2\sum_{\alpha,\beta,\gamma=i,j,k}(r'_\alpha - a_\alpha)\delta_{\beta\gamma}\sigma_{\alpha\beta\gamma}}{|\mathbf{r}-\mathbf{a}|^7} + \ldots . \tag{A.10}$$

The multipole moments of the potential scattered from a charge distribution $\rho(\mathbf{r},t)$ are usually defined by replacing the denominator in Eq. (A.2) with Eq. (A.10) and letting $\mathbf{a}\to 0$. The potential simplifies to

$$\begin{aligned}\Phi(\mathbf{r},t) &= \frac{1}{|\mathbf{r}|}\int \rho(\mathbf{r}',t)\,\mathrm{d}^3\mathbf{r}' + \sum_i \frac{r_i}{|\mathbf{r}|^3}\int r'_i\rho(\mathbf{r},t)\,\mathrm{d}^3\mathbf{r}' \\ &\quad + \sum_{ij}\frac{r_i r_j}{|\mathbf{r}|^5}\int \frac{1}{2}\left(3r'_i r'_j - \delta_{ij}|\mathbf{r}'|^2\right)\rho(\mathbf{r}',t)\,\mathrm{d}^3\mathbf{r}' \\ &\quad + \sum_{ijk}\frac{r_i r_j r_k}{|\mathbf{r}|^7}\int \frac{1}{6}\left(15r'_i r'_j r'_k - 3[r'_i\delta_{jk} + r'_j\delta_{ik} + r'_k\delta_{ij}]|\mathbf{r}'|^2\right)\rho(\mathbf{r}',t)\,\mathrm{d}^3\mathbf{r}' + \ldots \\ &= \frac{q(t)}{|\mathbf{r}|} + \frac{\mathbf{r}\cdot\mathbf{D}(t)}{|\mathbf{r}|^3} + \frac{\mathbf{r}\cdot\mathbf{Q}(t)\cdot\mathbf{r}}{|\mathbf{r}|^5} + \frac{\mathbf{r}\cdot(\mathbf{r}\cdot\mathbf{O}(t)\cdot\mathbf{r})}{|\mathbf{r}|^7} + \ldots\end{aligned} \tag{A.11}$$

where the monopole, dipole, quadrupole, and octupole moments have been defined, respectively, as

$$\begin{aligned} q(t) &= \int \rho(\mathbf{r}',t)\,\mathrm{d}^3\mathbf{r}', \\ \mathbf{D}(t) &= \int \mathbf{r}'\rho(\mathbf{r}',t)\,\mathrm{d}^3\mathbf{r}', \\ \mathbf{Q}(t) &= \frac{1}{2}\int \left(3\mathbf{r}'\mathbf{r}' - \mathbf{1}_2|\mathbf{r}'|^2\right)\rho(\mathbf{r}',t)\,\mathrm{d}^3\mathbf{r}', \\ \mathbf{O}(t) &= \frac{1}{6}\int \left(15\mathbf{r}'\mathbf{r}'\mathbf{r}' - 9\mathbf{r}'\mathbf{1}_2|\mathbf{r}'|^2\right)\rho(\mathbf{r}',t)\,\mathrm{d}^3\mathbf{r}' \end{aligned} \tag{A.12}$$

with $\mathbf{1}_2 = \sum_{ij} \delta_{ij} \hat{\mathbf{e}}_i \hat{\mathbf{e}}_j$ the 2×2 identity matrix. Each moment is a tensor of rank N with N the order of the multipole to which the moment corresponds ($N = 0$ for monopoles), and the dot products in Eq. (A.11) denote full contraction of the coordinates $\mathbf{r}$ with each tensor.

The moments in Eq. (A.12) are in their traceless forms. As a test, one can return to the index notation of Eq. (A.11) and sum over any index while holding any other index fixed to it, i.e. $\sum_i (3r'_i r'_i - \delta_{ii}|\mathbf{r}'|^2)$ or $\sum_j (15 r'_i r'_j r'_j - 3[r'_i \delta_{jj} + r'_j \delta_{ij} + r'_j \delta_{ij}]|\mathbf{r}'|^2)$. The result will always return zero for any trace taken.

A.1 Point Multipole Charge Distributions

While the problem of the resonances of a plasmonic nanocube interacting with each other via the polarization of a nearby substrate can be simplified by approximating each plasmon mode's charge distribution as that of a point multipole, some difficulty remains in defining the proper multipole charge distributions themselves. While the definition of a point dipole charge distribution can be commonly found (see, for example, Ref. [319]) and is usually written as

$$\rho(\mathbf{r}, t) = -\mathbf{D}(t) \cdot \nabla \delta(\mathbf{r} - \mathbf{r}_0) \tag{A.13}$$

for a dipole located at $\mathbf{r}_0$, the distributions of the rest are much harder to find. Defining them here for ourselves, we can follow the example of Eq. (A.13) and let

$$\rho^{(N)}(\mathbf{r}, t) = \mathbf{A}^{(N)} \circ \mathbf{M}^{(N)}(t) : (\nabla)^N \delta(\mathbf{r} - \mathbf{r}_0). \tag{A.14}$$

Here, $\mathbf{M}^{(N)}$ is a multipole moment of order N, $\mathbf{A}^{(N)}$ is a tensor-valued prefactor of rank N, $(\nabla)^N = \nabla\nabla\ldots\nabla$ is a direct product of gradients generating an N-dimensional derivative operator, $\circ$ denotes elementwise multiplication, and ":" denotes full contraction between the moment and derivative tensors. $A^{(0)} = 1$ and $\mathbf{A}^{(1)} = -(\hat{\mathbf{x}} + \hat{\mathbf{y}} + \hat{\mathbf{z}})$ can be used as limiting cases, where we assume that $\mathbf{M}^{(0)}(t) = q(t)$ and $(\nabla)^0 = 1$.

We'll also let $\boldsymbol{\kappa}^{(N)}(\mathbf{r})$ be the multipole kernels, i.e. the tensor-valued functions against which $\rho(\mathbf{r}, t)$ must be projected to produce the moments $\mathbf{M}^{(N)}(t)$. The kernels of the first four moments are given in Eq. (A.12). In general, our definitions of the individual charge

distributions $\rho^{(N)}(\mathbf{r},t)$ must satisfy an orthonormality condition that projection against the appropriate $\boldsymbol{\kappa}^{(N)}(\mathbf{r})$ produces $\mathbf{M}^{(N)}(t)$ without a prefactor and no other moments. Explicitly,

$$\mathbf{M}^{(N)}(t) = \int \boldsymbol{\kappa}(\mathbf{r}')\rho^{(N)}(\mathbf{r}',t)\ \mathrm{d}^3\mathbf{r}'. \tag{A.15}$$

This condition defines the values of $\mathbf{A}^{(N)}$.

The first two moments can be used as examples. Clearly,

$$\begin{aligned} q(t) = \int A^{(0)}q(t)\delta(\mathbf{r}'-\mathbf{r}_0)\ \mathrm{d}^3\mathbf{r}' = A^{(0)}q(t) \\ \implies A^{(0)} = 1. \end{aligned} \tag{A.16}$$

The prefactor for the dipole moments requires us to use integration by parts, which produces the required negative sign:

$$\begin{aligned} \mathbf{D}(t) &= \int \mathbf{r}'\mathbf{A}^{(1)} \circ \mathbf{D}(t) \cdot \nabla'\delta(\mathbf{r}'-\mathbf{r}_0)\ \mathrm{d}^3\mathbf{r}' \\ &= \int \nabla' \cdot \left\{\mathbf{r}'\mathbf{A}^{(1)} \circ \mathbf{D}(t)\delta(\mathbf{r}'-\mathbf{r}_0)\right\}\ \mathrm{d}^3\mathbf{r}' - \int \mathbf{A}^{(1)} \circ \mathbf{D}(t)\delta(\mathbf{r}'-\mathbf{r}_0) \cdot (\nabla'\mathbf{r}')\ \mathrm{d}^3\mathbf{r}' \\ &= 0 - \mathbf{A}^{(1)} \circ \mathbf{D}(t) \cdot \mathbf{1}_2 = -\mathbf{A}^{(1)} \circ \mathbf{D}(t) \\ \implies \mathbf{A}^{(1)} &= -(\hat{\mathbf{x}}+\hat{\mathbf{y}}+\hat{\mathbf{z}}). \end{aligned} \tag{A.17}$$

The first term on the second line of Eq. (A.17) can be seen to be zero by first applying the divergence theorem and then noting that the resulting surface integral over the boundary at infinity does not contain the (finite) point $\mathbf{r}_0$ within the region of integration and therefore must be zero by the properties of the Dirac delta.

Extending this analysis to higher-order moments becomes increasingly tedious and requires multiple rounds of integration by parts, so it's useful to speak in language as general as possible. Moving to index notation to make the discussion clearer, each multipole moment is defined via Eqs. (A.14) and (A.15) as

$$M^{(N)}_{\alpha_1,\ldots,\alpha_N}(t) = A^{(N)}_{\alpha_1,\ldots,\alpha_N}M^{(N)}_{\alpha_1,\ldots,\alpha_N}(t)\int \kappa_{\alpha_1,\ldots,\alpha_N}(\mathbf{r}')\frac{\partial}{\partial r'_{\alpha_1}}\cdots\frac{\partial}{\partial r'_{\alpha_N}}\left\{\delta(\mathbf{r}'-\mathbf{r}_0)\right\}\ \mathrm{d}^3\mathbf{r}' \tag{A.18}$$

where $\alpha_1, \ldots, \alpha_N$ are the N indices $i, j, \ldots$ of the multipole and kernel tensors. Explicitly, $\mathbf{M}^{(N)}(t) = \sum_{\alpha_1,\ldots,\alpha_N} M^{(N)}_{\alpha_1,\ldots,\alpha_N}(t)$. The integration by parts steps needed to move all of the derivative operators from the Dirac delta and onto the more tractable kernel can be inferred from the product rule. To shorten the notation, we can let $\boldsymbol{\alpha}(N) = (\alpha_1, \ldots, \alpha_N)$. Therefore,

$$\begin{aligned}
\frac{\partial}{\partial r'_{\alpha_1}} \cdots \frac{\partial}{\partial r'_{\alpha_N}} \left\{ \kappa_{\boldsymbol{\alpha}(N)}(\mathbf{r}') \delta(\mathbf{r}' - \mathbf{r}_0) \right\} &= \frac{\partial}{\partial r'_{\alpha_1}} \cdots \frac{\partial}{\partial r'_{\alpha_N}} \left\{ \kappa_{\boldsymbol{\alpha}(N)}(\mathbf{r}') \right\} \delta(\mathbf{r}' - \mathbf{r}_0) \\
&+ \sum_{i=1}^{C_1^N} \prod_{j \neq i} \left(\frac{\partial}{\partial r'_{\alpha_j}} \right) \left\{ \kappa_{\boldsymbol{\alpha}(N)}(\mathbf{r}') \right\} \frac{\partial}{\partial r'_{\alpha_i}} \{ \delta(\mathbf{r}' - \mathbf{r}_0) \} + \ldots \\
&+ \sum_{i=1}^{C_m^N} \prod_{j \in \boldsymbol{\beta}_i^m(N)} \left(\frac{\partial}{\partial r'_{\alpha_j}} \right) \left\{ \kappa_{\boldsymbol{\alpha}(N)}(\mathbf{r}') \right\} \prod_{\substack{k \in \boldsymbol{\alpha}(N) \\ \setminus \boldsymbol{\beta}_i^m(N)}} \left(\frac{\partial}{\partial r'_{\alpha_k}} \right) \{ \delta(\mathbf{r}' - \mathbf{r}_0) \} + \cdots \\
&+ \sum_{i=1}^{C_{N-1}^N} \frac{\partial}{\partial r'_{\alpha_i}} \{ \kappa_{\boldsymbol{\alpha}(N)}(\mathbf{r}') \} \prod_{j \neq i} \left(\frac{\partial}{\partial r'_{\alpha_j}} \right) \{ \delta(\mathbf{r}' - \mathbf{r}_0) \} \\
&+ \kappa_{\boldsymbol{\alpha}(N)}(\mathbf{r}') \frac{\partial}{\partial r'_{\alpha_1}} \cdots \frac{\partial}{\partial r'_{\alpha_N}} \{ \delta(\mathbf{r}' - \mathbf{r}_0) \}.
\end{aligned} \tag{A.19}$$

In other words, there are two terms, the first and last, which have all of the derivatives acting on either the kernel or delta. The other terms each have some number of derivatives acting on the kernel and the rest on the delta. The product rule dictates that, given N successive derivatives acting on a product of two functions, there are always N choose m or $C_m^N = N!/m!(N-m)!$ terms which have m derivatives acting on the first function and C_{N-m}^N on the second. Here we have let $\beta_i^m(N)$ be the i^{th} permutation of m indices that can be chosen from $\boldsymbol{\alpha}(N)$ such that $\boldsymbol{\alpha}(N) \setminus \boldsymbol{\beta}_i^m(N)$ is the set of the other $N - m$ indices.

To make the expression of Eq. (A.19) useful for the evaluation of Eq. (A.18), one needs to sort the intermediate terms that have delta functions acting on both the kernel and delta and convert them into terms that have all N derivatives acting on the kernel or the product of the kernel and delta. The first type of term is tractable and the other is a boundary term that produces zero under the integral. To do so, one can see that each term in Eq. (A.19)

that has only a single derivative acting on the delta can be rewritten using the identity

$$\prod_{k\neq i,j}\left(\frac{\partial}{\partial r'_{\alpha_k}}\right)\{\kappa_{\boldsymbol{\alpha}(N)}(\mathbf{r}')\}\frac{\partial}{\partial r'_{\alpha_i}}\frac{\partial}{\partial r'_{\alpha_j}}\{\delta(\mathbf{r}'-\mathbf{r}_0)\}= \\ \frac{\partial}{\partial r'_{\alpha_i}}\left\{\prod_{\neq i,j}\left(\frac{\partial}{\partial r'_{\alpha_k}}\right)\{\kappa_{\boldsymbol{\alpha}(N)}(\mathbf{r}')\}\frac{\partial}{\partial r'_{\alpha_j}}\{\delta(\mathbf{r}'-\mathbf{r}_0)\}\right\} \\ -\prod_{j\neq i}\left(\frac{\partial}{\partial r'_{\alpha_j}}\right)\{\kappa_{\boldsymbol{\alpha}(N)}(\mathbf{r}')\}\frac{\partial}{\partial r'_{\alpha_i}}\{\delta(\mathbf{r}'-\mathbf{r}_0)\}. \tag{A.20}$$

The first term on the right hand side of Eq. (A.20) is a boundary term that will produce zero under an integral. We will define it as $B_i^1(\mathbf{r}',N) = (\partial/\partial r'_{\alpha_i})[\prod_{k\neq i,j}(\partial/\partial r'_{\alpha_k})\{\kappa_{\boldsymbol{\alpha}(N)}(\mathbf{r}')\}(\partial/\partial r_{\alpha_j})\{\delta(\mathbf{r}'-\mathbf{r}_0)\}]$, i.e. the i^{th} boundary term with one external derivative. More importantly, we can define the cross terms with m derivatives acting on the delta as

$$K_i^m(\mathbf{r}',N)=\prod_{\substack{j\in\boldsymbol{\alpha}(N)\\ \backslash\boldsymbol{\beta}_i^m(N)}}\left(\frac{\partial}{\partial r'_{\alpha_j}}\right)\left\{\kappa_{\boldsymbol{\alpha}(N)}(\mathbf{r}')\right\}\prod_{k\in\boldsymbol{\beta}_i^m(N)}\left(\frac{\partial}{\partial r'_{\alpha_k}}\right)\{\delta(\mathbf{r}'-\mathbf{r}_0)\} \tag{A.21}$$

such that Eq. (A.20) demonstrates the substitution $K_i^1(\mathbf{r}',N)=B_i^1(\mathbf{r}',N)-K_i^2(\mathbf{r}',N)$.

Since terms $K_i^m(\mathbf{r}',N)$ of different i but identical m and N behave equivalently under the integral, all one need to do is keep track of the number of these terms that are generated by integration by parts. Since there are $C_1^N=N$ terms $K_i^1(\mathbf{r}',N)$, after the substitution of Eq. (A.20) the number of terms $K_i^2(\mathbf{r},N)$ is $C_2^N-C_1^N$, where C_2^N terms are originally generated by the expansion of Eq. (A.19). One can then replace the $K_i^2(\mathbf{r}',N)$ terms for $C_3^N-(C_2^N-C_1^N)$ terms $K_i^3(\mathbf{r}',N)$ and so on and so forth. Eventually, the cross terms are all substituted for terms $K_i^N(\mathbf{r},N)$, of which there are

$$S_N=\sum_{m=1}^{N}(-1)^{N-m}C_m^N, \tag{A.22}$$

as well as C_1^N terms $B_i^1(\mathbf{r}',N)$, $C_2^N-C_1^N$ terms $B_i^2(\mathbf{r}',N)$, etc. Finally, with the identity

$$\sum_{m=0}^{N}(-1)^m C_m^N=\delta_{N0}, \tag{A.23}$$

we can say for $N \neq 0$ that

$$\begin{aligned} 0 &= C_0^N + (-1)^N S_N \\ \implies S_N &= (-1)^{N+1}. \end{aligned} \tag{A.24}$$

Therefore, without counting the boundary terms (b.t.), we have

$$\begin{aligned} \frac{\partial}{\partial r'_{\alpha_1}} \cdots \frac{\partial}{\partial r'_{\alpha_N}} \left\{ \kappa_{\boldsymbol{\alpha}(N)}(\mathbf{r}') \delta(\mathbf{r}' - \mathbf{r}_0) \right\} &= \frac{\partial}{\partial r'_{\alpha_1}} \cdots \frac{\partial}{\partial r'_{\alpha_N}} \left\{ \kappa_{\boldsymbol{\alpha}(N)}(\mathbf{r}') \right\} \delta(\mathbf{r}' - \mathbf{r}_0) \\ &\quad + (-1)^{N+1} \kappa_{\boldsymbol{\alpha}(N)}(\mathbf{r}') \frac{\partial}{\partial r'_{\alpha_1}} \cdots \frac{\partial}{\partial r'_{\alpha_N}} \{ \delta(\mathbf{r}' - \mathbf{r}_0) \} + (\text{b.t.}). \end{aligned} \tag{A.25}$$

The integral of Eq. (A.18) can now be readily evaluated. Substituting the integrand as suggested by Eq. (A.25), we find

$$\begin{aligned} M^{(N)}_{\boldsymbol{\alpha}(N)}(t) &= A^{(N)}_{\boldsymbol{\alpha}(N)} M^{(N)}_{\boldsymbol{\alpha}(N)}(t) \int \left[(-1)^N \frac{\partial}{\partial r'_{\alpha_1}} \cdots \frac{\partial}{\partial r'_{\alpha_N}} \{ \kappa_{\boldsymbol{\alpha}(N)}(\mathbf{r}') \} \delta(\mathbf{r}' - \mathbf{r}_0) \right. \\ &\quad \left. + (-1)^{N+1} \frac{\partial}{\partial r'_{\alpha_1}} \cdots \frac{\partial}{\partial r'_{\alpha_N}} \{ \kappa_{\boldsymbol{\alpha}(N)}(\mathbf{r}') \delta(\mathbf{r}' - \mathbf{r}_0) \} + (-1)^N (\text{b.t.}) \right] \, \mathrm{d}^3\mathbf{r}' \\ &= (-1)^N A^{(N)}_{\boldsymbol{\alpha}(N)} M^{(N)}_{\boldsymbol{\alpha}(N)}(t) \int \frac{\partial}{\partial r'_{\alpha_1}} \cdots \frac{\partial}{\partial r'_{\alpha_N}} \{ \kappa_{\boldsymbol{\alpha}(N)}(\mathbf{r}') \} \delta(\mathbf{r}' - \mathbf{r}_0) \, \mathrm{d}^3\mathbf{r}' + 0. \end{aligned} \tag{A.26}$$

We now need to evaluate the many derivatives of the kernel. This is, in general, a difficult task as to do so would require a calculation of the general kernel $\boldsymbol{\kappa}^{(N)}(\mathbf{r}')$. We will instead calculate the nontrivial cases where $N < 4$ explicitly. With $\kappa^{(1)}_i(\mathbf{r}') = r'_i$, $\kappa^{(2)}_{ij}(\mathbf{r}') = (3r'_i r'_j - \delta_{ij}|\mathbf{r}'|^2)/2$, and $\kappa^{(3)}_{ijk}(\mathbf{r}') = (15r'_i r'_j r'_k - 3(r'_i \delta_{jk} + r'_j \delta_{ik} + r'_k \delta_{ij})|\mathbf{r}'|^2)/6$, one finds

$$\begin{aligned} \frac{\partial}{\partial r'_i} \kappa^{(1)}_i(\mathbf{r}') &= 1, \\ \frac{\partial}{\partial r'_i} \frac{\partial}{\partial r'_j} \kappa^{(2)}_{ij}(\mathbf{r}') &= \frac{3 + \delta_{ij}}{2}, \\ \frac{\partial}{\partial r'_i} \frac{\partial}{\partial r'_j} \frac{\partial}{\partial r'_k} \kappa^{(3)}_{ijk}(\mathbf{r}') &= \frac{15 + 9(\delta_{ij} + \delta_{jk} + \delta_{ik}) - 6\delta_{ij}\delta_{ik}\delta_{jk}}{6}. \end{aligned} \tag{A.27}$$

Therefore, with only the Dirac delta remaining as an $\mathbf{r}'$-dependent function in the integrand of Eq. (A.26), evaluation is trivial and one can see that $A^{(1)}_i = -1$, $A^{(2)}_{ij} = 2/(3 + \delta_{ij})$, and

$A^{(3)}_{ijk} = -6/(15 + 9[\delta_{ij} + \delta_{jk} + \delta_{ik}] - 6\delta_{ij}\delta_{jk}\delta_{ik})$ such that

$$\begin{aligned}
\mathbf{A}^{(1)} &= -\sum_i \hat{\mathbf{e}}_i = -\hat{\mathbf{x}} - \hat{\mathbf{y}} - \hat{\mathbf{z}} \\
\mathbf{A}^{(2)} &= \sum_{ij} \frac{2}{3 + \delta_{ij}} \hat{\mathbf{e}}_i \hat{\mathbf{e}}_j \\
\mathbf{A}^{(3)} &= -\sum_{ijk} \frac{6}{15 + 9[\delta_{ij} + \delta_{jk} + \delta_{ik}] - 6\delta_{ij}\delta_{jk}\delta_{ik}} \hat{\mathbf{e}}_i \hat{\mathbf{e}}_j \hat{\mathbf{e}}_k.
\end{aligned} \tag{A.28}$$

Therefore, for higher-order moments, on-diagonal components generally have smaller prefactors than do off-diagonal components.

Eq. (A.27) has provided us with the appropriate normality condition for each $\rho^{(N)}(\mathbf{r}, t)$. Interestingly, it also provides a notion of orthogonality. In the case where the multipole charge distribution of order N is projected against the kernel of order $M < N$, the $(N - M)^{\text{th}}$ through N^{th} derivatives acting on $\boldsymbol{\kappa}^{(M)}(\mathbf{r}')$ (after integration by parts) act on a function independent of $\mathbf{r}'$ and produce zero. In the case $M > N$, there are too few derivatives acting on $\boldsymbol{\kappa}^{(M)}(\mathbf{r}')$ to produce a quantity independent of $\mathbf{r}'$ such that integration of each element $(\partial/\partial r'_{\alpha_1}) \cdots (\partial/\partial r'_{\alpha_N}) \kappa_{\boldsymbol{\alpha}(N)}(\mathbf{r}')$ against $\delta(\mathbf{r}' - \mathbf{r}_0)$ produces a polynomial in $\mathbf{r}_0$ with no constant terms. In the case where $\mathbf{r}_0$ is not at the origin, then, the charge distributions of each multipole are *not* orthogonal. However, if $\mathbf{r}_0 \to 0$, as will usually be the case, the polynomial in $\mathbf{r}_0$ becomes zero and the multipole charge distributions are orthogonal.

A.2 Multipole Interaction Strengths

Interactions between multipoles centered at different origins $\mathbf{R}_1$ and $\mathbf{R}_2$ can be characterized using the definition of the interaction energy

$$U(t) = \iint \frac{\rho_1(\mathbf{r}_1, t)\rho_2(\mathbf{r}_2, t)}{|\mathbf{r}_1 - \mathbf{r}_2 + \mathbf{R}|} \, \mathrm{d}^3\mathbf{r}_1 \, \mathrm{d}^3\mathbf{r}_2, \tag{A.29}$$

where $\mathbf{r}_{1,2}$ are the coordinates stemming from each origin that sweep over the charge distributions $\rho_{1,2}(\mathbf{r}, t)$, and $\mathbf{R} = \mathbf{R}_1 - \mathbf{R}_2$ is the displacement between the two origins. The use of two separate origins is apparent from the previous section: the charge distributions of Eq.

(A.14) are not unique to a single multipole if they are not described with respect to an origin located at their center.

We can now begin to calculate U. Letting $\rho_1(\mathbf{r}_1,t) = \rho^{(N_1)}(\mathbf{r}_1,t)$ and $\rho_2(\mathbf{r}_2,t) = \rho^{(N_2)}(\mathbf{r}_2,t)$, Eq. (A.29) becomes

$$\begin{aligned} U(N_1,N_2) = \iint \mathbf{A}^{(N_1)} \circ \mathbf{M}_1^{(N_1)}(t) : \nabla_1 \cdots \nabla_1 \{\delta(\mathbf{r}_1)\} \frac{1}{|\mathbf{r}_1 - \mathbf{r}_2 + \mathbf{R}|} \\ \times \mathbf{A}^{(N_2)} \circ \mathbf{M}_2^{(N_2)}(t) : \nabla_2 \cdots \nabla_2 \{\delta(\mathbf{r}_2)\} \, \mathrm{d}^3\mathbf{r}_1 \, \mathrm{d}^3\mathbf{r}_2. \end{aligned} \tag{A.30}$$

Rewriting Eq. (A.30) in index notation and integrating by parts produces a pair of factors $(-1)^N$, as shown in Eqs.(A.19)–(A.25). Explicitly,

$$\begin{aligned} U(N_1,N_2) &= \iint \sum_{\boldsymbol{\alpha}} \left(A_{\boldsymbol{\alpha}}^{(N_1)} M_{1\boldsymbol{\alpha}}^{(N_1)}(t) \frac{\partial}{\partial r_{1,\alpha_1}} \cdots \frac{\partial}{\partial r_{1,\alpha_{N_1}}} \{\delta(\mathbf{r}_1)\} \right) \frac{1}{|\mathbf{r}_1 - \mathbf{r}_2 + \mathbf{R}|} \\ &\qquad \times \sum_{\boldsymbol{\beta}} \left(A_{\boldsymbol{\beta}}^{(N_2)} M_{2\boldsymbol{\beta}}^{(N_2)}(t) \frac{\partial}{\partial r_{2,\beta_1}} \cdots \frac{\partial}{\partial r_{2,\beta_{N_2}}} \{\delta(\mathbf{r}_2)\} \right) \\ &= (-1)^{N_1+N_2} \iint \delta(\mathbf{r}_1)\delta(\mathbf{r}_2) \sum_{\boldsymbol{\alpha},\boldsymbol{\beta}} A_{\boldsymbol{\alpha}}^{(N_1)} A_{\boldsymbol{\beta}}^{(N_2)} \frac{\partial}{\partial r_{2,\beta_1}} \cdots \frac{\partial}{\partial r_{2,\beta_{N_2}}} \Bigg\{ \\ &\qquad \times \frac{\partial}{\partial r_{1,\alpha_1}} \cdots \frac{\partial}{\partial r_{1,\alpha_{N_1}}} \left\{ \frac{1}{|\mathbf{r}_1 - \mathbf{r}_2 + \mathbf{R}|} \right\} \Bigg\} M_{1\boldsymbol{\alpha}}^{(N_1)}(t) M_{2\boldsymbol{\beta}}^{(N_2)}(t) \, \mathrm{d}^3\mathbf{r}_1 \, \mathrm{d}^3\mathbf{r}_2 + (\text{b.t.}), \end{aligned} \tag{A.31}$$

where $\boldsymbol{\alpha} = \alpha_1, \ldots, \alpha_{N_1}$ are the indices of the moment of ρ_1, $\boldsymbol{\beta} = \beta_1, \ldots, \beta_{N_2}$ are the indices of ρ_2, and (b.t.) are the boundary terms that go to zero upon evaluation of the Dirac deltas. The application of the many derivatives to $1/|\mathbf{r}_1 - \mathbf{r}_2 + \mathbf{R}|$ appears very complicated, however the tracelessness of the multipole moments as we have defined them simplifies the problem considerably.

From Eqs. (A.4)–(A.5), it's clear that the application of p successive derivatives onto $1/|\mathbf{r}_1 - \mathbf{r}_2 + \mathbf{R}|$ will produce one term proportional to $(r_{1,\alpha_1} - r_{2,\alpha_1} + R_{\alpha_1}) \cdots (r_{1,\alpha_p} - r_{2,\alpha_p} + R_{\alpha_p}) |\mathbf{r}_1 - \mathbf{r}_2 + \mathbf{R}|^{-2p-1}$ and a number of other terms that each contain at least one Kronecker delta and no factors of $(r_{1,i} - r_{2,i} + R_i)$ with an index i that matches the indices of any of the deltas. Thus, each of the terms proportional to a Kronecker delta will, when summed over all of the available indices, generate a sum over at least one of the traces of the relevant

multipole moment. Because the moments are all traceless, each of these "trace terms" contributes nothing to the sum.

Labeling the trace terms (t.t.) and neglecting to count them, we can see that

$$\begin{aligned} U(N_1,N_2) = (-1)^{N_1+N_2} \iint \delta(\mathbf{r}_1)\delta(\mathbf{r}_2) \sum_{\boldsymbol{\alpha},\boldsymbol{\beta}} A^{(N_1)}_{\boldsymbol{\alpha}} A^{(N_2)}_{\boldsymbol{\beta}} \frac{\partial}{\partial r_{2,\beta_1}} \cdots \frac{\partial}{\partial r_{2,\beta_{N_2}}} \Bigg\{ \\ \times (r_{1,\alpha_1} - r_{2,\alpha_1} + R_{\alpha_1}) \cdots (r_{1,\alpha_{N_1}} - r_{2,\alpha_{N_1}} + R_{\alpha_{N_1}}) \frac{(-1)^{(N_1)}(2N_1-1)!!}{|\mathbf{r}_1 - \mathbf{r}_2 + \mathbf{R}|^{2N_1+1}} \Bigg\} \\ \times M^{(N_1)}_{1\boldsymbol{\alpha}}(t) M^{(N_2)}_{2\boldsymbol{\beta}}(t)\, \mathrm{d}^3\mathbf{r}_1\, \mathrm{d}^3\mathbf{r}_2 + (\text{t.t.}) \end{aligned} \tag{A.32}$$

where the numerator $(-1)^{N_1}(2N_1-1)!!$ is generated by the chain rule. The remaining N_2 derivatives can act either on the product of separation terms $(r_{1,\alpha_1} - r_{2,\alpha_1} + R_{\alpha_1}) \cdots (r_{1,\alpha_{N_1}} - r_{2,\alpha_{N_1}} + R_{\alpha_{N_1}})$ or onto the Coulomb term $1/|\mathbf{r}_1 - \mathbf{r}_2 + \mathbf{R}|^{2N_1+1}$. As we saw in the previous section, between 0 and N_2 derivatives can act on the product, with the rest acting on the Coulomb term. Each of these N_2+1 cases contains $C^{N_2}_m$ arrangements in which m derivatives act on the product and the other $N_2 - m$ act on the Coulomb term. Further, because the moments $M^{(N)}_{2\boldsymbol{\beta}}(t)$ are invariant under the interchange of any two indices (see Eqs. (A.11) and (A.12)), the indices of each of the derivatives in each arrangement do not need to be tracked. Exchanging indices allows us to reorder them in any way we like, such that we can choose to rearrange all $C^{N_2}_m$ arrangements in the most orderly way. For example, if $N_2 = 5$ and $m = 2$,

$$\begin{aligned} & M^{(5)}_{2;\beta_1,\ldots,\beta_5}(t) \frac{\partial}{\partial r_{2,\beta_3}} \frac{\partial}{\partial r_{2,\beta_1}} \left\{ (r_{1,\alpha_1} - r_{2,\alpha_1} + R_{\alpha_1}) \cdots (r_{1,\alpha_{N_1}} - r_{2,\alpha_{N_1}} + R_{\alpha_{N_1}}) \right\} \\ & \qquad \times \frac{\partial}{\partial r_{2,\beta_2}} \frac{\partial}{\partial r_{2,\beta_4}} \frac{\partial}{\partial r_{2,\beta_5}} \left\{ \frac{1}{|\mathbf{r}_1 - \mathbf{r}_2 + \mathbf{R}|^{2N_1+1}} \right\} \\ = {} & M^{(5)}_{2;\beta_2,\beta_3,\beta_1,\beta_4,\beta_5}(t) \frac{\partial}{\partial r_{2,\beta_1}} \frac{\partial}{\partial r_{2,\beta_2}} \left\{ (r_{1,\alpha_1} - r_{2,\alpha_1} + R_{\alpha_1}) \cdots (r_{1,\alpha_{N_1}} - r_{2,\alpha_{N_1}} + R_{\alpha_{N_1}}) \right\} \\ & \qquad \times \frac{\partial}{\partial r_{2,\beta_3}} \frac{\partial}{\partial r_{2,\beta_4}} \frac{\partial}{\partial r_{2,\beta_5}} \left\{ \frac{1}{|\mathbf{r}_1 - \mathbf{r}_2 + \mathbf{R}|^{2N_1+1}} \right\} \\ = {} & M^{(5)}_{2;\beta_1,\beta_2,\beta_3,\beta_4,\beta_5}(t) \frac{\partial}{\partial r_{2,\beta_1}} \frac{\partial}{\partial r_{2,\beta_2}} \left\{ (r_{1,\alpha_1} - r_{2,\alpha_1} + R_{\alpha_1}) \cdots (r_{1,\alpha_{N_1}} - r_{2,\alpha_{N_1}} + R_{\alpha_{N_1}}) \right\} \\ & \qquad \times \frac{\partial}{\partial r_{2,\beta_3}} \frac{\partial}{\partial r_{2,\beta_4}} \frac{\partial}{\partial r_{2,\beta_5}} \left\{ \frac{1}{|\mathbf{r}_1 - \mathbf{r}_2 + \mathbf{R}|^{2N_1+1}} \right\}. \end{aligned} \tag{A.33}$$

We can therefore treat each of the arrangements as identical.

A similar argument can be made to simplify the application of the r_2-derivatives onto the product of separation terms. The applied derivatives will produce $N_1!/(N_1-m)! = C_m^{N_1} m!$ different terms, each a product of m negative Kronecker deltas and $N_1 - m$ separation terms. Encouragingly, any moment $M_{1\boldsymbol{\alpha}}^{(N_1)}$ is also symmetric under index exchange such that the indices of any Kronecker deltas and leftover separation terms can always be rearranged to produce the most ordered arrangement. For example, with $m = 2$ and $N_1 = 3$,

$$
\begin{aligned}
&M_{2\boldsymbol{\beta}}^{(N_2)}(t) M_{1\boldsymbol{\alpha}}^{(N_1)}(t) \frac{\partial}{\partial r_{2,\beta_1}} \frac{\partial}{\partial r_{2,\beta_2}} \left\{ (r_{1,\alpha_1} - r_{2,\alpha_1} + R_{\alpha_1})(r_{1,\alpha_2} - r_{2,\alpha_2} + R_{\alpha_2})(r_{1,\alpha_3} - r_{2,\alpha_3} + R_{\alpha_3}) \right\} \\
&\quad = M_{2\boldsymbol{\beta}}^{(N_2)}(t) M_{1\boldsymbol{\alpha}}^{(N_1)}(t) \left[(r_{1,\alpha_1} - r_{2,\alpha_1} + R_{\alpha_1})(\delta_{\beta_1\alpha_2}\delta_{\beta_2\alpha_3} + \delta_{\beta_2\alpha_2}\delta_{\beta_1\alpha_3}) \right. \\
&\qquad + (r_{1,\alpha_2} - r_{2,\alpha_2} + R_{\alpha_2})(\delta_{\beta_1\alpha_1}\delta_{\beta_2\alpha_3} + \delta_{\beta_2\alpha_1}\delta_{\beta_1\alpha_3}) \\
&\qquad \left. + (r_{1,\alpha_3} - r_{2,\alpha_3} + R_{\alpha_3})(\delta_{\beta_1\alpha_1}\delta_{\beta_2\alpha_2} + \delta_{\beta_2\alpha_1}\delta_{\beta_1\alpha_2}) \right] \\
&\quad = M_{2\boldsymbol{\beta}}^{(N_2)}(t) \left[M_{1;\alpha_1,\alpha_2,\alpha_3}^{(N_1)}(t) + M_{1;\alpha_2,\alpha_1,\alpha_3}^{(N_1)}(t) + M_{1;\alpha_3,\alpha_2,\alpha_1}^{(N_1)}(t) \right] \\
&\qquad \times (r_{1,\alpha_1} - r_{2,\alpha_1} + R_{\alpha_1})(\delta_{\beta_1\alpha_2}\delta_{\beta_2\alpha_3} + \delta_{\beta_2\alpha_2}\delta_{\beta_1\alpha_3}) \\
&\quad = 3 M_{2\boldsymbol{\beta}}^{(N_2)}(t) M_{1;\alpha_1,\alpha_2,\alpha_3}^{(N_1)}(t) (r_{1,\alpha_1} - r_{2,\alpha_1} + R_{\alpha_1})(\delta_{\beta_1\alpha_2}\delta_{\beta_2\alpha_3} + \delta_{\beta_2\alpha_2}\delta_{\beta_1\alpha_3}) \\
&\quad = 6 M_{2\boldsymbol{\beta}}^{(N_2)}(t) M_{1;\alpha_1,\alpha_2,\alpha_3}^{(N_1)}(t) (r_{1,\alpha_3} - r_{2,\alpha_3} + R_{\alpha_3})\delta_{\beta_1\alpha_1}\delta_{\beta_2\alpha_2}
\end{aligned}
\tag{A.34}
$$

where in the last line the indices β_m of the Kronecker deltas have been rearranged as allowed by the symmetry of $M_{2\boldsymbol{\beta}}^{(2)}$ to all lie in the simplest possible order. Thus, as long as $N_1 > m$, one can always rearrange to obtain $N_1!/(N_1-m)! = C_m^{N_1} m!$ identical ordered products of m Kronecker deltas and $N_1 - m$ separation terms.

Finally, the $N_2 - m$ derivatives that act on the Coulomb term produce a term with $N_2 - m$ factors of the separation term and many other trace terms that do not contribute to the sum. Thus, rearranging freely,

$$\frac{\partial}{\partial r_{2,\beta_1}}\cdots\frac{\partial}{\partial r_{2,\beta_{N_2}}}\left\{(r_{1,\alpha_1}-r_{2,\alpha_1}+R_{\alpha_1})\cdots(r_{1,\alpha_{N_1}}-r_{2,\alpha_{N_1}}+R_{\alpha_{N_1}})\frac{M_{1\boldsymbol{\alpha}}^{(N_1)}(t)M_{2\boldsymbol{\beta}}^{(N_2)}(t)}{|\mathbf{r}_1-\mathbf{r}_2+\mathbf{R}|^{2N_1+1}}\right\}$$
$$=\sum_{m=0}^{N_2}C_m^{N_2}\frac{\partial}{\partial r_{2,\beta_1}}\cdots\frac{\partial}{\partial r_{2,\beta_m}}\left\{(r_{1,\alpha_1}-r_{2,\alpha_1}+R_{\alpha_1})\cdots(r_{1,\alpha_{N_1}}-r_{2,\alpha_{N_1}}+R_{\alpha_{N_1}})\right\}$$
$$\times\frac{\partial}{\partial r_{2,\beta_{m+1}}}\cdots\frac{\partial}{\partial r_{2,\beta_{N_2}}}\left\{\frac{1}{|\mathbf{r}_1-\mathbf{r}_2+\mathbf{R}|^{2N_1+1}}\right\}M_{1\boldsymbol{\alpha}}^{(N_1)}(t)M_{2\boldsymbol{\beta}}^{(N_2)}(t)$$

$$=M_{1\boldsymbol{\alpha}}^{(N_1)}(t)M_{2\boldsymbol{\beta}}^{(N_2)}(t)\sum_{m=0}^{N_2}C_m^{N_2}(-1)^mC_m^{N_1}m!(r_{1,\alpha_{m+1}}-r_{2,\alpha_{m+1}}+R_{\alpha_{m+1}})\cdots$$
$$\times(r_{1,\alpha_{N_1}}-r_{2,\alpha_{N_1}}+R_{\alpha_{N_1}})\delta_{\alpha_1\beta_1}\ldots\delta_{\alpha_m\beta_m}\Bigg((r_{1,\beta_{m+1}}-r_{2,\beta_{m+1}}+R_{\beta_{m+1}})\cdots$$
$$\times(r_{1,\beta_{N-2}}-r_{2,\beta_{N_2}}+R_{\beta_{N_2}})\frac{1}{(2N_1-1)!!}\frac{(2N_1+2[N_2-m]-1)!!}{|\mathbf{r}_1-\mathbf{r}_2+\mathbf{R}|^{2N_1+2(N_2-m)+1}}+(\text{t.t.})\Bigg) \tag{A.35}$$

wherein any products of zero Kronecker deltas or separation terms in which the final index is larger than the initial index must be replaced with one ($\delta_{\alpha_1\beta_1}\cdots\delta_{\alpha_0\beta_0}=1$, etc.).

Finally, one can use Eq. (A.35) to write down the interaction energy of a pair of multipoles, such that

$$U(N_1,N_2)=(-1)^{N_1+N_2}\iint\delta(\mathbf{r}_1)\delta(\mathbf{r}_2)\sum_{\boldsymbol{\alpha},\boldsymbol{\beta}}A_{\boldsymbol{\alpha}}^{(N_1)}A_{\boldsymbol{\beta}}^{(N_2)}\sum_{m=0}^{N_2}(-1)^mC_m^{N_2}C_m^{N_1}m!$$
$$\times\left(\prod_{k=m+1}^{N_1}(r_{1,\alpha_k}-r_{2,\alpha_k}+R_{\alpha_k})\right)\left(\prod_{k=m+1}^{N_2}(r_{1,\beta_k}-r_{2,\beta_k}+R_{\beta_k})\right)\left(\prod_{k=1}^{m}\delta_{\alpha_k\beta_k}\right)$$
$$\times\frac{(2N_1+2[N_2-m]-1)!!}{|\mathbf{r}_1-\mathbf{r}_2+\mathbf{R}|^{2N_1+2(N_2-m)+1}}\frac{(-1)^{N_1}(2N_1-1)!!}{(2N_1-1)!!}M_{1\boldsymbol{\alpha}}^{(N_1)}(t)M_{2\boldsymbol{\beta}}^{(N_2)}(t)\ \mathrm{d}^3\mathbf{r}_1\ \mathrm{d}^3\mathbf{r}_2 \tag{A.36}$$

$$=\sum_{\boldsymbol{\alpha},\boldsymbol{\beta}}A_{\boldsymbol{\alpha}}^{(N_1)}A_{\boldsymbol{\beta}}^{(N_2)}M_{1\boldsymbol{\alpha}}^{(N_1)}(t)M_{2\boldsymbol{\beta}}^{(N_2)}(t)\sum_{m=0}^{N_2}(-1)^{N_2+m}C_m^{N_2}C_m^{N_1}m!$$
$$\times\frac{(2N_1+2[N_2-m]-1)!!}{R^{2N_1+2(N_2-m)+1}}\left(\prod_{k=m+1}^{N_1}R_{\alpha_k}\right)\left(\prod_{k=m+1}^{N_2}R_{\beta_k}\right)\left(\prod_{k=1}^{m}\delta_{\alpha_k\beta_k}\right).$$

This expression is rather daunting but leads to intuitive forms of the interaction energy. Letting $\hat{\mathbf{n}} = \sum_i R_i/R$, one can see that, for two interacting dipoles,

$$\begin{aligned} U(1,1) &= -3\sum_{ij} A_i^{(1)} A_j^{(1)} D_{1i}(t) D_{2j}(t) \frac{R_i R_j}{R^5} + \sum_{ij} A_i^{(1)} A_j^{(1)} D_{1i}(t) D_{2j}(t) \frac{\delta_{ij}}{R^3} \\ &= -3\frac{(\mathbf{D}_1(t)\cdot\hat{\mathbf{n}})(\mathbf{D}_2(t)\cdot\hat{\mathbf{n}})}{R^3} + \frac{\mathbf{D}_1(t)\cdot\mathbf{D}_2(t)}{R^3}. \end{aligned} \tag{A.37}$$

Further, for interacting dipoles, quadrupoles, and octupoles, we have

$$\begin{aligned} U(2,1) &= -15\sum_{ijk} A_{ij}^{(2)} A_k^{(1)} Q_{1ij}(t) D_{2k}(t) \frac{R_i R_j R_k}{R^7} + 6\sum_{ijk} A_{ij}^{(2)} A_k^{(1)} Q_{1ij}(t) D_{2k}(t) \frac{\delta_{ik} R_j}{R^5} \\ &= 15\frac{(\hat{\mathbf{n}}\cdot\mathbf{A}^{(2)}\circ\mathbf{Q}_1(t)\cdot\hat{\mathbf{n}})(\mathbf{D}_2(t)\cdot\hat{\mathbf{n}})}{R^4} - 6\frac{\hat{\mathbf{n}}\cdot\mathbf{A}^{(2)}\circ\mathbf{Q}_1(t)\cdot\mathbf{D}_2(t)}{R^4}, \end{aligned}$$

$$\begin{aligned} U(2,2) &= 105\frac{(\hat{\mathbf{n}}\cdot\mathbf{A}^{(2)}\circ\mathbf{Q}_1(t)\cdot\hat{\mathbf{n}})(\hat{\mathbf{n}}\cdot\mathbf{A}^{(2)}\circ\mathbf{Q}_2(t)\cdot\hat{\mathbf{n}})}{R^5} \\ &\quad - 60\frac{\hat{\mathbf{n}}\cdot\mathbf{A}^{(2)}\circ\mathbf{Q}_1(t)\cdot\mathbf{A}^{(2)}\circ\mathbf{Q}_2(t)\cdot\hat{\mathbf{n}}}{R^5} + 6\frac{\mathbf{A}^{(2)}\circ\mathbf{Q}_1(t):\mathbf{A}^{(2)}\circ\mathbf{Q}_2(t)}{R^5}, \end{aligned}$$

$$\begin{aligned} U(3,2) &= 945\frac{\hat{\mathbf{n}}\cdot(\hat{\mathbf{n}}\cdot\mathbf{A}^{(3)}\circ\mathbf{O}_1(t)\cdot\hat{\mathbf{n}})(\hat{\mathbf{n}}\cdot\mathbf{A}^{(2)}\circ\mathbf{Q}_2(t)\cdot\hat{\mathbf{n}})}{R^6} \\ &\quad - 630\frac{[\hat{\mathbf{n}}\cdot\mathbf{A}^{(3)}\circ\mathbf{O}_1(t)\cdot\hat{\mathbf{n}}]\cdot\mathbf{A}^{(2)}\circ\mathbf{Q}_2(t)\cdot\hat{\mathbf{n}}}{R^6} \\ &\quad + 90\frac{[\hat{\mathbf{n}}\cdot\mathbf{A}^{(3)}\circ\mathbf{O}_1(t)]:\mathbf{A}^{(2)}\circ\mathbf{Q}_2(t)}{R^6}, \end{aligned} \tag{A.38}$$

$$\begin{aligned} U(3,3) &= -10395\frac{\hat{\mathbf{n}}\cdot(\hat{\mathbf{n}}\cdot\mathbf{A}^{(3)}\circ\mathbf{O}_1(t)\cdot\hat{\mathbf{n}})(\hat{\mathbf{n}}\cdot\mathbf{A}^{(3)}\circ\mathbf{O}_2(t)\cdot\hat{\mathbf{n}})\cdot\hat{\mathbf{n}}}{R^7} \\ &\quad + 8508\frac{(\hat{\mathbf{n}}\cdot\mathbf{A}^{(3)}\circ\mathbf{O}_1(t)\cdot\hat{\mathbf{n}})\cdot(\hat{\mathbf{n}}\cdot\mathbf{A}^{(3)}\circ\mathbf{O}_2(t)\cdot\hat{\mathbf{n}})}{R^7} \\ &\quad - 1890\frac{[\hat{\mathbf{n}}\cdot\mathbf{A}^{(3)}\circ\mathbf{O}_1(t)]:[\mathbf{A}^{(3)}\circ\mathbf{O}_2(t)\cdot\hat{\mathbf{n}}]}{R^7} \\ &\quad + 90\frac{\mathbf{A}^{(3)}\circ\mathbf{O}_1(t):\mathbf{A}^{(3)}\circ\mathbf{O}_2(t)}{R^7}. \end{aligned}$$

Note that the prefactors in front of each term become quite large but are divided by the denominators of $\mathbf{A}^{(N)}$, such that the interaction strengths between the moments grow much more slowly than they appear in increasing multipole order.

A.3 Constructing the Hamiltonian

We are now ready to calculate the interactions between the corner-localized LSP modes of a substrate-supported nanocube. These interactions stem from the potential set up above a substrate of finite thickness t (not to be confused with the time coordinate, which will herein be neglected) and dielectric function ϵ_2 by a charge distribution $\rho(\mathbf{r}')$,

$$\begin{aligned}\Phi(\mathbf{r}) = &\int\limits_{z'>0} \frac{\rho(\mathbf{r}')}{\epsilon_1|\mathbf{r}-\mathbf{r}'|}\,\mathrm{d}^3\mathbf{r}' - \int\limits_{z'>0} \frac{\epsilon_2-\epsilon_1}{\epsilon_2+\epsilon_1}\frac{\rho(\mathbf{r}')}{\epsilon_1|\mathbf{r}-\mathbf{r}_0'|}\,\mathrm{d}^3\mathbf{r}' \\ &+ \int\limits_{z'>0} \frac{\epsilon_2-\epsilon_3}{\epsilon_2+\epsilon_3}\left[1-\left(\frac{\epsilon_2-\epsilon_1}{\epsilon_2+\epsilon_1}\right)^2\right]\sum_{n=1}^{\infty}\left(\frac{\epsilon_2-\epsilon_1}{\epsilon_2+\epsilon_1}\frac{\epsilon_2-\epsilon_3}{\epsilon_2+\epsilon_3}\right)^{n-1}\frac{\rho(\mathbf{r}')}{\epsilon_1|\mathbf{r}-\mathbf{r}_n'|}\,\mathrm{d}^3\mathbf{r}',\end{aligned} \tag{A.39}$$

where ϵ_1 is the dielectric function of the material above the substrate and ϵ_3 is the dielectric function of the material below [121]. The upper surface of the substrate exists in the $z=0$ plane. Additionally, the first term is just the potential set up throughout space as if the substrate were not present, such that the remaining terms $\Phi_{\mathrm{ind}}(\mathbf{r}) = \Phi(\mathbf{r}) - \int \rho(\mathbf{r}')/\epsilon_1|\mathbf{r}-\mathbf{r}'|\,\mathrm{d}^3\mathbf{r}'$ give the potential induced by the polarization of the substrate.

The numbered prime coordinates $\mathbf{r}_n' = \mathbf{x}'+\mathbf{y}'-\mathbf{z}'-2nt\hat{\mathbf{z}}$ in Φ_{ind} signify that the potential of each term is set up by a charge distribution that appears to be reversed in sign, inverted across the xy-plane, and displaced by a vector $-2nt\hat{\mathbf{z}}$. To see this, one can let $\rho(\mathbf{r}') = \xi(x')\upsilon(y')\zeta(z')$ such that

$$\begin{aligned}\int\limits_{z'>0}\frac{\rho(\mathbf{r}')}{|\mathbf{r}-\mathbf{r}_n'|}\,\mathrm{d}^3\mathbf{r}' &= \int\limits_{z'>0}\frac{\xi(x')\upsilon(y')\zeta(z')}{|\mathbf{r}-\mathbf{r}_n'|}\,\mathrm{d}x'\,\mathrm{d}y'\,\mathrm{d}z' \\ &= \int\limits_{z'>0}\frac{\xi(x')\upsilon(y')\zeta(z')}{|(\mathbf{r}+2nt\hat{\mathbf{z}})-\mathbf{x}'-\mathbf{y}'+\mathbf{z}'|}\,\mathrm{d}x'\,\mathrm{d}y'\,\mathrm{d}z' \\ &= -\int\limits_{-z'>0}\frac{\xi(x')\upsilon(y')\zeta(-z')}{|(\mathbf{r}+2nt\hat{\mathbf{z}})-\mathbf{x}'-\mathbf{y}'-\mathbf{z}'|}\,\mathrm{d}x'\,\mathrm{d}y'\,\mathrm{d}z' \\ &= \int\limits_{-\infty}^{0}\iint\frac{\xi(x')\upsilon(y')\zeta(-z')}{|(\mathbf{r}+2nt\hat{\mathbf{z}})-\mathbf{x}'-\mathbf{y}'-\mathbf{z}'|}\,\mathrm{d}x'\,\mathrm{d}y'\,\mathrm{d}z'\end{aligned} \tag{A.40}$$

where in the second-to-last line z' has been exchanged for $-z'$ in ζ, in the denominator, and in the volume element leaving the value of the integral unchanged. Also, one can see that the origin of the potential now lies at $(0, 0, -2nt)$ where $(\mathbf{r}+2nt\hat{\mathbf{z}}) = 0$, such that the electric field lines above the substrate appear to come from a flipped "image" of the real charge located beneath the substrates' surface at a location $-\mathbf{z}' - 2nt\hat{\mathbf{z}}$.

The interaction between the real charge distribution of one of the nanocube's plasmon modes and an image of another mode can thus be described as

$$\begin{aligned} U_{\alpha\beta} &= \int\limits_{z>0} \rho_\alpha(\mathbf{r})\Phi_{\beta,\mathrm{ind}}(\mathbf{r})\ \mathrm{d}^3\mathbf{r} \\ &= \iint\limits_{\substack{z>0,\\ z'>0}} \sum_{n=0}^{\infty} P_n \frac{\rho_\alpha(\mathbf{r})\rho_\beta(\mathbf{r}')}{|\mathbf{r}-\mathbf{r}'_- + 2nt\hat{\mathbf{z}}|}\ \mathrm{d}^3\mathbf{r}'\ \mathrm{d}^3\mathbf{r} \\ &= \iint\limits_{\substack{z>0,\\ z'\in(-\infty,0)}} \sum_{n=0}^{\infty} P_n \frac{\rho_\alpha(\mathbf{r})\rho_\beta(\mathbf{r}'_-)}{|\mathbf{r}-\mathbf{r}' + 2nt\hat{\mathbf{z}}|}\ \mathrm{d}^3\mathbf{r}'\ \mathrm{d}^3\mathbf{r} \end{aligned} \tag{A.41}$$

where α and β are the mode labels and $P_0 = -\Delta_{21}$ and $P_{n\geq 1} = \Delta_{23}(1-\Delta_{21}^2)(\Delta_{21}\Delta_{23})^{n-1}$ are the prefactors of each term of the induced potential with $\Delta_{mn} = (\epsilon_m - \epsilon_n)/(\epsilon_m + \epsilon_n)$. The minus subscript on $\mathbf{r}'$ denotes the inversion of its z' coordinate; we can perform the same rearrangement is in Eq. (A.40) to arrive at the last line of Eq. (A.41).

To analyze the effects of the inversion of the z'-coordinate in $\rho_\beta(\mathbf{r}'_-)$, it is convenient to redefine the integration coordinates as $\mathbf{r} = \mathbf{r}_\alpha - \mathbf{R}_\alpha$ and $\mathbf{r}' = \mathbf{r}_\beta - \mathbf{R}_\beta$, where the lowercase coordinates originate at $\mathbf{R}_{\alpha,\beta}$ and sweep over the individual charge distributions. Therefore, letting $\mathbf{R}_\alpha - \mathbf{R}_\beta = \mathbf{R}$ and substituting $\rho_\alpha(\mathbf{r}) \to \rho_\alpha(\mathbf{r}_\alpha)$ and $\rho_\beta(\mathbf{r}') \to \rho_\beta(\mathbf{r}_\beta)$ as can be done without loss of generality, we find that

$$U_{\alpha\beta} = \sum_{n=0}^{\infty} P_n \iint\limits_{\substack{z_\alpha>0,\\ z_\beta\in(-\infty,0)}} \frac{\rho_\alpha(\mathbf{r}_\alpha)\rho_\beta(\mathbf{r}_{\beta-})}{|\mathbf{r}_\alpha - \mathbf{r}_\beta + \mathbf{R} + 2nt\hat{\mathbf{z}}|}\ \mathrm{d}^3\mathbf{r}_\alpha\ \mathrm{d}^3\mathbf{r}_\beta. \tag{A.42}$$

The charge distributions defined with respect to $\mathbf{r}_{\alpha,\beta}$ are assumed to be located at $\mathbf{R}_{\alpha,\beta}$, such that the Dirac deltas in their definitions are centered at zero. The inversion of the

z_β-coordinate in $\rho_\beta(\mathbf{r}_\beta)$ thus only causes a reversal of the z_β-derivatives acting on the Dirac delta in its definition, as $\mathbf{r}_\beta = 0$ and $\mathbf{r}_{\beta-} = 0$ at the same point in space:

$$\rho(\mathbf{r}_{\beta-}) = \mathbf{A}^{(N)} \circ \mathbf{M}^{(N)} : \nabla_{\beta-} \cdots \nabla_{\beta-} \delta(\mathbf{r}_\beta). \tag{A.43}$$

If $\mathbf{M}^{(N)}$ is a single moment, e.g. $\mathbf{D}_z = D_z \hat{\mathbf{z}}$ or $\mathbf{Q}_{xy} = Q_{xy}\hat{\mathbf{x}}\hat{\mathbf{y}}$, then the negative signs preceding the derivatives $\partial/\partial(-z'_\beta) = -\partial/\partial z'_\beta$ can be incorporated into the moments themselves rather than the derivatives. The number of negatives signs moved this way is then equal to $n_z(\mathbf{M})$, the number of indices of $M^{(N)}_{i,j,\cdots}$ that are z.

Moments with incorporated inversion-induced negative signs can be defined as $\bar{\mathbf{M}}^{(N)} = (-1)^{n_z(\mathbf{M})}\mathbf{M}^{(N)}$. The set of moments used to model the corner-localized modes of the nanocube in the main text are $\mathbf{D}_{i=x,y,z}$, $\mathbf{Q}_{xz,yz}$, $\mathbf{Q}_{xy}$, and $\mathbf{O}_{xyz}$, and their inverted forms are

$$\begin{aligned} \bar{\mathbf{D}}_{x,y} &= \mathbf{D}_{x,y}, & \bar{\mathbf{D}}_z &= -\mathbf{D}_z, \\ \bar{\mathbf{Q}}_{xz,yz} &= -\mathbf{Q}_{xz,yz}, & \bar{\mathbf{Q}}_{xy} &= \mathbf{Q}_{xy}, \\ \bar{\mathbf{O}}_{xyz} &= -\mathbf{O}_{xyz}. \end{aligned} \tag{A.44}$$

With Eq. (A.44) as well as Eqs. (A.42) and (A.43), we can now calculate the interaction energies between nanocube's modes as

$$U_{\alpha\beta} = \sum_{n=0}^{\infty} P_n \iint\limits_{\substack{z_\alpha>0,\\ z_\beta\in(-\infty,0)}} \frac{\rho_\alpha(\mathbf{r}_\alpha)\bar{\rho}_\beta(\mathbf{r}_\beta)}{|\mathbf{r}_\alpha - \mathbf{r}_\beta + \mathbf{R} + 2nt\hat{\mathbf{z}}|}\, \mathrm{d}^3\mathbf{r}_\alpha\, \mathrm{d}^3\mathbf{r}_\beta, \tag{A.45}$$

where $\bar{\rho}(\mathbf{r}) = \mathbf{A} \circ \bar{\mathbf{M}} : \nabla \cdots \nabla \delta(\mathbf{r} - \mathbf{r}_0)$. Eq. (A.45) simplifies to an expression identical to Eq. (A.36) but with the appropriate transformations to the moments. Thus, beginning with

the dipole self-interactions, one can conclude that

$$\begin{aligned} U_{D_i,\bar{D}_i} &= \sum_n P_n \left(-3\frac{(\mathbf{D}_i \cdot \hat{\mathbf{z}})(\mathbf{D}_i \cdot \hat{\mathbf{z}})}{(2a+2nt)^3} + \frac{\mathbf{D}_i \cdot \mathbf{D}_i}{(2a+2nt)^3} \right) \\ &= \sum_n P_n \frac{D_i D_i}{(2a+2nt)^3}, \\ U_{D_z,\bar{D}_z} &= \sum_n P_n \left(-3\frac{-(\mathbf{D}_z \cdot \hat{\mathbf{z}})(\mathbf{D}_z \cdot \hat{\mathbf{z}})}{(2a+2nt)^3} + \frac{-\mathbf{D}_z \cdot \mathbf{D}_z}{(2a+2nt)^3} \right) \\ &= \sum_n P_n \frac{2D_z D_z}{(2a+2nt)^3}, \end{aligned} \tag{A.46}$$

where we have let $|R| = 2a$ and $\mathbf{R}/|\mathbf{R}| = \hat{\mathbf{z}}$, assuming the multipole moments exist a distance a above the substrate's surface along the z-axis. Also, $i = x, y$. With the same reasoning, the quadrupole interactions become

$$\begin{aligned} U_{Q_{iz},\bar{Q}_{iz}} &= \sum_n P_n \left(\frac{140}{3}\frac{-(\hat{\mathbf{z}} \cdot \mathbf{Q}_{iz} \cdot \hat{\mathbf{z}})(\hat{\mathbf{z}} \cdot \mathbf{Q}_{iz} \cdot \hat{\mathbf{z}})}{(2a+2nt)^5} - \frac{80}{3}\frac{-(\hat{\mathbf{z}} \cdot \mathbf{Q}_{iz} \cdot \mathbf{Q}_{iz} \cdot \hat{\mathbf{z}})}{(2a+2nt)^5} + \frac{8}{3}\frac{-\mathbf{Q}_{iz} : \mathbf{Q}_{iz}}{(2a+2nt)^5} \right) \\ &= \sum_n P_n \frac{72}{3}\frac{Q_{iz} Q_{iz}}{(2a+2nt)^5}, \end{aligned}$$

$$U_{Q_{xy},\bar{Q}_{xy}} = \sum_n P_n \left(0 + 0 + \frac{8}{3}\frac{\mathbf{Q}_{xy} : \mathbf{Q}_{xy}}{(2a+2nt)^5} \right) = \sum_n P_n \frac{8}{3}\frac{Q_{xy} Q_{xy}}{(2a+2nt)^5} \tag{A.47}$$

and the octupole self-interaction energy is

$$\begin{aligned} U_{O_{xyz},\bar{O}_{xyz}} &= \sum_n P_n \left(0 + 0 - \frac{1512}{5}\frac{-(\hat{\mathbf{z}} \cdot \mathbf{O}_{xyz} : \mathbf{O}_{xyz} \cdot \hat{\mathbf{z}})}{(2a+2nt)^7} + \frac{72}{5}\frac{-\mathbf{O}_{xyz} : \mathbf{O}_{xyz}}{(2a+2nt)^7} \right) \\ &= \sum_n P_n \frac{288 O_{xyz} O_{xyz}}{(2a+2nt)^7}. \end{aligned} \tag{A.48}$$

Moving to the cross-interactions, one can see from Eq. (A.38) that each is zero by

symmetry except for three. These are

$$\begin{aligned} U_{Q_{iz},\bar{D}_i} &= \sum_n P_n \left(10\frac{(\hat{\mathbf{z}}\cdot\mathbf{Q}_{iz}\cdot\hat{\mathbf{z}})(\hat{\mathbf{z}}\cdot\mathbf{D}_i)}{(2a+2nt)^4} - 4\frac{\hat{\mathbf{z}}\cdot\mathbf{Q}_{iz}\cdot\mathbf{D}_i}{(2a+2nt)^4} \right) \\ &= -\sum_n P_n \frac{4Q_{iz}D_i}{(2a+2nt)^4}, \\ U_{O_{xyz},\bar{Q}_{xy}} &= \sum_n P_n \left(-252\frac{\hat{\mathbf{z}}\cdot(\hat{\mathbf{z}}\cdot\mathbf{O}_{xyz}\cdot\hat{\mathbf{z}})(\hat{\mathbf{z}}\cdot\mathbf{Q}_{xy}\cdot\hat{\mathbf{z}})}{(2a+2nt)^6} + 168\frac{(\hat{\mathbf{z}}\cdot\mathbf{O}_{xyz}\cdot\hat{\mathbf{z}})\cdot\mathbf{Q}_{xy}\cdot\hat{\mathbf{z}}}{(2a+2nt)^6} \right. \\ &\qquad \left. -24\frac{\hat{\mathbf{z}}\cdot\mathbf{O}_{xyz}:\mathbf{Q}_{xy}}{(2a+2nt)^6} \right) \\ &= -\sum_n P_n 24\frac{O_{xyz}Q_{xy}}{(2a+2nt)^6}. \end{aligned} \tag{A.49}$$

Therefore, if we assign coordinates q to our multipoles such that $q_i = D_i/e$, $q_{ij} = Q_{ij}/ea$, and $q_{ijk} = O_{ijk}/ea^2$ and also define their conjugate momenta p_i, p_{ij}, and p_{ijk}, we can write down the Hamiltonian of the system. Assuming each multipole plasmon acts in free space as a frictionless oscillator, we find that

$$\begin{aligned} H = &\sum_{i=x,y,z}\left(\frac{p_i^2}{2m_i}+\frac{1}{2}m_i\omega_i^2q_i^2\right)+\sum_{j=x,y}\left(\frac{p_{jz}^2}{2m_{jz}}+\frac{1}{2}m_{jz}\omega_{jz}^2q_{jz}^2\right)+\frac{2p_{xy}^2}{2m_{xy}}+\frac{1}{2}m_{xy}\omega_{xy}^2q_{xy}^2 \\ &+\frac{2p_{xyz}^2}{2m_{xyz}}+\frac{1}{2}m_{xyz}\omega_{xyz}^2q_{xyz}^2+\sum_{i=x,y}\sum_n P_n\frac{e^2q_i^2}{(a2+2nt)^3}+\sum_n P_n\frac{2e^2q_z^2}{(2a+2nt)^3} \\ &+\sum_{j=x,y}\sum_n P_n\frac{72}{3}\frac{e^2a^2q_{jz}^2}{a^2(2a+2nt)^5}+\sum_n P_n\frac{8}{3}\frac{e^2a^2q_{xy}^2}{(2a+2nt)^5}+\sum_n P_n\frac{288e^2a^4q_{xyz}^2}{(2a+2nt)^7} \\ &-\sum_{i=x,y}\sum_n P_n\frac{4e^2aq_iq_{iz}}{(2a+2nt)^4}+\sum_n P_n\frac{24e^2a^3q_{xy}q_{xyz}}{(2a+2nt)^6}. \end{aligned} \tag{A.50}$$

Here, the masses of the dipole, quadrupole, and octupole modes are m_i, m_{ij}, and m_{ijk}, while their resonance frequencies are ω_i, ω_{ij}, and ω_{ijk}. To simplify the expression, one can define the self- and cross-coupling strengths f and g of Eqs. (2.8) and (2.9) (note that, in the main

text, $\epsilon_1 \to \epsilon_b$) such that

$$\begin{aligned} H = &\sum_{i=x,y,z} \left(\frac{p_i^2}{2m_i} + \frac{1}{2} m_i (\omega_i^2 - f_i) q_i^2 \right) + \sum_{j=x,y} \left(\frac{p_{jz}^2}{2m_{jz}} + \frac{1}{2} m_{jz} (\omega_{jz}^2 - f_{jz}) q_{jz}^2 \right) \\ &+ \frac{2p_{xy}^2}{2m_{xy}} + \frac{1}{2} m_{xy} (\omega_{xy}^2 - f_{xy}) q_{xy}^2 + \frac{2p_{xyz}^2}{2m_{xyz}} + \frac{1}{2} m_{xyz} (\omega_{xyz}^2 - f_{xyz}) q_{xyz}^2 \\ &+ \sum_{i=x,y} g_i \sqrt{m_i m_{iz}} q_i q_{iz} + \sqrt{m_{xy} m_{xyz}} q_{xy} q_{xyz}. \end{aligned} \tag{A.51}$$

Thus, it's clear that the coupling between the modes of the cube is bilinear. Standard diagonalization techniques produce the resonance frequencies of Eq. (2.3) that are plotted in Fig. 2.5, wherein the coordinate symbols of this Appendix have been exchanged for D_i, Q_{ij}, and O_{ijk}.

Appendix B

SUPPLEMENTARY INFORMATION — CONTINUOUS WAVE RESONANT PHOTON STIMULATED ELECTRON ENERGY-GAIN AND ELECTRON ENERGY-LOSS SPECTROSCOPY OF INDIVIDUAL PLASMONIC NANOPARTICLES

B.1 Derivation of the Interaction Potential

To model the interactions of an electron beam with a set of radiative dipole plasmons under continuous-wave laser excitation, it is convenient to discuss the dynamics of the plasmons and fast electron in second-quantization as one does with the dynamics of the photon field. Letting $\hat{H}_0 = \hat{H}_{0,ph} + \hat{H}_{0,pl} + \hat{H}_{0,el}$ be the unperturbed part of the Hamiltonian as a sum of the photon, plasmon, and electron free-space Hamiltonians, respectively, the transition to a completely second-quantized picture can be performed as

$$\begin{aligned}\hat{H}_0 &= \sum_{\alpha} \hbar\omega_\alpha \hat{a}_\alpha^\dagger \hat{a}_\alpha + \sum_{\lambda} \left(\frac{\hat{p}_\lambda^2}{2m_\lambda} + \frac{1}{2} m_\lambda \Omega_\lambda^2 \hat{q}_\lambda^2 \right) + \frac{\hat{p}_e^2}{2m_e} \\ &\rightarrow \sum_{\alpha} \hbar\omega_\alpha \hat{a}_\alpha^\dagger \hat{a}_\alpha + \sum_{\lambda} \hbar\Omega_\lambda \hat{b}_\lambda^\dagger \hat{b}_\lambda + \sum_{k} \hbar\omega_k \hat{c}_k^\dagger \hat{c}_k\end{aligned} \tag{B.1}$$

with the coordinates q and momenta p of each plasmon mode $\lambda = x, y, z$ replaced by lowering and raising operators $\hat{b}_\lambda \equiv \hat{b}(0)\exp(-\mathrm{i}\Omega_\lambda t)$ and $\hat{b}_\lambda^\dagger$ within the rotating wave approximation. Explicitly, the transformation is given by $\hat{q}_\lambda \rightarrow \sqrt{\hbar/2m_\lambda\omega_\lambda}(\hat{b}_\lambda + \hat{b}_\lambda^\dagger)$ and $\hat{p}_\lambda \rightarrow -\mathrm{i}\sqrt{\hbar m_\lambda \omega_\lambda/2}(\hat{b}_\lambda - \hat{b}_\lambda^\dagger)$ followed by the approximation $\omega_\lambda \rightarrow \Omega_\lambda$. Here $\hbar\omega_\alpha$ is the energy of the α^{th} mode of the photon field with annihilation operator $\hat{a}_\alpha \equiv \hat{a}(0)\exp(-\mathrm{i}\omega_\alpha t)$. Also, $\Omega_\lambda = \omega_\lambda - \mathrm{i}\gamma_\lambda(\omega)$ is the complex natural frequency of each plasmon mode such that $\gamma_\lambda(\omega) = \gamma_D + 2e^2\omega^2/3m_\lambda c^3$, γ_D is the Drude damping rate of the plasmon, and m_λ is the corresponding plasmon mass. In both lines of Eq. B.1, the state of the photon field is given

by $|\{N\}\rangle = |\{...,N_\alpha,N_{\alpha'},...\}\rangle$ with N_α the occupation number of the α^{th} photon mode, while the plasmon states are given by $|M_\lambda\rangle$ with $\hat{q}_\lambda |M_\lambda\rangle = \phi_{\lambda,M}(q_\lambda)$ the wavefunction of the M^{th} eigenstate of the λ-oriented term of the plasmon Hamiltonian.

The electron Hamiltonian $\hat{H}_{0,el} = \hat{p}_e^2/2m_e$ is described here with the assumption that the electron is a one-dimensional free particle with motion restricted to the z-direction and a delta-function charge density in the xy-plane, i.e. that the wavefunction of an electron with momentum $\hbar k$ is $\psi_k(\mathbf{r}) = \exp(ikz)\phi_k(\mathbf{R})/\sqrt{2\pi}$, with $\phi_{k'}^\dagger(\mathbf{R})\phi_k(\mathbf{R}) \approx \delta(\mathbf{R}-\mathbf{R}_0)$, $\mathbf{R}$ the cylindrical radial vector, and $\mathbf{R}_0 = R_{0x}\mathbf{e}_x + R_{0y}\mathbf{e}_y$ the impact parameter of the electron. Here $\mathbf{e}_{\{x,y\}}$ is the unit vector along the x- or y-direction. Thus, with $\langle\mathbf{r}'|\,\hat{p}^2\,|\mathbf{r}\rangle = -\hbar^2\delta(\mathbf{r}-\mathbf{r}')\partial^2/\partial z^2$, $\hat{H}_{0,el}$ can be transformed via projection onto real space and the basis of states $\phi_k(\mathbf{r})$ as

$$\begin{aligned}
\hat{H}_{0,el} &= \frac{1}{2m_e}\iiiint |k'\rangle\,\langle k'|\mathbf{r}'\rangle\,\langle\mathbf{r}'|\hat{p}_e^2|\mathbf{r}\rangle\,\langle\mathbf{r}|k\rangle\,\langle k|\;\mathrm{d}^3\mathbf{r}'\,\mathrm{d}^3\mathbf{r}\,\mathrm{d}k'\,\mathrm{d}k \\
&= \iiint \frac{\hbar^2k^2}{2m_e}\frac{e^{\mathrm{i}(k-k')z}}{2\pi}\phi_{k'}^\dagger(\mathbf{R})\phi_k(\mathbf{R})\,|k'\rangle\langle k|\;\mathrm{d}^3\mathbf{r}\,\mathrm{d}k\,\mathrm{d}k' \\
&= \int \frac{\hbar^2k^2}{2m_e}\frac{1}{2\pi}\,|k\rangle\langle k|\;\mathrm{d}k \\
&\to \sum_k \hbar\omega_k\hat{c}_k^\dagger\hat{c}_k,
\end{aligned} \tag{B.2}$$

where in the last line the continuous free-particle states are replaced with the discrete states of a one-dimensional box of length L such that $\langle\mathbf{r}|k\rangle/\sqrt{2\pi} = \phi_k(\mathbf{r})/\sqrt{2\pi} \to \langle\mathbf{r}|k\rangle_{\text{box}} = \exp(\mathrm{i}kz)\phi_{k,x}(x)\phi_{k,y}(y)/\sqrt{L}$ and the integration over k is replaced with a sum. Further, the operator transformation $|k\rangle\langle k|_{\text{box}} \to \hat{c}_k^\dagger\hat{c}_k$ replaces the projection operator with a number operator with $\hat{c}_k = \hat{c}_k(0)\exp(-\mathrm{i}\omega_k t)$ and $\omega_k = \hbar^2k/2m_e$. This, along with the transformation of the free particle states $|k\rangle \to |\{...,0,1_k,0,...\}\rangle$ completes the second quantization shown in Eq. B.1.

To calculate the stimulated electron energy-gain (sEEG) and energy-loss (sEEL) functions of the silver nanorod, the interaction Hamiltonian $\hat{H}_{int}$ must be similarly quantized. Letting

the longitudinal dipole plasmon of the nanorod be oriented along the x-direction and be the only mode to interact with the photon field, the interactions between the nanorod plasmon modes and external sources are described by

$$\begin{aligned}\hat{H}_{int} &= \hat{H}_{ph-pl} + \hat{H}_{el-pl} \\ &= -\sum_{\lambda} \hat{\mathbf{d}}_{\lambda} \cdot \hat{\mathbf{E}}_{ph} - \sum_{\lambda} \hat{\mathbf{d}}_{\lambda} \cdot \hat{\mathbf{E}}_{el},\end{aligned} \tag{B.3}$$

with $\hat{\mathbf{d}}_{\lambda} = e\hat{q}_{\lambda}\mathbf{e}_{\lambda}$ the plasmon's electric dipole operator. The transformation to second-quantization is then straightforward for this operator, given by $\hat{\mathbf{d}}_{\lambda} \rightarrow d_{\lambda}(\hat{b}_{\lambda} + \hat{b}_{\lambda}^{\dagger})\mathbf{e}_{\lambda}$, with $d_{\lambda} = e\sqrt{\hbar/2m_{\lambda}\omega_{\lambda}}$. The photon field operator can be found from standard sources (see Ref. [320]) and is given by

$$\hat{\mathbf{E}}_{ph} = \sum_{\alpha} -\mathrm{i}\sqrt{\frac{2\pi\hbar\omega_{\alpha}}{V}}(\hat{a}_{\alpha} - \hat{a}_{\alpha}^{\dagger})\boldsymbol{\epsilon}_{\alpha} \tag{B.4}$$

with $\boldsymbol{\epsilon}_{\alpha}$ the polarization unit vector of the α^{th} mode and V the quantization volume of the box-quantized photons. The electron field operator can be acquired from the STEM electron's evanescent field

$$\tilde{\mathbf{E}}_{el}(\mathbf{r},\omega) = \frac{2e|\omega|}{v^2\gamma^2}\left[\mathrm{i}\frac{\omega}{|\omega|}K_0\left(\frac{|\omega|R}{v\gamma}\right)\mathbf{e}_z - \gamma K_1\left(\frac{|\omega|R}{v\gamma}\right)\frac{\mathbf{R}}{R}\right]e^{\mathrm{i}\omega z/v}, \tag{B.5}$$

via projection onto the electron states $|k\rangle$ as is done in Eq. B.2 and Ref. [166]. Explicitly,

$$\begin{aligned}\hat{\mathbf{E}}_{\mathrm{el}} &= \iiiint |k'\rangle\langle k'|\mathbf{r}'\rangle\ \langle\mathbf{r}'|\hat{\tilde{\mathbf{E}}}_{el}(\omega)|\mathbf{r}\rangle\langle\mathbf{r}|k\rangle\langle k|\frac{e^{\mathrm{i}\omega t}}{2\pi}\,\mathrm{d}\omega\,\mathrm{d}^3\mathbf{r}'\,\mathrm{d}^3\mathbf{r}\,\mathrm{d}k'\,\mathrm{d}k \\ &= \iiint e^{\mathrm{i}\omega t}\delta(\omega - v[k'-k])\frac{2e|\omega|}{v\gamma^2 L}\left[\mathrm{i}\frac{\omega}{|\omega|}K_0\left(\frac{|\omega|R_0}{v\gamma}\right)\mathbf{e}_z - \gamma K_1\left(\frac{|\omega|R_0}{v\gamma}\right)\frac{\mathbf{R_0}}{R_0}\right] \\ &\qquad\qquad \times |k'\rangle\langle k|\frac{\mathrm{d}\omega}{2\pi}\,\mathrm{d}k'\,\mathrm{d}k \\ &\rightarrow \sum_{k,k'}\frac{2e|k'-k|}{\gamma^2 L}\left[\mathrm{i}\frac{k'-k}{|k'-k|}K_0\left(\frac{|k'-k|R_0}{\gamma}\right)\mathbf{e}_z - \gamma K_1\left(\frac{|k'-k|R_0}{\gamma}\right)\frac{\mathbf{R_0}}{R_0}\right]\hat{c}_{k'}^{\dagger}\hat{c}_k,\end{aligned} \tag{B.6}$$

with v the electron's velocity, $\gamma = \sqrt{1/(1-v^2/c^2)}$ the associated Lorentz contraction factor, and $\mathbf{R} = R\mathbf{e}_R$ the cylindrical radial vector. Finally, the interaction Hamiltonian can be defined in the rotating wave approximation using Eqs. B.4 and B.6 as

$$\hat{H}_{int} = \sum_{\alpha,\lambda} g_{\alpha\lambda}(\hat{a}_{\alpha}\hat{b}_{\lambda}^{\dagger} - \hat{a}_{\alpha}^{\dagger}\hat{b}_{\lambda}) + \sum_{k,k',\lambda}(g_{k'k\lambda}\hat{c}_{k'}^{\dagger}\hat{c}_k\hat{b}_{\lambda} + g_{k'k\lambda}^{*}\hat{c}_k^{\dagger}\hat{c}_{k'}\hat{b}_{\lambda}^{\dagger}) \tag{B.7}$$

in which the coupling strengths are defined as

$$g_{\alpha\lambda} = -\mathrm{i}d_\lambda\sqrt{\frac{2\pi\hbar\omega_\alpha}{V}}(\mathbf{e}_\lambda\cdot\boldsymbol{\epsilon}_\alpha),$$
$$g_{k'k\lambda} = \frac{2ed_\lambda|k'-k|}{\gamma^2 L}\left[\mathrm{i}\frac{k'-k}{|k'-k|}K_0\left(\frac{|k'-k|R_0}{\gamma}\right)(\mathbf{e}_\lambda\cdot\mathbf{e}_z)+\frac{\gamma(\mathbf{e}_\lambda\cdot\mathbf{R}_0)}{R_0}K_1\left(\frac{|k'-k|R_0}{\gamma}\right)\right]. \tag{B.8}$$

B.2 Characterization of the Interaction Processes

In sEEL and sEEG experiments, the longitudinal dipole plasmon is assumed to have come into steady-state with the exciting laser source before interaction with the STEM electron. The two transverse plasmons are assumed to remain in the ground state, as they are not appreciably driven by the laser. Therefore, in the calculation of the sEEL and sEEG observables, the initial plasmon state is taken to be $|\{M_x, M_y, M_z\}\rangle$, with $M_x \geq 0$ and $M_y = M_z = 0$. Further, the initial state of the photon field is $|\{..., N_\alpha, N_{\alpha'}, ...\}\rangle = |\{N\}\rangle$, in which it is assumed $N_\alpha = 0$ for all states with polarization not aligned along x. Last, the initial state of the STEM electron is $|\{..., 0, 1_{k_i}, 0, ...\}\rangle = |k_i\rangle$. Thus, the initial state of the system is given by the tensor product of the three states, $|i\rangle = |k_i, \{N\}, \{M_x, 0_y, 0_z\}\rangle$, assuming that the brief, weak nature of the interactions given by $\hat{H}_{int}$ allow the eigenstates of $\hat{H}_0$ to be approximate simultaneous eigenstates of $\hat{H} = \hat{H}_0 + \hat{H}_{int}$.

In the following calculations of the observable signals of a laser-stimulated electron beam spectroscopy experiment, it is assumed in the following that all interactions are sufficiently weak that only single-quantum energy exchange occurs between two objects during interactions. Therefore, all third-order and higher processes are neglected, and Fermi's golden rule may be employed at both first- and second-order to calculate the relevant transition rates to a final state $|f\rangle$.

At first order, the transition rates of processes driven by the electron beam are given by

$$w = \frac{2\pi}{\hbar} \sum_{\lambda} \left| \langle f | \hat{H}_{el-pl} | i \rangle \right|^2 \delta(E_f - E_i) \tag{B.9}$$

where the sum over plasmons λ gives the total EEL rate for anisotropic particles such as a nanorod and generalizes the results of Refs. [166, 321]. Because first-order interactions that only involve $\hat{H}_{ph-pl}$ are not measurable by the electron beam, they will be ignored in the following analysis.

At second order, the general form of the transition rate

$$w = \frac{2\pi}{\hbar} \left| \sum_{m} \frac{\langle f | \hat{H}_{el-pl} | m \rangle \langle m | \hat{H}_{ph-pl} | i \rangle}{E_i - E_m} + \sum_{m'} \frac{\langle f | \hat{H}_{ph-pl} | m' \rangle \langle m' | \hat{H}_{el-pl} | i \rangle}{E_i - E_{m'}} \right|^2 \delta(E_f - E_i) \tag{B.10}$$

allows one to infer which processes among the more complicated landscape of second-order transitions lead to measurable signals in the electron beam. Here, $|m\rangle$ and $|m'\rangle$ are intermediate states and E_i, E_m, and E_f are the energies of the initial, intermediate, and final states, respectively. Because each interaction Hamiltonian describes the transfer of a single quantum of energy to or away from the plasmon mode, it is clear upon careful examination of Eq. B.10 that only four classes of final states can be devised such that $w \neq 0$.

These four states describe processes in which the plasmon modes of the nanorod 1) absorb a photon from the photon field and a virtual photon from the STEM electron, 2) absorb a photon from the photon field and transfer a virtual photon to the electron, 3) emit a photon to the photon field and absorb a virtual photon from the electron, and 4) emit a photon to the photon field and transfer a virtual photon to the electron. These four processes are hereby referred to simultaneous plasmon excitation (SPE), stimulated electron energy-gain (sEEG), stimulated electron-induced radiation emission (sEIRE), and simultaneous plasmon deëxcitation (SPD), respectively. The corresponding final states are $|f_{\mathrm{SPE}}\rangle = |k_f, \{..., N_\alpha - 1, ...\}, \{M_x + 2, 0_y, 0_z\}\rangle$,

$|f_{\mathrm{sEEG}}\rangle = |k_f, \{..., N_\alpha - 1, ...\}, \{M_x, 0_y, 0_z\}\rangle$, $|f_{\mathrm{sEIRE}}\rangle = |k_f, \{..., N_\alpha + 1, ...\}, \{M_x, 0_y, 0_z\}\rangle$, and $|f_{\mathrm{SPD}}\rangle = |k_f, \{..., N_\alpha + 1, ...\}, \{M_x - 2, 0_y, 0_z\}\rangle$, wherein $k_f < k_i$ for SPE and sEIRE and $k_f > k_i$ for SPD and sEEG.

B.3 Calculation of the SPE and SPD Transition Rates

Because SPE is the direct stimulated analog of the well-known EEL process and SPD provides a hitherto undiscussed contribution to the electron energy-gain signal, the contributions of both to observable spectra in laser-stimulated electron spectroscopy are of great interest. First inserting $|f_{\mathrm{SPE}}\rangle$ into Eq. B.10, one finds that

$$w^{(2)}_{\mathrm{SPE}} = \frac{2\pi}{\hbar}\left|\sum_{m,\lambda}\sum_{k,k',\alpha}\frac{\langle f_{\mathrm{SPE}}|\, g_{k'k\lambda}\hat{c}^\dagger_{k'}\hat{c}_k\hat{b}_\lambda + g^*_{k'k\lambda}\hat{c}^\dagger_k\hat{c}_{k'}\hat{b}^\dagger_\lambda\,|m\rangle\,\langle m|\, g_{\alpha\lambda}(\hat{b}^\dagger_\lambda\hat{a}_\alpha - \hat{b}_\lambda\hat{a}^\dagger_\alpha)\,|i\rangle}{E_i - E_m}\right.$$
$$\left. + \sum_{m',\lambda}\sum_{k,k',\alpha}\frac{\langle f_{\mathrm{SPE}}|\, g_{\alpha\lambda}(\hat{b}^\dagger_\lambda\hat{a}_\alpha - \hat{b}_\lambda\hat{a}^\dagger_\alpha)\,|m'\rangle\,\langle m'|\, g_{k'k\lambda}\hat{c}^\dagger_{k'}\hat{c}_k\hat{b}_\lambda + g^*_{k'k\lambda}\hat{c}^\dagger_k\hat{c}_{k'}\hat{b}^\dagger_\lambda\,|i\rangle}{E_i - E_{m'}}\right|^2 \delta(E_f - E_i). \tag{B.11}$$

As alluded to in the previous section, only two intermediate terms, $|m\rangle = |k_i, \{..., N_\alpha - 1, ...\}, \{M_x + 1, 0_y, 0_z\}\rangle$ and $|m'\rangle = |k_f, \{N\}, \{M_x + 1, 0_y, 0_z\}\rangle$, contribute nonzero matrix elements to $w^{(2)}_{\mathrm{SPE}}$. Therefore, to simplify Eq. B.11, the energy differences $E_i - E_m$, $E_i - E_{m'}$, and $E_f - E_i$ must be defined. The nonrecoil approximation used to define the electron-plasmon operator in Eqs. B.6—B.7 is appropriate when the electron transfer momentum $\hbar q = \hbar k_i - \hbar k_f$ is much smaller than the initial electron momentum $\hbar k_i$ such that contributions of order q^2 to the electron energy can be ignored [166]. In other words,

$$\frac{\hbar^2 k_f^2}{2m_e} - \frac{\hbar^2 k_i^2}{2m_e} \approx -\hbar\omega_q, \tag{B.12}$$

where $\omega_q = vq$ is the transfer frequency and $\hbar k_i \approx m_e v$. The relevant energy differences in Eq. B.11 are then

$$\begin{aligned} E_i - E_m &= \sum_\beta N_\beta \hbar\omega_\beta + \frac{\hbar^2 k_i^2}{2m_e} + M_x \hbar\Omega_x^2 \\ &\quad - \sum_{\beta\neq\alpha} N_\beta \hbar\omega_\beta - (N_\alpha - 1)\hbar\omega_\alpha - \frac{\hbar^2 k_i^2}{2m_e} - (M_x + 1)\hbar\Omega_x \\ &= \hbar\omega_\alpha - \hbar\Omega_x, \end{aligned} \tag{B.13}$$

as well as $E_i - E_{m'} = \hbar\omega_q - \hbar\Omega_x$ and $E_f - E_i = 2\hbar\Omega_x - \hbar\omega_\alpha - \hbar\omega_q$, such that the expression for $w^{(2)}_{\mathrm{SPE}}$ simplifies to

$$\begin{aligned} w^{(2)}_{\mathrm{SPE}} = \frac{2\pi}{\hbar}|g_{k_f k_i x}|^2 |g_{\alpha x}|^2 (M_x + 1)(M_x + 2) N_\alpha \left| \frac{2\hbar\Omega_x - \hbar\omega_\alpha - \hbar\omega_q}{(\hbar\Omega_x - \hbar\omega_\alpha)(\hbar\Omega_x - \hbar\omega_q)} \right|^2 \\ \times \delta(2\hbar\Omega_x - \hbar\omega_\alpha - \hbar\omega_q). \end{aligned} \tag{B.14}$$

Eq. B.14 immediately gives $w^{(2)}_{\mathrm{SPE}} = 0$, by the property of the Dirac delta $f(z)g(z)\delta[g(z)] = 0$, with f and g here two general and well-behaved functions on the complex plane. Similarly, $w^{(2)}_{\mathrm{SPD}} = 0$, as can be seen by a substitution of $|f_{\mathrm{SPD}}\rangle$ into Eqs. B.10 - B.14. This produces the transition rate

$$\begin{aligned} w^{(2)}_{\mathrm{SPD}} = \frac{2\pi}{\hbar}|g_{k_f k_i x}|^2 |g_{\alpha x}|^2 M_x (M_x - 1)(N_\alpha + 1) \left| \frac{-2\hbar\Omega_x + \hbar\omega_\alpha - \hbar\omega_q}{(-\hbar\Omega_x + \hbar\omega_\alpha)(-\hbar\Omega_x - \hbar\omega_q)} \right|^2 \\ \times \delta(-2\hbar\Omega_x + \hbar\omega_\alpha - \hbar\omega_q), \end{aligned} \tag{B.15}$$

that is zero by the same property of the Dirac delta. Because both SPE and SPD cannot contribute to the observable spectrum in an stimulated STEM spectroscopy experiment, the observable signal must be generated entirely by sEEG, sEIRE, and EEL.

B.4 Calculation of the sEEG Function

The observable function of sEEG, $\Gamma_{\text{sEEG}}(\omega)$ can be calculated by substitution of $|f_{\text{sEEG}}\rangle$ into Eqs. B.9 and B.10. Beginning with the second-order transition rate, this produces

$$w^{(2)}_{\text{sEEG}} = \frac{2\pi}{\hbar}\left|\sum_{m,\lambda}\sum_{k,k',\alpha}\frac{\langle f_{\text{sEEG}}|\, g_{k'k\lambda}\hat{c}^\dagger_{k'}\hat{c}_k\hat{b}_\lambda + g^*_{k'k\lambda}\hat{c}^\dagger_k\hat{c}_{k'}\hat{b}^\dagger_\lambda\,|m\rangle\,\langle m|\, g_{\alpha\lambda}(\hat{b}^\dagger_\lambda\hat{a}_\alpha - \hat{b}_\lambda\hat{a}^\dagger_\alpha)\,|i\rangle}{E_i - E_m}\right.$$
$$\left. + \sum_{m',\lambda}\sum_{k,k',\alpha}\frac{\langle f_{\text{sEEG}}|\, g_{\alpha\lambda}(\hat{b}^\dagger_\lambda\hat{a}_\alpha - \hat{b}_\lambda\hat{a}^\dagger_\alpha)\,|m'\rangle\,\langle m'|\, g_{k'k\lambda}\hat{c}^\dagger_{k'}\hat{c}_k\hat{b}_\lambda + g^*_{k'k\lambda}\hat{c}^\dagger_k\hat{c}_{k'}\hat{b}^\dagger_\lambda\,|i\rangle}{E_i - E_{m'}}\right|^2 \tag{B.16}$$
$$\times\,\delta(E_f - E_i).$$

The two surviving terms can be evaluated and simplified to give

$$w^{(2)}_{\text{sEEG}} = \frac{2\pi}{\hbar}|g_{\alpha x}|^2|g_{k_f k_i x}|^2 N_\alpha(N_{k_f}+1)\left|\frac{M_x+1}{\hbar\Omega_x - \hbar\omega_\alpha} + \frac{M_x}{-\hbar\omega_q - \hbar\Omega_x}\right|^2\delta(-\hbar\omega_q - \hbar\omega_\alpha), \tag{B.17}$$

where $N_{k_f}+1 = 1$ is the occupation number of the final electron state. Notably, because $q > 0$, the transfer frequency ω_q as defined by Eq. B.12 is a negative quantity and the trailing Driac delta of Eq. B.17 does *not* assign the photon energy $\hbar\omega_\alpha$ a negative value.

The transition probability $\mathcal{P}^{(2)}_{\text{sEEG}}$ can be calculated simply from the rate $w^{(2)}_{\text{sEEG}}$ by integration over the entire period of interaction between the plasmon and STEM electron. As the electron travels along a box of length L at a constant speed v, the integration is very simple:

$$\mathcal{P}^{(2)}_{\text{sEEG}} = \int w^{(2)}_{\text{sEEG}}\,\mathrm{d}t = \frac{L}{v}w^{(2)}_{\text{sEEG}}. \tag{B.18}$$

The second-order sEEG function is defined as the sum of the second-order transition probabilities to all possible final states, weighted by the electron detector density of states, $\delta(\hbar\omega - \hbar\omega_q)$. Explicitly, this produces

$$\Gamma^{(2)}_{\text{sEEG}}(\omega) = \sum_{k_f}\sum_{\boldsymbol{\epsilon}_\alpha,\mathbf{k}_\alpha}\frac{L}{v}\frac{2\pi}{\hbar^3}|g_{\alpha x}|^2|g_{k_f k_i x}|^2 N_\alpha\left|\frac{M_x+1}{\hbar\Omega_x - \hbar\omega_\alpha} - \frac{M_x}{\hbar\Omega_x + \hbar\omega_q}\right|^2$$
$$\times\,\delta(-\omega_q - \omega_\alpha)\delta(\omega - \omega_q), \tag{B.19}$$

in which the sum over final photon states α has been replaced with explicit sums over the polarization $\boldsymbol{\epsilon}_\alpha$ and wavevector $\mathbf{k}_\alpha$ of each state. In the small particle limit, all radiation of wavelengths of interest propagates approximately radially, such that the two independent polarization vectors become $\boldsymbol{\epsilon}_\alpha = \mathbf{e}_\theta, \mathbf{e}_\phi$. Given that the only factor in the RHS of Eq. B.19 that depends on $\boldsymbol{\epsilon}_\alpha$ is the coupling coefficient $g_{\alpha x}$, the sum over the polarizations contributes a factor

$$\sum_{\boldsymbol{\epsilon}_\alpha = \mathbf{e}_\theta, \mathbf{e}_\phi} |g_{\alpha x}|^2 = d_x^2 \frac{2\pi\hbar\omega_\alpha}{V}(\cos^2\theta\cos^2\phi + \sin^2\phi) \tag{B.20}$$

to $\Gamma^{(2)}_{\mathrm{sEEG}}(\omega)$, where the identities $\mathbf{e}_x \cdot \mathbf{e}_\theta = \cos\theta\cos\phi$ and $\mathbf{e}_x \cdot \mathbf{e}_\phi = -\sin\phi$ have been employed.

Further, in order to move out of box-quantization, the sums of discrete momentum states are converted to integrals over continuous states. Letting N_{k_f} be the occupation number of the one-dimensional box-quantized electron state of wavenumber k_f, it is clear that $N_{k_f} = 0$ and that Eq. B.19 contains an implicit factor of $N_{k_f} + 1$. Therefore, the sum over k_f is converted simply as $\sum_{k_f}(N_{k_f}+1) \to \int [n_{\mathrm{el}}(k_f)+1]\rho_{\mathrm{el}}(k_f)\ \mathrm{d}k_f = \int \rho_{\mathrm{el}}(k_f)\ \mathrm{d}k_f$. Here, $n_{\mathrm{el}}(k_f) = 0$ is the continuous distribution of occupied final electron states and $\rho_{\mathrm{el}}(k_f)$ is the number of states per unit wavenumber. For the three-dimensional photon states, the density of states is only well-defined as number of states per unit wavenumber *per unit solid angle* Ω such that $\sum_{\mathbf{k}_\alpha} N_{\mathbf{k}_\alpha} \to \iint n_{\mathrm{ph}}(k_\alpha, \theta_\alpha, \phi_\alpha)\rho_{\mathrm{ph}}(k_\alpha, \theta_\alpha, \phi_\alpha)\ \mathrm{d}\Omega_\alpha\ \mathrm{d}k_\alpha$, with n_{el} and ρ_{el} defined as the occupation distribution and density of states of the photon field.

Indexing states with frequencies rather than wavenumbers, the density of photon states becomes $\rho_{\mathrm{ph}}(\omega_\alpha, \theta, \phi) = V\omega_\alpha^2/(2\pi c)^3$. As the sum over final electron states is equivalent to a sum over transfer momenta q, the (one-dimensional) density of electron states becomes $\rho_{\mathrm{el}}(\omega_\alpha) = (L/2\pi)\mathrm{d}q/\mathrm{d}\omega_q = L/2\pi v$. Therefore, the sums of Eq. B.19 can be rewritten in the

continuous ($V \to \infty$) limit as

$$\begin{aligned} \sum_{k_f} &\to \int \frac{L}{2\pi v}\, \mathrm{d}\omega_q, \\ \sum_{\mathbf{k}_\alpha} N_\alpha &\to \iiint n_{\mathrm{ph}}(\omega_\alpha, \theta, \phi) \frac{V\omega_\alpha^2}{(2\pi c)^3} \sin\theta\, \mathrm{d}\theta\, \mathrm{d}\phi\, \mathrm{d}\omega_\alpha, \end{aligned} \tag{B.21}$$

where $\{\theta_\alpha, \phi_\alpha\} \to \{\theta, \phi\}$ for simplicity. Expanding the coupling coefficients $g_{\alpha x}$ and $g_{k_f k_i x}$, one finds that

$$\begin{aligned} \Gamma^{(2)}_{\mathrm{sEEG}}(\omega) = \iiiint 2\pi\hbar\omega_\alpha d_x^4 \frac{4e^2\omega_q^2}{\hbar^3 v^4 \gamma^4} \left[\frac{\gamma^2 R_{0x}^2}{R_0^2} K_1^2\left(\frac{|\omega_q| R_0}{v\gamma}\right)\right] (\cos^2\phi \cos^2\theta + \sin^2\phi) \\ \times n_{\mathrm{ph}}(\omega_\alpha, \theta, \phi) \frac{\omega_\alpha^2}{(2\pi c)^3} \left| \frac{M_x + 1}{\hbar\Omega_x - \hbar\omega_\alpha} - \frac{M_x}{\hbar\Omega_x + \hbar\omega_q} \right|^2 \delta(-\omega_q - \omega_\alpha)\delta(\omega - \omega_q) \\ \times \sin\theta\, \mathrm{d}\theta\, \mathrm{d}\phi\, \mathrm{d}\omega_q\, \mathrm{d}\omega_\alpha. \end{aligned} \tag{B.22}$$

In Eq. B.22, ω is a negative quantity, fixed to the negative ω_q (see Eq. B.12) by a Dirac delta. Allowing the polarizability of the x-oriented plasmon to be $\alpha_x(\omega) = d_x^2/(\hbar\Omega_x - \hbar\omega)$ such that $\mathrm{Im}\{\alpha_x(\omega)\} = \hbar\gamma_x(\omega) d_x^2/|\hbar\Omega_x - \hbar\omega|^2$, it is then convenient to define the negative-frequency polarizability $\alpha_x^{(-)}(\omega) = d_x^2/(\hbar\Omega_x + \hbar\omega)$ with a resonance at $-\omega_x$ such that $\mathrm{Im}\{\alpha_x^{(-)}(\omega)\} = \hbar\gamma_x(\omega) d_x^2/|\hbar\Omega_x + \hbar\omega|^2$. Using the definition of the EEL function given by Ref. [166], Eq. B.22 simplifies to

$$\Gamma^{(2)}_{\mathrm{sEEG}}(\omega) = \frac{\omega^3}{4\pi c^3} \frac{d_x^2}{\hbar\gamma_x(\omega)} \Gamma^{(-)}_{\mathrm{EELx}}(\omega) \iint n_{\mathrm{ph}}(-\omega, \theta, \phi)(\cos^2\theta\cos^2\phi + \sin^2\phi)\sin\theta\, \mathrm{d}\theta\, \mathrm{d}\phi, \tag{B.23}$$

with

$$\Gamma^{(-)}_{\mathrm{EELx}}(\omega) = \frac{4e^2\omega^2}{\pi\hbar^2 v^4\gamma^4} \left[\frac{\gamma^2 R_{0x}^2}{R_0^2} K_1^2\left(\frac{|\omega| R_0}{v\gamma}\right)\right] \mathrm{Im}\{\alpha_x^{(-)}(\omega)\} \tag{B.24}$$

the EEL function of only the x-oriented plasmon mode with the resonance shifted to $-\omega_x$. If the laser is assumed to only populate states that propagate in the y-direction and that are polarized along x, the photon occupation number density is therefore

$$n_{\mathrm{ph}}(\omega, \theta, \phi) = A(\omega)\delta(\theta - \pi/2)\delta(\phi - \pi/2), \tag{B.25}$$

with $A(\omega)$ a unitless amplitude profile determined by the dynamics of the laser cavity and the geometry and material of the optical elements in the experiment. Additionally, Ref. [166]

gives the extinction cross-section of the plasmon as $\sigma_x(\omega) = (4\pi\omega/c)\mathrm{Im}\{\alpha_x(\omega)\}$ such that $\sigma_x(\omega_x) = (4\pi\omega_x/c)d_x^2/\hbar\gamma_x(\omega)$. With this, substitution of the photon occupation distribution (Eq. B.25) into the second-order sEEG function definition (Eq. B.23) produces

$$\Gamma^{(2)}_{\mathrm{sEEG}}(\omega) = \frac{1}{(4\pi)^2}\frac{\omega^3}{c^2\omega_x}\sigma_x(\omega_x)\Gamma^{(-)}_{\mathrm{EELx}}(\omega)A(-\omega). \tag{B.26}$$

With the definition of the field-field correlation function in Ref. [322], the total intensity of the laser field can be defined with the unit conventions of Ref. [323] as

$$\begin{aligned} I &= \frac{c}{V}\sum_{\alpha} N_\alpha \hbar\omega_\alpha \delta(\omega-\omega_\alpha) \\ &\rightarrow \iiint c\hbar\omega\, n(\omega,\theta,\phi)\rho(\omega,\theta,\phi)\sin\theta\ \mathrm{d}\theta\ \mathrm{d}\phi\ \mathrm{d}\omega \\ &= \int \frac{\hbar\omega^3}{8\pi^3c^2}A(\omega)\ \mathrm{d}\omega. \end{aligned} \tag{B.27}$$

The integrand of Eq. B.27 can then be defined as the intensity *density* $\mathcal{I}(\omega) = (\hbar\omega^3/8\pi^3c^2)A(\omega)$ to define the amplitude profile $A(\omega)$ in a simple manner as $A(\omega) = (8\pi^3c^2/\hbar\omega^3)\mathcal{I}(\omega)$. Therefore, $\mathcal{I}(-\omega) = -(\hbar\omega^3/8\pi^3c^2)A(-\omega)$ and the second-order sEEG function simplifies to

$$\Gamma^{(2)}_{\mathrm{sEEG}}(\omega) = \frac{\pi}{2}\frac{1}{\hbar\omega_x}\sigma_x(\omega_x)\mathcal{I}(-\omega)\Gamma^{(-)}_{\mathrm{EELx}}(\omega). \tag{B.28}$$

The first order sEEG function $\Gamma^{(1)}_{\mathrm{sEEG}}(\omega)$ can be similarly calculated. Starting from Eq. B.9, the first order transition rate $w^{(1)}_{\mathrm{sEEG}}$ becomes

$$w^{(1)}_{\mathrm{sEEG}} = \frac{2\pi}{\hbar}M_x|g_{k_fk_ix}|^2\delta(\hbar\Omega_x+\hbar\omega_q). \tag{B.29}$$

For narrow plasmon linewidths, one can approximate the delta function as $\delta(\hbar\Omega_x+\hbar\omega_q) \approx (1/\pi)\mathrm{Im}\{1/(\hbar\Omega_x+\hbar\omega_q)\}$. Further, since the broadened plasmon is formally a continuous distribution of states, the occupation number must be generalized to account for the fact that only those states of the distribution that are coresonant with the laser are excited when the electron arrives. Thus, one must let $M_x \rightarrow M_x(\omega) = M_x^{\max}\bar{A}(\omega)$, where maximum plasmon occupation number $M_x^{\max}$ lies at the frequency where the normalized laser amplitude

$\bar{A}(\omega)$ is equal to one. In this paper, $M_x^{\max}$ is inferred from experimental spectra. Calculation of the first-order sEEG function then delivers, via integration over the final electron states,

$$\begin{aligned}\Gamma_{\mathrm{sEEG}}^{(1)}(\omega) &= M_x(-\omega)\frac{4e^2\omega^2}{\pi\hbar^2 v^4\gamma^4}\left[\frac{\gamma^2 R_{0x}^2}{R_0^2}K_1^2\left(\frac{|\omega|R_0}{v\gamma}\right)\right]\mathrm{Im}\{\alpha_x^{(-)}\}(\omega)\\ &= M_x(-\omega)\Gamma_{\mathrm{EELx}}^{(-)}(\omega).\end{aligned} \tag{B.30}$$

The total probability per unit energy of the electron to lose energy to the laser-excited plasmon is then

$$\Gamma_{\mathrm{sEEG}}(\omega) = \Gamma_{\mathrm{sEEG}}^{(1)}(\omega) + \Gamma_{\mathrm{sEEG}}^{(2)}(\omega). \tag{B.31}$$

Finally, the initial state can be allowed to vary in order to calculate a measurable function $\langle\Gamma_{\mathrm{sEEG}}(\omega)\rangle$. Assuming the initial population of plasmon and photon states remains constant in every sEEG event conducted in an sEEGS experiment, the initial electron state can be varied around its average energy to model the zero-loss peak (ZLP) lineshape of the electron gun. Because for very high electron energies ($q \ll k_i$) $\Gamma_{\mathrm{sEEG}}(\omega)$ changes imperceptibly upon small changes in k_i aside from a uniform shift along the frequency axis, the ZLP can be included by convolving $\Gamma_{\mathrm{sEEG}}(\omega)$ with the ZLP lineshape $Z(\omega)$. In other words,

$$\langle\Gamma_{\mathrm{sEEG}}(\omega)\rangle = \int \Gamma_{\mathrm{sEEG}}(\omega')Z(\omega-\omega')\,\mathrm{d}\omega'. \tag{B.32}$$

As a check for consistency with the literature, the definition for $\Gamma_{\mathrm{sEEG}}(\omega)$ as seen in Ref. [166] can be acquired from its definition in Eq. B.22 by 1) using the weighted density of states of an ideal laser $n_{\mathrm{ph}}(\omega,\theta,\phi)\rho_{\mathrm{ph}}(\omega,\theta,\phi) \to D_{\mathrm{laser}}(\omega)$ that populates only a single mode (wavevector and polarization) of the photon field and 2) letting $g_{\alpha x} \to -\mathrm{i}d_x\sqrt{2\pi\hbar\omega_{\mathrm{laser}}/V}$ be the associated coupling coefficient with ω_{laser} the mode frequency and $\boldsymbol{\epsilon}_\alpha \to \mathbf{e}_x$ the mode polarization. Explicitly, these three substitutions can be performed on Eq. B.22 by letting $2\pi\hbar\omega_\alpha \to 2\pi\hbar\omega_{\mathrm{laser}}$, $(\cos^2\theta\cos^2\phi + \sin^2\phi) \to 1$, and $n_{\mathrm{ph}}(\omega_\alpha,\theta,\phi)\omega_\alpha^2/(2\pi c)^3 \to N_{\mathrm{laser}}\delta(\omega-\omega_{\mathrm{laser}})\delta(\theta-\pi/2)\delta(\phi-\pi/2)$, with N_{laser} the population of the single laser mode. Further using the definition of the intensity of a single-mode laser $I_{\mathrm{laser}} = c\hbar\omega_{\mathrm{laser}}N_{\mathrm{laser}}/V$, assuming $M_x(\omega) = 0$, and letting $-\omega \to \omega$ and $\alpha^{(-)}(\omega) \to \alpha(\omega)$ as appropriate to match

sign conventions, one arrives at

$$\Gamma_{\mathrm{sEEG}}(\omega) \rightarrow I_{\mathrm{laser}} \frac{8\pi e^2 \omega^2}{\hbar^3 v^4 c \gamma^4} \left[\frac{\gamma^2 R_{0x}^2}{R_0^2} K_1^2 \left(\frac{|\omega| R}{v\gamma} \right) \right] |\alpha_x(\omega)|^2 \delta(\omega - \omega_{\mathrm{laser}}), \tag{B.33}$$

precisely the result provided in Ref. [166]. Note that, contrary to the approach given in this paper, the definition of Eq. B.33 is defined with $\omega > 0$. A slight relaxation of this approach for a laser of narrow linewidth ($\gamma_{\mathrm{laser}} \ll \gamma_x$) but finite intensity with a Lorentzian profile can be performed by letting $\mathcal{I}(-\omega) \rightarrow I_{\mathrm{laser}} \gamma_{\mathrm{laser}} / \pi((-\omega - \omega_{\mathrm{laser}})^2 + \gamma_{\mathrm{laser}}^2)$ in Eq. B.28 and $M_x(\omega) \rightarrow M_x^{\max} \gamma_{\mathrm{laser}}^2 / ((\omega - \omega_{\mathrm{laser}})^2 + \gamma_{\mathrm{laser}}^2)$ in Eq. B.30, producing

$$\boxed{\Gamma_{\mathrm{sEEG}}(\omega) \approx M_x(-\omega) \Gamma_{\mathrm{EELx}}^{(-)}(-\omega_{\mathrm{laser}}) + \frac{\sigma_x(\omega_x) I_{\mathrm{laser}}}{2\hbar\omega_x} \frac{\gamma_{\mathrm{laser}}}{((-\omega - \omega_{\mathrm{laser}})^2 + \gamma_{\mathrm{laser}}^2)} \Gamma_{\mathrm{EELx}}^{(-)}(-\omega_{\mathrm{laser}}).} \tag{B.34}$$

The observable sEEG signal can then be approximated by a convolution with the ZLP as is plotted in Fig. 4 of the manuscript, detailing the influence of the laser intensity on the sEEG signal.

B.5 Calculation of the sEIRE Function

The sEIRE function can be calculated in a similar manner to the calculation of the electron energy-gain function. Beginning with Fermi's golden rule (Eq. B.10) and using the final state $|f_{\mathrm{sEIRE}}\rangle$, the transition rate $w_{\mathrm{sEIRE}}^{(2)}$ reduces to

$$\begin{aligned} w_{\mathrm{sEIRE}}^{(2)} = \frac{2\pi}{\hbar}(N_\alpha + 1) \Bigg| & \left(g_{\alpha x} g_{k_f k_i x}^* \frac{M_x + 1}{\hbar\Omega_x - \hbar\omega_q} - g_{\alpha x} g_{k_f k_i x} \frac{M_x}{\hbar\Omega_x - \hbar\omega_\alpha} \right) \\ & - g_{\alpha y} g_{k_f k_i y} \frac{1}{\hbar\Omega_y - \hbar\omega_q} - g_{\alpha z} g_{k_f k_i z} \frac{1}{\hbar\Omega_z - \hbar\omega_q} \Bigg|^2 \delta(\hbar\omega_\alpha - \hbar\omega_q) \delta(\hbar\omega_a - \hbar\omega_q), \end{aligned} \tag{B.35}$$

with $q > 0$ and thus $\omega_q = vq > 0$ (see Eq. B.12). Thus, all three plasmon modes of the nanorod contribute to the sEIRE signal. To further simplify Eq. B.35, one can recognize that the spectral overlap between the longitudinal and transverse plasmon modes of the nanorod is small, and thus terms that are proportional to $1/(\hbar\Omega_x - \hbar\omega_{\{q,\alpha\}})(\hbar\Omega_y - \hbar\omega_q)$ or $1/(\hbar\Omega_x - \hbar\omega_{\{q,\alpha\}})(\hbar\Omega_z - \hbar\omega_q)$ can be neglected. Further approximating $\Omega_y \approx \Omega_z$ for

a nanorod with a circular cross-section and noting that $g^*_{\alpha\lambda} = -g_{\alpha\lambda}$, $g^*_{k_f k_i y} = g_{k_f k_i y}$, and $g^*_{k_f k_i z} = -g_{k_f k_i z}$, Eq. B.35 becomes

$$\begin{aligned} w^{(2)}_{\text{sEIRE}} \approx \frac{2\pi}{\hbar}(N_\alpha + 1)\Bigg(& |g_{\alpha x}|^2 |g_{k_f k_i x}|^2 \left| \frac{M_x + 1}{\hbar\Omega_x - \hbar\omega_q} - \frac{M_x}{\hbar\Omega_x - \hbar\omega_\alpha} \right|^2 \\ & + |g_{\alpha y}|^2 |g_{k_f k_y}|^2 \frac{1}{|\hbar\Omega_y - \hbar\omega_q|^2} + |g_{\alpha z}|^2 |g_{k_f k_z}|^2 \frac{1}{|\hbar\Omega_z - \hbar\omega_q|^2} \Bigg), \end{aligned} \tag{B.36}$$

with all cross-terms eliminated. The sEIRE function can then be broken into three parts, each calculated in a similar manner to the procedure given by Eqs. B.17 - B.19. Letting the first term of Eq. B.36 be referred to as the x-oriented plasmon sEIRE rate $w^{(2)}_{\text{sEIREx}}$, the corresponding sEIRE function is

$$\begin{aligned} \Gamma^{(2)}_{\text{sEIREx}}(\omega) = \sum_{k_f} \sum_{\boldsymbol{\epsilon}_\alpha, \mathbf{k}_\alpha} \frac{L}{v} \frac{2\pi}{\hbar^2} (N_\alpha + 1) |g_{\alpha x}|^2 |g_{k_f k_i x}|^2 \left| \frac{M_x + 1}{\hbar\Omega_x - \hbar\omega_q} - \frac{M_x}{\hbar\Omega_x - \hbar\omega_\alpha} \right|^2 \\ \times \delta(\hbar\omega_\alpha - \hbar\omega_q)\delta(\omega - \omega_q). \end{aligned} \tag{B.37}$$

As is shown in Eqs. B.20–B.28, the sums can be taken as integrals over the proper densities of states and the resulting expression simplified algebraically to give an intuitive result. Due to the factor $N_\alpha + 1$, the integration of $\Gamma^{(2)}_{\text{sEIREx}}(\omega)$ can be done in two pieces, one detailing the contribution from spontaneous EIRE and the other scaling with the intensity of the laser. Letting

$$\begin{aligned} \sum_{\mathbf{k}_\alpha} (N_\alpha + 1) &\to \iiint [n_{\text{ph}}(\omega_\alpha, \theta, \phi) + 1] \frac{V\omega_\alpha^2}{(2\pi c)^3} \sin\theta \, \mathrm{d}\theta \, \mathrm{d}\phi \, \mathrm{d}\omega_\alpha \\ &= \iiint [A(\omega_\alpha)\delta(\theta - \pi/2)\delta(\phi - \pi/2) + 1] \frac{V\omega_\alpha^2}{(2\pi c)^3} \sin\theta \, \mathrm{d}\theta \, \mathrm{d}\phi \, \mathrm{d}\omega_\alpha, \end{aligned} \tag{B.38}$$

as well as $\sum_{k_f} \to \int (L/2\pi v) \, \mathrm{d}\omega_q$, the sEIRE function becomes

$$\begin{aligned} \Gamma^{(2)}_{\text{sEIREx}}(\omega) = \iiint & 2\pi\hbar\omega_\alpha d_x^4 \frac{4e^2\omega_q^2}{\hbar^3 v^4 \gamma^4} \frac{\gamma^2 R_{0x}^2}{R_0^2} K_1^2 \left(\frac{|\omega_q| R}{v\gamma} \right) (\cos^2\phi \cos^2\theta + \sin^2\phi) \\ & \times \left[A(\omega_\alpha)\delta\left(\theta - \frac{\pi}{2}\right)\delta\left(\phi - \frac{\pi}{2}\right) + 1 \right] \frac{\omega_\alpha^2}{(2\pi c)^3} \left| \frac{M_x + 1}{\hbar\Omega_x - \hbar\omega_q} - \frac{M_x}{\hbar\Omega_x - \hbar\omega_\alpha} \right|^2 \\ & \times \delta(\omega_\alpha - \omega_q)\delta(\omega - \omega_q) \sin\theta \, \mathrm{d}\theta \, \mathrm{d}\phi \, \mathrm{d}\omega_q \, \mathrm{d}\omega_\alpha. \end{aligned} \tag{B.39}$$

Simple evaluation of the integrals and rearrangement delivers

$$\begin{aligned}\Gamma^{(2)}_{\mathrm{sEIREx}}(\omega) &= \frac{8e^2\omega^5}{3\pi\hbar^2 v^4\gamma^4 c^3}\frac{\gamma^2 R_{0x}^2}{R_0^2}K_1^2\left(\frac{|\omega|R}{v\gamma}\right)|\alpha_x(\omega)|^2 + \frac{1}{(4\pi)^2}\frac{\omega^3}{c^2\omega_x}\Gamma_{\mathrm{EELx}}(\omega)\sigma_x(\omega_x)A(\omega)\\ &= \Gamma^{(2)}_{\mathrm{EIREx}}(\omega) + \frac{\pi}{2}\frac{1}{\hbar\omega_x}\sigma_x(\omega_x)\mathcal{I}(\omega)\Gamma_{\mathrm{EELx}}(\omega),\end{aligned} \tag{B.40}$$

in which all quantities are to be evaluated at positive frequencies, in contrast with the final result in Eq. B.28. The implicit definition in Eq. B.40 of $\Gamma^{(2)}_{\mathrm{EIREx}}(\omega)$, the spontaneous EIRE function from the x-oriented plasmon, is consistent with the definition given in Ref. [166]. A similar treatment applied to the two remaining terms of Eq. B.36 results in

$$\begin{aligned}\Gamma^{(2)}_{\mathrm{EIREy}}(\omega) &= \frac{8e^2\omega^5}{3\pi\hbar^2 v^4\gamma^4 c^3}\frac{\gamma^2 R_{0y}^2}{R_0^2}K_1^2\left(\frac{|\omega|R}{v\gamma}\right)|\alpha_y(\omega)|^2,\\ \Gamma^{(2)}_{\mathrm{EIREz}}(\omega) &= \frac{8e^2\omega^5}{3\pi\hbar^2 v^4\gamma^4 c^3}K_0^2\left(\frac{|\omega|R}{v\gamma}\right)|\alpha_z(\omega)|^2,\end{aligned} \tag{B.41}$$

in which neither term depends on the laser power and so both contribute to the spontaneous EIRE signal from the nanorod. Finally, the sEIRE function is

$$\boxed{\Gamma^{(2)}_{\mathrm{sEIRE}}(\omega) \approx \Gamma^{(2)}_{\mathrm{EIRE}}(\omega) + \frac{\pi}{2}\frac{1}{\hbar\omega_x}\sigma_x(\omega_x)\mathcal{I}(\omega)\Gamma_{\mathrm{EELx}}(\omega),} \tag{B.42}$$

with $\Gamma^{(2)}_{\mathrm{EIRE}} = \Gamma^{(2)}_{\mathrm{EIREx}} + \Gamma^{(2)}_{\mathrm{EIREy}} + \Gamma^{(2)}_{\mathrm{EIREz}}$.

Using an approximation similar to that of Eq. B.34, $\Gamma^{(2)}_{\mathrm{sEIRE}}(\omega)$ can be simplified when the laser linewidth is narrow. One can approximate the occupation density term in Eq. B.39 as

$$[A(\omega_\alpha)+1]\frac{\omega_\alpha^2}{(2\pi c)^3} \to \frac{1}{c\hbar\omega_\alpha}\left[I_{\mathrm{laser}} + \frac{I_{\mathrm{laser}}}{N}\right]\frac{1}{\pi}\frac{\gamma_{\mathrm{laser}}}{(\omega_\alpha-\omega_{\mathrm{laser}})^2+\gamma_{\mathrm{laser}}^2}, \tag{B.43}$$

integrate as normal, then let $\Gamma_{\mathrm{EELx}}(\omega) \to \Gamma_{\mathrm{EELx}}(\omega_{\mathrm{laser}})$ to find

$$\boxed{\Gamma^{(2)}_{\mathrm{sEIRE}}(\omega) \approx \frac{\sigma_x(\omega_{\mathrm{laser}})I_{\mathrm{laser}}}{2\hbar\omega_x}\frac{N+1}{N}\frac{\gamma_{\mathrm{laser}}}{(\omega-\omega_{\mathrm{laser}})^2+\gamma_{\mathrm{laser}}^2}\Gamma_{\mathrm{EEL}}(\omega_{\mathrm{laser}}).} \tag{B.44}$$

The transformation given by Eq. B.43 is consistent with the transformation used to simplify the sEEG function. Expanding $n_{\rm ph}(\omega_\alpha)$ in Eq. B.22 and letting $A(\omega)\omega_\alpha^2/(2\pi c)^3 \to (I_{\rm laser}/c\hbar\omega_\alpha)\gamma_{\rm laser}/((\omega-\omega_{\rm laser})^2+\gamma_{\rm laser}^2)$, one is returned precisely Eq. B.34.

B.6 Calculation of the sEEL Function

The measurable signal in a sEEL experiment will include contributions from processes of all orders in $\hat{H}_{int}$ in which the STEM electron loses energy. The processes that contribute are then both sEIRE, first-order sEEL, and EEL, with EEL including contributions from all three plasmons. As these processes have different final photon states, they do not interfere and their functions may be added directly. Beginning with the total EEL rate as defined in Eq. B.9, one finds after simplification that

$$\begin{aligned} w_{\rm EEL}+w_{\rm sEEL}^{(1)} = \frac{2\pi}{\hbar}\big[(M_x+1)|g_{k_fk_ix}|^2\delta(\hbar\Omega_x-\hbar\omega_q)+|g_{k_fk_iy}|^2\delta(\hbar\Omega_y-\hbar\omega_q) \\ +|g_{k_fk_iz}|^2\delta(\hbar\Omega_z-\hbar\omega_q)\big], \end{aligned} \tag{B.45}$$

wherein the first-order sEEL rate has been defined as $\omega_{\rm sEEL}^{(1)} = (2\pi/\hbar)M_x|g_{k_fk_ix}|^2\delta(\hbar\Omega_x-\hbar\omega)$. With the approximation that $\delta(\hbar\Omega_\lambda-\hbar\omega_q)\approx(1/\pi){\rm Im}\{1/(\hbar\Omega_\lambda-\hbar\omega_q)\}$ and the generalization $M_x\to M_x(\omega)$, one finds that the contributions from EEL and first-order sEEL to the total sEEL function are

$$\begin{aligned} \Gamma_{\rm EEL}(\omega)+\Gamma_{\rm sEEL}^{(1)}(\omega) &= \frac{4e^2\omega^2}{\pi\hbar^2v^4\gamma^4}\left[(M_x+1)\frac{\gamma^2R_{0x}^2}{R_0^2}K_1^2\left(\frac{|\omega|R_0}{v\gamma}\right){\rm Im}\{\alpha_x(\omega)\}\right. \\ &\quad \left.+\frac{\gamma^2R_{0y}^2}{R_0^2}K_1^2\left(\frac{|\omega|R_0}{v\gamma}\right){\rm Im}\{\alpha_y(\omega)\}+K_0^2\left(\frac{|\omega|R_0}{v\gamma}\right){\rm Im}\{\alpha_z(\omega)\}\right] \\ &= \Gamma_{\rm EEL}(\omega)+M_x(\omega)\Gamma_{\rm EELx}(\omega). \end{aligned} \tag{B.46}$$

Here, $\Gamma_{\rm EELy}(\omega) = (4e^2\omega^2/\pi\hbar^2v^4\gamma^4)(\gamma^2R_{0y}^2/R_0^2)K_1^2(|\omega|R_0/v\gamma){\rm Im}\{\alpha_y(\omega)\}$ and $\Gamma_{\rm EELz}(\omega) = (4e^2\omega^2/\pi\hbar^2v^4\gamma^4)K_0^2(|\omega|R_0/v\gamma){\rm Im}\{\alpha_z(\omega)\}$ are the EEL functions of the transverse plasmons such that $\Gamma_{\rm EEL}(\omega)=\sum_\lambda\Gamma_{{\rm EEL}\lambda}$, to be compared with Refs. [166, 321]. The sEEL function

can then be constructed as $\Gamma_{\mathrm{sEEL}}(\omega) = \Gamma_{\mathrm{EEL}}(\omega) + \Gamma^{(1)}_{\mathrm{sEEL}}(\omega) + \Gamma^{(2)}_{\mathrm{sEIRE}}(\omega)$ to give

$$\boxed{\Gamma_{\mathrm{sEEL}}(\omega) \approx \Gamma_{\mathrm{EEL}}(\omega) + \Gamma^{(2)}_{\mathrm{sEIRE}}(\omega) + \left(M_x(\omega) + \frac{\pi}{2}\frac{1}{\hbar\omega_x}\sigma_x(\omega_x)\mathcal{I}(\omega) \right) \Gamma_{\mathrm{EELx}}(\omega).} \tag{B.47}$$

Here, it should be noted that the EIRE function is dropped from the expressions displayed in the main text, as it is $\sim 1/100$ the magnitude of the EEL functions and is thus negligible. However, EIRE is retained here for completeness. Note also that Eq. B.47 reduces immediately to $\Gamma_{\mathrm{EEL}}(\omega)$ in the limit of zero laser power. It can also be simplified in the narrow-laser limit as

$$\boxed{\begin{aligned}\Gamma_{\mathrm{sEEL}}(\omega) \approx{}& \Gamma_{\mathrm{EEL}}(\omega) + M_x(\omega)\Gamma_{\mathrm{EELx}}(\omega) \\ &+ \left(\frac{\sigma_x(\omega_x) I_{\mathrm{laser}}}{2\hbar\omega_x} \frac{N+1}{N} \frac{\gamma_{\mathrm{laser}}}{(\omega - \omega_{\mathrm{laser}})^2 + \gamma^2_{\mathrm{laser}}} \right) \Gamma_{\mathrm{EELx}}(\omega_{\mathrm{laser}}),\end{aligned}} \tag{B.48}$$

the ZLP-convolved version of which is plotted in Fig. 4 of the main text.

Appendix C

SUPPLEMENTARY INFORMATION — ELECTRON BEAM INFRARED NANO-ELLIPSOMETRY OF INDIVIDUAL INDIUM TIN OXIDE NANOCRYSTALS

C.1 Analysis of Cubic Nanoparticle Structures

The EEL probabilities of a series of cuboid nanoparticles are numerically calculated in order to estimate the impact of the cuboid geometries of the synthesized nanocrystals on their spectra. The lack of symmetry of the cuboids prevents the analytical derivation of their individual mode responses such that numerical calculations must suffice.

Fig. C.1 shows that the primary consequence of the conversion of a spherical nanoparticle to a cubic one with large corner radii is the change of the appearance of the surface plasmon peak when the beam is placed near the particle's surface. In particular, the many independent surface plasmon modes contained within the peak become spectrally rearranged and see their polarizabilities rise and fall such that the surface plasmon peak loses its unimodal appearance and grows a shoulder. The bulk plasmon peak is virtually unchanged throughout the evolution.

The consequence of measuring a cuboid in experiment and assuming its response to be that of a sphere is to overestimate the values of ε_∞, ω_p, and γ in the Drude dielectric model extracted from the experiment. To see this, one can first consider the penetrating cuboid spectrum: the surface plasmon feature is quite similar in cuboid and sphere spectra, except that the peak energies of the surface and bulk plasmon features are less separated.

Because the distance between the two peaks increases with decreasing ε_∞ (explicitly, $\Delta\Omega \approx \omega_p/\sqrt{\varepsilon_\infty} - \omega_p\sqrt{3/[3\varepsilon_\infty + 4]}$), the value of ε_∞ is inferred to have an overlarge value when the cuboid is analytically assumed to be a sphere. Consequently, the value of ω_p is

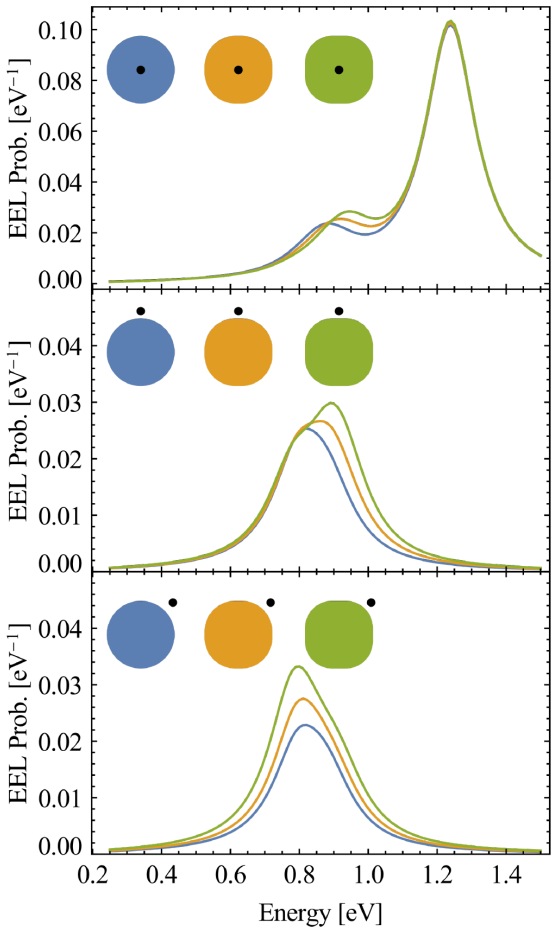

Figure C.1: The EEL probability of cuboid nanoparticles with face-to-face widths $d = 20$ nm and composed of a Drude model metal with parameters equal to the extracted 10% Sn4+ ITO parameter averages displayed in the main text. The corner radii of the cuboids are $R = d/2$ (blue), $d/2.2$ (gold), and $d/2.5$ (green). The $R = d/2$ cuboid is a sphere. Each cuboid is depicted in the three panels from above along the z-axis, with the upper and lower faces of each cuboid assumed to lie parallel to the xy-plane. The trajectory of the STEM electron lies along the z-axis and is depicted by the black dots in each panel. The three panels show one penetrating (top) and two aloof (middle,bottom) beam trajectories.

also overestimated in order to maintain the constant peak energy of the bulk feature at $\approx \omega_p/\sqrt{\varepsilon_\infty}$.The value of the damping rate γ is overestimated in aloof-beam experiments, due to the gradual splitting of the surface plasmon modes and subsequent broadening of the surface plasmon feature. The damping rate is faithfully recovered in penetrating-beam spectra as

the surface plasmon feature maintains its shape, but since both aloof and penetrating spectra contribute to the extracted average value of γ, the overall effect is to overestimate it.

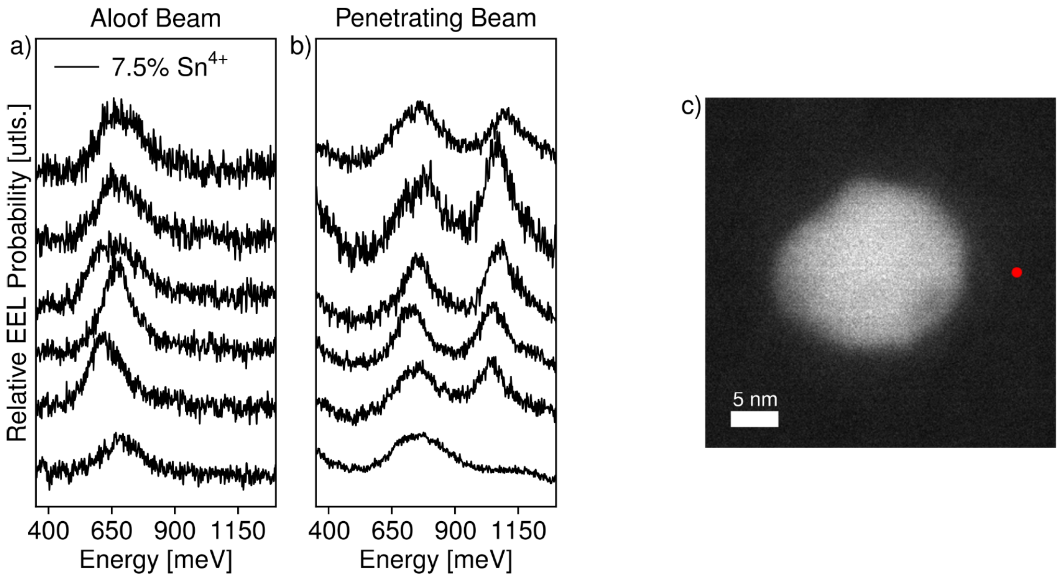

Figure C.2: The aloof (a) and penetrating (b) EELS spectra for each ITO 7.5% sample measured in this study. These plots highlight the variation in peak energy and linewidth for individual particles of the same dopant concentration, which contribute to linewidth broadening and peak energy maxima differences in ensemble measurements.

However, the surface spectra also provide the clearest evidence that the measured spectra are very similar to those of spheres. Even for cuboids of corner radii as large as $d/2.2$, Fig. C.1, middle panel clearly shows that the surface plasmon feature becomes markedly non-Lorentzian when the aloof beam is passed near the particle's face at the midpoint between the its corners. The spectra of cuboids of smaller corner radii show surface features that are even more obviously multimodal. Such surface features are absent from the analyzed experimental data, of which a sample is shown in Fig. C.2a. In each spectrum, the beam is passed across the particle's face away from any corners or protrusions (see Fig C.2c), such that one would expect to see significant deformations of the surface plasmon feature were the particle to support cuboid surface plasmon modes.

For these reasons, we estimate that the nanoparticles under investigation in this work behave like cuboids with corner radii greater than or equal to $d/2.2$, such that the effects of the corners on the plasmon spectra are minimal. We estimate that the dielectric parameters ω_p, γ, and ε_∞ are only slightly, if at all, overestimated and are within 10% of their true values.

C.2 Heuristic Model of the Background Signal of the EEL Probability

To fit the loss probability $\Gamma(\omega)$ of Eq. (C.43) to the EEL spectra collected from experiment, the background signal must be eliminated. In the EELS low-loss energy region (< 5 eV) LSPs can overlap with losses due to Cherenkov radiation, transition radiation, inter- and intraband transitions, bulk plasmons, phonon-polaritons, and other radiative features. The position and intensity of these features will vary due to sample heterogeneity, but when studying LSPs they are considered background and therefore subject to removal. Additionally, the intense elastic scattering of the ZLP and its tail arise from a statistical process and can further obscure low-loss EELS data [120, 220, 235]. As one might expect, the wide variety of background media in different EELS experiments leads to a corresponding variety of characteristic background signals and subtraction methods. Numerous model-based methods have been explored, including the use of power-law, reflected-tail, Gaussian, combined Gaussian and Lorentzian, Fourier and log-Fourier deconvolution, and polynomial models, as well as combinations of the above.

In order to approximate the background signal as accurately as possible, we utilized the undoped In_2O_3 NCs as a non-plasmonic "blank" to develop the model used herein. To do this, five EEL spectra from undoped In_2O_3 nanocrystals were collected with the beam passing both along the nanocrystal axis and 5 nm outside of its surface. The background signal was dominated by the uppermost portion of the zero loss peak (ZLP) of the electron beam below 0.3 eV and included, depending on the beam trajectory and target dopant concentration, up to two Lorentzian-like features at ~ 0.4 eV and ~ 0.8 eV. In general, the lower-energy resonance was most prominent in penetrating-beam experiments. These spectra are used to

determine a characteristic range of the fitting parameters of the model

$$\Gamma^{\text{back}}(\omega) = C + \sum_{i=1}^{3} A_i \mathrm{e}^{-p_i \omega} + \sum_{j=1}^{2} \frac{B_i}{(\omega - \omega_j)^2 + \gamma_j^2}. \tag{C.1}$$

This model was then numerically fit to the doped ITO samples, with the fitting parameter ranges used to determine the fitting constraints.

C.3 Analysis of Nonlinear Dielectric Effects and Beam Deflection Upon the Measured EEL Probability

In this work we take the transverse detection of the fast electron probe by the target to be negligible. This approximation, known as the non-recoil approximation, is known to describe the EEL signal of plasmons and other low-loss responses well when the dielectric material under investigation shows weak dependence on carrier crystal momentum and the electron detector's acceptance angle is small.

In the limit where the dielectric material of the target is strictly local, i.e., has no dependence on the momentum of the carriers contained within, the detection of a STEM electron is suffciently weak that the induced change in its velocity perpendicular to the direction of propagation is $\sim$ 10 nm/s [324]. This behavior is similar for dielectric and metallic particles. With the axial velocity of a 60 keV electron being $0.45c$, the STEM electrons in this investigation are detected at angles $\sim 10^{-18}$ rad, imperceptible to the detector which has an acceptance angle of 20 mrad and can be safely set to zero in the theoretical model.

The broadening of plasmonic responses due to nonlocal effects is unimportant when examining isolated particles larger than $\sim$ 15 nm, especially those with low carrier densities. As is shown in work done by Ref. [109], nonlocal effects can significantly contribute to the plasmonic responses of coupled gold particles of this size, but do not matter much when the particles are well-isolated. Further, as can be devised from a simple hydrodynamic model of metals [325], the nonlocal response of a metal nanoparticle decreases with increasing carrier mass and decreasing carrier concentration. As compared to gold, ITO has heavier and fewer carriers. Thus, the polarization of an ITO nanoparticle is expected to have an even smaller

dependence on nonlocal dielectric behaviors.

We do, however, concede that these effects are not nonexistent within ITO nanoparticles. Especially as the particles decrease in size and surface-scattering effects become exaggerated [326], the nonlocal response of carriers can significantly affect their plasmon spectra. These effects represent a very interesting avenue for investigation, but they can be safely neglected when modeling plasmonic spectra of isolated ~ 20 nm ITO nanoparticles. As such, they lie outside the scope of this first investigation into the feasibility of nanoellipsometry.

C.4 Derivation of the EEL Probability

The dielectric model of electron energy-loss spectroscopy (EELS) begins with an electron of charge $-e$ that travels along the $-z$-direction with a speed v at a lateral distance b from the z-axis. It begins moving at a time $t \to -\infty$ and location $z \to \infty$ such that its charge distribution at a time t is

$$\rho(\mathbf{r}, t) = -\frac{e}{s}\delta(s - b)\delta(\phi - 0)\delta(z + vt), \tag{C.2}$$

with $s = \sqrt{x^2 + y^2}$ the cylindrical radial coordinate and e the elementary charge. The azimuthal angle of the trajectory has been chosen to be 0 for simplicity, although any angle would adequately describe the system. As this electron travels toward, through, and away from a nanosphere of radius a and dielectric function $\epsilon(\omega)$ that lies centered at the origin in an otherwise isotropic universe of dielectric constant $\epsilon_b = 1$, it interacts with the electric field $\mathbf{E}_{\text{res}}(\mathbf{r}, t)$ that scatters from the nanosphere. The power transfered to the moving electron from this scattered field is given by the Lorentz force as

$$P(t) = \int \mathbf{J}(\mathbf{r}, t) \cdot \mathbf{E}_{\text{res}}(\mathbf{r}, t)\ \mathrm{d}^3\mathbf{r}, \tag{C.3}$$

wherein $\mathbf{J}$ is the electron's current and is defined via the continuity equation as

$$\mathbf{J}(\mathbf{r}, t) = \frac{ev}{s}\delta(s - b)\delta(\phi - 0)\delta(z + vt)\hat{\mathbf{z}}. \tag{C.4}$$

Moving to a picture in which we work with charges and potentials rather than currents and fields (for simplicity), the transferred power to the electron can be simply described in the

quasistatic limit as

$$\begin{aligned} P(t) &= \int -\nabla\Phi_{\text{res}}(\mathbf{r},t)\cdot\mathbf{J}(\mathbf{r},t)\ \mathrm{d}^3\mathbf{r} \\ &= \int \Phi_{\text{res}}(\mathbf{r},t)\nabla\cdot\mathbf{J}(\mathbf{r},t)\ \mathrm{d}^3\mathbf{r} \\ &= -\int \Phi_{\text{res}}(\mathbf{r},t)\frac{\partial\rho(\mathbf{r},t)}{\partial t}\ \mathrm{d}^3\mathbf{r}. \end{aligned} \tag{C.5}$$

The total transferred energy along the electron's entire trajectory from $t\to-\infty$ to $t\to\infty$ is then

$$\begin{aligned} \Delta W &= \int_{-\infty}^{\infty} P(t)\ \mathrm{d}t \\ &= -\int_{-\infty}^{\infty}\int \Phi_{\text{res}}(\mathbf{r},t)\frac{\partial\rho(\mathbf{r},t)}{\partial t}\ \mathrm{d}^3\mathbf{r}\ \mathrm{d}t. \end{aligned} \tag{C.6}$$

The goal of the mechanical derivation of the energy transfered between the electron and the scattered fields along the electron's trajectory is to provide a concise description of the probability that the electron loses energy within a window $E+\Delta E=\hbar\omega+\hbar\Delta\omega$ to its surroundings. This probability, called the electron energy-loss (EEL) probability and given in this derivation in units of 1/energy is defined implicitly as

$$\Delta W = \hbar\int_0^{\infty}\Gamma(\omega)\hbar\omega\ \mathrm{d}\omega. \tag{C.7}$$

It is thus clear that any description of ΔW that will be useful must depend on the measurable quantities of the nanoparticle system as described in frequency space. The strategy for pulling $\Gamma(\omega)$ out of the integral will then involve equating the integrand above with the integrand of a Fourier-type integral. Letting

$$\begin{aligned} \tilde{P}(\omega) &= \int_{-\infty}^{\infty} P(t)e^{i\omega t}dt, \\ P(t) &= \int_{-\infty}^{\infty}\tilde{P}(\omega)e^{-i\omega t}\frac{\mathrm{d}\omega}{2\pi}, \end{aligned} \tag{C.8}$$

we find that, from the convolution theorem,

$$\tilde{P}(\omega) = -\iint (i[\omega - \omega'])\tilde{\Phi}_{\text{res}}(\mathbf{r}, \omega')\tilde{\rho}(\mathbf{r}, \omega - \omega')\frac{\mathrm{d}\omega'}{2\pi}\,\mathrm{d}^3\mathbf{r}. \tag{C.9}$$

Substituting Eq. C.9 into the second line of Eq. C.8 and then substituting the entire RHS of the resulting expression (of which the LHS is $P(t)$) into Eq. C.6, one quickly finds from an analysis of the infinite integral of an exponential function that

$$\Delta W = \tilde{P}(0). \tag{C.10}$$

Therefore, because both Φ and ρ are real quantities in time,

$$\begin{aligned}\tilde{P}(0) &= \int \int_{-\infty}^{\infty} \frac{i\omega'}{2\pi}\tilde{\Phi}_{\text{res}}(\mathbf{r}, \omega')\tilde{\rho}^*(\mathbf{r}, \omega')\,\mathrm{d}\omega'\,\mathrm{d}^3\mathbf{r} \\ &= \int \int_{0}^{\infty} \frac{i\omega'}{2\pi}\left[\tilde{\Phi}_{\text{res}}(\mathbf{r}, \omega')\tilde{\rho}^*(\mathbf{r}, \omega') - \text{c.c.}\right]\,\mathrm{d}\omega'\,\mathrm{d}^3\mathbf{r}.\end{aligned} \tag{C.11}$$

Letting the dummy variable ω' be changed as $\omega' \to \omega$ above and equating the above expression with the integral definition of the EEL probability, one finds

$$\Gamma(\omega) = \frac{i}{2\pi\hbar^2}\int \left[\tilde{\Phi}_{\text{res}}(\mathbf{r}, \omega)\tilde{\rho}^*(\mathbf{r}, \omega) - \text{c.c.}\right]\,\mathrm{d}^3\mathbf{r}. \tag{C.12}$$

The response potential of the system can be described with the aid of a Green function as

$$\tilde{\Phi}_{\text{res}}(\mathbf{r}, \omega) = \int \tilde{G}_{\text{res}}(\mathbf{r}, \mathbf{r}'; \omega)\tilde{\rho}(\mathbf{r}', \omega)\,\mathrm{d}^3\mathbf{r}', \tag{C.13}$$

such that, if $\tilde{G}_{\text{res}}(\mathbf{r}, \mathbf{r}'; \omega)$ is known, the potential's dependence on the electron's charge distribution is clear. This form of the potential also builds in a natural symmetry to the definition of the loss probability, as

$$\Gamma(\omega) = \frac{i}{2\pi\hbar^2}\iint \left[\tilde{\rho}(\mathbf{r}', \omega)\tilde{G}_{\text{res}}(\mathbf{r}, \mathbf{r}'; \omega)\tilde{\rho}^*(\mathbf{r}, \omega) - \text{c.c.}\right]\,\mathrm{d}^3\mathbf{r}\,\mathrm{d}^3\mathbf{r}'. \tag{C.14}$$

The quantities of interest when defining the loss probability are then the double integrals over all space, which can be shorthanded as

$$I(\omega) = \iint \tilde{\rho}(\mathbf{r}', \omega)\tilde{G}_{\text{res}}(\mathbf{r}, \mathbf{r}'; \omega)\tilde{\rho}^*(\mathbf{r}, \omega)\,\mathrm{d}^3\mathbf{r}\,\mathrm{d}^3\mathbf{r}' \tag{C.15}$$

such that

$$\begin{aligned}\Gamma(\omega) &= \frac{i}{2\pi\hbar^2}(I(\omega) - I^*(\omega)) \\ &= -\frac{1}{\pi\hbar^2}\mathrm{Im}\{I(\omega)\}.\end{aligned} \tag{C.16}$$

C.5 Relation of the EEL Probability to Nanoparticle Properties

The potential $\tilde{\Phi}$ set up by a free charge distribution $\tilde{\rho}$ in the vicinity of dielectric objects is given by

$$\tilde{\Phi}(\mathbf{r},\omega) = \int \tilde{G}(\mathbf{r},\mathbf{r}';\omega)\tilde{\rho}(\mathbf{r}',\omega)\ \mathrm{d}^3\mathbf{r}' \tag{C.17}$$

where $\tilde{G}$ is the Green function of the dielectric system. The response potential $\tilde{\Phi}(\mathbf{r},\omega)$ of the system is defined as

$$\tilde{\Phi}_{\mathrm{res}}(\mathbf{r},\omega) = \int G_{\mathrm{res}}(\mathbf{r},\mathbf{r}';\omega)\tilde{\rho}(\mathbf{r}',\omega)\ \mathrm{d}^3\mathbf{r}' \tag{C.18}$$

where

$$\tilde{G}_{\mathrm{res}}(\mathbf{r},\mathbf{r}';\omega) = \tilde{G}(\mathbf{r},\mathbf{r}';\omega) - \frac{1}{|\mathbf{r}-\mathbf{r}'|} \tag{C.19}$$

with $1/|\mathbf{r}-\mathbf{r}'|$ the Green function of free space. The free space Green function will always be present in addition to the response part, building in the direct Coulomb potential of any free charges that are present. Additionally, in general, the Green function of a system of dielectric objects with sharp boundaries takes a different form for each pair of regions that $\mathbf{r}'$ and $\mathbf{r}$ lie in. For example, when a charge distribution lies inside a sphere of radius a and dielectric $\epsilon(\omega)$ centered at the origin in an otherwise empty universe, the response Green function is given by

$$\begin{aligned}\tilde{G}_{\mathrm{res}}^{r'<a}(\mathbf{r},\mathbf{r}';\omega) = &\sum_{\ell=0}^{\infty}\sum_{m=-\ell}^{\ell}\frac{4\pi}{2\ell+1}\left(\frac{2\ell+1}{\eta_\ell(\omega)} - \frac{1}{\epsilon(\omega)}\right)\frac{r^\ell r'^\ell}{a^{2\ell+1}}Y_{\ell m}(\theta,\phi)Y^*_{\ell,m}(\theta',\phi')\Theta(a-r) \\ &+ \frac{1}{|\mathbf{r}-\mathbf{r}'|}\left(\frac{1}{\epsilon(\omega)} - 1\right)\Theta(a-r) \\ &+ \sum_{\ell m}\frac{4\pi}{2\ell+1}\left(\frac{2\ell+1}{\eta_\ell(\omega)} - 1\right)\frac{r'^\ell}{r^{\ell+1}}Y_{\ell m}(\theta,\phi)Y^*_{\ell m}(\theta',\phi')\Theta(r-a),\end{aligned} \tag{C.20}$$

where the Heaviside functions Θ dictate that the first two terms are nonzero when the observer is inside the sphere, and the third is nonzero when the observer is outside. Also, $\eta_\ell(\omega) = \ell\epsilon(\omega) + (\ell+1)$ and we have empoyed the identity

$$\frac{1}{|\mathbf{r}-\mathbf{r}'|} = \sum_{\ell m} \frac{4\pi}{2\ell+1} \frac{\min\{r,r'\}^\ell}{\max\{r,r'\}^{\ell+1}} Y_{\ell m}(\theta,\phi) Y^*_{\ell m}(\theta',\phi') \tag{C.21}$$

in the third term. Note here that, in the second term, the subtraction of the free-space potential leaves behind a term that, although it goes like $1/|\mathbf{r}-\mathbf{r}'|$, actually only describes the polarization of the sphere's medium: in the limit $\epsilon(\omega) \to 1$, this part of the response drops to zero. When the charge distribution lies outside the sphere, the response Green function becomes

$$\begin{aligned} \tilde{G}^{r'>a}_{\text{res}}(\mathbf{r},\mathbf{r}';\omega) = &\sum_{\ell m} \frac{4\pi}{2\ell+1} \frac{\ell[1-\epsilon(\omega)]}{\eta_\ell(\omega)} \frac{a^{2\ell+1}}{r^{\ell+1} r'^{\ell+1}} Y_{\ell m}(\theta,\phi) Y^*_{\ell m}(\theta',\phi') \Theta(r-a) \\ &+ \sum_{\ell m} \frac{4\pi}{2\ell+1} \left(\frac{2\ell+1}{\eta_\ell(\omega)} - 1 \right) \frac{r^\ell}{r'^{\ell+1}} Y_{\ell m}(\theta,\phi) Y^*_{\ell m}(\theta',\phi') \Theta(a-r). \end{aligned} \tag{C.22}$$

If a background medium had been included, a term proportional to $(1/\epsilon_b - 1) \times 1/|\mathbf{r}-\mathbf{r}'|$ would be present in the first term, but this term has been eliminated as $\epsilon_b \to 1$. From here, the derivation of $\Gamma(\omega)$ for a penetrating electron beam trajectory and a nanosphere target is straightforward, if nontrivial. First, with the electron treated as an unchanging point charge along its entire trajectory,

$$\begin{aligned} \tilde{\rho}(\mathbf{r},\omega) &= -\frac{e}{sv} \delta(s-b)\delta(\phi-0) e^{-i\omega\frac{z}{v}} \\ &= -\frac{e}{sv} \delta(s-b)\delta(\phi-0) e^{-i\omega\frac{z}{v}} \Theta(a-r) - \frac{e}{sv} \delta(s-b)\delta(\phi-0) e^{-i\omega\frac{z}{v}} \Theta(r-a), \end{aligned} \tag{C.23}$$

the characteristic integral $I(\omega)$ contains four pieces:

$$\begin{aligned} I(\omega) &= \iint \tilde{\rho}(\mathbf{r}',\omega)\tilde{G}_{\rm res}(\mathbf{r},\mathbf{r}';\omega)\tilde{\rho}^*(\mathbf{r},\omega)\Theta(a-r')\Theta(a-r)\ \mathrm{d}^3\mathbf{r}\ \mathrm{d}^3\mathbf{r} \\ &+ \iint \tilde{\rho}(\mathbf{r}',\omega)\tilde{G}_{\rm res}(\mathbf{r},\mathbf{r}';\omega)\tilde{\rho}^*(\mathbf{r},\omega)\Theta(a-r')\Theta(r-a)\ \mathrm{d}^3\mathbf{r}\ \mathrm{d}^3\mathbf{r} \\ &+ \iint \tilde{\rho}(\mathbf{r}',\omega)\tilde{G}_{\rm res}(\mathbf{r},\mathbf{r}';\omega)\tilde{\rho}^*(\mathbf{r},\omega)\Theta(r'-a)\Theta(a-r)\ \mathrm{d}^3\mathbf{r}\ \mathrm{d}^3\mathbf{r} \\ &+ \iint \tilde{\rho}(\mathbf{r}',\omega)\tilde{G}_{\rm res}(\mathbf{r},\mathbf{r}';\omega)\tilde{\rho}^*(\mathbf{r},\omega)\Theta(r'-a)\Theta(r-a)\ \mathrm{d}^3\mathbf{r}\ \mathrm{d}^3\mathbf{r} \\ &= I_1(\omega)+I_2(\omega)+I_3(\omega)+I_4(\omega). \end{aligned} \tag{C.24}$$

Here we have implicitly defined the total response Green function as

$$\tilde{G}_{\rm res}(\mathbf{r},\mathbf{r}';\omega) = \tilde{G}_{\rm res}^{r'<a}(\mathbf{r},\mathbf{r}';\omega)\Theta(a-r') + \tilde{G}_{\rm res}^{r'>a}(\mathbf{r},\mathbf{r}';\omega)\Theta(r'-a). \tag{C.25}$$

Next, we can see the $I_2(\omega)$ and $I_3(\omega)$ both contain a product of an integral over the space outside the nanoparticle and another over the space within via the action of the Heaviside functions. To simplify these terms, it is useful to first simplify the Green function terms that are nonzero in the case where $\mathbf{r}$ and $\mathbf{r}'$ are in different regions. Letting

$$\begin{aligned} f_{\ell m}^{<}(\mathbf{r}) &= \sqrt{\frac{4\pi}{2\ell+1}}\frac{r^\ell}{a^\ell}Y_{\ell m}(\theta,\phi), \\ f_{\ell m}^{>}(\mathbf{r}) &= \sqrt{\frac{4\pi}{2\ell+1}}\frac{a^{\ell+1}}{r^{\ell+1}}Y_{\ell m}(\theta,\phi) \end{aligned} \tag{C.26}$$

be the mode functions that describe the spatial variation of the potential set up by the $(\ell,m)^{\rm th}$ nanosphere mode and

$$\begin{aligned} \tilde{g}_\ell^{>}(\omega) &= \frac{\ell[\epsilon(\omega)-1]}{\eta_\ell(\omega)}, \\ \tilde{g}_\ell^{<}(\omega) &= \frac{2\ell+1}{\eta_\ell(\omega)}, \\ \tilde{g}_\ell^{><}(\omega) &= \tilde{g}_\ell(\omega)-1, \\ \tilde{g}_B(\omega) &= \frac{1}{\epsilon(\omega)}, \\ \tilde{g}_\infty(\omega) &= \tilde{g}_B(\omega)-1, \end{aligned} \tag{C.27}$$

be the functions that describe the nanosphere's spectral response, we have

$$\begin{aligned}\tilde{G}_{\text{res}}(\mathbf{r},\mathbf{r}';\omega)\Theta(a-r')\Theta(r-a) &= \sum_{\ell m}\frac{1}{a}\tilde{g}_\ell^{><}(\omega)f_{\ell m}^{<}(\mathbf{r}')f_{\ell m}^{>*}(\mathbf{r})\;\Theta(a-r')\Theta(r-a),\\ \tilde{G}_{\text{res}}(\mathbf{r},\mathbf{r}';\omega)\Theta(r'-a)\Theta(a-r) &= \sum_{\ell m}\frac{1}{a}\tilde{g}_\ell^{><}(\omega)f_{\ell m}^{>}(\mathbf{r}')f_{\ell m}^{<*}(\mathbf{r})\;\Theta(r'-a)\Theta(a-r).\end{aligned} \tag{C.28}$$

In general, the spectral responses $\tilde{g}_\ell$ of both kinds describe the excitation of surface-bound phenomena (plasmons for metallic $\epsilon(\omega)$) and the responses $\tilde{g}_B$ describe the excitation of bulk phenomena. Using these identities,

$$\begin{aligned}I_2(\omega) &= \sum_{\ell m}\frac{\tilde{g}_\ell^{><}(\omega)}{a}\int\limits_{r'<a}\tilde{\rho}(\mathbf{r}',\omega)f_{\ell m}^{<*}(\mathbf{r}')\;\mathrm{d}^3\mathbf{r}'\int\limits_{r>a}\tilde{\rho}^*(\mathbf{r},\omega)f_{\ell m}^{>}(\mathbf{r})\;\mathrm{d}^3\mathbf{r},\\ I_3(\omega) &= \sum_{\ell m}\frac{\tilde{g}_\ell^{><}(\omega)}{a}\int\limits_{r'>a}\tilde{\rho}(\mathbf{r}',\omega)f_{\ell m}^{>*}(\mathbf{r}')\;\mathrm{d}^3\mathbf{r}'\int\limits_{r<a}\tilde{\rho}^*(\mathbf{r},\omega)f_{\ell m}^{<}(\mathbf{r})\;\mathrm{d}^3\mathbf{r}.\end{aligned} \tag{C.29}$$

Additionally, with the spatial integrals shorthanded as

$$\begin{aligned}A_{\ell m}^{<}(\omega) &= \int\limits_{r<a}\tilde{\rho}^*(\mathbf{r},\omega)f_{\ell m}^{<}(\mathbf{r})\;\mathrm{d}^3\mathbf{r},\\ A_{\ell m}^{>}(\omega) &= \int\limits_{r>a}\tilde{\rho}^*(\mathbf{r},\omega)f_{\ell m}^{>}(\mathbf{r})\;\mathrm{d}^3\mathbf{r},\end{aligned} \tag{C.30}$$

we have

$$\begin{aligned}I_2(\omega)+I_3(\omega) &= \sum_{\ell m}\frac{\tilde{g}_\ell^{><}(\omega)}{a}\left(A_{\ell m}^{<*}(\omega)A_{\ell m}^{>}(\omega)+A_{\ell m}^{<}(\omega)A_{\ell m}^{>*}(\omega)\right)\\ &= \sum_{\ell m}\frac{2\tilde{g}_\ell^{><}(\omega)}{a}\mathrm{Re}\left\{A_{\ell m}^{<*}(\omega)A_{\ell m}^{>}(\omega)\right\}.\end{aligned} \tag{C.31}$$

The fourth term of $I(\omega)$ also reduces simply using the above identities to

$$I_4(\omega) = \sum_{\ell m}\frac{\tilde{g}_\ell^{>}(\omega)}{a}\left|A_{\ell m}^{>}(\,\omega)\right|^2 \tag{C.32}$$

while the first causes more of a problem. Explicitly,

$$\begin{aligned}I_1(\omega) = &\sum_{\ell m}\frac{\tilde{g}_\ell^{<}(\omega)}{a}\left|A_{\ell m}^{<}(\omega)\right|^2-\sum_{\ell m}\frac{\tilde{g}_B(\omega)}{a}\left|A_{\ell m}^{<}(\omega)\right|^2\\ &+\iint\limits_{\substack{r<a\\ r'<a}}\tilde{\rho}(\mathbf{r}',\omega)\tilde{\rho}^*(\mathbf{r},\omega)\frac{\tilde{g}_\infty(\omega)}{|\mathbf{r}-\mathbf{r}'|}\;\mathrm{d}^3\mathbf{r}\;\mathrm{d}^3\mathbf{r}'\end{aligned} \tag{C.33}$$

where the third term describes the interaction of the passing electron with the point-like screening charge set up by the polarized medium. The integral is divergent due to the behavior of the Coulombic $1/|\mathbf{r}-\mathbf{r}'|$ potential and must be treated by including additional physical phenomena to the model. One simple strategy involves replacing the Coulombic potential with a Yukawa potential with decay parameter k_0, such that

$$\frac{1}{|\mathbf{r}-\mathbf{r}'|} \to \frac{e^{-k_0|\mathbf{r}-\mathbf{r}'|}}{|\mathbf{r}-\mathbf{r}'|}. \tag{C.34}$$

Together with the identity

$$\frac{e^{-k_0|\mathbf{r}-\mathbf{r}'|}}{|\mathbf{r}-\mathbf{r}'|} = \frac{1}{2\pi^2}\int \frac{1}{k^2+k_0^2} e^{i\mathbf{k}\cdot(\mathbf{r}-\mathbf{r}')}\,\mathrm{d}^3\mathbf{k}, \tag{C.35}$$

this replacement allows one to quickly simplify the third term of Eq. C.33 which, due to its resemblance to similar integrals that appear in the treatment of electron energy losses to bulk materials [16, 24, 42], will be herein dubbed the "infinite-medium" integral $I_\infty(\omega)$. Expanding the spatial integrals and wavevector $\mathbf{k} = \mathbf{k}_\perp + \mathbf{k}_z \doteq (k_\perp, \psi, k_z)$ of I_∞ in cylindrical coordinates and substituting the explicit forms for $\tilde{\rho}$ and $\tilde{\rho}^*$, one arrives at

$$\begin{aligned} I_\infty(\omega) = \lim_{k_0\to\infty} \frac{e^2\tilde{g}_\infty(\omega)}{2\pi^2 v^2} &\int_{-a}^{a}\int_{0}^{2\pi}\int_{0}^{a}\int_{-a}^{a}\int_{0}^{2\pi}\int_{0}^{a} \int \frac{1}{k^2+k_0^2} e^{-i\frac{\omega}{v}(z'-z)} e^{-ik_z(z-z')} \\ &\times e^{-ik_\perp s\cos(\psi-\phi)} e^{-ik_\perp s'\cos(\psi-\phi')} \delta(s-b)\delta(s'-b)\delta(\phi-0)\delta(\phi'-0) \\ &\times \Theta(a-\sqrt{s^2+z^2})\Theta(a-\sqrt{s'^2+z'^2})\,\mathrm{d}^3\mathbf{k}\,\mathrm{d}s\,\mathrm{d}\phi\,\mathrm{d}z\,\mathrm{d}s'\,\mathrm{d}\phi'\,\mathrm{d}z' \\ = \lim_{k_0\to\infty} \frac{e^2\tilde{g}_\infty(\omega)}{2\pi^2 v^2} &\iint_{-\mathrm{Re}\{\sqrt{a^2-b^2}\}}^{\mathrm{Re}\{\sqrt{a^2-b^2}\}} \int \frac{1}{k_\perp^2+k_z^2+k_0^2} e^{-i(k_z-\frac{\omega}{v})(z-z')}\,\mathrm{d}^3\mathbf{k}\,\mathrm{d}z\,\mathrm{d}z'. \end{aligned} \tag{C.36}$$

Further, with

$$\iint_{-\mathrm{Re}\{\sqrt{a^2-b^2}\}}^{\mathrm{Re}\{\sqrt{a^2-b^2}\}} e^{-i\frac{\omega}{v}(z'-z)} e^{-ik_z(z-z')}\,\mathrm{d}z\,\mathrm{d}z' = \frac{4\sin^2\left(\left[k_z-\frac{\omega}{v}\right]\mathrm{Re}\{\sqrt{a^2-b^2}\}\right)}{\left(k_z-\frac{\omega}{v}\right)^2}, \tag{C.37}$$

one finds that

$$I_\infty(\omega) = \lim_{k_0\to\infty} \frac{e^2\tilde{g}_\infty(\omega)}{2\pi^2 v^2} \int \frac{4\sin^2\left(\left[k_z-\frac{\omega}{v}\right]\mathrm{Re}\{\sqrt{a^2-b^2}\}\right)}{\left(k_z-\frac{\omega}{v}\right)^2\left(k_\perp^2+k_z^2+k_0^2\right)}\,\mathrm{d}^3\mathbf{k}. \tag{C.38}$$

The k_z-integral of Eq. C.38 can be evaluated analytically with the aid of the symbolic integration library of Mathematica 12.1. Explicitly,

$$I_\infty(\omega) = \lim_{k_0\to\infty} \frac{e^2\tilde{g}_\infty(\omega)}{\pi v^2} \int_0^\infty k_\perp \, \mathrm{d}k_\perp \left(\frac{4\pi \mathrm{Re}\{\sqrt{a^2-b^2}\}}{\frac{\omega^2}{v^2}+k_\perp^2+k_0^2} \right.$$
$$+ \frac{2\pi}{\sqrt{k_\perp^2+k_0^2}} \mathrm{Re}\left\{ \frac{1}{\left(\frac{\omega}{v}-i\sqrt{k_\perp^2+k_0^2}\right)^2} \left(1-\cos\left[2\left(\frac{\omega}{v}-i\sqrt{k_\perp^2+k_0^2}\right)\mathrm{Re}\{\sqrt{a^2-b^2}\}\right]\right.\right.$$
$$\left.\left.\left. +i\sin\left[2\left(\frac{\omega}{v}-i\sqrt{k_\perp^2+k_0^2}\right)\mathrm{Re}\{\sqrt{a^2-b^2}\}\right]\right)\right\}\right), \tag{C.39}$$

where the ψ-integral has simply produced a factor of 2π as the integrand of Eq. C.38 is independent of ψ. Taking the integral above requires the introduction of a cutoff wavevector for the $k_\perp$ integral such that the highest spatial frequency components of the Yukawa potential are removed. Using Mathematica and the limit $k_0 \to 0$, one can see that the above integral diverges without this approximation. Therefore, with the integration bounds of $k_\perp$ limited to $[0, k_c]$, we have

$$I_\infty(\omega) \approx \frac{e^2\tilde{g}_\infty(\omega)}{\pi v^2} \left(2\pi\sqrt{a^2-b^2}\ln\left[1+\frac{k_c^2v^2}{\omega^2}\right] + \frac{2\pi k_c}{k_c^2+(\omega/v)^2} - \frac{2\pi\sin\left[2\sqrt{a^2-b^2}(\omega/v)\right]}{\omega/v} + \right.$$
$$\frac{2\pi}{k_c^2+(\omega/v)^2} e^{-2k_c\sqrt{a^2-b^2}} \left[\frac{\omega}{v}\sin\left(2\sqrt{a^2-b^2}[\omega/v]\right) - k_c\cos\left(2\sqrt{a^2-b^2}[\omega/v]\right)\right] +$$
$$\left. 2\pi\sqrt{a^2-b^2}\left[\pi + 2\mathrm{Re}\left\{\Gamma\left(0, 2[k_c+i(\omega/v)]\sqrt{a^2-b^2}\right)\right\}\right] \right). \tag{C.40}$$

Here, $\Gamma(n,x)$ is the upper incomplete Euler gamma function and should not be confused with a loss probability. For physical values of the parameters ($\omega \sim 10^{15}$ Hz, $v \sim 10^{10}$ cm/s, $a, b \sim 10^{-6}$ cm), the result of Eq. C.40 is $\sim 10^{-4}$ cm^{2}g and becomes increasingly dominated by the first term as k_c becomes much greater than $\sim 10^6$ cm^{-1}. In particular, the second and fourth terms decrease straightforwardly with increasing k_c, while the fifth is generally

monotonically decreasing in k_c for $k_c > \omega/v$ and the third provides a small ($\sim 10^{-6}$ cm^{2}g) negative correction to the total integral.

Closely related strategies to simplify $I_\infty(\omega)$ exist in Refs. [24, 42]. These models treat a simpler form of the infinite-medium integral of Eq. C.36 that is appropriate for an electron moving through an infinite, uniform material. First calculating an EEL probability per unit path length for such an electron, it is shown that one can then integrate along the electron's path through a sphere to calculate the infinite-medium EEL probability in bulk. This method can be used to approximate the bulk plasmon EEL probability in spheres as well by integrating the EEL probability per unit distance (calculated as if the electron were in bulk) only along the electron's path within the sphere. At the level of the integral $I_\infty(\omega)$, this is performed by allowing the integration bounds on z' to go to infinity, such that

$$I_\infty(\omega) \to \frac{e^2 \tilde{g}_\infty(\omega)}{2\pi^2 v^2} \int_{-\infty}^{\infty} \int_{-\mathrm{Re}\{\sqrt{a^2-b^2}\}}^{\mathrm{Re}\{\sqrt{a^2-b^2}\}} \int \frac{k_\perp}{k^2} e^{-i(k_z - \frac{\omega}{v})(z-z')} \, \mathrm{d}^3\mathbf{k} \, \mathrm{d}z \, \mathrm{d}z'. \tag{C.41}$$

Using the same cutoff wavenumber k_c to regularize the Yukawa potential, this delivers

$$I_\infty(\omega) \approx \frac{2e^2 \tilde{g}_\infty(\omega) \sqrt{a^2 - b^2}}{v^2} \ln\left(1 + \frac{k_c^2 v^2}{\omega^2}\right), \tag{C.42}$$

which is simply the first term of Eq. C.40 and is appropriate for large enough k_c. Comparison with Ref. [42] can be made by letting $\phi_{\mathrm{out}} = \tan^{-1}(\hbar k_c / m_e v) \approx \hbar k_c / m_e v$ be the detector's maximum collection half-angle.

Because the dielectric model without momentum dispersion neglects many important phenomena that affect the bulk EEL probability [24, 42], the simpler expression for I_∞ found in Eq. C.42 is used in this work. The relative magnitudes of the bulk and surface plasmon EEL features are unimportant to the inference of the Drude parameters, so k_c is fit as necessary but is not examined for its physical significance. A detailed determination of the contributions of the latter terms of Eq. C.40 to the bulk EEL probability, as well of terms that arise due to the inclusion of physics beyond the dielectric model, is beyond the scope of this investigation.

Finally, one can see that the imaginary parts of I_1, I_2, I_3, I_4, and I_∞ are all determined solely by the imaginary parts of the response functions $\tilde{g}_i$:

$$\begin{aligned}\Gamma(\omega) = &-\frac{1}{a\pi\hbar^2}\sum_{\ell m}\Big(\left|A^<_{\ell m}(\omega)\right|^2 \mathrm{Im}\{\tilde{g}^<_\ell(\omega)\} + 2\mathrm{Re}\left\{A^<_{\ell m}(\omega)A^>_{\ell m}(\omega)\right\}\mathrm{Im}\{\tilde{g}^{><}_\ell(\omega)\} \\ &+ \left|A^>_{\ell m}(\omega)\right|^2 \mathrm{Im}\{\tilde{g}^>_\ell(\omega)\}\Big) + \frac{1}{a\pi\hbar^2}\sum_{\ell m}\left|A^<_{\ell m}(\omega)\right|^2 \mathrm{Im}\{\tilde{g}_B(\omega)\} - \frac{1}{\pi\hbar^2}\mathrm{Im}\{I_\infty(\omega)\} \\ &= \Gamma^{\mathrm{surf}}(\omega) + \Gamma^{\mathrm{geo}}(\omega) + \Gamma^{\infty}(\omega).\end{aligned} \tag{C.43}$$

C.6 Dependence upon Drude-Model Parameters of the Mixing Angle between an LSP and a Nearby Resonance

The instantaneous interaction energy between a localized surface plasmon (LSP) mode of multipole order ℓ, m and a neighboring resonance is given by

$$U(t) = \int \Phi_{\ell m}(\mathbf{r}, t)\rho_n(\mathbf{r}, t)\ \mathrm{d}\mathbf{r}, \tag{C.44}$$

where $\Phi_{\ell m}$ is the potential set up by the oscillating LSP mode and ρ_n is the charge density of the resonance. If the resonance is taken to be an oscillating dipole centered at a location $\mathbf{r}_0$, then

$$\rho_n(\mathbf{r}, t) = -\mathbf{p}(t)\cdot\nabla\delta(\mathbf{r}-\mathbf{r}_0), \tag{C.45}$$

where $\mathbf{p}(t)$ is the resonance's time-dependent dipole moment. Further, with the LSP's charge distribution taken to be a surface charge density given by

$$\rho_{\ell m}(\mathbf{r}, t) = \frac{q_{\ell m}(t)}{a^{\ell+2}}Y_{\ell m}(\theta,\phi)\delta(r-a) \tag{C.46}$$

that is proportional to its multipole moment $q_{\ell m}(t)$ (given here in the spherical coordinate convention for convenience), the interaction energy can be redefined using Coulomb's law to give

$$\begin{aligned}U(t) &= \iint \frac{\rho_{\ell m}(\mathbf{r}', t)\rho_n(\mathbf{r}, t)}{|\mathbf{r}-\mathbf{r}'|}\ \mathrm{d}^3\mathbf{r}\ \mathrm{d}^3\mathbf{r}' \\ &= -\frac{q_{\ell m}(t)\mathbf{p}(t)}{a^{\ell+2}}\cdot\int\frac{\mathbf{r}_0-\mathbf{r}'}{|\mathbf{r}_0-\mathbf{r}'|^3}Y_{\ell m}(\theta',\phi')\delta(r'-a)\ \mathrm{d}^3\mathbf{r}',\end{aligned} \tag{C.47}$$

where the second line was derived using integration by parts. Further, as the time-dependent multipole moments encode the motion of two massive oscillators, it is sensible to assign to each of them a coordinate Q, such that $eQ_{\ell m}(t) = q_{\ell m}(t)$ and $eQ_n(t)\hat{\mathbf{p}} = \mathbf{p}(t)$. Therefore, letting

$$\sigma = \frac{e^2}{a^{\ell+2}}\hat{\mathbf{p}} \cdot \int \frac{\mathbf{r}_0 - \mathbf{r}'}{|\mathbf{r}_0 - \mathbf{r}'|^3} Y_{\ell m}(\theta', \phi')\delta(r' - a)\, \mathrm{d}^3\mathbf{r}' \tag{C.48}$$

be the coupling strength between the two resonances, one is left with the simple equations of motion of the coupled system

$$\begin{aligned} m_\ell \ddot{Q}_{\ell m}(t) + m_\ell \gamma \dot{Q}_{\ell m}(t) + m_\ell \omega_\ell^2 Q_{\ell m}(t) - \sigma Q_n(t) = F_{\ell m}(t), \\ m_n \ddot{Q}_n(t) + m_n \gamma \dot{Q}_n(t) + m_n \omega_n^2 Q_n(t) - \sigma Q_{\ell m}(t) = F_n(t), \end{aligned} \tag{C.49}$$

where the definitions of the effective masses m_i, natural frequencies ω_i, and external forces $F_i(t)$ of each oscillator are implied with the knowledge that $\omega_{\ell m} = \omega_\ell$ and $m_{\ell m} = m_\ell$. The above equations can be decoupled in the limit where the damping rate is small to give

$$\begin{aligned} \ddot{Q}_+(t) + \Omega_+^2 Q_+(t) = \frac{F_+(t)}{m_{\ell m}}, \\ \ddot{Q}_-(t) + \Omega_-^2 Q_-(t) = \frac{F_-(t)}{m_n}, \end{aligned} \tag{C.50}$$

where $Q_\pm$, $\Omega_\pm$, and $F_\pm$ are the normal mode coordinates, resonance frequencies, and forces of the system. We will define only the resonance frequencies here, which take the form

$$\Omega_\pm^2 = \omega_{\ell m}^2 \cos^2(\beta) + \omega_n^2 \sin^2(\beta) \mp \frac{\sigma}{\sqrt{m_\ell m_n}} \sin(2\beta), \tag{C.51}$$

where β is the mixing angle defined by

$$\beta = \frac{1}{2} \tan^{-1} \left\{ \frac{2\sigma}{\sqrt{m_\ell m_n}(\omega_\ell^2 - \omega_n^2)} \right\}. \tag{C.52}$$

The LSP masses are defined by convention when the generalized coordinate displacements are related to the time-dynamics of the external forces. They cannot be uniquely determined, however the choice of LSP masses cannot affect the time-evolution of any observable quantities. One convenient convention for m_ℓ is chosen in Ref. [119], wherein

$$m_\ell = \frac{2\pi e^2(\ell\epsilon_\infty + [\ell + 1])}{(2\ell + 1)\omega_\ell^2 a^3}, \tag{C.53}$$

such that, with $\omega_\ell = \omega_p\sqrt{\ell/(\ell\epsilon_\infty + [\ell+1])}$, the LSP effective mass scales with the material parameters as $m_\ell \sim (\ell\epsilon_\infty + [\ell+1])^2/\omega_p^2$. Assuming the coupled system is maintained at a fixed detuning $\Delta^2 = \omega_\ell^2 - \omega_n^2$, coupling strength σ, nanosphere radius a, and resonance mass m_n, it is readily apparent that the mixing angle then becomes

$$\beta = \frac{1}{2}\tan^{-1}\left\{\frac{2g\sqrt{\ell(2\ell+1)a^3}}{e\sqrt{2\pi m_n}\Delta^2}\frac{\omega_p}{\ell\epsilon_\infty + (\ell+1)}\right\}, \tag{C.54}$$

such that the leftmost fraction in the curly braces of Eq. C.54 is a constant. Thus, maximal mixing always occurs a large ω_p and small ϵ_∞.

Appendix D

SUPPLEMENTARY INFORMATION — PROBING NANOPARTICLE SUBSTRATE INTERACTIONS WITH SYNCHROTRON INFRARED NANOSPECTROSCOPY: COUPLING GOLD NANOROD FABRY-PÉROT RESONANCES WITH SIO_2 AND HBN PHONONS

D.1 Derivation of the Tip and Target Polarizabilities

The responses to electrical stimulus of both the AFM tip and target rod are assumed to be those of prolate spheroids. The tip spheroids is modeled with its long axis coaligned with the z-axis and its short axes in the xy-plane. Target spheroid is rotated 90 degrees, with its short axes lying in the yz-plane and its long axis along x. Additionally, radiation is neglected such that the electrostatic potential $\Phi(\mathbf{r},\omega)$ everywhere satisfies

$$-\nabla\cdot[\varepsilon(\mathbf{r},\omega)\nabla\Phi(\mathbf{r},\omega)] = 4\pi\rho_{\text{ext}}(\mathbf{r},\omega). \tag{D.1}$$

Here, $\varepsilon(\omega)$ is the frequency-dependent dielectric function of either the tip or target and $\rho_{\text{ext}}(\mathbf{r},\omega)$ is the free charge distribution of the driving source. Eq. D.1 can be rewritten using a Green function $G(\mathbf{r},\mathbf{r}';\omega)$ such that

$$\Phi(\mathbf{r},\omega) = \int G(\mathbf{r},\mathbf{r}';\omega)\rho_{\text{ext}}(\mathbf{r}',\omega)d^3r', \tag{D.2}$$

wherein $G(\mathbf{r},\mathbf{r}';\omega)$ satisfies Eq. D.1 with the modification $\rho_{\text{ext}}(\mathbf{r};,\omega)\rightarrow\delta(\mathbf{r}-\mathbf{r}')$.

The solution of G can be found using the method of separation of variables using the spheroidal radial, vertical, and azimuthal coordinates (ξ,η,ϕ), which are defined as

$$\xi = \frac{r_- + r_+}{2C}, \qquad \eta = \frac{r_- - r_+}{2C}, \qquad \phi = \tan^{-1}\frac{y}{x}, \tag{D.3}$$

with $r_\pm = \sqrt{x^2+y^2+(z\mp C)^2}$ the distance from the point $\mathbf{r}$ to the focus at $\pm C\hat{\mathbf{z}}$. Thus, the definitions of the coordinates depend on the choice of $C=\sqrt{a^2-b^2}$, where a and b are the

long and short axes of the spheroids. The coordinates always fall in the regions $\xi \in [1, \infty)$, $\eta \in [-1, 1]$, and $\phi \in [0, 2\pi)$.

The functions that allow for the separation of G are supplied by the expansion of the Green function of free space,

$$\frac{1}{|\mathbf{r}-\mathbf{r}'|} = \sum_{p=0}^{1}\sum_{\ell=0}^{\infty}\sum_{m=0}^{\ell}(-1)^m(2-\delta_{m0})\frac{2\ell+1}{C}\left[\frac{(\ell-m)!}{(\ell+m)!}\right]^2 P_{\ell m}(\eta)P_{\ell m}(\eta')S_p(m\phi)S_p(m\phi') \\ \times\left[\mathcal{Q}_{\ell m}(\xi)\mathcal{P}_{\ell m}(\xi')\Theta(\xi-\xi') + \mathcal{P}_{\ell m}(\xi)\mathcal{Q}_{\ell m}(\xi')\Theta(\xi'-\xi)\right], \tag{D.4}$$

in which it must be noted that, in free space, any choice of c will do [304]. Here, $S_p(\phi) = \delta_{p,\text{even}}\cos(\phi) + \delta_{p,\text{odd}}\sin(\phi)$ are the sinusoidal functions of even and odd parity. Further, $P_{\ell m}$ and $\mathcal{P}_{\ell m}$ are associated Legendre functions of the first kind of types 1 and 3, respectively, while $Q_{\ell m}$ and $\mathcal{Q}_{\ell m}$ are the corresponding associated Legendre functions of the second kind.

Their definitions stem from the Legendre polynomials of the first kind, $P_{\ell 0}(x) = \mathcal{P}_{\ell 0}(x) = (1/2^\ell \ell!)\, d^\ell/dx^\ell\{(x^2-1)^\ell\}$. Letting x be a real number in the interval $-1 \le x \le 1$ and $z \in \mathbb{C}$ an unbounded complex number, the Legendre functions of the second kind follow: $Q_{\ell 0}(x) = (1/2)\int_{-1}^{1} P_{\ell 0}(y)/(x-y)\ dy$ and $\mathcal{Q}_{\ell 0}(z) = (1/2)\int_{-1}^{1} P_{\ell 0}(y)/(z-y)\ dy + (\mathrm{i}\pi/2)\,\mathrm{sign}(\mathrm{Im}\{z\})P_{\ell 0}(z)\Theta(1-|\mathrm{Re}\{z\}|)$. The associated Legendre functions are then defined, using Rodrigues' formula, as $P_{\ell m}(x) = (-1)^m(1-x^2)^{m/2}\ d^m/dx^m\,\{P_{\ell 0}(x)\}$ and $Q_{\ell m}(x) = (-1)^m(1-x^2)^{m/2}d^m/dx^m\,\{Q_{\ell 0}(x)\}$ as well as

$$\begin{aligned}\mathcal{P}_{\ell m}(z) &= i^m \mathrm{sign}^m(\mathrm{Im}\{z\})(1-z^2)^{\frac{m}{2}}\frac{d^m}{dz^m}\left\{P_{\ell 0}(z)\right\}, \\ \mathcal{Q}_{\ell m}(z) &= i^m \mathrm{sign}^m(\mathrm{Im}\{z\})(1-z^2)^{\frac{m}{2}}\frac{d^m}{dz^m}\left\{\mathcal{Q}_{\ell 0}(z)\right\}.\end{aligned} \tag{D.5}$$

Letting the spheroid's surface lie at $\xi = X = a/C$ and the source lie strictly outside the spheroid's volume, the Green function is

$$G(\mathbf{r},\mathbf{r}';\omega) = \frac{1}{|\mathbf{r}-\mathbf{r}'|} + \sum_{p=0}^{1}\sum_{\ell=1}^{\infty}\sum_{m=0}^{\ell}(-1)^m(2-\delta_{m0})\frac{2\ell+1}{C}\left[\frac{(\ell-m)!}{(\ell+m)!}\right]^2 \\ \times\left[\Theta(X-\xi)g^{<}_{\ell m}(\omega)\mathcal{P}_{\ell m}(\xi) - \Theta(\xi-X)g^{>}_{\ell m}(\omega)\mathcal{Q}_{\ell m}(\xi)\right]\mathcal{Q}_{\ell m}(\xi')P_{\ell m}(\eta)P_{\ell m}(\eta')S_p(m\phi)S_p(m\phi'), \tag{D.6}$$

with $\psi^{(1)}(z) = d/dz\{\mathcal{P}_{\ell m}(z)\}$ and $\psi^{(2)}(z) = d/dz\{\mathcal{Q}_{\ell m}(z)\}$. The resonances of the spheroid thus occur at spectral locations where the real parts of

$$g^{<}_{\ell m}(\omega) = \frac{(-1)^m(\ell+m)!/(\ell-m)!}{(X^2-1)\mathcal{P}_{\ell m}(X)\psi^{(1)}_{\ell m}(X)} \frac{1}{\frac{\mathcal{Q}_{\ell m}(X)}{\mathcal{P}_{\ell m}(X)}\varepsilon(\omega) - \frac{\psi^{(2)}(X)}{\psi^{(1)}(X)}} - 1 \tag{D.7}$$

and

$$g^{>}_{\ell m}(\omega) = \frac{\varepsilon(\omega)-1}{\frac{\mathcal{Q}_{\ell m}(X)}{\mathcal{P}_{\ell m}(X)}\varepsilon(\omega) - \frac{\psi^{(2)}_{\ell m}(X)}{\psi^{(1)}_{\ell m}(X)}} \tag{D.8}$$

go to zero. Contracting the notation with the definition of the spheroid mode functions

$$\left.\begin{matrix} f^{<}_{p\ell m}(\mathbf{r}) \\ f^{>}_{p\ell m}(\mathbf{r}) \end{matrix}\right\} = \frac{(2-\delta_{m0})(2\ell+1)}{C^{\ell+1}} \left[\frac{(\ell-m)!}{(\ell+m)!}\right]^2 P_{\ell m}(\eta) S_p(m\phi) \begin{cases} \mathcal{P}_{\ell m}(\xi), & \xi < X, \\ \mathcal{Q}_{\ell m}(\xi), & \xi > X \end{cases} \tag{D.9}$$

and scaling coefficients $K_{\ell m} = (-1)^m[(\ell+m)!/(\ell-m)!]/(2-\delta_{m0})(2\ell+1)$, the potential everywhere is

$$\begin{aligned} \Phi(\mathbf{r},\omega) = \int \frac{\rho_{\text{ext}}(\mathbf{r}',\omega)}{|\mathbf{r}-\mathbf{r}'|}\, d^3\mathbf{r}' + \sum_{p\ell m} K_{\ell m} c^{2\ell+1} \left(\Theta(X-\xi) g^{<}_{\ell m}(\omega) f^{<}_{p\ell m}(\mathbf{r}) - \Theta(\xi-X) g^{>}_{\ell m}(\omega) f^{>}_{p\ell m}(\mathbf{r})\right) \\ \times \int\limits_{\xi'>X} f^{>}_{p\ell m}(\mathbf{r}') \rho_{\text{ext}}(\mathbf{r}',\omega)\, d^3r'. \end{aligned} \tag{D.10}$$

From this potential, it is sensible to define a set of multipole moments $q_{p\ell m}(\omega)$ that describe the magnitude and phase of the oscillations of each of the resonant modes of the spheroid. It is most convenient to define them from the potential outside the spheroid, such that

$$q_{p\ell m}(\omega) = -K_{\ell m} C^{2\ell+1} g^{>}_{\ell m}(\omega) \int\limits_{\xi'>X} f^{>}_{p\ell m}(\mathbf{r}') \rho_{\text{ext}}(\mathbf{r}',\omega) d^3r' \tag{D.11}$$

and $\Phi(\mathbf{r},\omega)\Theta(\xi-X) = \sum_{p\ell m} q_{p\ell m}(\omega) f^{>}_{p\ell m}(\mathbf{r})$. Eq. D.11 provides a notion of the polarizability of each multipole mode, in which the magnitude of the response of $q_{p\ell m}$ is determined by the frequency dependence of $g^{>}_{\ell m}(\omega)$ as well as the magnitude and symmetry of ρ_{ext}.

Formally, then, one can let $\rho_{\text{ext}} = (1/4\pi)\nabla \cdot \mathbf{E}_{\text{ext}}$ and use integration by parts to redefine the multipole moments of the excited spheroid as

$$q_{p\ell m}(\omega) = \alpha_{\ell m}(\omega)\mathcal{E}_{p\ell m}(\omega), \tag{D.12}$$

wherein

$$\mathcal{E}_{p\ell m}(\omega) = \frac{C^{\ell-1}}{4\pi} \int\limits_{\xi'>X} \mathbf{E}_{\text{ext}}(\mathbf{r}', \omega) \cdot \nabla' f^{>}_{p\ell m}(\mathbf{r}') d^3r' \tag{D.13}$$

is the portion of the impinging electric field that is allowed by symmetry to excite the $(p, \ell, m)^{\text{th}}$ mode of the spheroid, and

$$\alpha_{p\ell m}(\omega) = (-1)^m \frac{C^{\ell+2}}{(2-\delta_{m0})(2\ell+1)} \left[\frac{(\ell+m)!}{(\ell-m)!}\right]^2 g^{>}_{\ell m}(\omega) \tag{D.14}$$

is the $(p, \ell, m)^{\text{th}}$ mode's polarizability. The long-axis dipole of the target rod therefore has a polarizability $\alpha_2(\omega) = \alpha_{010}(\omega)$ with $\varepsilon(\omega) \to \varepsilon_2(\omega) = 1 + \omega_{p2}^2/(\omega_2^2 - \omega^2 - \mathrm{i}\omega\gamma_2)$, $C \to C_2 = \sqrt{a_2^2 - b_2^2}$, and $X \to X_2 = a_2/C_2$. Explicitly,

$$\alpha_2(\omega) = \frac{c_2^3}{3} \frac{\varepsilon_2(\omega) - 1}{\frac{\mathcal{Q}_{10}(X_2)}{\mathcal{P}_{10}(X_2)}\varepsilon_2(\omega) - \frac{\psi_{10}^{(2)}(X_2)}{\psi_{10}^{(1)}(X_2)}}. \tag{D.15}$$

The long-axis (α_1^l) and short-axis (α_1^s) modes of the tip are modeled similarly with polarizabilities α_{010} and α_{011}, respectively, as well as $\varepsilon(\omega) \to \varepsilon_1(\omega) = 1 - \omega_{p1}^2/(\omega^2 + i\omega\gamma_1)$ a Drude model of PtSi, $C \to C_1 = \sqrt{a_1^2 - b_1^2}$ the focus length of the tip, and $X \to X_1 = a_1/C_1$ its spheroid radius. The resulting forms are very similar to Eq. D.15, such that

$$\begin{aligned}
\alpha_1^l(\omega) &= \frac{C_1^3}{3} \frac{\varepsilon_1(\omega) - 1}{\frac{\mathcal{Q}_{10}(X_1)}{\mathcal{P}_{10}(X_1)}\varepsilon_1(\omega) - \frac{\psi_{10}^{(2)}(X_1)}{\psi_{10}^{(1)}(X_1)}}, \\
\alpha_1^s(\omega) &= -\frac{C_1^3}{3} \frac{\varepsilon_1(\omega) - 1}{\frac{\mathcal{Q}_{11}(X_1)}{\mathcal{P}_{11}(X_1)}\varepsilon_1(\omega) - \frac{\psi_{11}^{(2)}(X_1)}{\psi_{11}^{(1)}(X_1)}}.
\end{aligned} \tag{D.16}$$

D.2 Effective Polarizabilities of the Coupled Sample Components

The effective polarizability of the target rod can be calculated simply by tabulating the total electric field $\boldsymbol{\mathcal{E}}_2(\mathbf{r}, \omega)$ that impinges on the target while the entire sample is illuminated by the

synchrotron light. With the target centered at the origin, its long-axis spheroidal mode can be approximated as a point dipole at the spheroid's center, such that $\mathbf{p}_2(\omega) = \alpha_2(\omega)\boldsymbol{\mathcal{E}}_{2x}(0,\omega)$ [304]. Here, $\alpha_2(\omega)$ and $\boldsymbol{\mathcal{E}}_{2x}(\mathbf{r},\omega)$ are the polarizability of the rod's dipole mode and the x-component of the total field, as respectively defined in Section 5.3.

The effective polarizability of the rod, $\hat{\alpha}_2(\omega)$, is defined such that $\mathbf{p}_2(\omega) = \hat{\alpha}_2(\omega)\mathbf{E}_{0x}(\omega)$, with $\mathbf{E}_{0x}(\omega)$ the synchrotron's (uniform) electric field, $\mathbf{E}_0(\omega)$. In this way, the influence of the scattered field of the substrate, $\mathbf{E}_3(\mathbf{r},\omega)$, is self-contained within the dipole's polarizability and the target's full spectral behavior can be recovered simply by knowing the spectral content of the synchrotron field.

The substrate's field is most conveniently decomposed into a sum $\mathbf{E}_3(\mathbf{r},\omega) = \mathbf{E}_3^{(0)}(\mathbf{r},\omega) + \mathbf{E}_3^{(2)}(\mathbf{r},\omega)$ of the electric field $\mathbf{E}_3^{(0)}$ scattered by the substrate from the incoming light and the image field $\mathbf{E}_3^{(2)}$ set up by the substrate due to the presence of the polarized rod. With the substrate modeled as an infinitely thick slab with an upper surface lying parallel to the xy-plane at $z = -b_2$, an analysis of the boundary conditions imposed by the substrate leads to the definition $\mathbf{E}_3^{(0)}(\mathbf{r},\omega) = \beta(\omega)\mathbf{E}_{0z}(\omega)$, wherein $\beta(\omega) = [\varepsilon_3(\omega) - 1]/[\varepsilon_3(\omega) + 1]$ is the frequency response function of the substrate.

Further,

$$\mathbf{E}_3^{(2)}(\mathbf{r},\omega) = \beta(\omega)\nabla \int \frac{\rho_2(\mathbf{r}',\omega)}{|\mathbf{r} - \mathbf{r}'_-|} d^3r', \tag{D.17}$$

where $\rho_2(\mathbf{r}',\omega)$ is the charge distribution of the polarized target and $\mathbf{r}'_- = \mathbf{r}' - 2(z' + b_2)\hat{\mathbf{z}}$ [121]. Allowing the target to be approximated as a point dipole centered at the origin, its charge distribution becomes $\rho_2(\mathbf{r}',\omega) = -\mathbf{p}_2(\omega)\cdot\nabla'\delta(\mathbf{r}')$ which produces via integration-by-parts

$$\mathbf{E}_{3x}^{(2)}(0,\omega) = \frac{\beta(\omega)}{8b_2^3}\mathbf{p}_2(\omega). \tag{D.18}$$

Neglecting the effects of the tip's field on the target such that $\boldsymbol{\mathcal{E}}_{2x}(0,\omega) = \beta(\omega)\mathbf{E}_{0x}(\omega) + \mathbf{p}_2(\omega)\beta(\omega)/8b_2^3$, one finds

$$\mathbf{p}_2(\omega) = \alpha_2(\omega)\left(\frac{\beta(\omega)}{8b_2^3}\mathbf{p}_2(\omega) + \mathbf{E}_{0x}(\omega)\right). \tag{D.19}$$

Rearrangement quickly produces the definition of $\hat{\alpha}_2(\omega)$ in Eq. (5.2).

The same treatment can be extended to define the effective polarizabilities of the tip dipoles. Using the dipoles' definitions $\mathbf{p}_1^{l,s}(\omega) = \alpha_1^{l,s}(\omega)\boldsymbol{\mathcal{E}}_{1z,1x}(\mathbf{r}_1,\omega)$ from Section 5.3 where $\mathbf{r}_1 = -a_2\hat{\mathbf{x}} + (h-b_2)\hat{\mathbf{z}}$, one can implicitly define the effective polarizabilities $\hat{\alpha}_1(\omega)$ with $\mathbf{p}_1^{l,s}(\omega) = \hat{\alpha}_1^{l,s}(\omega)\mathbf{E}_{0z,0x}(\omega)$. To derive the polarizabilities' explicit forms, one can break the components of the total field $\boldsymbol{\mathcal{E}}_1(\mathbf{r},\omega) = \mathbf{E}_0(\omega)+\mathbf{E}_2(\mathbf{r},\omega)+\mathbf{E}_3(\mathbf{r},\omega)$ into terms that highlight the individual interactions between the system's components.

Starting with the target rod's scattered field, one can let $\mathbf{E}_2(\mathbf{r},\omega) = \hat{\mathbf{E}}_2^{(0)}(\mathbf{r},\omega)+\hat{\mathbf{E}}_2^{(1)}(\mathbf{r},\omega)$ be the sum of its responses to excitation by the synchrotron field (0) and the nearby tip (1). The hats signify that the components of the rod's scattered field include the effects of its coupling to the substrate through the use of its effective polarizability. The field of the rod induced by the polarized substrate, $\mathbf{E}_2^{(3)}(\mathbf{r},\omega)$, is therefore redundant and is neglected.

The terms $\hat{\mathbf{E}}_2^{(0,1)}(\mathbf{r},\omega) = -\nabla\int\rho_2^{(0,1)}(\mathbf{r}',\omega)/|\mathbf{r}-\mathbf{r}'|d^3r'$ are defined by the independent charge distributions of the rod, $\rho_2^{(0,1)}(\mathbf{r}',\omega) = -\mathbf{p}_2^{(0,1)}(\omega)\cdot\nabla'\delta(\mathbf{r}')$, that are produced by the two excitation sources. These charges encode the substrate's modification of the target's spectrum, such that $\mathbf{p}_2^{(0,1)}(\omega) = \hat{\alpha}_2(\omega)\mathbf{E}_{0x,1x}(\omega)$, wherein $\mathbf{E}_1(\mathbf{r},\omega)$ is the field produced by the polarized tip. Explicitly,

$$\begin{aligned}\mathbf{E}_1(\mathbf{r},\omega) &= -\nabla\int\frac{\rho_1(\mathbf{r}',\omega)}{|\mathbf{r}-\mathbf{r}'|}d^3r' \\ &= \nabla\int\frac{\left[\mathbf{p}_1^l(\omega)+\mathbf{p}_1^s(\omega)\right]}{|\mathbf{r}-\mathbf{r}'|}\cdot\nabla'\delta(\mathbf{r}'-\mathbf{r}_1)d^3r',\end{aligned} \tag{D.20}$$

which can be rewritten using integration by parts as

$$\begin{aligned}\mathbf{E}_1(\mathbf{r},\omega) = &\left(\frac{3(x+a_2)(z-[h-b_2])}{|\mathbf{r}-\mathbf{r}_1|^5}\hat{\mathbf{x}}+\frac{3y(z-[h-b_2])}{|\mathbf{r}-\mathbf{r}_1|^5}\hat{\mathbf{y}}-\frac{|\mathbf{r}-\mathbf{r}_1|^2-3(z-[h-b_2])^2}{|\mathbf{r}-\mathbf{r}_1|^5}\hat{\mathbf{z}}\right)p_1^l(\omega) \\ &+\left(-\frac{|\mathbf{r}-\mathbf{r}_1|^2-3(x+a_2)^2}{|\mathbf{r}-\mathbf{r}_1|^5}\hat{\mathbf{x}}+\frac{3(x+a_2)y}{|\mathbf{r}-\mathbf{r}_1|^5}\hat{\mathbf{y}}+\frac{3(x+a_2)(z-[h-b_2])}{|\mathbf{r}-\mathbf{r}_1|^5}\hat{\mathbf{z}}\right)p_1^s(\omega).\end{aligned} \tag{D.21}$$

In the limit where the rod is much longer than it is wide ($b_2 \ll a_2$) and also much longer than the tip's height above the substrate ($h \ll a_2$), $|z-h| \ll |x+a_2|$ for $\mathbf{r}$ near the origin. Therefore, when evaluating $\mathbf{E}_1(0,\omega)$ one can ignore all terms in D.21 except those that go

like $(x+a_2)^2/|\mathbf{r}-\mathbf{r}_1|$ to give

$$\mathbf{E}_1(0,\omega) \approx \frac{2\mathbf{p}_1^s(\omega)-\mathbf{p}_1^l(\omega)}{(a_2^2+[h-b_2]^2)^{\frac{3}{2}}}, \tag{D.22}$$

such that

$$\mathbf{p}_2^{(1)}(\omega) \approx \frac{2\hat{\alpha}_2(\omega)}{(a_2^2+[h-b_2]^2)^{\frac{3}{2}}}\mathbf{p}_1^s(\omega). \tag{D.23}$$

The target's scattered field $\mathbf{E}_2(\mathbf{r},\omega) = -\nabla\int[\rho_2^{(0)}(\mathbf{r}',\omega)+\rho_2^{(1)}(\mathbf{r}',\omega)]/|\mathbf{r}-\mathbf{r}'|d^3r'$ can then be rewritten as

$$\mathbf{E}_2(\mathbf{r},\omega) = \hat{\alpha}_2(\omega)\left(E_{0x}(\omega) - \frac{2\tilde{p}_1^s(\omega)}{(a_2^2+[h-b_2]^2)^{\frac{3}{2}}}\right)\nabla\int\frac{\hat{\mathbf{x}}\cdot\nabla'\delta(\mathbf{r}')}{|\mathbf{r}-\mathbf{r}'|}d^3r', \tag{D.24}$$

which simplifies at the location of the tip dipole to

$$\mathbf{E}_2(\mathbf{r}_1,\omega) \approx 2\hat{\alpha}_2(\omega)\frac{1}{(a_2^2+[h-b_2]^2)^{\frac{3}{2}}}\left[\mathbf{E}_{0x}(\omega) - \frac{2\mathbf{p}_1^s(\omega)}{(a_2^2+[h-b_2]^2)^{\frac{3}{2}}}\right]. \tag{D.25}$$

The substrate's scattered field can be expanded as $\mathbf{E}_3(\mathbf{r},\omega) = \mathbf{E}_3^{(0)}(\mathbf{r},\omega)+\mathbf{E}_3^{(1)}(\mathbf{r},\omega)$, wherein the term $\mathbf{E}_3^{(2)}(\mathbf{r},\omega)$ that details the substrate's response to the polarized rod is neglected. While this term is important for calculating the spectral response of the target rod, its influence on the tip's polarization is assumed to be minimal. The charge of the tip can be substituted for the charge of the target in Eq. D.17 to produce

$$\mathbf{E}_3^{(1)}(\mathbf{r}_1,\omega) = \frac{\beta(\omega)}{8h^3}\mathbf{p}_1^s(\omega)+\frac{\beta(\omega)}{4h^3}\mathbf{p}_1^l(\omega), \tag{D.26}$$

such that the tip dipole moments can be rewritten as

$$\mathbf{p}_1^l(\omega)\left(1-\frac{\alpha_1^l(\omega)\beta(\omega)}{4h^3}\right) = \left[\alpha_1^l(\omega)+\alpha_1^l(\omega)\beta(\omega)\right]\mathbf{E}_{0z}(\omega),$$

$$\mathbf{p}_1^s(\omega)\left(1-\frac{\alpha_1^s(\omega)\beta(\omega)}{8h^3}+\frac{4\alpha_1^s(\omega)\hat{\alpha}_2(\omega)}{(a_2^2+[h-b_2]^2)^3}\right) = \left(\alpha_1^s(\omega)+\frac{2\alpha_1^s(\omega)\hat{\alpha}_2(\omega)}{(a_2^2+[h-b_2]^2)^{\frac{3}{2}}}\right)\mathbf{E}_{0x}(\omega). \tag{D.27}$$

Rearrangement produces Eq. (5.1) of Section 5.3.

D.3 Oscillator Model of the Sample System

The construction of an oscillator model of the interactions of the polarized target rod and substrate begins with $\mathbf{p}_2(\omega)$. The dielectric function $\varepsilon_2(\omega) = 1 + \omega_{p2}^2/(\omega_2^2 - \omega^2 - i\omega\gamma_2)$ can be substituted into the polarizability $\alpha_2(\omega)$ to rewrite the definition of $\mathbf{p}_2(\omega)$ as

$$\mathbf{p}_2(\omega) = e\frac{C_2^3\omega_{p2}^2}{3e^2[A_{10}(X_2) - B_{10}(X_2)]}\frac{e\boldsymbol{\mathcal{E}}_{2x}(0,\omega)}{\omega_2^2 + \frac{A_{10}(X_2)\omega_{p2}^2}{A_{10}(X_2)-B_{10}(X_2)} - \omega^2 - \mathrm{i}\omega\gamma_2}, \tag{D.28}$$

wherein $A_{10}(X_2) = \mathcal{Q}_{10}(X_2)/\mathcal{P}_{10}(X_2)$ and $B_{10} = \psi^{(2)}(X_2)/\psi^{(1)}(X_2)$. If a plasmon oscillator coordinate $x(\omega) = p_2(\omega)/e$ is defined, Eq. D.28 can be rewritten as

$$x(\omega) = \frac{1}{m_2}\frac{e\mathcal{E}_{2x}(0,\omega)}{\Omega_2^2 - \omega^2 - \mathrm{i}\omega\gamma_2}, \tag{D.29}$$

where

$$\begin{aligned} m_2 &= \frac{3e^3[A_{10}(X_2) - B_{10}(X_2)]}{c_2^3\omega_{p2}^2}, \\ \Omega_2^2 &= \omega_2^2 + \frac{A_{10}(X_2)\omega_{p2}^2}{A_{10}(X_2) - B_{10}(X_2)}, \end{aligned} \tag{D.30}$$

are the mass and natural frequency of the coordinate. From the form of Eq. *D*.28, it is clear that $x(\omega)$ acts as a damped oscillator driven by the total external field $\boldsymbol{\mathcal{E}}_2(\mathbf{r},\omega) = \mathbf{E}_3^{(0)}(\mathbf{r},\omega) + \mathbf{E}_3^{(2)}(\mathbf{r},\omega)$, which includes the field set up by the substrate. The target can influence this field just as it is influenced by it, such that a definition of a substrate oscillator coordinate leads to a simple description of the coupled motion of the sample. This definition is most easily built from the potential set up above the substrate's surface by its polarization,

$$\Phi_3(\mathbf{r},\omega) = -\beta(\omega)\int\frac{\rho_2(\mathbf{r}',\omega) + \rho_0(\mathbf{r}',\omega)}{|\mathbf{r} - \mathbf{r}'_-|}d^3r', \tag{D.31}$$

where $\rho_0(\mathbf{r}',\omega)$ is the charge distribution generating the synchrotron light and $\rho_2(\mathbf{r}',\omega) = -\mathbf{p}_2(\omega)\cdot\nabla'\delta(\mathbf{r}')$ is the charge distribution of the target. Modeling the substrate as a simple Lorentz-model dielectric, $\varepsilon_3(\omega) = \varepsilon_{\infty 3} + \omega_{p3}^2/(\omega_3^2 - \omega^2 - i\omega\gamma_3)$, one finds

$$\beta(\omega) = \frac{\varepsilon_{\infty 3} - 1}{\varepsilon_{\infty 3} + 1} + \frac{\omega_{p3}^2}{(\varepsilon_{\infty 3} + 1)^2}\frac{1}{\omega_3^2 + \frac{\omega_{p3}^2}{\varepsilon_{\infty 3}+1} - \omega^2 - \mathrm{i}\omega\gamma_3}. \tag{D.32}$$

The second term resembles the RHS of Eq. D.28 and signifies that part of the substrate's polarization oscillates with a natural frequency $\omega_3^2 + \omega_{p3}^2/(\varepsilon_{\infty 3}+1)$ and a damping rate γ_3. The first is absent in Eq. D.28 and describes an instantaneous response to external stimuli. Analogous to the definition of $\tilde{x}$, one can map these two independent types of substrate motion onto two coordinates.

Their precise definitions stem simply from an expansion of the substrate's Green function, $1/|\mathbf{r}-\mathbf{r}'|$, into mode functions. Explicitly,

$$\frac{1}{|\mathbf{r}-\mathbf{r}'_-|} = \sum_{pm}(2-\delta_{m0})\int_0^\infty J_m(ks)J_m(ks')S_p(m\phi)S_p(m\phi')\mathrm{e}^{-k(z+z'+2b_2)}\,dk, \tag{D.33}$$

which can be simplified to $1/|\mathbf{r}-\mathbf{r}'_-| = \sum_{pm}\int_0^\infty \lambda_{pm}(k,\mathbf{r})\lambda_{pm}(k,\mathbf{r}')dk$ by using the mode functions

$$\lambda_{pm}(k,\mathbf{r}) = (2-\delta_{m0})J_m(ks)S_p(m\phi)\mathrm{e}^{-k(z+b_2)}. \tag{D.34}$$

These describe the spatial variations of the potentials of independent modes of the substrate's responses, both oscillatory and instantaneous. One can then describe the motion of the excited oscillatory modes of symmetry (p,m,k) with the motion of a coordinate $q_{pm}(k,\omega)$, and similarly do so for the substrate's instantaneous response with the coordinates $y_{pm}(k,\omega)$. With the explicit definitions

$$q_{pm}(k,\omega)+y_{pm}(k,\omega) = -\frac{d}{e}\beta(\omega)\int_{V_>}\lambda_{pm}(k,\mathbf{r}')\left[\rho_0(\mathbf{r}',\omega)+\rho_2(\mathbf{r}',\omega)\right]\,d^3r', \tag{D.35}$$

wherein integration is taken over $V_>$, the region above the substrate's surface, the substrate's scattered potential can be redefined as

$$\Phi_3(\mathbf{r},\omega) = \frac{e}{d}\sum_{pm}\int_0^\infty\left[q_{pm}(k,\omega)+y_{pm}(k,\omega)\right]\lambda_{pm}(k,\mathbf{r})dk. \tag{D.36}$$

Further, with the definitions of the forces

$$F_{pm}^{(i)}(k,\omega) = -\frac{e}{d^2}\int_{V_>}\rho_i(\mathbf{r}',\omega)\lambda_{pm}(k,\mathbf{r}')d^3r' \tag{D.37}$$

that describe the excitation of the modes (p, m, k) by the synchrotron field ($i = 0$) or target rod ($i = 2$), as well as the masses

$$M_m = (2 - \delta_{m0}) \frac{e^2(\varepsilon_{\infty 3} + 1)^2}{2\omega_{p3}^2 d^3}, \tag{D.38}$$

and natural frequencies

$$\Omega_3^2 = \omega_3^2 + \frac{\omega_{p3}^2}{(\varepsilon_{\infty 3} + 1)}, \tag{D.39}$$

the coordinates can be defined explicitly as mechanical oscillators:

$$\begin{aligned} q_{pm}(k, \omega) &= \frac{1}{M_m} \frac{F_{pm}^{(2)}(k, \omega) + F_{pm}^{(0)}(k, \omega)}{\Omega^3 - \omega^2 - \mathrm{i}\omega\gamma_3}, \\ y_{pm}(k, \omega) &= \frac{d^3}{e^2} \frac{\beta_\infty}{(2 - \delta_{m0})} \left(F_{pm}^{(2)}(k, \omega) + F_{pm}^{(0)}(k, \omega) \right) \end{aligned} \tag{D.40}$$

with $\beta_\infty(\omega) = [\varepsilon_{\infty 3} - 1]/[\varepsilon_{\infty 3} + 1]$.

The definition of $F_{pm}^{(0)}(k, \omega)$ in Eq. D.37 is inconvenient, as the form of the synchrotron's charge distribution is not simple. However, if one loosens the approximation made in Appendix D.2 and allows the synchrotron field to vary slowly over the substrate, integration by parts can be used to rewrite Eq. D.37 as

$$F_{pm}^{(0)}(k, \omega) = \frac{e}{4\pi d^2} \int_{V_>} \mathbf{E}_0(\mathbf{r}', \omega) \cdot \nabla \lambda_{pm}(k, \mathbf{r}') \, d^3 r' + \frac{e}{4\pi d^2} \int \mathbf{E}_0(\mathbf{r}', \omega) \cdot \hat{\mathbf{z}} \delta(z' + b_2) \lambda_{pm}(k, \mathbf{r}') \, d^3 r' \tag{D.41}$$

Letting ϵ be a small parameter with units of wavevector, the slowly-varying field can be written as $\mathbf{E}_0(\mathbf{r}', \omega) = (E_{0x}(\omega)\hat{\mathbf{x}} + E_{0z}(\omega)\hat{\mathbf{z}}) \mathrm{e}^{-\epsilon s'} \mathrm{e}^{-\epsilon |z + b_2|}$, which produces

$$F_{pm}^{(0)}(k, \omega) = (E_{0x}(\omega)\delta_{p0}\delta_{m1} - E_{0z}(\omega)\delta_{p0}\delta_{m0}) \frac{e\epsilon k}{2d^2} \frac{1}{(k + \epsilon)(k^2 + \epsilon^2)^{\frac{3}{2}}} + E_{0z}(\omega)\delta_{p0}\delta_{m0} \frac{e\epsilon}{2d^2} \frac{1}{(k^2 + \epsilon^2)^{\frac{3}{2}}}, \tag{D.42}$$

which is only nonzero for $p = 0$ and $m = \{0, 1\}$ [327]. Either of these terms is small for $k > \mathrm{e}\epsilon$, such that, with a very nearly uniform field ($\epsilon \ll 1$), only modes with small k are forced. Additionally, the latter term, which does not include a factor of $E_{0x}(\omega)$, is at minimum twice as large as the former. This agrees with the approximation of Appendix D.2 that the substrate's response to a uniform field only produces a response proportional to

the perpendicular component $E_{0z}(\omega)$. The first term is accordingly neglected such that the forces proportional to $F_{01}^{(0)}(k,\omega) \sim E_{0x}(\omega)$ are taken to be zero. Thus, the substrate remains driven by the synchrotron light only through the forces $F_{00}^{(0)}(k,\omega)$.

The coupling force $F_{pm}^{(2)}(k,\omega)$ between the target and substrate is more straightforward to produce from Eq. D.37. Letting $\rho_2(\mathbf{r}',\omega) = -ex(\omega)\hat{\mathbf{x}} \cdot \nabla'\delta(\mathbf{r}')$ in Eq. D.37, one finds via integration-by-parts

$$F_{pm}^{(2)}(k,\omega) = -\frac{e^2}{d^2}\delta_{p0}\delta_{m1}k\mathrm{e}^{-kb_2}x(\omega) \tag{D.43}$$

using the identities $\partial/\partial s\{J_m(ks)\} = (k/2)[J_{m-1}(ks) - J_{m+1}(ks)]$, $J_m(0) = \delta_{m0}$, $S_p(0) = \delta_{p0}$, and $(2-\delta_{m0})\delta_{m1} = 2\delta_{m1}$ while neglecting terms that go like $\delta_{m,-1}$. Clearly, then, all substrate modes with $p = 0$, $m = 1$, and $k \neq 0$ can push on the target. However, rather than continue to keep track of the individual motion of each substrate mode of wavenumber k, one can note that the modes of differing k but common (p,m) all have the same mass, natural frequency, and damping rate, such that they move in phase with each other when forced equally.

It makes the most sense to group all modes of common (p,m) into a single supermode with coordinate $Q_{pm}(\omega)$ or $Y_{pm}(\omega)$ that is independent of k. The most convenient definition of these new coordinates is

$$\begin{aligned} Q_{pm}(\omega) &= \sqrt{2db_2^3}\int_0^\infty k\mathrm{e}^{-kb_2}q_{pm}(k,\omega)\,dk, \\ Y_{pm}(\omega) &= \sqrt{2db_2^3}\int_0^\infty k\mathrm{e}^{-kb_2}y_{pm}(k,\omega)\,dk. \end{aligned} \tag{D.44}$$

The forces that act on these new coordinates are then

$$\mathcal{F}_{pm}^{(i)}(\omega) = \sqrt{2db_2^3}\int_0^\infty k\mathrm{e}^{-kb_2}F_{pm}^{(i)}(k,\omega)\,dk \tag{D.45}$$

such that

$$\begin{aligned} Q_{pm}(\omega)\left(\Omega_3^2 - \omega^2 - \mathrm{i}\omega\gamma_3\right) &= \frac{\mathcal{F}_{pm}^{(0)}(\omega)}{M_m} - \frac{e^2\delta_{p0}\delta_{m1}x(\omega)}{M_m\sqrt{8d^3b_2^3}}, \\ Y_{pm}(\omega) &= \frac{d^3}{e^2}\frac{\beta_\infty\mathcal{F}_{pm}^{(0)}(\omega)}{2-\delta_{m0}} - \sqrt{\frac{d^3}{8b_2^3}}\beta_\infty x(\omega) \end{aligned} \tag{D.46}$$

wherein the identity

$$\int_0^\infty k^n \mathrm{e}^{-nkb_2} dk = \frac{(n-1)!}{n^n b_2^{n+1}} \tag{D.47}$$

has been employed. Further, with

$$\begin{aligned} \mathbf{E}_3(0,\omega) = -\frac{e}{d}\sum_{pm}\int_0^\infty \frac{k}{2}\mathrm{e}^{-kb_2}\left[q_{pm}(k,\omega)+y_{pm}(k,\omega)\right] \\ \times\left(\delta_{p0}\delta_{m1}\hat{\mathbf{x}}-2\delta_{p0}\delta_{m0}\hat{\mathbf{z}}\right)dk, \end{aligned} \tag{D.48}$$

the target coordinate becomes

$$x(\omega)\left(\Omega_2^2-\omega^2-\mathrm{i}\omega\gamma_2\right) = \frac{e\mathbf{E}_0(\omega)\cdot\hat{\mathbf{x}}}{m_2} - \frac{e^2}{m_2\sqrt{8d^3b_2^3}}Q_{01}(\omega) - \frac{e^2}{m_2\sqrt{8d^3b_2^3}}Y_{01}(\omega). \tag{D.49}$$

The definitions of the coordinates can be combined and simplified by eliminating the coordinates Y_{01}, which do not carry their own degrees of freedom. Inserting the definition of Y_{pm} from Eq. D.46 into Eq. D.49 and recognizing that all $\mathcal{F}_{pm}^{(0)}(\omega)$ are zero for $(p,m)\neq(0,0)$, one finds

$$\begin{aligned} x(\omega)\left(\bar{\Omega}_2^2-\omega^2-\mathrm{i}\omega\gamma_2\right) - \frac{g}{m_2}Q_{01}(\omega) &= \frac{F_0(\omega)}{m_2} \\ Q_{01}(\omega)\left(\Omega_3^2-\omega^2-\mathrm{i}\omega\gamma_3\right) - \frac{g}{M_1}x(\omega) &= 0, \\ Q_{p,m\neq0,1}(\omega)\left(\Omega_3^2-\omega^2-\mathrm{i}\omega\gamma_3\right) &= \frac{\mathcal{F}_{p,m\neq0,1}^{(0)}(\omega)}{M_1}, \end{aligned} \tag{D.50}$$

where $F_0(\omega)=eE_{0x}(\omega)$ is the synchrtron's force onto the target rod and $g=-e^2/\sqrt{8d^3b_2^3}$ is the coupling strength of the target-substrate system. Moreover, $\bar{\Omega}_2^2=\Omega_2^2-\beta_\infty e^2/8b_2^3m_2$ is the lowered resonance frequency of the rod, which is redshifted from its free-space value by the target's interaction with the static response of the substrate.

From Eq. D.50, it is clear that the target rod is coupled only to the $(p,m)=(0,1)$ supermode of the substrate, while the remaining substrate modes are driven only by the external field. This simple, bilinear coupling allows for the definition of hybridized modes

$$\begin{aligned} x_+(\omega) &= x(\omega)\cos\theta + Q_{10}(\omega)\sin\theta, \\ x_-(\omega) &= -x(\omega)\sin\theta + Q_{10}(\omega)\cos\theta \end{aligned} \tag{D.51}$$

that have resonance frequencies $\Omega_{\pm}(\theta)$ determined by the mixing angle θ defined in Section 5.4.

D.4 Relation of Oscillator Model and Effective Polarizability

Conversion of the oscillator model in Appendix D.3 to an effective polarizability is straightforward if one begins with Eq. D.50. Omitting the subscripts on the substrate coordinate and allowing $M_1 = m_3$, the substrate coordinate's equation of motion can be rearranged to read

$$Q(\omega) = x(\omega)\frac{g}{m_3}\frac{1}{\Omega_3^2 - \omega^2 - \mathrm{i}\omega\gamma_3}. \tag{D.52}$$

Plugging this back into the rod coordinate's equation of motion, expanding $\bar{\Omega}_2^2 = \Omega_2^2 - \beta_\infty e^2/8b_2^3 m_2$, and letting $\alpha_2(\omega) = e^2/m_2(\Omega_2^2 - \omega^2 - \mathrm{i}\omega\gamma_2)$, one finds

$$x(\omega)\left[1 - \alpha_2(\omega)\frac{\beta_\infty}{8b_2^3} - \alpha_2(\omega)\frac{e^2}{8d^3b_2^3m_3}\frac{1}{\Omega_3^2 - \omega^2 - \mathrm{i}\omega\gamma_3}\right] = \alpha_2(\omega)\frac{F_0(\omega)}{e^2} \tag{D.53}$$

Furthermore, from Eqs. D.35, D.37, and D.40, it can be concluded that

$$\beta(\omega) = \frac{e^2}{m_3 d^3}\frac{1}{\Omega_3^2 - \omega^2 - \mathrm{i}\omega\gamma_3} + \beta_\infty, \tag{D.54}$$

which quickly leads to

$$x(\omega) = \alpha_2(\omega)\frac{1}{1 - \alpha_2(\omega)\beta(\omega)/8b_2^3}\frac{F_0(\omega)}{e^2}. \tag{D.55}$$

With $p_2(\omega) = ex(\omega)$ and $F_0(\omega) = eE_{0x}(\omega)$, one can immediately reconcile Eq. D.55 with Eq. 5.2.

D.5 Additional Experimental Details

The SINS observables for the SiO_2 substrate (see Fig. D.1) are collected by moving the AFM tip over a bare section of the substrate, away from any lithographed rod features, and taking a point spectra at the second harmonic. The SINS observables for the hBN substrate (see Fig. D.2) are collected in a similar manner. In both instances, the magnitude is shown in red and the phase in blue.

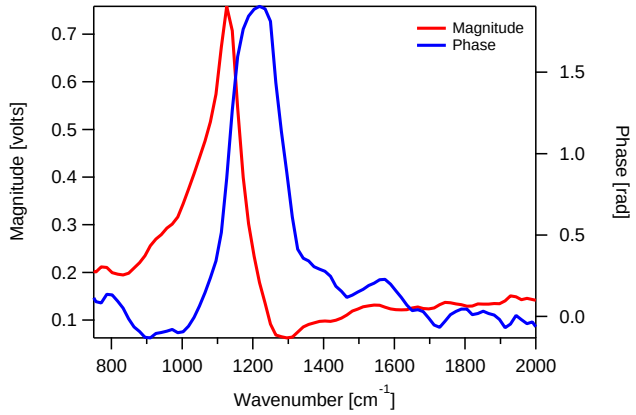

Figure D.1: SINS observables of 100 nm SiO_2 on Si.

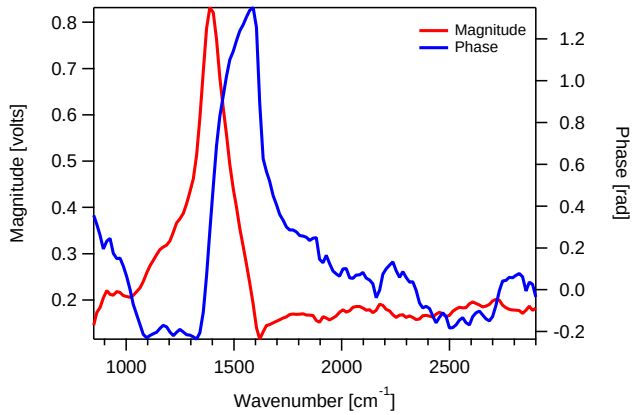

Figure D.2: SINS observables of 330 nm hBN on Si.

The length of each rod used to create the phase waterfall plot (Fig. 3 of the main text) are reported in Table D.1. They are extracted directly from AFM images taken immediately before the SINS measurements.

While the main text utilizes the SINS magnitude observable for figures 3 and 4, the same trends are recovered from the phase observable which are shown here in figures D.3 and D.4. The asymptotic energies of the branches in the avoided crossing are at 1234 and 1018 cm^{-1}

for SiO_2 and 1527 and 1296 cm^{-1} for hBN.

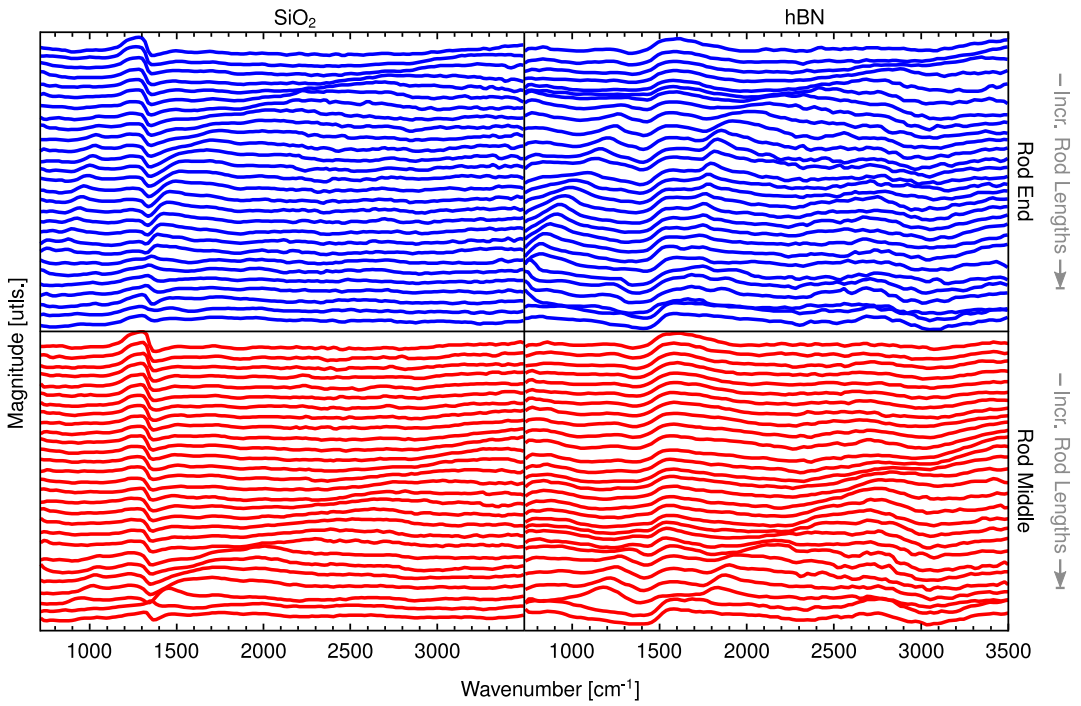

Figure D.3: SINS phase spectra from a series of nanorods ($L = 0.7 - 10.0$ μm) obtained at the end (blue traces) or middle (red traces) of the nanorod on SiO_2 (first column) and hBN (second column) substrates. The spectrum obtained from the shortest nanorod is plotted at the top in each panel with longer nanorod spectra vertically offset until the longest nanorod in each series is plotted at the bottom.

To gain a better understanding of when a F-P mode and a SPhP are at zero detuning, the separation between peaks in the avoided crossing (main text, Fig. 4) are calculated and the minimal values are reported for each F-P mode on each substrate. These results are summarized in Table D.2 along with the length of rod supporting the associated F-P mode and its peak resonance positions.

We highlight the reproducibility of our data by presenting a second avoided crossing diagram created from mixing gold rod F-P modes with a SPhP on a 100 nm thick SiO_2 substrate. Here we extract peak positions from data taken during separate visits to the ALS nearly half a year apart. The most recent experiments, those presented here as part of figure D.3, are shown in figure D.5 as red and blue markers representing the $m = 1$ and $m = 2$ F-P modes as before. The green (pink) dots represent the $m = 1$ ($m = 2$) F-P mode extracted from the previous data. With both experiments plotted on the same axes, the anti-crossing behaviour is clearly visible.

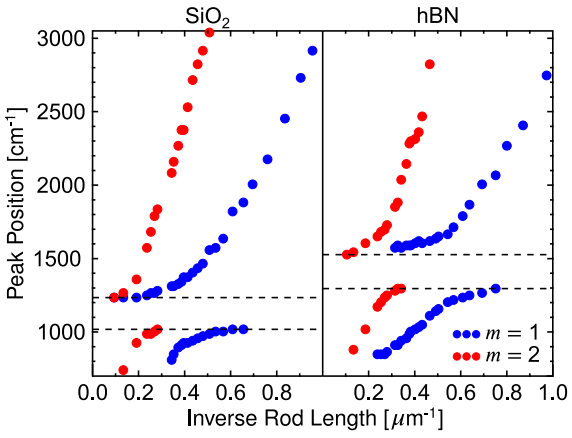

Figure D.4: Avoided crossing diagram derived from the SINS phase measurements for the complete nanorod series on both SiO_2 and hBN substrates. The $m = 1$ (blue) and $m = 2$ (red) F-P modes are plotted versus inverse nanorod length. Dotted black lines are the asymptotic energies.

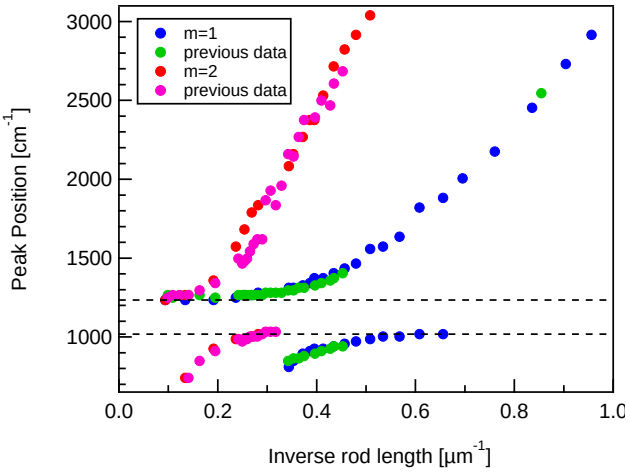

Figure D.5: Avoided crossings in SINS phase of Au rods on a 100 nm SiO_2 substrate, taken during two separate visits to ALS.

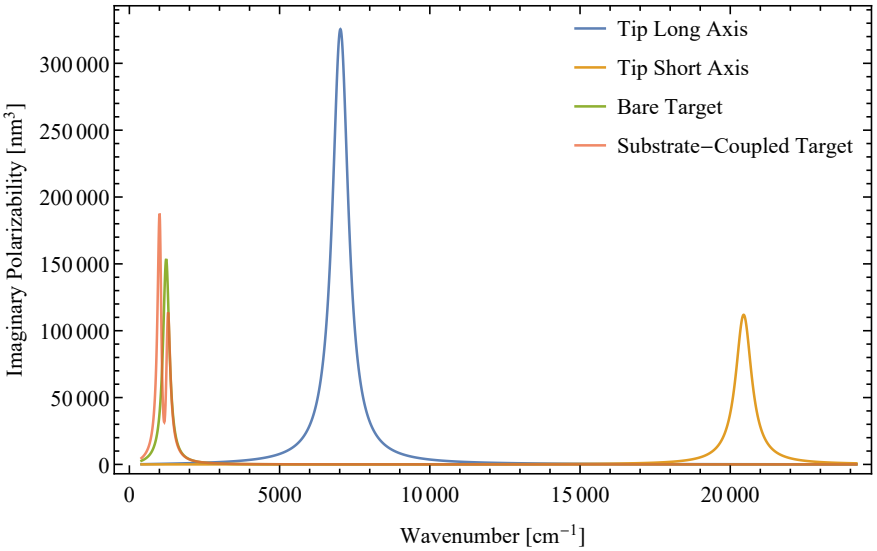

Figure D.6: A comparison of the spectral responses of the PtSi tip's long-axis (blue) and short-axis (yellow) dipoles as well as target nanorod's polarizability in free space (green) and in the presence of an SiO_2 substrate (red) as calculated by the analytical model.

Rod Length [nm]	
SiO_2 series	hBN series
772	815
881	906
1046	1028
1106	1149
1196	1249
1315	1331
1438	1443
1525	1567
1644	1643
1762	1760
1871	1841
1968	1987
2086	2034
2191	2148
2301	2311
2420	2396
2529	2487
2589	2610
2688	2654
2835	2752
2908	2933
3550	3066
3940	3180
4230	3576
5230	3720
7460	3950
10650	4210
	7480
	9560

Table D.1: Measured rod lengths, in nm, for each reported spectra in Fig. 3.

	SiO_2 substrate		hBN substrate	
Rod Length [nm]	1968	3940	1841	3720
F-P mode	m=1	m=2	m=1	m=2
Upper Peak Resonance[cm^{-1}]	1358	1373	1620	1651
Lower Peak Resonance [cm^{-1}]	957	957	1142	1157
Peak Separation [cm^{-1}]	401	417	478	494

Table D.2: Minimum split peak separation between the respective F-P and substrate SPhP from SINS magnitude spectra.